Adam Mickiewicz University in Poznań
Faculty of Physics and Astronomy
Division of Molecular Biophysics

Light Conversion in Photosystem I-based Artificial Systems

A thesis submitted in partial fulfillment of the requirements for the degree of Doctor in Physics

Mgr Alice Goyal Wypychowska

Phd Supervisor:
Dr hab. Krzysztof Gibasiewicz, prof. UAM

PhD Co-supervisor:
Dr Sebastian Szewczyk

Poznań, June 2025

Acknowledgements

I would like to express my deepest gratitude to everyone who has been part of this journey.

First and foremost, I would like to thank my husband, whose constant support, patience, and belief in me have been my greatest source of strength. His encouragement and understanding, even during the most challenging times, especially during the final stage of writing the thesis have made this journey possible.

I am grateful to my supervisor, prof. UAM dr. hab. Krzysztof Gibasiewicz, for his invaluable guidance and mentorship. I feel fortunate to be given the freedom and the constant support to be able explore different ideas throughout my research. It allowed me to develop skills necessary to conduct independent research. I would also like to mention my co-supervisor, dr. Sebastian Szewczyk for passing on his expertise in the field of photosynthesis research and his valuable input, which have significantly contributed to the success of this work.

A special thanks to my colleagues and fellow researchers, whose collaboration and discussions have made this journey both intellectually stimulating and enjoyable. The friendships I have built along the way have made the occasional long hours in the lab and research hurdles much more bearable.

I am grateful to my parents for their faith, love, encouragement, and support that have paved the way for my academic and personal growth.

Lastly, a very special mention to my little niece, whose boundless energy, joy, and facetime calls have been a constant source of positivity and inspiration.

Table of contents

ACKNOWLEDGEMENTS **3**
ABSTRACT **7**
STRESZCZENIE **9**
LIST OF FIGURES **11**
LIST OF TABLES **18**
LIST OF ABBREVIATIONS **19**
LIST OF FREQUENTLY USED SYMBOLS **21**
LIST OF PUBLICATIONS **23**

CHAPTER 1: INTRODUCTION **24**

1.1 BACKGROUND AND MOTIVATION **24**
1.2 SCOPE AND SIGNIFICANCE OF THE RESEARCH **25**
1.3 PHOTOSYNTHESIS AND ENERGY STORAGE **26**
1.4 BIOPHOTOVOLTAICS BASED ON PHOTOSYSTEM I **30**
1.4.1 PHOTOVOLTAICS 30
1.4.2 BIOPHOTOVOLTAICS 32
1.5 NANOPARTICLES AND THEIR USE IN BIOPHOTOVOLTAICS **34**
1.6 OBJECTIVES OF THE STUDY **35**
1.7 OVERVIEW OF THE THESIS STRUCTURE **36**

CHAPTER 2: LITERATURE REVIEW: ENHANCING EFFICIENCY OF PHOTOSYSTEM I-BASED BIOHYBRID SOLAR CELLS **37**

2.1 INTRODUCTION **37**
2.2 PROGRESS IN PHOTOCURRENT GENERATION IN PSI-BASED BIOHYBRID DEVICES **37**
2.3 ADVANCEMENTS IN PSI-NANOMATERIALS BASED HYBRID SYSTEMS **40**
2.4 STUDY OF EXCITATION DYNAMICS OF METAL NANOPARTICLES ALONE AND SYSTEMS INTEGRATING PSI AND AGNPS BY TIME-RESOLVED ULTRAFAST SPECTROSCOPY **47**

CHAPTER 3: METHODOLOGY **49**

3.1 INTRODUCTION **49**
3.2 PREPARATION OF PSI PARTICLES **49**
3.3 PREPARATION OF PSI PARTICLES FOR STUDIES IN SOLUTION AND FABRICATION OF PSI-FTO CONDUCTING GLASS ELECTRODES **50**
3.4 FABRICATION OF SILVER NANOPARTICLES **51**
3.5 APPROACHES TOWARDS FABRICATION OF PHOTOSYSTEM I-SILVER NANOPARTICLES COMPLEXES **55**
3.5.1 COMPLEXATION OF PSI PARTICLES AND HYDROPHILIC AGNPS IN SOLUTION 55
3.5.2 FABRICATION OF PSI-AGNPS FILMS ON FTO SUBSTRATES 56
3.5.2.1 PSI electrodeposition on FTO coated with hydrophobic AgNPs (PSI-(Ag-FTO)) 56
3.5.2.2 PSI electrodeposition on FTO coated with hydrophilic AgNPs (PSI-(Ag-MPA)-FTO) 57
3.5.2.3 PSI electrodeposition on 3-MPA-treated FTO coated with hydrophobic AgNPs (PSI-Ag-(MPA-FTO)) 59

3.5.2.4 PSI electrodeposition on 3-MPA-treated Ag-FTO substrates (PSI-MPA-(Ag-FTO)) 59
3.6 OPTICAL SPECTROSCOPY TECHNIQUES 61
3.6.1 STEADY STATE ABSORPTION 61
3.6.2 FLUORESCENCE 61
3.6.3 DYNAMIC LIGHT SCATTERING 61
3.6.4 TRANSIENT ABSORPTION SPECTROSCOPY 61
3.6.4.1 Millisecond transient absorption spectroscopy 62
3.6.4.2 Ultrafast transient absorption spectroscopy 63
3.7 MICROSCOPIES 65
3.7.1. TRANSMISSION ELECTRON MICROSCOPY 65
3.7.2 ATOMIC FORCE MICROSCOPY 65
3.7.3 SCANNING ELECTRON MICROSCOPY 65
3.8 PHOTOELECTROCHEMICAL MEASUREMENTS 66

CHAPTER 4: RESULTS AND DISCUSSIONS 67

4.1 INTRODUCTION 67
4.2 ELECTRON TRANSFER IN AND AROUND PHOTOSYSTEM I IN SOLUTION AND IMMOBILIZED ON FTO CONDUCTING GLASS 68
4.2.1 ELECTRON TRANSFER IN AND AROUND PHOTOSYSTEM I SOLUBILIZED IN AQUEOUS SOLUTIONS 68
4.2.1.1 Control photocurrent measurements 68
4.2.1.2 Time-resolved absorption measurements 70
4.2.1.2.1 Exploring P^+ decay kinetics: dependence on exogenous mediators (sodium ascorbate and DCPIP) 70
4.2.1.2.2 Exploring P^+ decay kinetics: systematic comparison across multiple experimental conditions 78
4.2.1.2.3 Conclusions from studies on electron transfer in Photosystem I solubilized in aqueous solutions 83
4.2.2 ELECTRON TRANSFER IN A BIO-PHOTOELECTRODE BASED ON PHOTOSYSTEM I MULTILAYER IMMOBILIZED ON THE CONDUCTING GLASS 83
4.2.2.1 Photocurrent measurements 83
4.2.2.2 Time-resolved absorption measurements 86
4.3 COMPARISON OF TIME-RESOLVED ABSORPTION AND PHOTOCURRENT RESULTS OBSERVED FOR CMH PSI IN SOLUTION AND IMMOBILIZED ON FTO 96
4.4 CHARACTERIZATION OF COLLOIDAL SILVER NANOPARTICLES 98
4.4.1 STEADY-STATE ABSORPTION SPECTRA AND STABILITY OF SILVER NANOPARTICLES 98
4.4.2 FLUORESCENCE SPECTRA 101
4.4.3 DYNAMIC LIGHT SCATTERING - DETERMINATION OF SIZE OF SILVER NANOPARTICLES 103
4.4.4 TRANSMISSION ELECTRON MICROSCOPY - DETERMINATION OF SIZE AND AGGREGATION OF SILVER NANOPARTICLES 105
4.5 OUTCOMES OF COMPLEXING PSI WITH BOTH HYDROPHOBIC AND HYDROPHILIC AGNPS 106
4.5.1 COMPLEXATION OF PSI PARTICLES AND HYDROPHILIC AGNPS-F127 IN SOLUTION 106
4.5.2 CHARACTERIZATION OF PSI-AGNPS FILMS ON FTO SUBSTRATES 110
4.5.2.1 PSI electrodeposited on FTO coated with hydrophobic AgNPs (PSI-(Ag-FTO)) 110
4.5.2.2 PSI electrodeposition on FTO coated with hydrophilic/hydrophobic AgNPs with 3-MPA as a linker 123
4.5.2.2.1 PSI electrodeposition on (Ag-MPA)-FTO – (PSI-(Ag-MPA)-FTO) 124

4.5.2.2.2 PSI electrodeposition on 3-MPA treated FTO coated with hydrophobic AgNPs – (PSI-Ag-(MPA-FTO)) 126
4.5.2.2.3 PSI electrodeposition on 3-MPA treated Ag-FTO substrates – (PSI-MPA-(Ag-FTO)) 128

CHAPTER 5: CONCLUSION 130

5.1 CONCLUSIONS 130
5.2 LIMITATIONS OF THE STUDY AND FUTURE RECOMMENDATIONS 131
APPENDIX 132
REFERENCES 133

JOURNAL CONTRIBUTION 145

Abstract

Photosystem I (PSI) is a protein-pigment complex found in oxygenic photosynthetic organisms such as higher plants, algae, and cyanobacteria. It is the photoactive protein most commonly used in artificial biophotovoltaic devices due to its exceptionally high internal quantum efficiency (IQE) close to 100%. The efficiency of biophotovoltaic devices, especially those based on PSI, is constantly increasing. However, it still remains low compared to traditional photovoltaic cells, not to mention the natural efficiency of PSI.

The first objective of this thesis was to find the reasons for the limited internal quantum efficiency (IQE) of photocurrent generation in PSI-FTO based photovoltaic devices, which is below 1%. For this purpose, electron transfer (ET) reactions in and around PSI were studied using time-resolved absorption spectroscopy. PSI protein was studied in two artificial systems: as a thin layer covering an FTO conducting glass plate (PSI-FTO) and, as a control, in an aqueous solution. The results obtained from the kinetics of the oxidized primary P^+ donor decay using millisecond time-resolved absorption spectroscopy (for *C. merolae* PSI both in solution and immobilized on FTO) and photocurrent measurements (for the PSI-FTO system) were compared. The first observation from the absorption change studies was that the fraction of proteins in solution capable of charge separation in the presence of mediators was 100%, whereas this fraction decreased to 10–35% when PSI particles were deposited on FTO, with the range being determined by the concentration of redox mediators in solution and the electrical potential applied to the PSI-FTO electrode. The second observation was that in solution, charge recombination was observed in 98% of PSI proteins, while for PSI on FTO it was difficult to precisely determine this value. Consequently, only 2% of PSI proteins in solution were able to transfer an electron outside of PSI. It was estimated that the corresponding fraction of PSI proteins deposited on FTO, capable of transferring an electron to the electrolyte, was only 0.4% (at a strongly negative PSI-FTO electrode potential, -180 mV). At the open circuit potential (OCP) this value was even lower – 0.14%. These fractions, 0.14% at OCP and 0.4% at -180 mV, estimated from the results of transient absorption experiments for PSI-FTO electrodes, correspond well to the internal quantum efficiencies (IQE), estimated from photocurrent measurements for the same electrodes, equal to 0.073% and 0.47% at the corresponding potentials. In summary, the main reason for the limited efficiency of photocurrent generation in the PSI-FTO-based systems was the too slow electron transfer between PSI and the electrolyte and between PSI and the FTO substrate compared to the charge recombination rate in PSI.

The second objective of the thesis was to improve the low efficiency of PSI-containing biophotovoltaic systems by using the surface plasmon resonance of silver nanoparticles (AgNPs), which have been reported in the literature as the plasmon antennas for PSI complexes, increasing the efficiency of light absorption by PSI. For this purpose, uniform hydrophobic AgNPs as well as hydrophilic AgNPs coated with different detergents (pluronic F127 and P123 and β-DM) were prepared and characterized. Among them, AgNPs-F127 systems showed the highest stability and were used for attempts to form PSI-AgNP complexes in solution as well as in thin films. However, steady state absorption and fluorescence measurements did not reveal any signature of interaction between PSI from *C. merolae* and AgNPs-F127 in solution. Then, PSI particles from the cyanobacterium *Synechocystis sp.* PCC 6803 were immobilized on FTO plates coated with hydrophobic AgNPs (Ag-FTO electrodes) as substrates. The fabricated three-component PSI-(Ag-FTO) electrodes were investigated using ultrafast transient absorption spectroscopy.

Systematic comparison of normalized decay associated spectra (DAS) obtained from the fits of the experimental results for PSI-(Ag-FTO) and Ag-FTO electrodes in the blue part of the spectrum (475-630 nm) revealed some differences in spectral shapes and lifetimes. The signal from Ag-FTO was characterized by a shorter lifetime (12 ps) band with a maximum at 522 nm, whereas the corresponding DAS spectrum for PSI-(Ag-FTO) had a broader band, with a maximum shifted to ~546 nm and was characterized by a longer lifetime (~21 ps). This broadening and red shift by 24 nm as well as the extension of the lifetime from 12 to 21 ps can be interpreted as an increased absorption in the 500-600 nm region caused by the interaction between PSI and AgNPs. It can be hypothesized that the light energy absorbed due to this additional absorption is delivered to the reaction centre (RC) and used to increase the charge separation efficiency in the RC. Contrary to this expected effect, the comparison of the photocurrents measured in photoelectrochemical cells containing either PSI-FTO or PSI-(Ag-FTO) electrodes showed that the silver nanoparticle layer did not improve the photovoltaic efficiency of the PSI-based system. It is possible that the positive effect of silver nanoparticles present in the PSI-(Ag-FTO) electrode on the absorption is compensated by the additional negative effect of their presence on the photocurrent generation related to some undiscovered mechanism.

In order to force the interaction between PSI and AgNPs, we also tested 3-mercaptopropionic acid (3-MPA) as a linker between these components. It has been suggested in the literature that the alkyl chain of the 3-MPA molecule resembles the environment of a biological membrane, i.e., a lipid bilayer containing hydrocarbon chains, which would help in the interaction with the PSI protein without causing its denaturation. However, none of the procedures performed using 3-MPA as a linker to facilitate the attachment of silver nanoparticles to PSI gave steady-state absorption spectra clearly showing the interaction between PSI and AgNPs.

Streszczenie

Fotosystem I (PSI – ang. photosystem I) to kompleks białkowo-pigmentowy występujący w organizmach fotosyntetycznych tlenowych, takich jak rośliny wyższe, glony i sinice. Jest to białko fotoaktywne najczęściej wykorzystywane w sztucznych urządzeniach biofotowoltaicznych ze względu na wyjątkowo wysoką naturalną wydajność kwantową bliską 100%. Wydajność urządzeń biofotowoltaicznych, w szczególności tych opartych na PSI, stale rośnie. Nadal jednak pozostaje niska w porównaniu do tradycyjnych ogniw fotowoltaicznych, nie wspominając naturalnej wydajności PSI.

Pierwszym celem tej rozprawy było znalezienie przyczyn ograniczonej wewnętrznej wydajności kwantowej (IQE – ang. internal quantum efficiency) generowania fotoprądu w urządzeniach fotowoltaicznych opartych na białkach PSI zdeponowanych na płytce ze szkła przewodzącego (PSI-FTO; FTO – ang. fluorine tin oxide – cienka warstwa przewodząca na powierzchni płytki szklanej). Wydajność ta wynosi poniżej 1%. W tym celu badano reakcje przenoszenia elektronów (ET – ang. electron transfer) w i wokół PSI przy użyciu czasowo-rozdzielczej spektroskopii absorpcyjnej. Białko PSI było badane w dwóch sztucznych układach: w postaci cienkiej warstwy pokrywającej płytkę ze szkła przewodzącego (PSI-FTO) oraz, kontrolnie, w roztworze wodnym. Porównano wyniki uzyskane z badań kinetyki zaniku utlenionego pierwotnego donora P^+ przy użyciu czasowo-rozdzielczej spektroskopii absorpcyjnej w milisekundowej skali czasu (dla białka PSI z czerwonego glonu z *C. merolae* zarówno w roztworze, jak i unieruchomionego na FTO) i pomiarów fotoprądu (dla układu PSI-FTO). Pierwszą obserwacją z badań zmian absorpcji było to, że frakcja białek w roztworze zdolnych do rozdzielenia ładunku w obecności mediatorów wynosiła 100%, natomiast frakcja ta zmniejszyła się do 10–35%, gdy cząstki PSI były osadzane na FTO, przy czym zakres ten wynikał z zależności od stężenia mediatorów redoks w roztworze i potencjału elektrycznego przyłożonego do elektrody PSI-FTO. Drugim spostrzeżeniem było to, że w roztworze rekombinację ładunku zaobserwowano w 98% białek PSI, podczas gdy dla PSI na FTO trudno było precyzyjnie określić tę wielkość. W konsekwencji, tylko 2% białek PSI w roztworze było w stanie przenieść elektron poza PSI. Oszacowano, że analogiczna frakcja białek PSI osadzonych na FTO, zdolnych do przeniesienia elektronu do elektrolitu, wyniosła zaledwie 0.4% (przy silnie ujemnym potencjale elektrody PSI-FTO, -180 mV). Przy potencjale obwodu otwartego (OCP – ang. open circuit potential) wartość ta była jeszcze niższa – 0.14%. Te frakcje, 0,14% dla OCP i 0,4% dla -180 mV, oszacowane na podstawie wyników eksperymentów absorpcji przejściowej dla elektrod PSI-FTO, dość dobrze odpowiadają wewnętrznym wydajnościom kwantowym (IQE), oszacowanym na podstawie pomiarów fotoprądu dla tych samych elektrod, równym 0,073% i 0,47% przy odpowiednich potencjałach. Podsumowując, główną przyczyną ograniczonej wydajności generowania fotoprądu w układach opartych na elektrodach PSI-FTO był zbyt wolny transfer elektronów pomiędzy PSI a elektrolitem i pomiędzy PSI a podłożem FTO w porównaniu z szybkością rekombinacji ładunku w PSI.

Drugim celem rozprawy było poprawienie niskiej wydajności systemów biofotowoltaicznych zawierających PSI poprzez wykorzystanie powierzchniowego rezonansu plazmonowego nanocząstek srebra (AgNPs – ang. Ag nanoparticles), o których donoszono w literaturze, że mogą stanowić anteny plazmonowe dla kompleksów PSI zwiększające efektywność absorpcji światła przez te kompleksy. W tym celu wytworzono i scharakteryzowano jednolite hydrofobowe AgNPs a także hydrofilowe AgNPs pokryte różnymi detergentami (pluroniki F127 i P123 oraz β-DM).

Spośród nich, układy AgNPs-F127 wykazywały najwyższą stabilność i były stosowane do prób tworzenia kompleksów PSI-AgNP w roztworze wodnym, jak również w cienkich warstwach. Jednakże stacjonarne pomiary absorpcji i fluorescencji nie wykazały żadnej interakcji między PSI pochodzącym z *C. merolae* a AgNPs-F127 w roztworze. Następnie cząstki PSI z sinicy *Synechocystis sp.* PCC 6803 zostały unieruchomione na substratach w postaci płytek FTO powleczonych hydrofobowymi AgNPs (elektrody Ag-FTO). Wytworzone elektrody trójskładnikowe, oznaczone jako PSI-(Ag-FTO), zostały przebadane przy użyciu ultraszybkiej spektroskopii absorpcji przejściowej. Systematyczne porównanie znormalizowanych widm zaniku DAS (DAS – ang. decay associated spectra) uzyskanych z dopasowań wyników eksperymentalnych dla elektrod PSI-(Ag-FTO) i Ag-FTO w niebieskiej części widma (475-630 nm) wykazało pewne różnice w kształtach widm i czasach życia. Sygnał od Ag-FTO charakteryzował się krótszym czasem życia (12 ps) i pasmem z maksimum przy 522 nm, natomiast odpowiednie widmo DAS dla PSI-(Ag-FTO) miało szersze pasmo, z maksimum przesuniętym do ~546 nm i charakteryzowało się wydłużonym czasem życia (~21 ps). To poszerzenie i przesunięcie ku czerwieni o 24 nm oraz wydłużenie czasu życia z 12 do 21 ps można interpretować jako zwiększoną absorpcję w obszarze 500-600 nm spowodowaną interakcją między PSI i AgNP. Można postawić hipotezę, że energia światła pochłonięta dzięki tej dodatkowej absorpcji jest dostarczana do centrum reakcji (RC – ang. reaction center) i wykorzystywana do zwiększenia efektywności rozdzielenia ładunku w RC. Wbrew temu spodziewanemu efektowi, porównanie wartości fotoprądów generowanych w układach zawierających elektrody PSI-FTO i PSI-(Ag-FTO) wykazało, że warstwa nanocząstek srebra nie poprawiła wydajności fotowoltaicznej układu na bazie PSI. Być może pozytywny wpływ nanocząstek srebra obecnych w elektrodzie PSI-(Ag-FTO) na absorpcję jest niwelowany dodatkowym niekorzystnym wpływem ich obecności na generację fotoprądu związanym z jakimś nieodkrytym mechanizmem.

W celu wymuszenia oddziaływania między PSI i AgNP, przetestowaliśmy również kwas 3-merkaptopropionowy (3-MPA – ang. mercaptopropionic acid) jako łącznik między tymi składnikami. W literaturze sugerowano, że łańcuch alkilowy cząsteczki 3-MPA przypomina środowisko błony biologicznej, tj. dwuwarstwy lipidowej zawierającej łańcuchy węglowodorowe, co ma pomóc w interakcji z białkiem PSI bez powodowania jego denaturacji. Jednak żadne procedury wykonane przy użyciu 3-MPA jako łącznika ułatwiającego przyłączenie nanocząstek srebra do PSI nie dały stacjonarnych widm absorpcji wyraźnie pokazujących interakcję między PSI i AgNP.

List of figures

Chapter 1

Figure 1.1 Illustration of four phases in photosynthesis process for energy storage and transfer combined into light-dependent and light-independent reactions.

Figure 1.2 A part of a natural molecular photosynthetic apparatus, including PSI embedded in a thylakoid membrane.

Figure 1.3 Energetic-kinetic-distance scheme of forward (solid arrows) and backward (charge recombination; dashed arrows) PSI ET reaction with their time constants.

Figure 1.4 Best research cell efficiency chart displaying the emerging PV as highlighted from 1975 until present tested by NREL.

Figure 1.5 (a) A part of a natural molecular photosynthetic apparatus, including PSI embedded in a thylakoid membrane and **(b)** Working principle of a biophotovoltaic system.

Figure 1.6 Illustration of AgNPs acting as an antenna in the vicinity of PSI enhancing PSI light absorption capabilities.

Chapter 3

Figure. 3.1 PSI multilayer immobilized on FTO glass plate: **(a)** illustration depicting the configuration for electrodeposition of PSI particles onto the FTO conducting glass and **(b)** image showcasing the prepared bio-photoelectrode, containing ~40 layers of PSI.

Figure 3.2 (a) Apparatus for AgNPs synthesis and **(b)** color change from golden orange of oleylamine-diphenyl ether mixture (top) to brown-black upon $AgNO_3$ addition (bottom) represents the formation of silver nanoparticles.

Figure 3.3 (a) Phase transfer set-up used to convert hydrophobic AgNPs into hydrophilic, **(b)** AgNPs before phase transfer (dispersed in n-hexane) and **(c)** after phase transfer (dispersed in water); n-hexane in (c) was added after phase transfer.

Figure 3.4 Structures of detergents utilized for coating hydrophilic AgNPs: **(a)** pluronic F127, **(b)** pluronic P123, **(c)** β-DM and **(d)** oleylamine.

Figure 3.5 Schematic representation of complexation procedure between PSI from *C. merolae*-CmM and hydrophilic AgNPs coated with pluronic F127.

Figure 3.6 Schematic of **(a)** spin coating of hydrophobic AgNPs on FTO conducting glass and **(b)** setup for electrodeposition of PSI particles on the Ag-FTO conducting glass.

Figure 3.7 (a) Structure of 3-MPA, **(b)** schematic showing the phase transfer process and deposition of the phase transferred AgNPs coated with 3-MPA on FTO, **(c)** AgNPs before phase transfer (dispersed in n-hexane) and **(d)** two separate layers after phase transfer (AgNPs dispersed in water solution of 3-MPA).

Figure 3.8 Schematic representation of **(a)** surface modification of FTO conducting glass using 3-MPA and hydrophobic AgNPs (oleylamine) and **(b)** electrodeposition of PSI on modified Ag-MPA FTO.

Figure 3.9 Schematic of **(a)** spin coating of hydrophobic AgNPs on FTO conducting glass and **(b)** surface modification of Ag-FTO plate by incubating in 3-MPA solution and electrodeposition of PSI particles on the Ag-MPA-FTO plate.

Figure 3.10 Schematic representation of four types of electrodes towards fabrication of PSI-AgNPs films on FTO substrates: **(a)** PSI-(Ag-FTO), **(b)** PSI-(Ag-MPA)-FTO, **(c)** PSI-Ag-(MPA-FTO), and (**d)** PSI-MPA-(Ag-FTO).

Figure 3.11 Schematic of the **(a)** photoelectrochemical cell used for transient absorption measurements of PSI-FTO WE under different experimental conditions: **(b)** with electrolyte, **(c)** with electrolyte containing mediators (ascorbate - yellow dots; DCPIP – blue dots) and **(d)** same as (c) but with potential applied to WE of -280 to +620 mV vs. RE.

Figure 3.12 Schematic of the **(a)** photoelectrochemical cell used for transient absorption measurements of WE: 1. PSI-FTO, 2. Ag-FTO, and 3. PSI-(Ag-FTO) under different experimental conditions: **(b)** "dry" – without electrolyte, **(c)** with electrolyte containing mediators (ascorbate - yellow dots; DCPIP/PMS – pink dots) and **(d)** same as (c) but with potential applied to WE of -400 mV vs. RE.

Figure 3.13 Schemes of the three-electrode photoelectrochemical cells used for measurements of photocurrent generated in two types of WE: 1. PSI-FTO and 2. PSI-(Ag-FTO).

Chapter 4

Figure 4.1 (a) Photochronoamperometric and **(b)** steady-state absorption data for PSI complexes isolated from three species and immobilized on FTO glass.

Figure 4.2 Representative time-resolved absorption kinetics of five PSI complexes suspended either in buffer only (blue fit curves) or with an addition of saturating amount of mediators (ascorbate: 4–10 mM and DCPIP: 4–40 μM) (red fit curves).

Figure 4.3 Model of ET reactions leading to observed (P^+- P) ΔA signals in PSI complexes from *Synechocystis* (**a**, **b**) and *C. merolae/C. reinhardtii* (**c**, **d**).

Figure 4.4 Dependence of the maximal initial amplitude ($-\Delta A_0$) for each of the PSI preparation on the P/N_{Chls} ratio in each type of PSI complex (estimated from the kinetics measured in ~ 54–130-ms time windows).

Figure 4.5 Comparison of the results of the P^+ decay measurements performed under a range of experimental conditions (represented by numbers 1–12 shown under the abscissa).

Figure 4.6 Photocurrent generated in the PSI-FTO electrode with ~40 monolayers of PSI complexes. **(a)** Chronoamperometric data recorded for the PSI-FTO electrode of the photoactive surface of ~0.25 cm^2 at OCP and **(b)** stable photocurrent amplitudes (left axis) and corresponding IQE (right axis) vs. potential applied to WE.

Figure 4.7 Diagrammatic representation of the ET processes in the PSI-based photoelectrode as a function of the external bias. **(a)** Relatively large cathodic photocurrent due to very low potential applied, **(b)** relatively small cathodic photocurrent at OCP, **(c)** no photocurrent at neutral potential and **(d)** relatively large anodic photocurrent due to a very high potential.

Figure 4.8 The kinetics of the P^+ photobleaching decay at 700 nm in the PSI complexes deposited on FTO glass. (**a**) Examples of experimental kinetics together with fitted bi-exponential curves (fit curves 6 and 8 from Table 4.3), (**b**) the fit curves 1–17 from Table 4.3, lumped into four distinct groups (A–D) and (**c**) normalized fit curves 1–17 (groups A-D from panel b are indicated).

Figure 4.9 Initial photobleaching amplitudes as a function of voltage applied to PSI-FTO electrode.

Figure 4.10 Extreme theoretical electric potential effects on the photoactivity of PSI particles in the absence of the mediators in solution. (**a**) Low potential and (**b**) High potential.

Figure 4.11 Dependence of bi-exponential fit parameters on the potential applied to the PSI-FTO electrode (with no mediators added; experiments no. 1–9 in Table 4.3). (**a**) Lifetime τ_1 with the average value indicated, (**b**) lifetime τ_2 with the average values indicated separately for the kinetics fitted with *const* = 0 (54 ms; points in the red ellipses), *const* ≠ 0 (27 ms; remaining points), and for all kinetics (42 ms), (**c**) initial amplitude, $-\Delta A_0$, (**d**) amplitude A_1 of the fast phase (~1.7 ms) and (**e**) the sum of the amplitude A_2 of the slow phase (~42-ms) and *const* parameter.

Figure 4.12 Fractions of active (green) and inactive (red) PSI complexes under **(a)** low (-280 mV) and **(b)** high (+620 mV) potential.

Figure 4.13 (a, b) Two models of the active (green) vs. inactive (red) PSI particles distribution across their multilayer on the FTO substrate. Semi-transparent yellow and blue rectangles are the areas of the effective P^+ re-reduction by the low voltage (-180 mV) and by redox compounds (10 mM ascorbate and 200 μM DCPIP), respectively.

Figure 4.14 Steady-state spectra of **(a)** hydrophobic AgNPs-oleylamine dispersed at different concentrations in n-hexane, **(b)** hydrophilic AgNPs-F127 dispersed at different concentrations in distilled water and **(c)** hydrophilic AgNPs with different detergent coating (F127, P123, and β-DM) compared with hydrophobic AgNPs.

Figure 4.15 Steady-state absorption spectra comparing the stability of **(a)** hydrophobic AgNPs and **(b)** hydrophilic AgNPs-F127 over time labeled as fresh sample (measured right after synthesis) vs. aged sample (measured at different time after fabrication).

Figure 4.16 Illustration showing **(a)** varying stability of hydrophilic AgNPs coated with different detergents (F127, P123, and β-DM), ranked from least stable to most stable.

Figure 4.17 Fluorescence emission spectra of hydrophobic AgNPs at excitation wavelengths **(a)** 250 nm, **(b)** 325 nm and **(c)** 415 nm.

Figure 4.18 Fluorescence emission spectra of hydrophilic AgNPs at excitation wavelengths **(a)** 250 nm, **(b)** 325 nm and **(c)** 415 nm.

Figure 4.19 Hydrodynamic size distribution of hydrophobic AgNPs coated with oleylamine and hydrophilic AgNPs coated with different detergents (F127, P123, and β-DM) obtained by DLS.

Figure 4.20 Illustration representing the assembling of hydrophobic PPO and hydrophilic PEO pluronic detergent units around AgNP core in aqueous solution.

Figure 4.21 Illustration showing hydrophilic AgNPs coated with different detergents (F127, P123, and β-DM), ranked from smallest to largest.

Figure 4.22 TEM micrograph of **(a)** hydrophobic AgNPs in n-hexane and **(b)** hydrophilic AgNPs-F127 in distilled water. Size distribution of AgNPs in **(c)** n-hexane and **(d)** distilled water obtained from analysis of TEM micrographs.

Figure 4.23 Comparison of the absorption spectra of **(a)** 2 ml of *C. merolae* (CmM) PSI complex solution (green dotted) with the mixture of PSI solution and varying volume of hydrophilic AgNPs-F127 solution and **(b)** 2 ml of same PSI complex solution (green dotted) with the mixture of PSI solution and varying volume of pluronic F127 solution. Spectra were measured at room temperature.

Figure 4.24 Comparison of fluorescence emission spectra of **(a)** *C. merolae* PSI complex alone (green dotted spectra) with the mixture of PSI and varying volume of hydrophilic AgNPs with pluronic F127 coating and **(b)** PSI complex alone with the mixture of PSI and varying volume of pluronic F127. Spectra were measured at room temperature. Excitation wavelength was 400 nm.

Figure 4.25 (a) Comparison of steady-state absorption spectra of PSI-FTO (blue colored), Ag-FTO (orange colored), PSI-(Ag-FTO) (purple colored), and Buffer-Ag-FTO (magenta colored).

Figure 4.26 Spectral variety among various samples: (**a)** PSI-FTO absorption spectra, **(b)** Ag-FTO absorption spectra and **(c)** PSI-(Ag-FTO) absorption spectra.

Figure 4.27 AFM images of **(a)** bare FTO and **(b)** Ag-FTO, and SEM images of **(c)** bare FTO and **(d)** Ag-FTO.

Figure 4.28 Comparison of the results of time-resolved absorbance measurements of the Ag-FTO plate placed in PEC at different experimental conditions: **(a)** dry Ag-FTO plate (without electrolyte in contact with the Ag-FTO plate), **(b)** Ag-FTO plate in PEC filled with electrolyte containing mediators (20mM ascorbate and 10μM PMS), and **(c)** same as (b) but with potential of -180 mV applied to the Ag-FTO plate.

Figure 4.29 Comparison of the results of time-resolved absorbance measurements of the PSI-FTO plate in PEC at different experimental conditions: **(a)** without electrolyte in PEC (dry conditions), **(b)** with electrolyte containing mediators (20 mM ascorbate and 10 μM PMS), and **(c)** same as (b) but with potential of -180 mV applied to the PSI-FTO plate. Excitation wavelength was 425 nm.

Figure 4.30 Comparison of the results of time-resolved absorbance measurements of the PSI-(Ag-FTO) plate in PEC at different experimental conditions: **(a)** without electrolyte in PEC (dry conditions), **(b)** with electrolyte containing mediators (20 mM ascorbate and 10 μM PMS), and **(c)** same as (b) but with potential of -180 mV applied to the PSI-(Ag-FTO) plate. Excitation wavelength was 425 nm.

Figure 4.31 Comparison of normalized DASes and decay kinetics obtained from the fits of the data for the PSI-(Ag-FTO) and Ag-FTO samples at different experimental conditions: **(a)** without electrolyte (dry conditions), **(b)** with electrolyte containing mediators (20 mM ascorbate and 10 μM PMS), and **(c)** – same as (b) but with potential of -180 mV applied to the PSI-(Ag-FTO) plate.

Figure 4.32 Comparison of decay kinetics at 546 nm and 686 nm obtained from the fits of the data for the PSI-(Ag-FTO) and Ag-FTO samples at different experimental conditions: **(a)** without electrolyte (dry conditions), **(b)** with electrolyte containing mediators (20 mM ascorbate and 10 μM PMS), and **(c)** – same as (b) but with potential of -180 mV applied to the PSI-(Ag-FTO) plate.

Figure 4.33 Chronoamperometric data recorded at OCP obtained in three-electrode system showing net cathodic photocurrent for **(a)** PSI-FTO and **(b)** PSI-(Ag-FTO) WE.

Figure 4.34 (a) Structure of 3-MPA and **(b)** 3-MPA molecule adsorbed on Ag-FTO in: 1. Trans, and 2. gauche conformations.

Figure 4.35 Photographic images of Ag-MPA-FTO sample **(a)** before sintering, **(b)** after sintering and **(c)** a droplet of PSI solution on the Ag-MPA-FTO plate before electrodeposition.

Figure 4.36 Comparison of steady-state absorption spectra of the (Ag-MPA)-FTO (red colored) and PSI-(Ag-MPA)-FTO plates (blue colored).

Figure 4.37 Absorption spectra of MPA-FTO (light blue "24 hr"), AgNPs spin-coated on MPA-FTO (red), PSI electrodeposited on Ag-(MPA-FTO) (black).

Figure 4.38 Absorption spectra of Ag-FTO (red), Ag-FTO immersed in 3-MPA solution: MPA-Ag-FTO (blue), PSI electrodeposited on MPA Ag-FTO (black).

List of tables

Chapter 1

Table 1.1 Comparison between the PSI from the three species depending on the presence and/or absence of light harvesting antennas, specific subunits etc.

Chapter 2

Table 2.1 A comparison of photocurrent output for PSI-based biohybrid solar cells in different studies.

Table 2.2 Approaches to enhance efficiency in bio-solar cells based on photosynthetic systems using nanomaterials.

Table 2.3 Ultrafast spectroscopy and electron dynamics in metal nanoparticles and/or energy transfer dynamics between metal nanoparticles and PSI.

Chapter 3

Table 3.1 Characteristics of detergents used for the replacement of hydrophobic oleylamine coating with hydrophilic coating.

Chapter 4

Table 4.1 Selected parameters related to the absorbance changes kinetics (at 700 nm) of PSI samples shown in Figure 4.2.

Table 4.2 Experimental conditions of absorbance change measurements in which P^+ decay kinetics were recorded.

Table 4.3 Experimental conditions and parameters of transient absorption kinetics of CmH PSI complexes recorded at 700 nm. (A) PSI complexes deposited on FTO; (B) PSI suspended in aqueous solution[(1)].

Table 4.4 Comparison of time-resolved absorption and photocurrent results observed for CmH PSI in solution and immobilized on FTO.

Table 4.5 Comparison of SPR peak positions of the AgNPs with different coatings.

Table 4.6 Comparison between experimental and theoretical hydrodynamic radii of hydrophilic AgNPs coated with different detergents (theoretical calculation were done assuming the core AgNPs radius to be ~4.5 nm).

List of abbreviations

3-MPA	3-mercaptopropionic acid
AFM	atomic force microscopy
Ag	silver
Ag/AgCl	silver/silver-chloride
$AgNO_3$	silver nitrate
AgNPs	silver nanoparticles
APS	Aminopropyltriethoxy-silane
Asc	ascorbate
Au	gold
AuNPs	gold nanoparticles
cTAB	cetyltrimethylammonium bromide
C. merolae	*Cyanidioschyzon merolae*
C. reinhardtii	*Chlamydomonas reinhardtii*
CdSe	cadmium selenide
CE	counter electrode
Chls	chlorophylls
CMC	critical micelle concentration
CmH	*C. merolae* particles grown under high light
CmM	*C. merolae* particles grown under medium light
Cr	*Chlamydomonas reinhardtii*
C. reinhardtii	*Chlamydomonas reinhardtii*
Cu	copper
DAS	decay associated spectra
DCPIP	Dichlorophenolindophenol
DCBQ	2,6-dichloro-1,4-benzoquinone
DDM	n-dodecyl-β-D-maltoside
DLS	dynamic light scattering
ET	electron transfer
Fe_2O_3	ferric oxide
FTO	fluorine-doped tin oxide
FWHM	full width at half maximum
HOPG	Highly oriented pyrolytic graphite
IQE	internal quantum efficiency
ITO	indium tin oxide
IUPAC	International Union of Pure and Applied Chemistry
KCl	potassium chloride
LHC	light harvesting complex
LB	lipid bilayer
LSPR	localised surface plasmon resonance

MWCNTs	multi-walled carbon nanotubes
NQDs	nanocrystalline quantum dots
NREL	National Renewable Energy Laboratory
NPGL	nanoporous gold leaf
OCP	open circuit potential
PEC	photoelectrochemical cell
PEO	poly-(ethylene oxide)
PMS	phenazine methosulfate
PPO	poly-(propylene oxide)
PSI	Photosystem I
PSII	Photosystem II
PV	photovoltaics
RC	reaction centre
RE	reference electrode
RMS	root mean square
SAMs	self-assembled monolayers
SEM	scanning electron microscopy
SHE	standard hydrogen electrode
SIF	silver island film
SLG	single graphene layer
SM	cyanobacterium *synechocystis sp.* PCC 6803 monomeric PSI
SPR	surface plasmon resonance
ST	cyanobacterium *synechocystis sp*. PCC 6803 trimeric PSI
TEM	transmission electron microscopy
TiO_2	titanium dioxide
ZnO	zinc oxide

List of frequently used symbols

A_0	electron acceptor
A_{679}	absorbance of the PSI multilayer at Q_y band
A_i	amplitude associated with lifetime
Chl*	photoexcited antenna Chls
COOH	carboxylic group
const	non-decaying component
d	diameter of PSI complex
ε_{679}	Molar extinction coefficient of Chls a in PSI
E_0	redox midpoint potential
E_{exc}	excitation energy
$F_{A/B}$	final acceptor in *C. merolae* and *C. reinhardtii*
F_X	final acceptor in cyanobacterial PSI
f	excitation frequency
λ_{exc}	excitation wavelength
$\lambda_{Raman\ peak}$	Raman peak wavelength
m	number of Chls a per PSI complex
N_A	Avogadro number
N_{Chls}	number of antenna Chls
$n_{absorbed\ photons}$	number of absorbed photons
n_{PSI}	number of PSI monolayers
$n_{photoelectrons}$	number of photoelectrons
OD_{411nm}	optical density of hydrophobic AgNPs at 411 nm
OD_{424nm}	optical density of hydrophilic AgNPs at 424 nm
OD_{679nm}	optical density of PSI at 679 nm
P_{700}/P	primary electron donor (ground state)
P_{700}^*	excited state of primary donor
P_{700}^+/P^+	photo-oxidized primary donor
PCP	peridinin-chlorophyll-protein
Q_y	band maximum of PSI at 679 nm
SH	thiol group
τ_{av}	time constant of average charge recombination
τ_{out}	time constant of electron transfer outside PSI
v/v	volume per volume
ΔA_o	initial amplitude of photobleaching signal
$\Delta A_{o,rel}$	relative initial transient absorption signal

$\Delta A_{o,max}$	maximal value of absorbance change	$\Delta\tilde{\nu}$	wave number

List of publications

1. Goyal, A., Szewczyk, S., Burdziński, G., Abram, M., Kargul, J., Gibasiewicz, K. (2022). Competition between intra-protein charge recombination and electron transfer outside photosystem I complexes used for photovoltaic applications. Photochemical Photobiological Science, 21, 319–336.
   https://doi.org/10.1007/s43630-022-00170-x

2. Szewczyk, S., Goyal, A., Abram, M., Burdziński, G., Kargul, J., & Gibasiewicz, K. (2022). Electron Transfer in a Bio-Photoelectrode Based on Photosystem I Multilayer Immobilized on the Conducting Glass. International journal of molecular sciences, 23, 4774.
   https://doi.org/10.3390/ijms23094774

3. Koralewski, M., Paprzycka, M., Goyal, A., & Gibasiewicz, K. (2023). Faraday rotation enhancement for colloidal spherical Au and Ag nanoparticles and their mixtures. Journal of magnetism and Magnetic Materials, 588, 171461.
   https://doi.org/10.1016/j.jmmm.2023.171461

Chapter 1: Introduction

1.1 Background and motivation

Photosystem I (PSI) serves as a crucial photosynthetic chlorophyll-protein complex, effectively converting light energy into electrical current [1]. With its exceptional internal quantum efficiency (IQE) defined as a ratio of the number of photo-generated electrons to the number of absorbed photons surpassing 99% and relatively high voltage output, of ~1 V, PSI possesses attributes conducive to biosolar cell prototypes [2]. Despite variations in structure among photosynthetic organisms, the core component of PSI remains largely identical [3].

The physiological function of PSI lies in its ability to catalyze the light-induced trans-membrane electron transfer (ET) process. Specifically, PSI facilitates the transfer of electrons from reduced plastocyanin (or cytochrome c6 in certain organisms) located on the luminal side of the thylakoid membrane to ferredoxin situated on the opposite (stromal) side [4]. This process is integral to the conversion of light energy into chemical energy within the photosynthetic apparatus.

Within PSI, the ET process is composed of a series of intricate steps involving various cofactors, including chlorophylls (Chls), phylloquinones, and iron-sulfur complexes [4]. The energy of incoming light reaches the primary electron donor, P_{700}, resulting in its excited state (P_{700}^{*}), which initiates charge separation and ET. Subsequent ET steps occur through a series of secondary electron acceptors, ultimately leading to the generation of oxidized and reduced states of key cofactors [5].

To enhance PSI light absorption properties, one proposed strategy involves leveraging the surface plasmon resonance (SPR) of metal nanoparticles, particularly silver nanoparticles (AgNPs). SPR, known for modifying emission and excitation rates in adjacent biomolecules, has gained popularity in photosynthesis applications [6]. Noteworthy studies have reported enhanced absorbance and fluorescence in systems integrating PSI with AgNPs [7-9].

While natural photosynthesis seamlessly integrates PSI into its energy conversion processes, the adaptation of PSI for use in artificial biosolar cells poses unique challenges but also opportunities. Efforts to enhance the efficiency of PSI-based photovoltaic devices have been ongoing, with a focus on elucidating the underlying mechanisms governing ET dynamics and exploring novel strategies for improving light absorption properties.

In this context, the motivation for this study arises from the need to address key limitations hindering the widespread application of PSI in biosolar cell technologies. Specifically, the incomplete forward ET inside isolated PSI and the slow rates of charge uptake from PSI in artificial environments present significant barriers to achieving optimal device performance [10]. Furthermore, the potential for enhancing PSI's light absorption properties through interactions with metal nanoparticles, such as AgNPs, remains underexplored.

By delving into the fundamental processes governing PSI function and exploring innovative approaches for enhancing its performance, this research aims to contribute valuable insights to the development of efficient biosolar cell technologies.

Through a combination of advanced spectroscopic techniques and fabrication of novel artificial systems incorporating PSI, conductive glass and AgNPs, this study seeks to unravel the complexities of PSI-based systems and pave the way for their practical application in renewable energy solutions.

1.2 Scope and significance of the research

This research holds substantial scope and significance within the realm of renewable energy technologies. By delving into the intricacies of PSI behavior and its interactions with AgNPs, this study seeks to:

- Enhance the understanding of factors limiting the efficiency of PSI-based photovoltaic devices.
- Explore novel strategies for improving light absorption properties
- Explore ET dynamics in PSI-based systems to assess the impact of PSI's artificial environment on ET reactions.
- Contribute to the development of efficient energy conversion technologies leveraging biological systems.

Ultimately, the findings of this research are poised to advance the field of photosynthesis-based technologies and pave the way for the development of more efficient energy solutions.

1.3 Photosynthesis and energy storage

Photosynthesis is a process utilized by green plants, algae, and certain bacteria such as cyanobacteria where light captured from the sun is stored and used for its metabolic processes. It is divided into four phases as illustrated in Figure 1.1. The process begins with light absorption and energy transfer and is completed with the delivery of stable carbon products. These four phases represented can be further sorted as light reactions (constituting first three phases) and dark reactions/light-independent reactions (fourth phase).

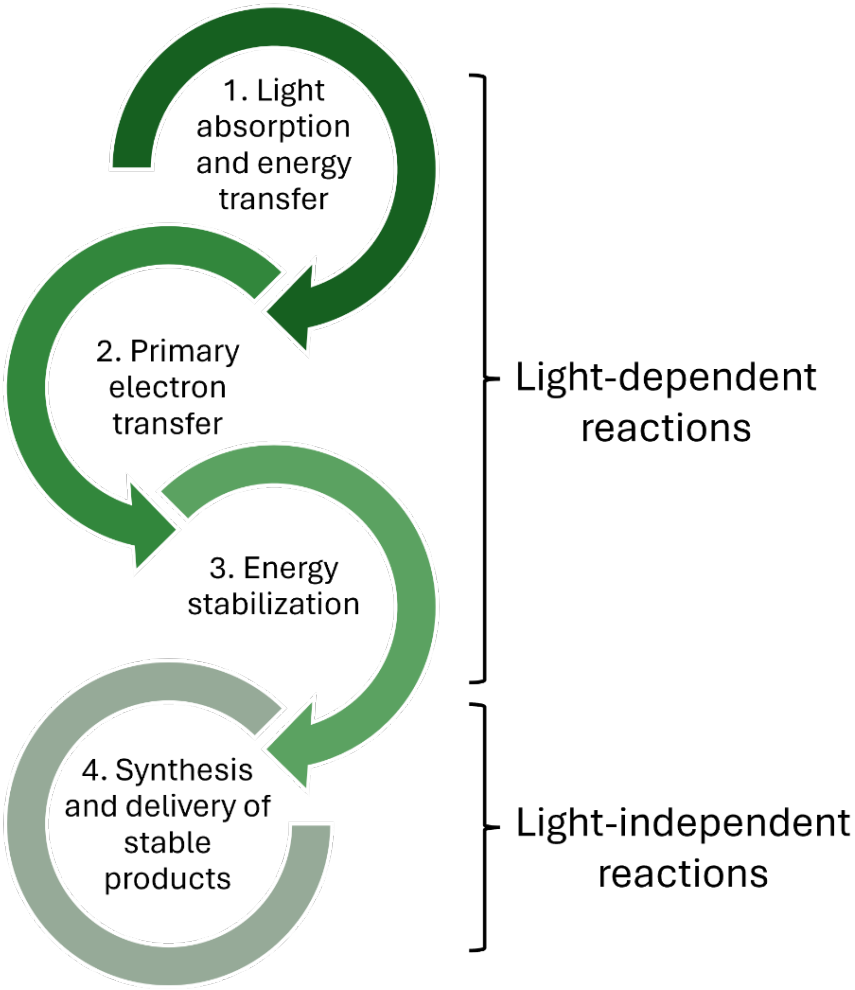

Figure 1.1 Illustration of four phases in photosynthesis process for energy storage and transfer combined into light-dependent and light-independent reactions (Reproduced from [11] under Creative Commons Attribution v4.0 International License[§]).

The early-stage processes comprising the first three phases occur within or near the thylakoid membrane whereas the final phase of producing stable products takes place in a complex called antenna system (Figure 1.1 and Figure 1.5a). An incoming photon absorbed by the protein-pigment creates an excited state resulting in charge separation in the reaction center (RC). The RC incorporates light-absorbing chlorophylls and carotenoids as well as other cofactors such as quinones and iron-sulfur clusters involved in the ET reactions [11]. These ET components and processes differ, dependent on the structural differences among different species of photosynthetic organisms and different types of photosystems (Photosystem I and Photosystem II). In this thesis, we utilized PSI complexes isolated from three different species 1) cyanobacterium *Synechocystis* sp. PCC 6803, 2) red alga *Cyanidioschyzon merolae* (*C. merolae*), and 3) green alga *Chlamydomonas reinhardtii* (*C. reinhardtii*). Although, PSI complexes from these species have a similar physiological function, they differ in structure.

Cyanobacterial PSI occurs in monomeric and trimeric forms with no external antenna [12]. PSI from *C. merolae* occurs in monomeric form with crescent like light harvesting antenna complexes (LHCI) [13]. *C. merolae* combines features from both cyanobacteria (phycobilisomes, PsaM subunit) as well as green algae/higher plants (monomeric PSI with asymmetrical LHCI), serving as an evolutionary intermediate between the two [14]. PSI from *C. reinhardtii* occurs in monomeric form with external LHCI, [15]). *C. reinhardtii* represents more complex eukaryotic algae with PSI antenna size much larger than that of higher plant and has ten LHCI subunits which forms an extensive LHC system (20 LHC genes) [16,17]. Table 1.1 below summarizes the similarities and differences between the PSI from three species.

Table 1.1 Comparison between the PSI from three species depending on the presence and/or absence of light harvesting antennas, specific subunits etc.

	***Synechocystis* sp. PCC 6803**	***C. merolae***	***C. reinhardtii***
Light harvesting antenna (LHC)	No	Yes (LHCI)	Yes (LHCI)
Monomeric/Trimeric (M/T)	M/T	M	M
PsaM subunit	Yes	Yes	No
Phycobilisomes	Yes	Yes	No
Cytochrome c6	Yes	Yes	No
Plastocyanin	Yes	No	Yes

The PSI ET chain (Figure 1.2) of any PSI-containing organism consists of 6 chlorophylls (Chls) (two of them forming the primary electron donor P or P_{700}, two accessory Chls A (not labelled), and two primary electron acceptors labelled A_0), two phylloquinones (A_1), and three iron-sulfur complexes (F_X, F_A, F_B) [18]. From a functional point of view, incoming light is directly absorbed by P_{700} or, most likely, delivered to P_{700} from the antenna system, resulting in its excited state, P_{700}^*. Excitation of P_{700} leads to charge separation (electron transfer) and formation of the oxidized state of the primary donor, P_{700}^+. The electron from excited P_{700} reaches the primary acceptor, A_0, and is then further transferred along a series of secondary electron acceptors, A_1, F_X, F_A, and F_B thereby crossing the membrane (Figure 1.2). This excited electron is collected by the water-soluble redox protein, ferredoxin, and P_{700}^+ is reduced by plastocyanin or cytochrome c_6 (Table 1.1 and Figure 1.2).

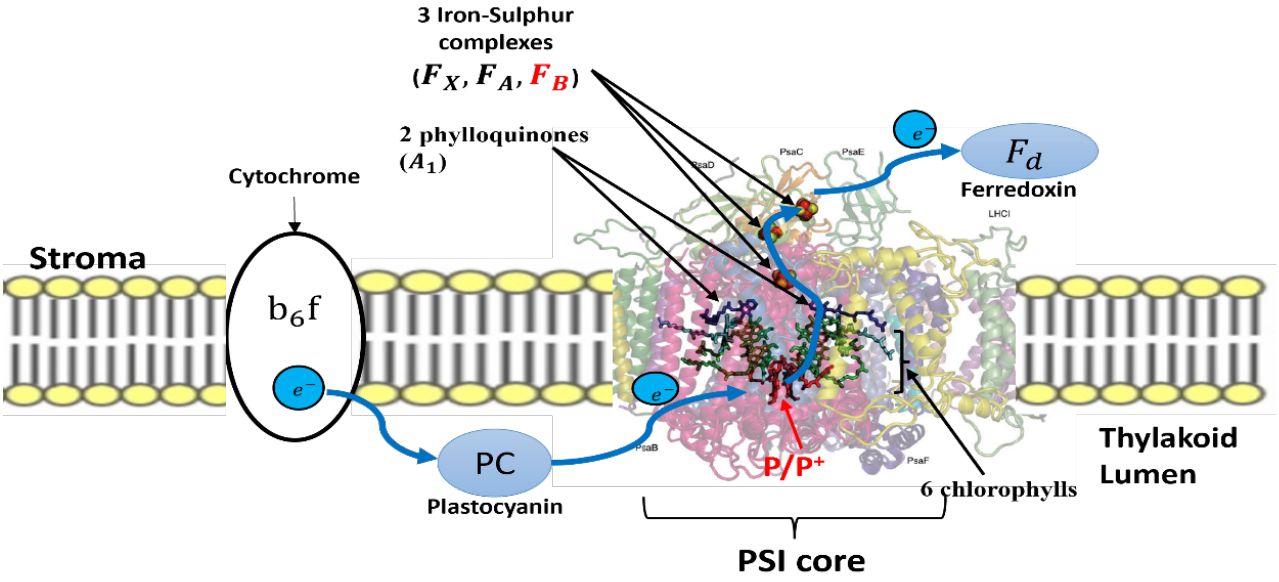

Figure 1.2 A part of a natural molecular photosynthetic apparatus, including PSI embedded in a thylakoid membrane (Reproduced from [19] under Creative Commons Attribution v4.0 International License§).

Time scales of forward and backward electron transfer (ET) steps between internal PSI cofactors are shown in Figure 1.3. The primary electron transfer steps, from excited P_{700}, to A_0 and to A_1 are ultrafast processes and occur on a picosecond time scale, whereas further electron transfer steps to F_X, F_A, and F_B occur on a nanosecond time scale [5]. When the forward ET is blocked, charge recombination back reactions are observed mostly on the time scale of the order of micro- and milliseconds (Figure 1.3).

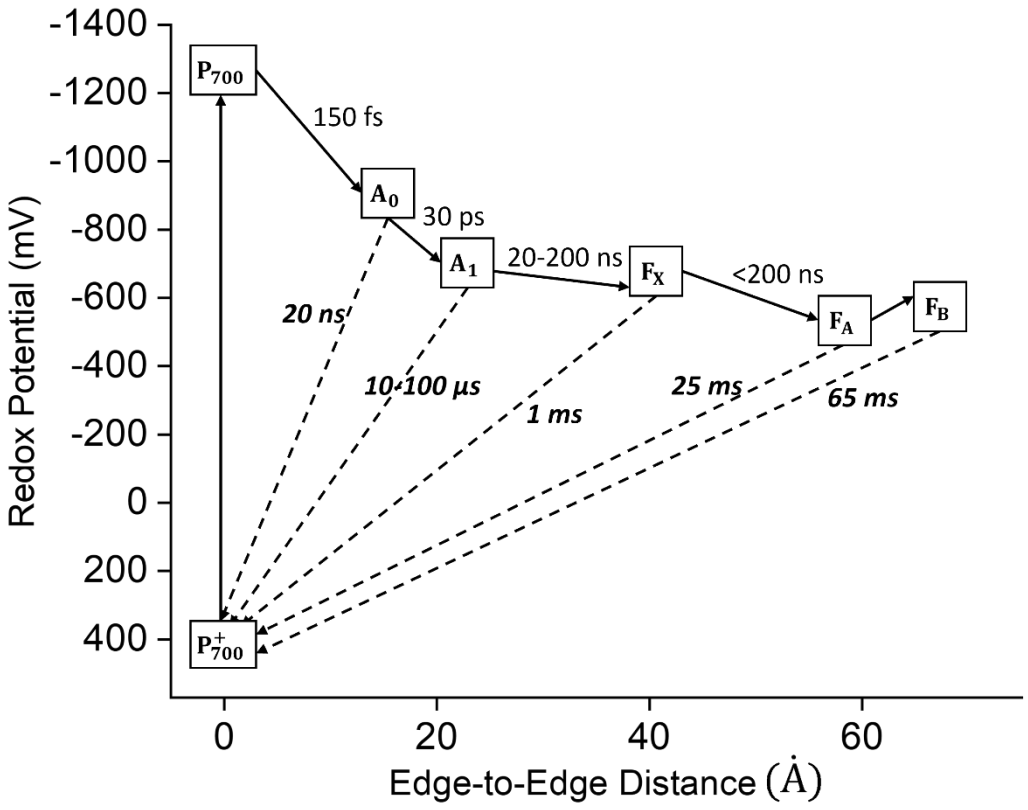

Figure 1.3 Energetic-kinetic-distance scheme of forward (solid arrows) and backward (charge recombination; dashed arrows) PSI ET reactions with their time constants (Reproduced from [20] under Creative Commons Attribution v4.0 International License[§]).

1.4 Biophotovoltaics based on Photosystem I

1.4.1 Photovoltaics

Solar energy conversion, a crucial field of research and development, focuses on harnessing visible electromagnetic radiation to generate electricity. This process is primarily achieved through photovoltaic devices, which can be categorized into three generations [21]. The first generation of solar cells, exemplified by single-crystal silicon solar cells, has long dominated the market. However, their widespread adoption is hindered by high production costs despite their high efficiencies. In response to these challenges, the second generation of solar cells emerged, offering alternative technologies such as amorphous silicon cells. While these solutions are more cost-effective, they typically exhibit lower efficiency compared to their single-crystal counterparts. Advancements in solar cell technology continue with the ongoing development of third-generation cells.

These innovative constructions, currently in the experimental phase, aim to overcome the limitations of earlier photovoltaic technologies by addressing both cost and efficiency concerns. Examples of these novel approaches include organic [22, 23], perovskite [24-26], and dye-sensitized solar cells [27-29]. In comparison to traditional photovoltaic cells where the semiconductor performs both the light absorption and electron transport, the dye-sensitized solar cells (DSSCs) by Michael Gratzel utilized an organic dye embedded in a mesoporous and nanocrystalline substrate for the light absorption [30, 31]. The DSSCs design is equivalent to that of natural photosynthesis where the dye mimics the function of chlorophyll, and ET, similar to that in photosynthesis is assisted by redox mediators [32]. This utilization of biological materials leads to a subcategory of DSSCs known as biosolar cells, described more in detail in the next section.

The efficiency of solar cells under illumination of AM1.5 spectrum (1000W/m^2) is an important factor in comparing the progress achieved by different categories and subcategories of solar cells. This is represented in Figure 1.4 as a chart from the National Renewable Energy Laboratory (NREL) which keeps a track record of the efficiencies for different photovoltaic technologies. The plot for “emerging PV” has been highlighted. It is to be noted that perovskite solar cells while being cost effective are able to reach the efficiency closer (~26%) and even higher (~29% - perovskite tandem solar cell) in comparison to silicone solar cells. However, biosolar cells despite being reported extensively in literature (see below) have yet not been able to claim their place on the chart.

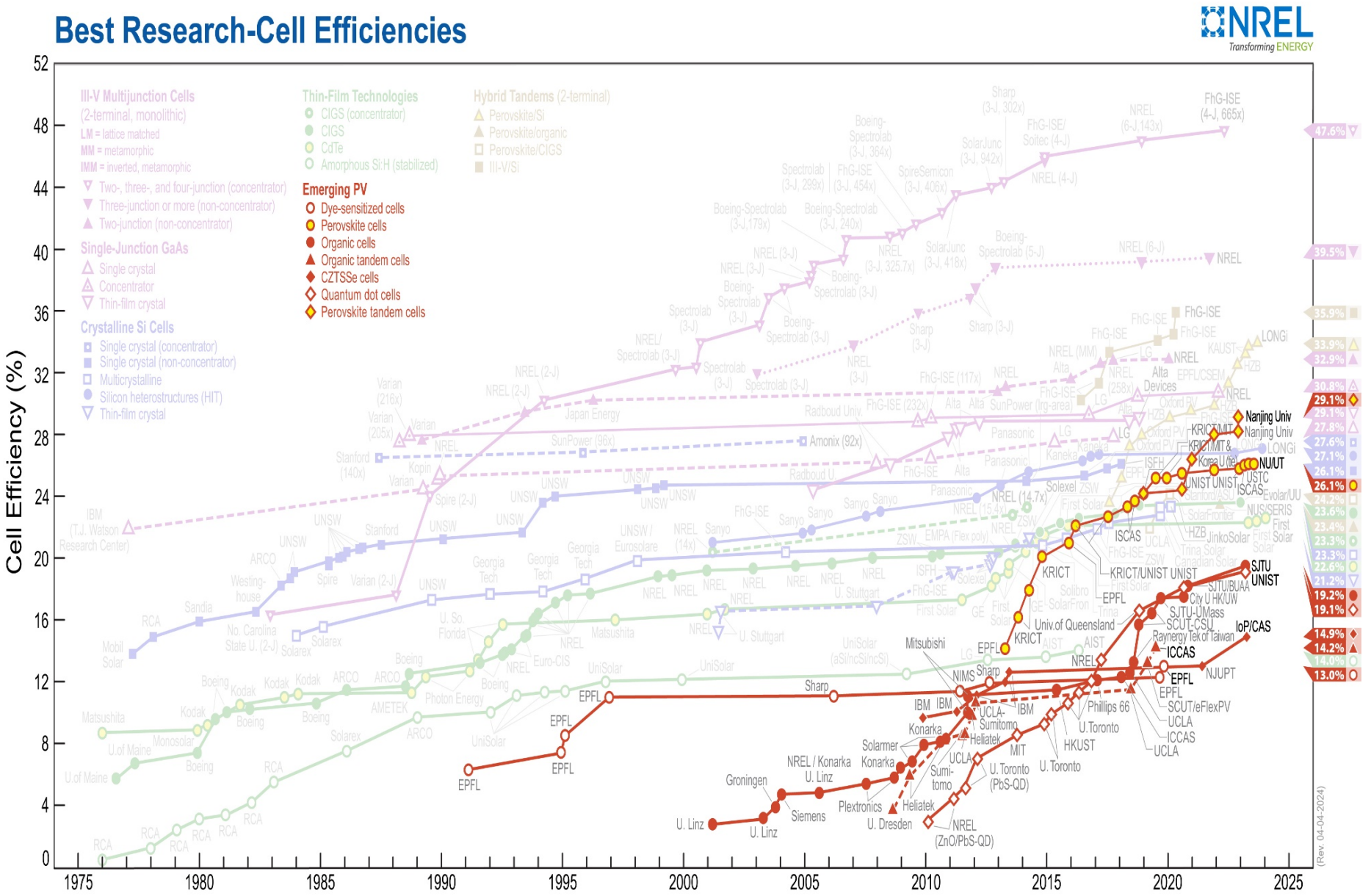

Figure 1.4 Best research cell efficiency chart displaying the emerging PV as highlighted from 1975 until present tested by NREL (Reproduced from [33]).

1.4.2 Biophotovoltaics

The emerging field of photovoltaics draws on the natural photosynthesis process of converting light into electrical current and is called biophotovoltaics. The utilization of biological light harvesting proteins into biohybrid devices is a source of ready-to-use light energy nanoconverters – photosynthetic proteins such as PSI. The incorporation of photosynthetic proteins and membranes in an artificial setting was first studied in the end of 1970s [34, 35]. At that time, the limited knowledge and resources did not allow for an in-depth understanding of the topic. However, it drew attention of researchers in the last couple of decades leading to many reports published on different biohybrid solar cells [1, 36-42, 43].

PSI core, being the common part of Photosystem I of all photosynthetic organisms, in its biological system is shown in Figure 1.5a. It consists of ~100 chlorophylls (Chls) evenly distributed inside the protein. Energy of incoming light when captured by the primary donor P produces its excited state P* which reduces the final acceptor $F_{A/B}$ at the opposite side of the protein, producing a meta-stable charge separated state $P^+F^-_{A/B}$. $F^-_{A/B}$ designates the mixture of the states F^-_A and F^-_B which are often assumed to be in an equilibrium (refer to section 1.4 for detailed function of PSI). This charge separation can be utilized for photocurrent generation in bio-solar cells. In the device, natural external electron acceptor and donor are replaced with electrodes supported by artificial electron mediators as shown in Figure 1.5b.

Further, when incorporating PSI in an artificial system, it is of particular importance to focus on the following components of the system: a) intact protein, b) choosing artificial electron mediators between counter electrode (CE) and protein, and c) effective connection between protein and working electrode (WE) and d) matching redox potential of mediators to PSI. When choosing mediators, in solution or in solid-state must ensure efficient ET from/to the protein while minimizing charge recombination with the WE and inside PSI.

The efficiency of biophotovoltaic devices, particularly based on PSI has been steadily increasing [1, 2]. However, it remains low in comparison to the traditional photovoltaics. One of the reasons is short-circuiting, *i.e.* dissipative ET from acceptor side of one PSI to the donor side of another one.

A possible approach to increase the efficiency of photovoltaic devices based on PSI is integration of PSI complexes with AgNPs. It can help in increasing this efficiency through enhancement of the absorption by plasmon resonance effect described in the next section.

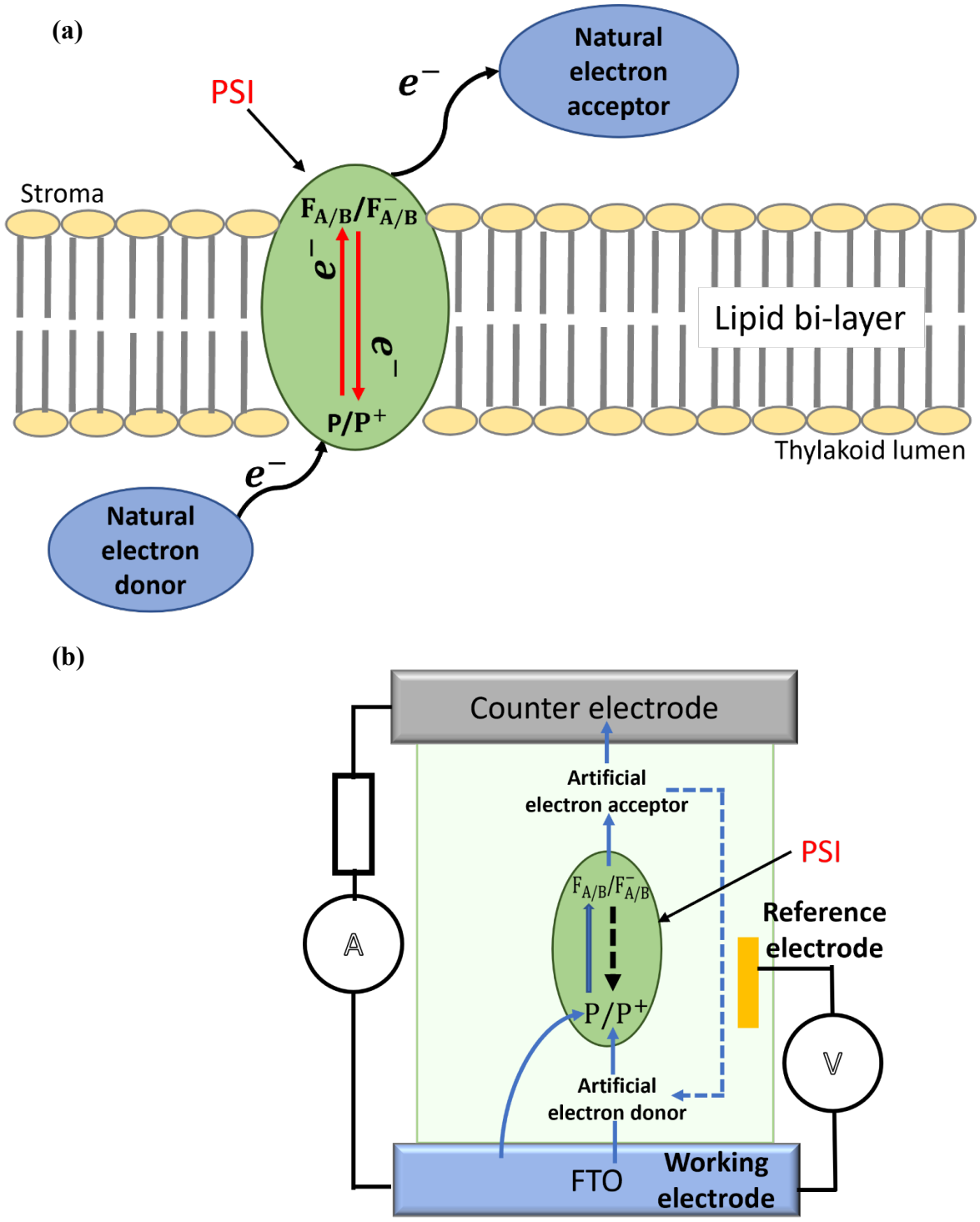

Figure 1.5 (a) A part of a natural molecular photosynthetic apparatus, including PSI embedded in a thylakoid membrane (reproduced from [19] under Creative Commons Attribution v4.0 International License[§]) and **(b)** Working principle of a biophotovoltaic system (Reproduced from [1] under Creative Commons Attribution v4.0 International License[§]).

1.5 Nanoparticles and their use in biophotovoltaics

As mentioned above, the photocurrent generated in the PSI-based biophotovoltaic devices is low as pointed out in many scientific reports [1, 10,]. In recent years, localized surface plasmon resonance (LSPR) of metal nanoparticles, in particular silver (AgNPs) and gold nanoparticles (AuNPs) beside others (e.g. platinum and cadmium) have gained interest in photosynthesis application [7, 8, 44, 45, 46-48]. LSPR of metal nanoparticles is the collective oscillation of electrons on a particle surface in response to its illumination [49]. Such nanoparticles can be used as an antenna to increase the absorbance of PSI.

Metal nanoparticles can be utilized in biophotovoltaic devices in colloidal form, deposited on substrates, and/or embedded in a matrix [50-52]. In this work, we utilized the SPR of AgNPs to study the effect of AgNPs on PSI. The interaction between PSI and AgNPs highlights its importance as a building block in photovoltaic devices. This idea is illustrated in Figure 1.6. It has been found that the AgNPs can enhance the fluorescence of the nearby chlorophylls up to 18-fold in peridinin-chlorophyll-protein and 5-20-fold for cyanobacterial PSI thin films [7, 53]. Other advantages of AgNPs are stability in suspensions, ease of synthesis and that they are considered non-toxic.

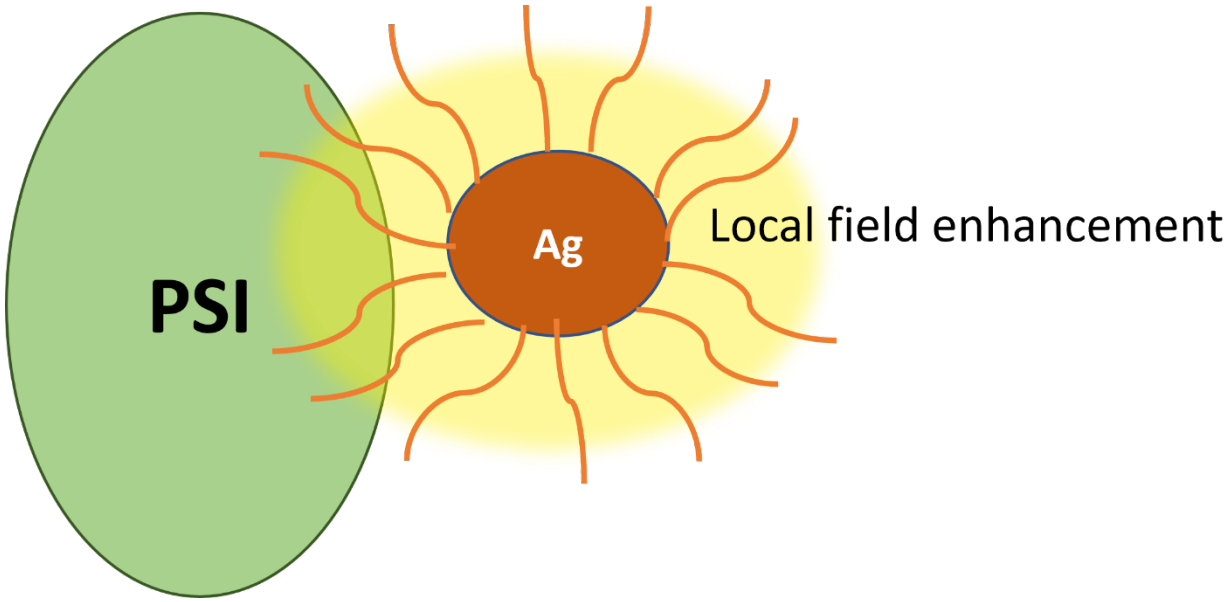

Figure 1.6 Illustration of AgNPs acting as an antenna in the vicinity of PSI enhancing PSI light absorption capabilities.

The SPR of AgNPs is well understood and existing literature further reports the electron relaxation dynamics in AgNPs detected using time-resolved ultrafast spectroscopy [54-56]. The metal nanoparticles behave differently than their bulk counterparts due to their optical properties being dependent on the electron's behavior. For instance, when the size of the nanoparticle becomes comparable or less than the wavelength of visible light, electron confinement takes place [57]. Depending on the various levels of electron confinement, differences in the electron dynamics are observed which depends on the size of the nanoparticles.

Noble metals have an absorption peak in the UV-region of the visible spectrum due to the excitation of metal's d-electron. However, AgNPs have a SPR peak well distinguished from the d absorption peak. In literature, many ultrafast studies conducted on AgNPs show different relaxation processes occurring at different lifetimes when excited with femtosecond pulse. The first step in this process is the electron dephasing occurring at 10-100 fs which determines the SPR lifetime. This is followed by electron-electron scattering at a time scale of 100-1000 fs. This process helps in balancing the temperature of electrons. The next step in the process is electron-phonon scattering at a time scale of 1-10 ps counterbalancing the lattice and electron temperatures. There is also heat transfer to the neighboring environment which is the slowest process of all and occurs on a time scale of 10-100 ps [54,55].

Understanding of the electron excitation dynamics in metal nanoparticles, especially AgNPs, will further help in understanding the results from PSI and AgNPs complexing utilized in this work providing useful insights into photosynthesis based-technologies.

1.6 Objectives of the study

This research endeavors to address key questions surrounding the efficiency and functionality of PSI-based photovoltaic systems. The primary objectives include:

1. Investigating the ET processes within PSI and its artificial systems, both for PSI suspended in solution and immobilized on conducting glass substrates.
2. Exploring modifications of PSI complexes through integration with silver nanoparticles (AgNPs) in solution and thin film configurations.
3. Utilizing advanced spectroscopic techniques to elucidate the excitation dynamics of systems integrating PSI and AgNPs in thin film configurations.

By elucidating the underlying mechanisms governing PSI performance and its interactions with AgNPs, this study aims to provide valuable insights to improve the efficiency of photosynthesis-based technologies.

1.7 Overview of the thesis structure

This thesis is structured to provide a comprehensive investigation into the utilization of PSI in artificial systems for light conversion, with a particular focus on the interaction between PSI and AgNPs. The following chapters outline the systematic exploration of this research topic:

- **Chapter 1: Introduction** provides the background and motivation, objectives, scope, and significance of the research, along with an overview of the thesis structure.
- **Chapter 2: Literature Review** presents previous studies on light conversion efficiency in PSI-based systems, including systems utilizing plasmonic interaction between AgNPs and PSI.
- **Chapter 3: Methodology** details the procedures for PSI particle preparation, fabrication of PSI-based electrodes, AgNPs synthesis, fabrication of PSI-AgNPs hybrid systems and the techniques used for characterization of the PSI-based systems.
- **Chapter 4: Results and Discussion** presents and analyzes the results of ET studies and excitation dynamics in PSI-based systems, presents characterization of AgNPs, and discuss on plasmonic interaction in AgNPs-PSI systems in light of the previous studies.

Each chapter contributes to understanding the principles and practical applications of PSI-based artificial systems for improved light conversion efficiency.

Chapter 2: Literature Review: Enhancing Efficiency of Photosystem I-Based Biohybrid Solar Cells

2.1 Introduction

Amidst the quest for better energy solutions, biohybrid solar cells have gained popularity among other photovoltaic technologies. Recent advancements include the utilization of photosynthetic structures such as photosystems, thylakoid membranes, and entire cyanobacterial cells immobilized on nanostructured electrodes, carbon nanotubes, and nanoparticles of ZnO and TiO_2 [58]. The use of Photosystem I (PSI) in biohybrid devices has emerged as a promising solution due to remarkable capabilities of this protein. In comparison to isolated thylakoids, PSI offers distinct advantages: the steric proximity of reaction centers to the electrode allows for direct electron transfer, enhancing overall efficiency. Moreover, PSI demonstrates greater stability compared to Photosystem II (PSII) and serves as an excellent photobiocatalyst [48].

In this review, we summarize the progress in photocurrent generation from the PSI-based biophotovoltaic devices. It highlights how utilization of plasmonic nanostructures with photosynthetic proteins can be a way of enhancing the efficiency of PSI-based systems. Among various plasmonic nanostructures, noble metals such as silver (Ag) and gold (Au) have been most widely explored in photovoltaic technologies. Their unique optical properties and ability to functionalize biomolecules and proteins make them an ideal candidate to be used in the PSI-based biophotovoltaic devices. It also explores the literature studies on excitation dynamics of AgNPs alone, and interactions between PSI and AgNPs by time-resolved ultrafast spectroscopy. It is to be noted that it is challenging to compare results of different studies due to the lack of consistency between studies. Many studies either do not report the photocurrent density in International Union of Pure and Applied Chemistry (IUPAC) units of mA/m^2 or they do not include the active surface area of the electrode to calculate the efficiency of the system. The larger area will naturally produce more current. Other parameters not reported in literature that make it difficult to compare are temperature (^0C), redox mediators, cell culture growth conditions, number of PSI layers deposited on the substrate etc. In this review, a comparison is presented in tabular form.

2.2 Progress in photocurrent generation in PSI-based biohybrid devices

There are PSI particles derived from different species used in biohybrid devices. This enlists cyanobacterial species constituting *Synechocystis* sp. PCC 6803 [12, 20, 59], *Synechococcus* [37, 60, 61] to name a few. Other PSI particles used in biohybrid systems include those isolated from green alga *Chlamydomonas reinhardtii* [62-64] and red alga *Cyanidioschyzon merolae* [65].

In reviewing the photocurrent output from biohybrid devices, 0.06 mA/cm^2 was the reported photocurrent density in a study where cells of *Chlamydomonas reinhardtii* was used with DCBQ as mediator [66]. In another study, the photocurrent reported was ~0.0482 mA/cm^2 where the authors used thylakoids from *Leptolyngbya sp*. CYN826, a graphite anode, and ferricyanide as a mediator [67]. It has been shown by McCormick et al. that if the biohybrid systems were optimized, then photocurrent densities between 0.34 to 2.46 mA/cm^2 can be achieved [68.].

Some studies have shown that PSI complexes from genetically modified strains of photosynthetic organisms [69,70] and *Rhodobacter sphaeroides* [71] have produced higher current output. Furthermore, the choice of electrode material and presence of external redox mediators can also affect the photocurrent output of the electrochemical cell. These studies presenting multiple arrays of substrates, biological materials, and mediators contributing to the performance of the biohybrid solar cells have been summarized in Table 2.1.

Table 2.1 A comparison of photocurrent output for PSI-based biohybrid solar cells in different studies.

Biological Material PSI-type	Working Electrode (WE)	Redox Mediators	Photocurrent	Year	Ref.
Theromo-synechococcus elongatus	PSI/osmium complex-modified polymer	Methyl viologen	322 μA/cm²	2014	[69]
Theromo-synechococcus elongatus	PSI/transparent mesoporous indium tin oxide	NA	150 μA/cm²	2016	[70]
Spinach	ITO glass functionalized with Ni^{2+}-NTA (Nitrilotriacetic acid)	NA	NA	2004	[72]
Thermo synechococcus elongatus	TiO_2 on FTO glass or ZnO on ITO glass	NA	362 μA/cm²	2012	[60]
Spinach	graphene	NA	550 nA/cm²	2013	[73]
Theromo-synechococcus elongatus	1. APS-ITO 2. TiO2	NA	1. 11.9 nA/cm² 2. 230 nA/cm²	2014	[37]
Spinach	PSI multilayer film/p doped silicone thin film	Methyl viologen; polyviologen	33 μA/cm²	2018	[74]
Synechocystis sp. PCC 6803	PSI/FTO glass	Sodium ascorbate and DCPIP	0.5 μA/cm²	2020	[1]
Spinach	PSI multilayer/ reduced graphene oxide	Ferrocyanide; methylene blue; sodium ascorbate; methyl viologen; 2,6-dichlorophenol-indophenol; ruthenium(II) hexamine	1.2 μA/cm²	2014	[75]
Spinach	PSI–polyaniline/ titanium dioxide	Methyl viologen	72 μA/cm²	2015	[76]

Spinach	Solid-state unetched p-doped silicon/PSI	Methyl viologen	Non-etched: 21μA/cm² Etched: 127μA/cm²	2015	[77]
Spinach	PSI–poly(3,4-ethylene-dioxythiophene) : polystyrene sulfonate/fluorine-doped tin oxide	NA	960 μA/cm²	2017	[78]
Spinach	PSI films/ p-doped silicon	Methyl viologen	875 μA/cm²	2012	[36]
Theromo-synechococcus elongatus	PSI/pyrene-based graphene electrodes	Methyl viologen	0.13 ± 10 μA - 23 ± 0.5 μA	2015	[79]

A notable early study by Das et al. (2004) utilized PSI from spinach immobilized on the Ni^{2+}-Nitrilotriacetic acid (NTA) functionalized indium tin oxide (ITO) glass, achieving an internal quantum efficiency (IQE) of 12%. His work demonstrated the potential of PSI in biohybrid applications [72]. Mershin et al. (2012) advanced this by using PSI from the cyanobacterium *Thermosynechococcus elongatus* on titanium dioxide (TiO_2) on fluorine doped tin-oxide (FTO) glass or zinc oxide (ZnO) on ITO glass, resulting in a photocurrent of 362 μA/cm² and a total external efficiency defined as the ratio of the power of electrical photocurrent and the power of incident light of 0.08%. This study highlighted the significance of substrate choice in enhancing photocurrent [60].

Further studies have explored the use of graphene and silicon substrates. Zhang et al. (2013) reported a modest current of 550 nA/cm² using PSI from spinach on graphene [73]. Kondo et al. (2014) examined the effects of different substrates, finding that 3-aminopropyltriethoxysilane (APS)-ITO and TiO_2 yielded currents of 11.9 nA/cm² and 0.23 μA/cm², respectively, when combined with PSI from *Thermosynechococcus elongatus* [37].

Subsequent investigations have focused on enhancing the interface between PSI and the substrate. PSI films on p-doped silicon, coupled with methyl viologen as a mediator, achieved a notable current of 33 μA/cm² [74]. In yet another study, Szewczyk et al. (2020) utilized PSI from cyanobacterium *Synechocystis* sp. PCC 6803 on FTO conducting glass coupled with mediators: sodium ascorbate and dichlorophenoloindophenol (DCPIP), resulting in IQE of 0.37 % and photocurrent density of up to 0.5 μA/cm² [1]. Additionally, multilayer PSI on reduced graphene oxide, mediated by a combination of ferrocyanide, methylene blue, sodium ascorbate, methyl viologen, 2,6-dichlorophenolindophenol, and ruthenium (II) hexamine, produced a current of 1.2 μA/cm² [75]. These studies underscore the importance of both mediator and substrate in optimizing performance.

Significant advancements were made with the incorporation of polyaniline and titanium dioxide. A setup using PSI-polyaniline on titanium dioxide with methyl viologen as a mediator reached 72 μA/cm² [76]. Further optimization of p-doped silicon substrates, both etched and unetched, resulted in currents of 21 μA/cm² and 127 μA/cm², respectively, when coupled with

methyl viologen [77]. This demonstrates the critical role of surface treatment in enhancing photocurrent.

One of the most impressive results was achieved with PSI-poly(3,4-ethylenedioxythiophene)/poly-styrene sulfonate on fluorine-doped tin oxide, which reached a photocurrent of 960 μA/cm² [78]. This study highlights the potential for significant improvements through the careful selection of conducting polymers and substrates.

In another study, PSI on p-doped silicon mediated by methyl viologen achieved a remarkable 875 μA/cm². This setup demonstrated a 2500-fold enhancement with methyl viologen in comparison to photocurrent of 0.35 μA/cm² observed for PSI on p-doped silicon substrate covered with a thin film of gold without any mediator, emphasizing the importance of mediator selection [36]. Additionally, Feifel (2015) explored various pyrene-based graphene electrodes with PSI from *T. elongatus*, achieving currents from 130 ± 10 nA to 23 ± 0.5 μA, depending on the specific pyrene modification used. In this work, it was shown that photocurrent increased with the addition of mediator regardless of the applied positive overpotential of 100-400 mV [79].

Studies involving *Rhodobacter sphaeroides* have also shown promising results, with biohybrid cells and graphene substrates yielding currents up to 630 μA/cm² [80]. The integration of PSI with various modifications and substrates continues to be a key research area, with significant potential for optimizing solar cell performance.

2.3 Advancements in PSI-nanomaterials based hybrid systems

Despite significant efforts to optimize the configuration of PSI-based biohybrid devices by varying parameters such as substrates, redox mediators, and growth conditions, the efficiency of these devices has remained relatively low. Further, studies have demonstrated that the incorporation of nanomaterials into the electrode design can significantly enhance the photocurrent output. This section presents an overview of these advancements, highlighting the role of nanomaterials aimed at improving the performance of PSI-based biohybrid solar cells.

Ciesielski et al. (2010) reported a photocurrent of 2 μA/cm² using PSI from spinach with DCPIP and ascorbic acid on gold plates over silicon substrates (refer to Table 2.2), showcasing the potential of combining PSI and traditional semiconductor materials with nanomaterials [81].

Sekar et al. (2014) immobilized whole cells from cyanobacterium on multi-walled carbon nanotubes (MWCNTs), achieving a significant photocurrent density of 25 μA/cm². This showed the importance of utilizing nanostructured carbon materials to enhance electron transfer processes [82]. Yang (2016) reported a photocurrent of 8 μA/cm² using PSI from spinach on gold substrates [83].

Robinson (2018) explored the effects of PSI film thickness on gold surfaces, using ferricyanide and achieving a photocurrent range from 0-0.84 μA/cm² for PSI film thickness 0-1.3 μm respectively [84]. Similarly, Stieger et al. (2014) used thiol-modified gold with PSI from *Thermosynechococcus elongatus*, recording a photocurrent of 1 μA/cm² with ascorbate-reduced dichloroindophenol and methyl viologen [85]. The incorporation of self-assembled monolayers (SAMs) and lipid bilayers with gold substrates was examined by Niroomand (2018), who demonstrated that different SAM compositions could affect photocurrent outputs

significantly, with values ranging from 4.2 to 63 nA/cm² depending on the detergent used for PSI reconstitution. This highlights the crucial role of surface chemistry in optimizing biohybrid solar cell performance [46].

Ocakoglu (2014) explored PSI from *C. merolae* with TiO_2 and Fe_2O_3 substrates, noting a remarkable 60-fold increase in anodic photocurrent with PSI-Fe_2O_3 electrode, reaching 56.9 μA compared to a photocurrent of 0.94 μA generated from PSI-TiO_2 electrode. This study underscores the importance of pH and substrate material in modulating photocurrent output [86]. Gizzie (2015) and Ciesielski (2008) also made significant contributions by investigating PSI on polyaniline films and nanoporous gold leaf electrodes, respectively. Gizzie's work achieved a photocurrent of 5.7 μA/cm², representing a 200-fold enhancement over traditional PSI multilayer films, while Ciesielski demonstrated the advantages of nanoporous structures, achieving 300 nA/cm² compared to 100 nA/cm² with planar gold electrodes [76, 87].

Further, Kim et al. (2011) demonstrated a 5-20-fold enhancement in fluorescence intensity by immobilizing PSI from *Synechococcus leopoliensis* on AgNPs thin-film [53]. Other research groups have explored PSI from *Theromosynechococcus elongatus* on different substrates utilizing various nanomaterials in order to enhance the photocurrent and fluorescence of PSI. LeBlanc et al. (2014) reported a photocurrent of ~95 nA/cm² using PSI from spinach on an Ag-NP/ITO substrate [88]. Studies utilizing PSI on SAM-modified gold surface showed varied results, with Yamanoi et al. (2012) achieving 0.088 μA/cm² and Bennett et al. (2016) reporting a lower current of 0.006 μA/cm² [89, 90]. Baker et al. (2014) reported the photocurrent of 4 μA/cm² using Nafion films with osmium complexes [91]. Further, Ciornii et al. (2017) showed a significant enhancement when cytochrome c was introduced, increasing the photocurrent to 18 μA/cm² from 0.8 μA/cm² with no cytochrome [92]. Ashraf et al. (2017) studied PSI-AuNPs films, observing a fluorescence enhancement factor increasing with temperature, from 4.3 at 1.6K to 84.0 at 250K [93]. Jung et al. (2010) demonstrated voltage-dependent photocurrent with PSI from *Chlamydomonas reinhardtii* attached to-CdSe quantum dots and immobilized on glass slides, yielding photocurrents of 1.5 μA/cm² at -2V [94].

Beside other nanomaterials, the use of silver and gold nanoparticles (AgNPs and AuNPs) has also shown great promise. Carmeli (2010) and Nieder (2010) reported enhancements in absorbance and fluorescence when PSI was combined with AgNPs and AuNPs, with Carmeli observing a 2-4-fold increase in absorbance [51] and Nieder et. al., noting a fluorescence enhancement factor up to 36 [95].

Furthermore, it is worth mentioning the extensively work done by Mackowski group in studying the role of plasmonic materials, particularly AuNPs and AgNPs and their interactions with PSI and other proteins. Mackowski et al. (2013) utilized peridinin-chlorophyll-protein (PCP) complexes coupled with spherical gold nanoparticles in three different geometries, demonstrating that direct conjugation led to fluorescence quenching, while controlled spacing (12 nm silica spacer) resulted in a 5-fold fluorescence enhancement [96]**.** Czechowski et al. (2014) reported a ~200-fold fluorescence enhancement for PSI from *Thermosynechococcus elongatus* deposited on silver island films (SIF) [97]. Kaminska et al. (2018) observed a remarkable 500-fold fluorescence enhancement in PCP coupled with colloidal gold and silver nanoparticles functionalized with 25T DNA-oligonucleotides which is the highest value recorded for such complexes so far [98]. The group further investigated photocurrent generation where Kowalska et al. (2020) reported a 5.4-fold enhancement in photocurrent obtained from PSI from *C. merolae* immobilized on silver island film (SIF) glass electrode (1.5 μA/cm^2) at negative potential of -300 mV in comparison to photoelectrode without SIF (0.28

μA /cm^2) [99]. In the same year, Szalkowski et al. (2020) highlighted the impact of substrate fabrication on fluorescence enhancement, showing that PSI-LHCI from *C. merolae* exhibited enhancement factors of 5-7 on glucose-treated SIF but significantly lower values for formaldehyde- and CTAB-treated substrates [100]. Szalkowski et al. (2023) further recorded the fluorescence enhancement factor of ∼50 for PSI-LHCI from *C. merolae* immobilized on silver island film (SIF) [101], while their recent study demonstrated a 15-fold fluorescence enhancement for PSI from *C. merolae* deposited on SIF placed between single-layer graphene (SLG) and glass electrode, achieving a 3.7-fold increase in photocurrent generation compared to the substrate without SIF [102]. These plasmonic effects highlight the potential of nanoparticles to significantly boost the light-harvesting capabilities of PSI-based systems.

Table 2.2 Approaches to enhance efficiency in bio-solar cells based on photosynthetic systems using nanomaterials.

Biological material	**Working Electrode**	**Redox Mediators**	**Photocurrent**	**Enhance-ment factor (Absorbance/ Fluorescence)**	**Year**	**Ref.**
PSI-spinach	**Thin film** Gold plate on silicon substrate	DCPIP & Ascorbic acid	2 μA/cm²	NA	2010	[81]
Cells from Cyanobacterium *Nostoc Sp*	**Thin film** MWCNT-modified carbon electrode	NA	25 μA/cm²	NA	2014	[82]
PSI - spinach	**Thin film** Gold substrate	DCPIP & sodium ascorbate	~8 μA/cm²	NA	2016	[83]
PSI - spinach	**Thin film** Gold/ SAM/ amino-ethane-thiol	$[Fe(CN)6]^{4-}$ $[Fe(CN)6]^{3-}$	0–0.84 μA/cm²	NA	2018	[84]
PSI – *Theromo-synechococcus elongatus*	**Thin film** Thiol-modified gold	Ascorbate-reduced 2,6-dichloro indophenol; methyl viologen	1 μA/cm²	NA	2014	[85]
PSI - not mentioned	**Thin film PSI-LB/SAM/ Au** LB- lipid bilayer;	Detergent – Triton X100	~40 nA/cm² - 63 nA/cm²	NA	2018	[46]

	SAM – self assembled monolayer Au - gold					
	Thin film	Detergent n-dodecyl-β-D-maltoside (DDM)	~4 nA/cm²-8 nA/cm²	NA		
	Thin film PSI/C_6OH SAM/ AgNP/ ITO substrate	NA	~95 nA/cm²	NA		
	Thin film PSI/ITO	NA	~10 nA/cm²	NA		
	Thin film PSI/ C_6OH SAM/ Planar Ag	NA	~30 nA/cm²	NA		
PSI – *C. merolae*	**Thin film** PSI/TiO_2/ FTO PSI/Fe_2O_3/ FTO	NA	PSI/TiO_2/FTO (pH 4) – 0.94 µA PSI/Fe_2O_3/ FTO (pH 4) - 56.9 µA PSI/Fe_2O_3/ FTO (pH 7.4) - 18.7 µA	NA	2014	[86]
PSI - spinach	**Thin film** PSI/ITO	NA	~10 nA/cm²	NA	2015	[76]
PSI-spinach	**Thin film** PSI/nano porous gold leaf (NPGL) electrode PSI/planar gold electrode	NA	PSI/NPGL ~300 nA/cm² PSI/planar gold electrode ~100 nA/cm²	NA	2008	[87]

PSI–*Synechococcus leopoliensis*	**Thin film** - AgNPs film	NA	NA	~5-20-fold enhancement in fluorescence	2011	[53]
PSI - spinach	**Thin film** PSI/C_6OH SAM/Ag-NP/ITO substrate	NA	~95 nA/cm²	NA	2014	[88]
PSI - *Theromo-synechococcus elongatus*	**Thin film** PSI/SAM on gold surface	Sodium ascorbate	0.088 µA/cm²	NA	2012	[89]
PSI - *Theromo-synechococcus elongatus*	**Thin film** PSI on C9 alkane-thiolate SAM/Au	Methyl viologen	0.006 µA/cm²	NA	2016	[90]
PSI - *Theromo-synechococcus elongatus*	**Thin film** PSI/ Nafion film	Osmium bis(2,20-bipyridine) chloride; methyl viologen	4 µA/cm²	NA	2014	[91]
PSI - *Theromo-synechococcus elongatus*	**Thin film** PSI/carbo-xylated pyrene derivative multi-walled carbon nanotubes	Sodium ascorbate; methyl viologen	No cyt c: 0.8 µA/cm² Cyt c present: 18 µA/cm²	NA	2017	[92]
PSI - *Theromo-synechococcus elongatus*	**Thin film** PSI sandwich between a bare glass coverslip and the AuNPs deposited on glass coverslips	NA	NA	Average Fluorescence enhancement factor: At 1.6K – 4.3 At 90 K- 19.4 At 190K- 57.6 At 250K- 84.0	2017	[93]

PSI-*Chlamydomonas reinhardtii*	**Thin film** PSI-CdSe nano-crystalline quantum dots (NQDs)-glass slide	NA	At -2V: 1.5 μA/cm² At +2V: 1 μA/cm²	NA	2010	[94]
PSI (not mentioned)	**Solution** PSI-AgNPs PSI-AuNPs	NA	NA	~ 2-4-fold increase in absorbance	2010	[51]
PSI - *Theromo-synechococcus elongatus*	**Solution-** PSI-AuNPs **Thin film-** PSI-Silver Island film (SIF) on glass slides	NA	NA	Max Fluorescence Enhancement factors: PSI-SIF– 36 PSI-Au- 37	2010	[95]
Peridinin-chlorophyll-protein (PCP) complex - *Amphidinium carterae*	**Thin film** Silver island film	NA	NA	~ 18-fold increase in fluorescence	2008	[7]
Peridinin–chlorophyll–protein – *Amphidinium carterae*	**Solution** gold nano-particles	NA	NA	NA	2013	[96]
	Thin film- gold nano particles – glass coverslip			NA		
	Solution- silica-gold nano particles (silica used as a spacer between PCP and gold nano			Fluorescence Enhancement 5-fold (12 nm-thick silica spacer)		

	particle)					
PSI - *Thermo-synechococcus elongatus*	**Thin film-** Silver island film (SIF)	NA	NA	Fluorescence Enhancement Factor ~200 (λ_{exc} = 640 nm)	2014	[97]
Peridinin–chlorophyll–protein - *Amphidinium carterae*	**Solution-** Colloidal spherical gold and silver nano particles function-nalized with 25T DNA-oligo-nucleotide	NA	NA	Fluorescence enhancement of 500-fold	2018	[98]
PSI - *C. merolae*	**Thin film-** Single layer graphene (SLG) deposited on the silver island film (SIF)	NA	5.4-fold enhancement PSI@SLG/SIF 1.5 μA/cm^2 PSI@SLF 0.28 μA /cm^2	NA	2020	[99]
1. PSI-LHCI – *C. merolae*	**Thin film-** Silver island film (SIF) SIF (glucose) SIF (formalde hyde) SIF (CTAB)	NA	NA	**Fluorescence enhancement factors λ_{exc} – 405 nm (570nm)** SIF (glucose) – 5 (7) SIF (formal-dehyde) - 5 (1) SIF (CTAB) – 1 (0.2)	2020	[100]
2. PSI – *Thermo-synechococcus elongatus*				SIF (glucose) – 5 (8) SIF (formal-dehyde)-3 (12) SIF (CTAB) –		

				1 (0.8)		
PSI-LHCI – *C. merolae*	**Thin film-** Silver island film (SIF) glass coverslips	NA	NA	**Fluorescence enhancement factor** ~50	2023	[101]
PSI - *C. merolae*	**Thin film-Working Electrode** SLG/SIF/ Glass **Reference electrode** SLG/FTO SLG- single layer graphene SIF – silver island film	NA	**Enhancement** 3.7-fold **PSI on SLG/SIF/glass** – 1 μA/cm^2 **PSI on SLG/FTO –** 0.28 μA/cm^2	**Fluorescence enhancement factor** 15-fold with incorporation of SIF	2025	[102]

2.4 Study of excitation dynamics of metal nanoparticles alone and systems integrating PSI and AgNPs by time-resolved ultrafast spectroscopy

Different groups investigated the electron dynamics in metal nanoparticles such as silver (Ag), gold (Au), copper (Cu), cadmium selenide (CdSe) using the time-resolved ultrafast spectroscopy. These studies, summarized in Table 2.3, describe the processes that occur after the metal nanostructures are excited with short laser pulses. The dynamics observed in these studies were assigned to three processes:

1. **Electron-electron scattering**: occurring on a time scale of 10-100 fs.
2. **Electron-phonon coupling**: occurring on a time scale of 1-10 ps.
3. **Heat transfer to the surroundings**: occurring on a time scale of 10-100 ps.

These processes have been detailed in several studies, including those by Gaal (2009), Gaal and Bugar (2009), Warth (2011), Averitt (1998), Lehman (2000), Hoodak (2000), Bigot (2000), and Lysenko (2006) [54-56, 103-107].

However, limited studies have explored the interactions between PSI and nanoparticles using time-resolved ultrafast spectroscopy [94]. Jung (2010) explored the energy transfer dynamics in PSI-CdSe nanocrystalline quantum dot (NQD) composites, demonstrating that the excited state decay of nanoparticle is extremely fast (~6 ps) compared to a sample with only NQDs (~98 ps). This indicates a rapid energy transfer from the NQDs to PSI, which may be important for improving the efficiency of biohybrid solar cells.

This necessitates further research to better understand the excitation dynamics within the photoelectrochemical systems composed of PSI and nanoparticles. In our work, we address this gap by employing advanced spectroscopic techniques to explain the excitation dynamics in a thin film composed of interacting PSI and silver nanoparticles.

Table 2.3 Ultrafast spectroscopy and electron dynamics in metal nanoparticles and/or energy transfer dynamics between metal nanoparticles and PSI.

Biological material/ nanoparticle	**Configuration (solution/ thin film)**	**Working Electrode (Substrate)**	**Year**	**Ref.**
Copper and silver nanoparticles	Thin films	SiO_2, PbO, Na_2O, K_2O doped Glass	2000	[54]
Silver nanoparticles (diameter 10-30 nm)	Colloidal	NA	2009	[55]
Gold nanoshells vs. Gold nanoshell films	Thin Films	PVA	1998	[103]
Silver nanoparticles	Thin Films	Highly oriented pyrolytic graphite (HOPG)	2000	[104]
Gold nanoparticles (2.5 nm to 8 nm size)	Aqueous solution	NA	2000	[105]
Silver nanoparticles	Thin films	Aluminophosphate Glass	2006	[106]
Silver nanoparticles	Colloidal	NA	2009	[107]
PSI- *Chlamydomonas reinhardtii*/CdSe	Thin film	CdSe nanocrytalline quantum dots (NQDs)-glass slide	2010	[94]

Chapter 3: Methodology

3.1 Introduction

This chapter provides a detailed methodology for the preparation of PSI particles, silver nanoparticles, and the fabrication of PSI-FTO electrodes. Further, it describes the experimental techniques used for characterization of the samples.

The chapter outlines the preparation of PSI particles from various organisms, such as the cyanobacterium *Synechocystis* sp. PCC 6803, red alga *Cyanidioschyzon merolae* (*C. merolae*), and green alga *Chlamydomonas reinhardtii* (*C. reinhardtii*). It discusses the fabrication of AgNPs and their subsequent transformation from hydrophobic to hydrophilic form. Additionally, it provides insight into the immobilization of PSI particles and silver nanoparticles on FTO conducting glass and discusses the approaches towards the fabrication of PSI-AgNPs complexes. Next, the transient absorption spectroscopy, various microscopies, and photoelectrochemical techniques are described.

3.2 Preparation of PSI particles

Preparation of PSI particles from cyanobacterium Synechocystis sp. PCC 6803

The preparation of PSI particles was conducted by Dr. Sebastian Szewczyk. Shortly, PSI core complexes were isolated in two forms: monomeric (SM) and trimeric (ST). The number of Chls per PSI monomer in both forms, SM and ST was assumed to be 96 [4]. The isolation procedure followed a specific protocol outlined previously [12]. Initially, PSI complexes were extracted using n-dodecyl-β-d-maltoside (β-DM). Subsequently, the isolated complexes underwent further purification via ion exchange chromatography and after purification, cyanobacterial PSI complexes were stored at -20°C (at high concentration corresponding to $OD_{678nm,1cm}$ ~40, in a solution containing 20 mM Bis-Tris (pH 7.0), 5 mM $CaCl_2$, 5 mM $MgCl_2$, 10 mM NaCl, and 0.03% β-DM (*v*/*v*)) before any further treatment and spectroscopic, microscopic or electrochemical experiments.

Preparation of PSI particles from thermo-acidophilic red microalga Cyanidioschyzon merolae

The PSI particles from *C. merolae* were obtained from Dr. Kargul from the Solar Fuels Lab, Centre of New Technologies, University of Warsaw. They were isolated in two distinct structural forms, which were obtained from cells grown under different light conditions. High-light-intensity particles (CmH; cultivated under continuous white light of 350 µE m^{-2} s^{-1}) contained the PSI core and the peripheral antenna, light-harvesting complex I (LHCI), with an average of four Lhcr antenna subunits resulting in total number of ~159 Chls per single PSI particle. Conversely, medium-light-intensity particles (CmM; cultivated under continuous white light of 90 µE m^{-2} s^{-1}) comprised the PSI core and LHCI with an average of six external Lhcr subunits and ~186 Chls per PSI. The exact procedures were detailed elsewhere [65, 108]. They involved the extraction of PSI complexes using β-DM and subsequent purification through ion exchange chromatography. For storage, CmH as well as CmM particles were kept frozen at -55°C at high concentration corresponding to $OD_{678nm,1cm}$ ~40, in a solution containing 20 mM Hepes (pH 8.0), 3 mM $CaCl_2$, and 0.03% β-DM (*v*/*v*) and 20-25% (*w*/*v*) glycerol.

Preparation of PSI core particles from mesophilic green alga Chlamydomonas reinhardtii CC2696

The preparation of PSI particles was conducted by Dr. Sebastian Szewczyk. Isolation of PSI particles from *C. reinhardtii* followed a previously described procedure [64, 109]. The number of Chls in such PSI core complexes were estimated at 60 [110], 85 [111], and 96 with recent cryoEM studies [112]. Like other species, extraction and purification were conducted using β-DM and ion exchange chromatography. The resulting PSI particles were stored at -20°C at high concentration corresponding to $OD_{678nm,1cm}$ ~40, in a solution containing 20 mM Bis-Tris (pH 7.0), 5 mM $CaCl_2$, 5 mM $MgCl_2$, 10 mM NaCl, and 0.03% β-DM (*v*/*v*) and 20-25% (*w*/*v*) glycerol.

3.3 Preparation of PSI particles for studies in solution and fabrication of PSI-FTO conducting glass electrodes

PSI particles in aqueous solutions

The PSI samples in solution were derived from the three aforementioned species. The concentrated stock solutions of PSI particles derived from *Synechosytis* sp. PCC 6803 and green alga *C. reinhardtii* were diluted using a buffer A composed of 20 mM Bis-Tris (pH 7.0), 5 mM $CaCl_2$, 5 mM $MgCl_2$, 10 mM NaCl, and 0.03% β-DM (*v*/*v*). PSI particles from *C. merolae* were prepared by diluting their stock solution in buffer B comprising 20 mM Hepes (pH 8.0), 3 mM $CaCl_2$, and 0.03% β-DM (*v*/*v*). For transient absorption studies, each sample solution was standardized to $OD_{680nm,\ 1cm}$ ~ 1 using its respective buffer.

Immobilization of PSI particles on FTO conducting glass

The immobilization of the PSI on the FTO was performed using an electrodeposition method. A detailed procedure was described previously [1, 12]. Briefly, before immobilization, ~1 ml of PSI solution underwent dialysis in ~500 ml of aqueous solution of 5 mM Bis-Tris buffer (pH 7.0) using a float-A-Lyzer G2 filter with 100 kDa pore size to reduce the concentration of salts and detergent. Subsequently, a 30 µL droplet of the dialyzed PSI solution characterized by an absorbance $A_{679nm,1cm} \approx 1$ (or $A_{679nm,1cm} \approx 8.5$ in some experiments) was placed on the conductive side of the FTO glass followed by placing another bare FTO on top of it. The two FTO electrodes were placed in such a way that their conductive sides faced the PSI solution, separated by a ~2-mm-thick spacer (Figure 3.1a). Further, a potential difference of +2V between the bottom and top electrodes was applied for 5 min facilitating the partial orientation of PSI particles and their migration toward the bottom FTO plate. Next, the samples were dried at 4 ^{0}C overnight and stored at the same temperature before further measurements. The resulting PSI layer on the FTO substrate was round in shape with a diameter of about 5 mm (Figure 3.1b).

The number of PSI monolayers, n_{PSI} formed on FTO was calculated using the following formula:

$$n_{PSI} = \frac{A_{679} N_A d^2}{\varepsilon_{679} m} \qquad (3.1)$$

Where A_{679} is the absorbance of the dry PSI multilayer at Q_y band maximum, N_A is the Avogadro number, d is diameter of PSI complex, m is the number of Chls a per PSI complex, and ε_{679} is molar extinction coefficient of Chls a in PSI.

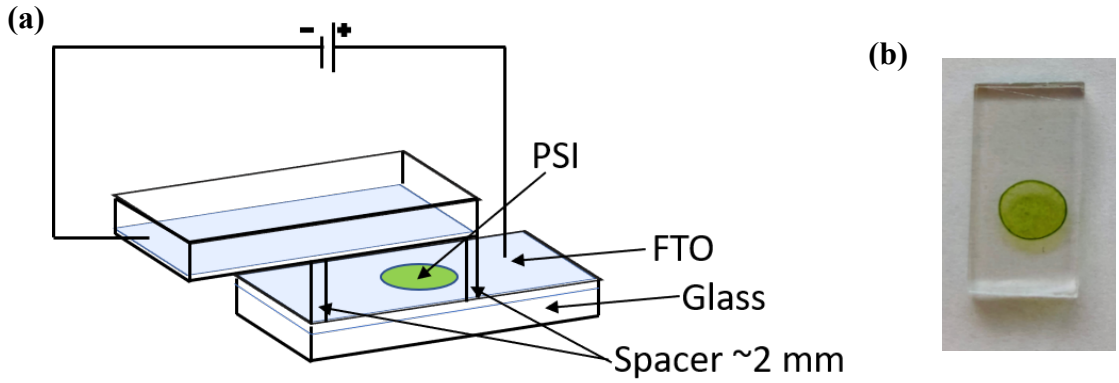

Figure. 3.1 PSI multilayer immobilized on FTO glass plate: **(a)** illustration depicting the configuration for electrodeposition of PSI particles onto the FTO conducting glass (Reproduced from [113]. under Creative Commons Attribution v4.0 International License[§]) and **(b)** image showcasing the prepared bio-photoelectrode, containing ~40 layers of PSI.

3.4 Fabrication of silver nanoparticles

Synthesis of hydrophobic AgNPs (AgNPs suspended in n-hexane)

We adopted a simple one-pot method [114] to produce relatively uniform AgNPs. Oleylamine was used both as a capping and a silver reducing agent. In a typical experiment, oleylamine and diphenyl ether (v/v 1:4) purchased from Sigma-Aldrich were mixed in a 3-neck round bottom flask with total volume of the mixture of ~25 ml. The set-up was equipped with a stirrer, condenser, and a thermometer (Figure 3.2a). The mixture was heated from room temperature to 200 °C at a rate of 3 °C/min using a heater equipped with magnetic stirrer (IKA C-MAG HS 7). 510 mg of silver nitrate ($AgNO_3$) obtained from Sigma-Aldrich was added to the oleylamine–diphenyl ether mixture under continuous stirring and refluxed at 180 °C for half an hour. Upon addition of $AgNO_3$, the golden orange color of the mixture immediately turned brown-black (Figure 3.2b). This change in color indicates the formation of AgNPs. Further, mixture was cooled down to 150 ^{0}C by rapid change of the heater's setting. The mixture was agitated and ripened at 150 °C for another 4 h. The product was purified by precipitation–redispersion process in the following way: approximately 25 mL of absolute ethanol (volume equal to the volume of mixture after synthesis) was added to the mixture once it was cooled to room temperature. AgNPs were span down from the suspension by centrifugation (MPW 250 – medical instruments) at 12,000 rpm (11376 g) for ~13 mins. The supernatant was discarded, and the precipitate was redispersed in 25 mL of n-hexane. The dispersion was again centrifuged at 6,000 rpm (2844 g) for ~13 mins, and undispersed residues (pellet, if any) were removed. This process was repeated 3 times. After purification, the AgNPs were dispersed in n-hexane (Sigma-Aldrich) and stored at 4 °C. The synthesized stock solution of AgNPs diluted 3200-fold with n-hexane resulted in $OD_{411nm,\ 1cm} \sim 0.57$.

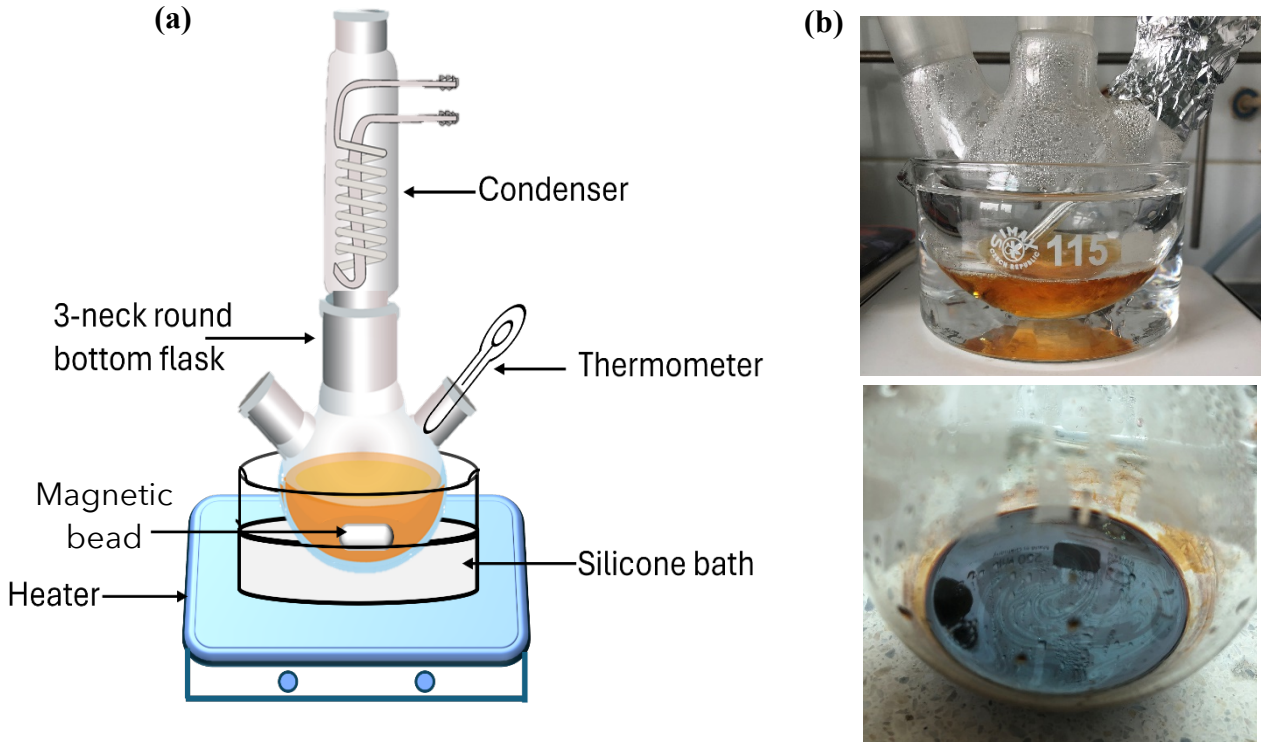

Figure 3.2. (a) Apparatus for AgNPs synthesis (Reproduced from [115] under Creative Commons Attribution v4.0 International License[§]) and **(b)** color change from golden orange of oleylamine-diphenyl ether mixture (top) to brown-black upon $AgNO_3$ addition (bottom) represents the formation of silver nanoparticles.

Fabrication of hydrophilic AgNPs

The synthesized hydrophobic AgNPs, soluble in hydrophobic n-hexane, have been transformed into hydrophilic one by the facile phase transfer protocols [114]. The equal parts of the stock solution of concentrated hydrophobic AgNPs in n-hexane and 2 mM pluronic F127 (Sigma-Aldrich) solution in distilled water were poured to a beaker and covered with perforated aluminum foil (Figure 3.3a). The obtained liquid was then continuously stirred for 24 hours to evaporate the n-hexane from the beaker. The phase transfer could be confirmed by eye. Figure 3b, c shows the image of the beaker with separated hydrophobic and hydrophilic liquids before stirring (b) and after phase transfer (c), respectively, with AgNPs dispersed in the two media. Original AgNPs were easily dispersed in n-hexane. By exchanging the original ligands (oleylamine) with block co-polymer pluronic F127, the transferred AgNPs exhibited good stability in water, even after being washed with n-hexane.

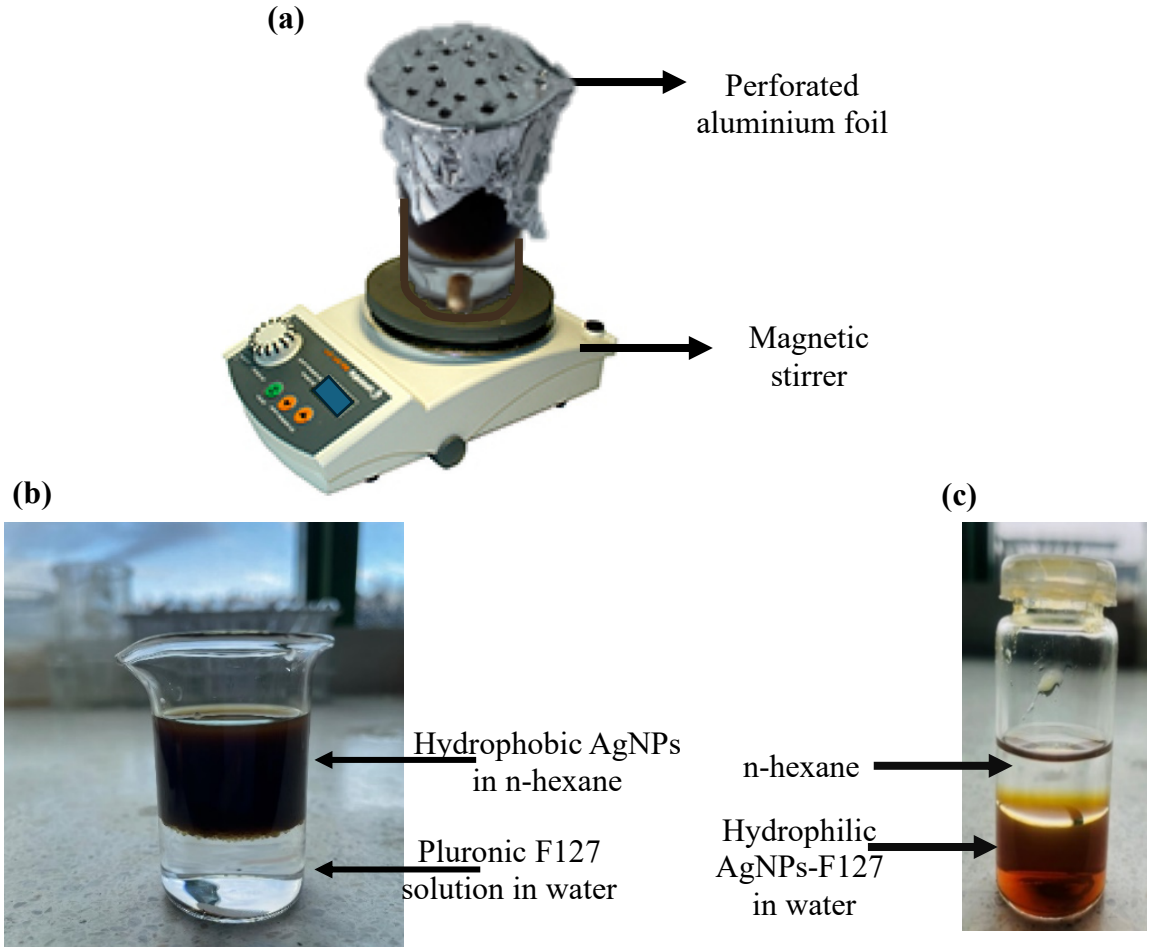

Figure 3.3. (a) Phase transfer set-up used to convert hydrophobic AgNPs into hydrophilic, **(b)** AgNPs before phase transfer (dispersed in n-hexane) and **(c)** after phase transfer (dispersed in water); n-hexane in (c) was added after phase transfer.

A similar procedure was employed to replace oleylamine with other detergents such as pluronic P123 (0.26 mM) and β-DM (0.098 mM). The pluronic detergents comprise both hydrophobic (poly-(propylene oxide)- PPO) and hydrophilic (poly-(ethylene oxide)- PEO) components, as illustrated in Figure 3.4.

Upon transferring the nanoparticles with pluronic P123, some sedimentation was observed at the bottom of the beaker after 24 hours of continuous stirring and evaporation of n-hexane. Consequently, an additional 24 hours of stirring was administered. Finally, after a total of 52 hours, the nanoparticles exhibited reduced stability, evidenced by sedimentation when left undisturbed, necessitating sonication prior to measurement.

For the β-DM detergent, 48 hours of continuous stirring was required to achieve complete phase transfer. However, the resulting suspension of nanoparticles was observed to be viscous with a brown muddy color, in contrast to the typical brown-black color of AgNPs suspended in n-hexane.

When comparing the stability of hydrophilic AgNPs coated with different detergents, it can be ranked from most to least stable as follows: hydrophilic AgNPs with F127 coating exhibited the highest stability, while those with P123 demonstrated the least stability. For this reason, only hydrophilic AgNPs with F127 coating were used for further investigations. It's noteworthy that concentrations of all detergents used were prepared based on their critical micelle concentration (CMC), ensuring the stability and effectiveness of the phase transfer process (Table 3.1).

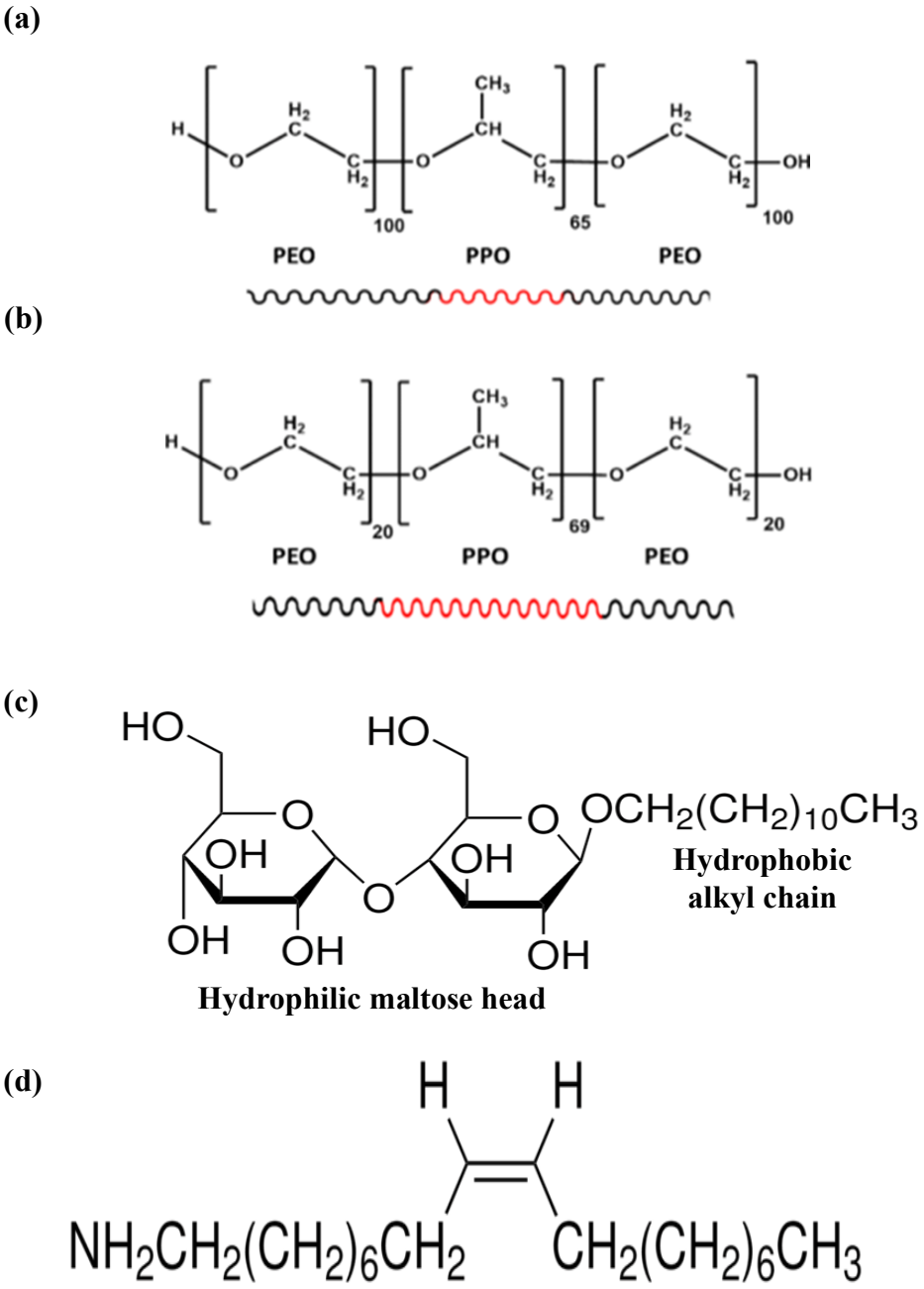

Figure 3.4. Structures of detergents utilized for coating hydrophilic AgNPs: **(a)** pluronic F127, **(b)** pluronic P123 [116], **(c)** β-DM [117], and **(d)** oleylamine [117]. PPO: poly (propylene oxide); PEO: poly (ethylene oxide).

Table 3.1 Characteristics of detergents used for the replacement of hydrophobic oleylamine coating with hydrophilic coating.

S.NO	Detergent	Molecular weight (g/mol)	CMC (20 °C) (mM)	Concentration of detergent used (mM)	Hydrophobic chain length pluronic** (nm)	Hydrophilic chain length pluronic** (nm)
1.	F127*	12,600	3.96	2	26	80
2.	P123*	5,800	0.313	0.26	27.6	16
3.	β-DM***	510.6	0.17	0.098	2.82	0.62

*CMC was calculated from the phase diagram from [118] except for β-DM (mentioned on the bottle purchased from Sigma-Aldrich). **hydrophobic and hydrophilic chain lengths were estimated by multiplying the number of units in PPO/PEO by the length of an individual unit (e.g. for F127, PPO chain length = 65 × 0.4 nm = 26 nm; PEO chain length = 100 × 0.4 nm = 40 nm) (compare Figure 3.4a). ***Values of chain lengths of hydrophobic and hydrophilic parts of β-DM were taken from [119].

3.5 Approaches towards fabrication of Photosystem I-silver nanoparticles complexes

In this section, different approaches towards fabrication of stable PSI-AgNPs complexes are detailed. Both hydrophilic and hydrophobic AgNPs were employed, and the attachment of AgNPs to PSI was tested in solution as well as in thin films, using various procedures. Monomeric PSI particles derived from the cyanobacterium *Synechocystis* sp. 6803 were utilized in these approaches predominantly. However, for PSI complexation in solution, PSI derived from *C. merolae* was employed.

3.5.1 Complexation of PSI particles and hydrophilic AgNPs in solution

In this section, we describe the complexation of PSI derived from *C. merolae* grown under medium light condition (CmM) with hydrophilic AgNPs coated with pluronic F127. The procedure involved the mixing of 2 ml of PSI solution of $OD_{680nm, 1cm} \sim 1$ with varying volumes of hydrophilic AgNPs of $OD_{424nm, 1cm} \sim 2$, ranging from 20 µl to 200 µl, as illustrated in Figure 3.5. For each volume of AgNPs added, following the mixing step, the PSI-AgNPs mixture solution was incubated for about 10 min at room temperature to allow sufficient interaction between the components before spectroscopic measurements. Additionally, to assess the specific contribution of AgNPs to the complexation process, a control experiment was performed where PSI solution was mixed with equivalent volumes of the solvent (pluronic F127 in water) used for diluting/dispersing AgNPs, without the addition of any AgNPs.

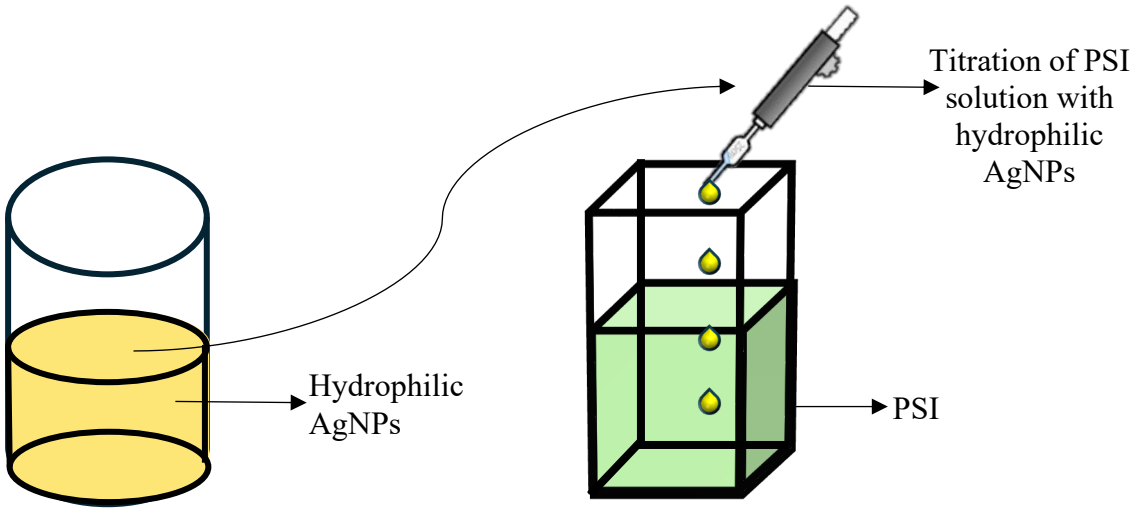

Figure 3.5 Schematic representation of complexation procedure between PSI from *C. merolae*-CmM and hydrophilic AgNPs coated with pluronic F127.

3.5.2 Fabrication of PSI-AgNPs films on FTO substrates

A few different approaches towards fabrication of PSI-AgNPs films on FTO substrates have been tested and are described below. Figure 3.10 summarises schematically the configuration of the four types of FTOs fabricated by the diiferent approaches described below.

3.5.2.1 PSI electrodeposition on FTO coated with hydrophobic AgNPs (PSI-(Ag-FTO))

The FTO plates (Sigma-Aldrich, sheet resistance of ≈13 Ω/sq) measuring 1.5 cm × 1.5 cm x 0.2 cm were sequentially: brushed with aqueous solution of detergent (Hellmanex), followed by consecutive rinses in ultrasonic baths containing either aqueous solution of detergent, or distilled water, or ethanol, for 10 minutes each. Finally, they were exposed to a UV ozone cleaner for 10 minutes. A thin semi-transparent layer of AgNPs was formed by spin-coating 40 µL of colloidal hydrophobic AgNPs (suspended in n-hexane of "$OD_{411nm,\ 1cm}$" ~ 12.6) for 30 seconds at 1000 rpm. The formed Ag-FTO plates were incubated for 24 hrs at room temperature in a container of silica beads to help absorb the moisture from the surroundings encountering the Ag-FTO. Further, Ag-FTO was sintered at 80 °C for 1 hr (Figure 3.6a). The immobilization of the PSI on the Ag-FTO was performed using an electrodeposition method following the same procedure as described in section 3.3 (Figure 3.6b)

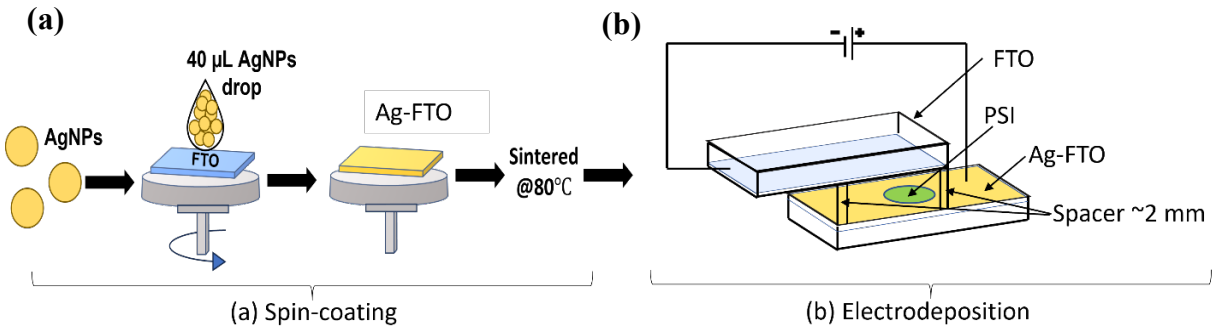

Figure 3.6 Schematic of **(a)** spin coating of hydrophobic AgNPs on FTO conducting glass and **(b)** setup for electrodeposition of PSI particles on the Ag-FTO conducting glass (Reproduced with changes from [113] under Creative Commons Attribution v4.0 International License[§]).

3.5.2.2 PSI electrodeposition on FTO coated with hydrophilic AgNPs (PSI-(Ag-MPA)-FTO)

To prepare the substrate, the phase transfer protocol described in section 3.4 was initially employed to replace oleylamine coating of AgNPs with 2 mM 3-mercaptopropionic acid (3-MPA- structure shown in Figure 3.7a and procedure outlined in Figure 3.7b-d). The phase-transferred nanoparticles treated with 3-MPA exhibited distinctive features, notably two separate layers upon settling (Figure. 3.7d). The phase transfer process was not entirely efficient. A portion of the AgNPs remained hydrophobic in the upper layer, whereas those coated with 3-MPA were concentrated in the lower layer. We do not know the reason for the formation of two separate layers after the evaporation of n-hexane.

Next, drop-casting technique was used for the deposition of the solution of AgNPs coated with 3-MPA (Ag-MPA) instead of spin-coating method due to observed problem in retaining the hydrophilic Ag-MPA on the FTO substrate - the entire volume of the solution disperses away from the FTO surface during spin-coating. The drop-casting was done as follows. The solution of AgNPs coated with 3-MPA was carefully drawn from the bottom layer and a droplet of 40 µl of the solution was deposited on the FTO substrate. As a result, a three-component system was formed: (Ag-MPA)-FTO. The FTO was further sintered at 80 °C for 1 hour. Subsequently, 30 µl PSI of absorbance $A_{679nm,1cm} \approx 1$ was electrodeposited onto the (Ag-MPA)-FTO substrate following the procedure outlined in the previous section.

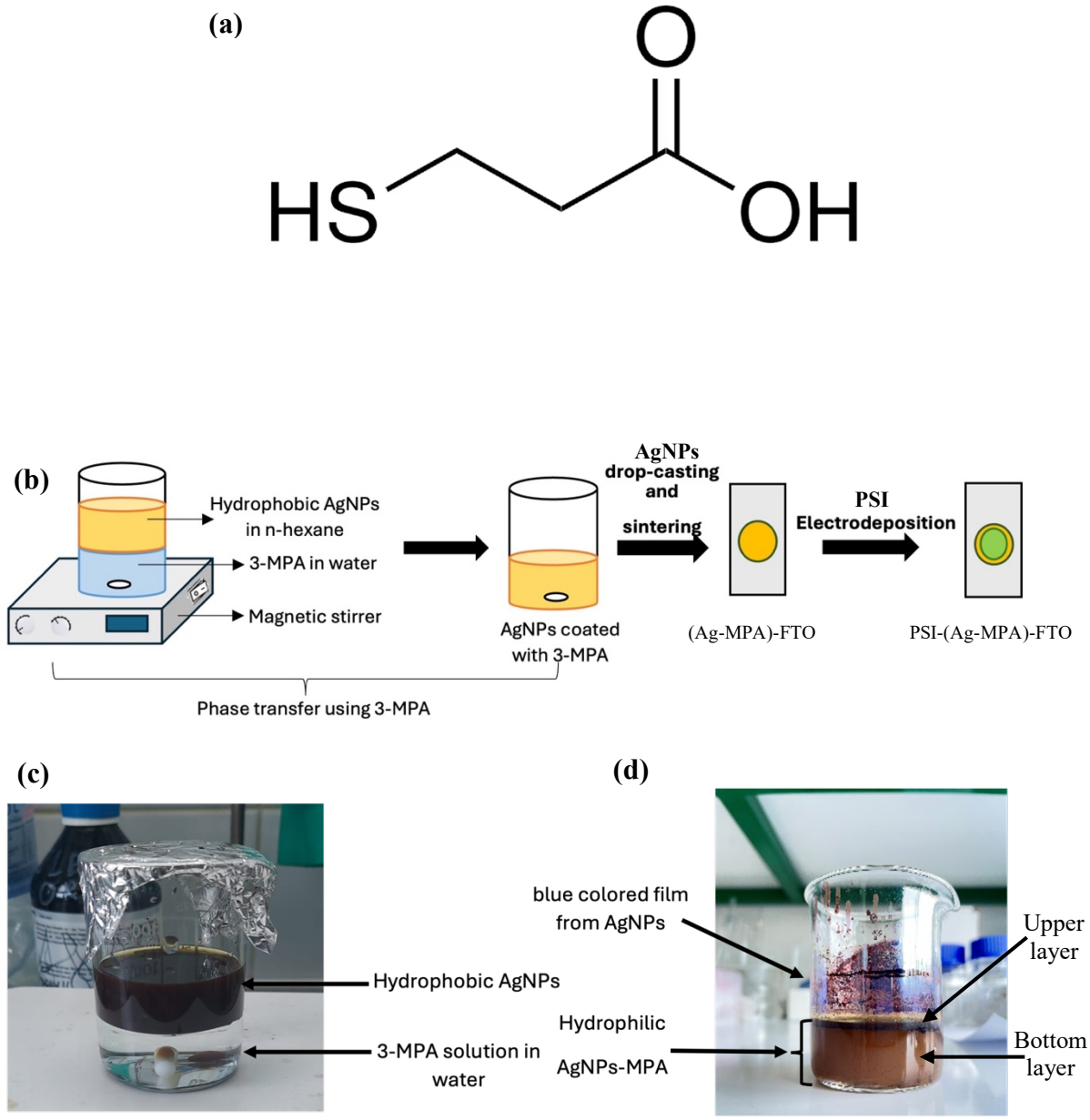

Figure 3.7 (a) Structure of 3-MPA, **(b)** schematic showing the phase transfer process and deposition of the phase transferred AgNPs coated with 3-MPA on FTO, **(c)** AgNPs before phase transfer (dispersed in n-hexane) and **(d)** two separate layers after phase transfer (AgNPs dispersed in water solution of 3-MPA).

3.5.2.3 PSI electrodeposition on 3-MPA-treated FTO coated with hydrophobic AgNPs (PSI-Ag-(MPA-FTO))

Bare FTO was initially immersed in a 0.2 mM aqueous solution of 3-MPA for 24 hours to facilitate surface modification. Subsequently, hydrophobic AgNPs were spin-coated onto the modified FTO substrate. The formed Ag-(MPA-FTO) plates were incubated for 24 hrs at room temperature. Next, PSI of absorbance $A_{679nm,1cm} \approx 1$ was electrodeposited onto the Ag-(MPA-FTO) substrate. No sintering was done to avoid evaporation of 3-MPA. The spin coating and electrodeposition procedures were carried out following the same protocol as described in the section 3.5.2.1.

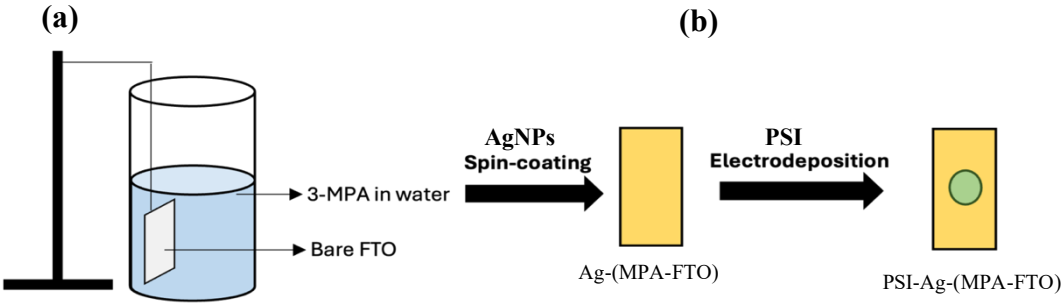

Figure 3.8 Schematic representation of **(a)** surface modification of FTO conducting glass using 3-MPA and hydrophobic AgNPs (oleylamine) and **(b)** electrodeposition of PSI on modified Ag-(MPA-FTO).

3.5.2.4 PSI electrodeposition on 3-MPA-treated Ag-FTO substrates (PSI-MPA-(Ag-FTO))

Ag-FTO substrate was initially prepared by spin-coating of hydrophobic AgNPs on FTO glass plate as described in section 3.5.2.1 but without the sintering step (Figure 3.9). The formed Ag-FTO plates were incubated for 24 hrs at room temperature. Next, the Ag-FTO was immersed in a 0.2 mM solution of 3-MPA for a total of 24 hours to facilitate surface modification. Further, the MPA-(Ag-FTO) plate was dried using a compressed air gun. Following the surface modification step, PSI of absorbance $A_{679nm,1cm} \approx 1$ was electrodeposited onto the MPA-(Ag-FTO) plate. The spin coating and electrodeposition procedures were carried out using the same protocol as described in section 3.5.2.1.

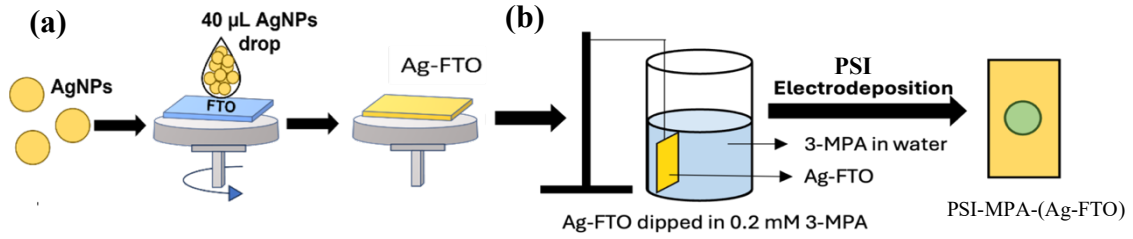

Figure 3.9 Schematic of **(a)** spin coating of hydrophobic AgNPs on FTO conducting glass and **(b)** surface modification of Ag-FTO plate by incubating in 3-MPA solution and electrodeposition of PSI particles on the plate.

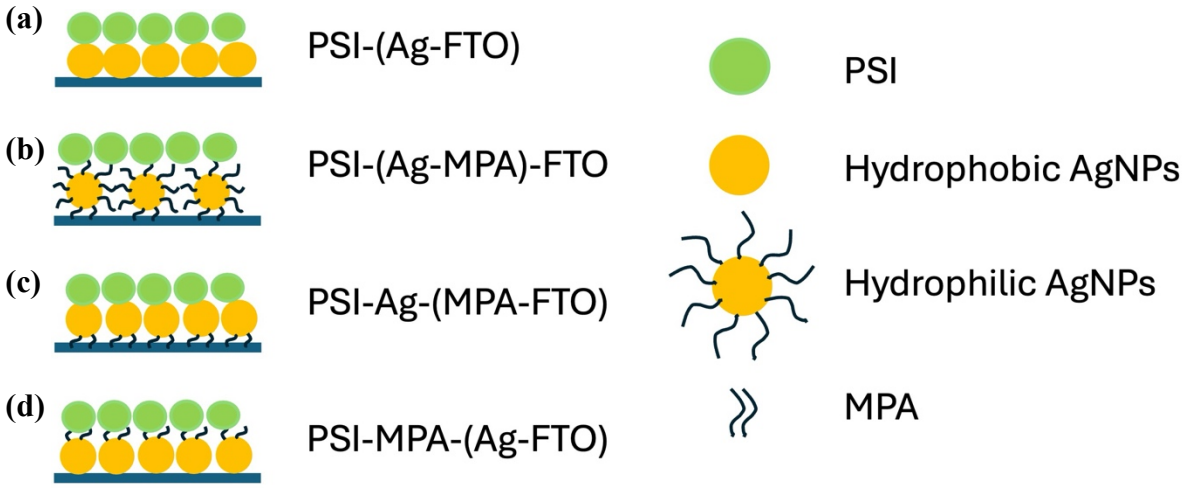

Figure 3.10 Schematic representation of four types of electrodes towards fabrication of PSI-AgNPs films on FTO substrates: **(a)** PSI-(Ag-FTO), **(b)** PSI-(Ag-MPA)-FTO, **(c)** PSI-Ag-(MPA-FTO), and (**d)** PSI-MPA-(Ag-FTO).

3.6 Optical spectroscopy techniques

3.6.1 Steady state absorption

All presented steady-state absorption spectra were recorded at room temperature from 200 to 700 nm using a Hitachi U-2800A spectrophotometer. The measurements were conducted in a quartz cuvette with a path length of 1 cm. Reference measurements for colloidal samples were performed for respective solvents – either n-hexane or water, while for thin film samples on FTO plates, a bare FTO plate was the reference. In order to measure the absorption spectrum of the central semi-transparent part of PSI layer on FTO plate, a mask was used with a rectangular hole of ~1 mm x 3 mm size, transmitting the light beam in the spectrometer.

3.6.2 Fluorescence

Fluorescence emission spectra were carried out at room temperature using Hitachi F-7000 spectrofluorometer. The measurements were conducted in a glass cuvette of the size 1 cm × 1 cm, at 90 degrees angle between excitation beam and detection direction. The spectra were not corrected for wavelength-dependent sensitivity of the detector.

3.6.3 Dynamic light scattering

The hydrodynamic size of both hydrophobic and hydrophilic colloidal AgNPs in n-hexane and in water, respectively, was studied using a home-build setup consisting of a thermostated goniometer (ALV, Germany), optical fiber splitter (Schäfter + Kirchhoff GmbH, Germany), two avalanche photodiodes (SPCM-AQR, Perkin Elmer), and an ALV7002 digital correlator (ALV, Germany). Measurement parameters for hydrophobic AgNPs were as follows: a laser wavelength of 660 nm, a scattering angle of 90° (fixed), a measurement temperature of 20 °C, a medium (n-hexane) viscosity of 0.3 mPa·s, and a medium refractive index of 1.37. Similarly, for hydrophilic AgNPs, all parameters remained the same except for the medium (water) viscosity, which was adjusted to 1.0 mPa·s, and the medium refractive index which was 1.33. The samples were loaded into ~5-cm long round glass cuvette of 10 mm diameter. Before dynamic light scattering measurement, the colloidal suspensions were centrifuged for 10 min at 5000 rpm to get rid of any bubbles. The hydrodynamic radius was calculated by analyzing the autocorrelation function of the scattered light using the CONTIN algorithm embedded in the native software of the correlator. The results were presented in the form of mass distribution of hydrodynamic radius.

3.6.4 Transient absorption spectroscopy

Time-resolved absorption spectroscopy measurements were performed using two different setups – the slower one with hundreds of milliseconds time window, and the ultrafast one with 3-ns time window. The slower setup was used to record the dynamics of the oxidation state of the primary electron donor in PSI (neutral, P, vs. oxidized, P^+) while the ultrafast one was used mostly to record excitation dynamics in the samples containing PSI and/or AgNPs.

Thin film samples on FTO in both milliseconds as well as femtosecond time scales were studied using a home-made 3-D printed photoelectrochemical cell (PEC, [1]).

These samples, designated as working electrodes (WE), were positioned within the cell, forming one of its walls with AgNPs and/or PSI deposited on the internal side, interacting with the electrolyte solution (Figure 3.11a).

The PEC consists of two interconnected parts - an upper part which is an electrolyte chamber (encircled in Figure 3.11b,c,d) and a lower part (formed by WE and another glass plate separated by a spacer with thin space between the plates also filled with the same solution as in the upper chamber). The cell was mounted on a stand equipped with a mechanical motion controller to move the sample holder in a plane perpendicular to the probe beam only for the ultrafast measurements.

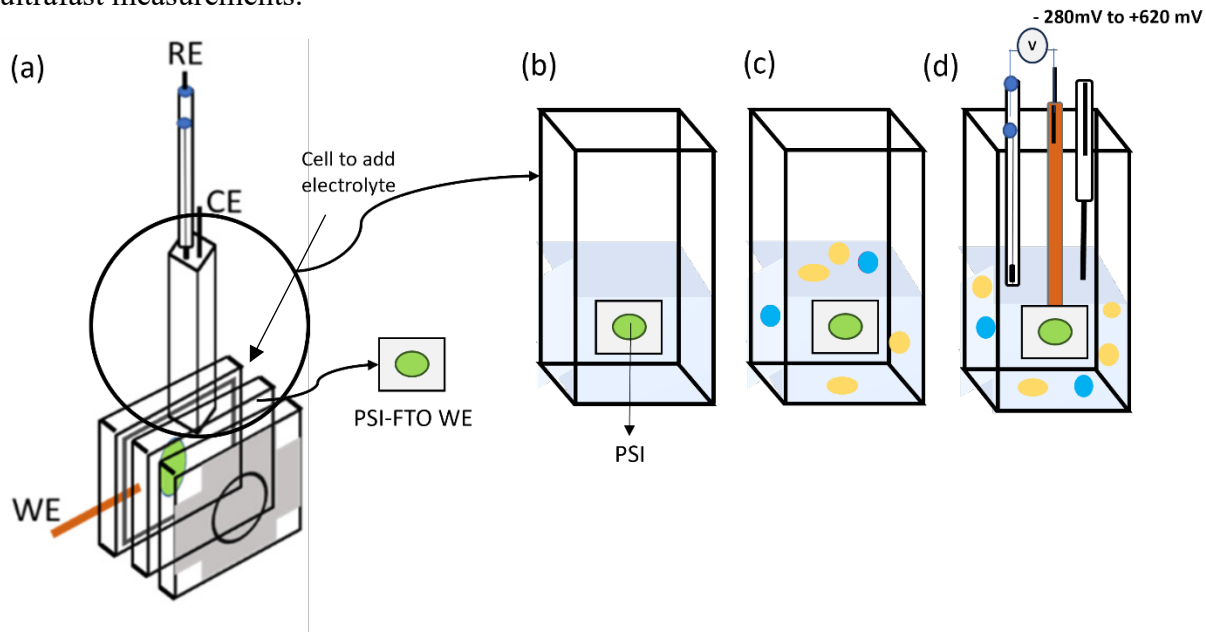

Figure 3.11 Schematic of the **(a)** photoelectrochemical cell used for transient absorption measurements of PSI-FTO WE under different experimental conditions: **(b)** with electrolyte, **(c)** with electrolyte containing mediators (ascorbate - yellow dots; DCPIP – blue dots) and **(d)** same as (c) but with potential applied to WE of -280 to +620 mV vs. RE. WE – working electrode, RE – reference electrode (Ag/AgCl), CE – counter electrode (platinum wire). In (d) – from left to right one can see RE, WE, and CE.

3.6.4.1 Millisecond transient absorption spectroscopy

Millisecond time-resolved absorption spectroscopy was employed to investigate the decay of kinetics of photo-oxidized P^+ in PSI complex suspensions and in PSI immobilized on FTO-based substrates. For PSI complex suspensions, the experiments were conducted in 1cm × 1 cm quartz cuvettes. The samples from different species were diluted to an optical density $A_{680nm,1cm} \sim 1$. PSI particles from *Synechocystis* and *C. reinhardtii* were suspended in buffer A, while PSI from *C. merolae* was suspended in buffer B (refer to section 3.3). Measurements were performed with and without exogenous redox mediators, followed by the addition of 4-10 mM sodium ascorbate and 4-40 µM dichlorophenolindophenol (DCPIP) with different combinations of pulse energy values (1 mJ, 5 mJ) and repetition rates (0.5 Hz, 0.05 Hz) of ~10-ns excitation pulses. The time window of most of the experiments was ~54 ms or ~130 ms broad. However, to resolve a faster component, time window of ~0.5 ms was also used. In contrast, for PSI (isolated from *C. merolae*) immobilized on FTO (~40 monolayers), measurements were conducted under various electrolyte compositions (either pure 30 mM buffer (pH 7.0) or supplemented with 10 mM sodium ascorbate and 0-200 µM DCPIP) and at applied potentials ranging from -280 mV to +620 mV (Figure 3.11b,c,d), and at two frequencies of repetition (0.5 Hz and 0.05 Hz) and a time window of ~54 ms. It is to be noted that all the electric potentials given in this work are given vs. standard hydrogen electrode (SHE), unless indicated otherwise

Time-resolved absorption data were acquired using a setup described previously [120]. For both experiments, the probe wavelength was fixed at 700 nm and was selected from thw white light of 150 W xenon arc lamp using an interference filter (10 nm FWHM, FB700-10 from Thorlabs). Excitation was achieved using a Q-switched Nd:YAG laser emitting pulses at 532 nm with a pulse duration of 8 ns. The configuration of the pump and probe beams varied slightly between experiments (perpendicular to each other for PSI complex suspensions and almost antiparallel (close to 180 degrees) for PSI on FTO). For PSI complex suspensions, the diameters of the pump and probe beams were approximately 6 mm and 1.5 mm, respectively and for PSI immobilized on FTO, the diameters were 5 mm and 3 mm, respectively. A continuous 150-W xenon arc lamp equipped with a 700-nm interference filter 10 nm FWHM, FB700-10 from Thorlabs) was employed as the probing light source. Each analyzed kinetic curve was an average of 50 individual traces. The obtained kinetic traces were fitted using a sum of two exponentials and an offset (*const*) (Eq. 3.2) using OriginPro software.

$$\Delta A(t) = \sum_{i=1}^{2} A_i e^{-\frac{t}{\tau_i}} + const, \tag{3.2}$$

where τ_i is the lifetime of the i^{th} component and A_i is the amplitude associated with this lifetime.

The relative value of the non-decaying component, const (Eq. 3.2), was assumed to be proportional to the fraction of RCs in which electron escapes from final intrinsic electron acceptor (F_X^- in cyanobacterial PSI particles under study and F_B in the remaining PSI particles) to the electrolyte. The time constant of electron transfer outside PSI, τ_{out}, can be estimated from Eq. 3.3 [121]:

$$\tau_{out} = \tau_{av} \frac{A_1 + A_2}{const}, \tag{3.3}$$

The amplitudes A_1, A_2, and *const* are defined in Eq. 3.2, and τ_{av} is an average charge recombination time constant given by Eq. 3.4:

$$\tau_{av} = \frac{\tau_1 A_1 + \tau_2 A_2}{A_1 + A_2}, \tag{3.4}$$

3.6.4.2 Ultrafast transient absorption spectroscopy

The investigation of excitation dynamics was conducted in thin films comprising (1) AgNPs on FTO (Ag-FTO), (2) PSI on FTO (PSI-FTO), and (3) PSI on Ag-FTO (PSI-(Ag-FTO)) measured under distinct experimental conditions: (a) under "dry" conditions – without any electrolyte; (b) in an electrolyte (30 mM Bis-Tris buffer, pH 7.0) supplemented with mediators (20 mM ascorbate and 10 μM phenazine methosulfate, PMS); and (c) subjected to a negative potential of -400 mV vs. Ag/AgCl applied to the working electrode in conjunction with an electrolyte containing the mediators (Figure 3.12b, c, d). A Mai-Tai Ti:Sapphire oscillator, pumped optically with the Empower Holmium:YAG laser emitting 425 nm pulses at a repetition rate of 1000 Hz served as the excitation source. The energy of a single pulse was 50 nJ at a spot size (diameter) of approximately 200 μm. The time window for the experiments was set at 3 ns. Each analyzed curve was an average of 2 scans with 58 temporal points per scan distributed unevenly from -5 ps to 3 ns. The obtained data underwent correction for the spectral chirp of white-light continuum and the spectral background using the SurfaceXplorer software (Ultrafast Systems).

A global analysis of the results was conducted using the Asufit software (https://www.public.asu.edu/~laserweb/asufit/asufit.html) made available by Dr. Evaldas Katilius (Arizona State University). Selected spectra and kinetics were normalized to better comprehend the trends among different experimental conditions when comparing PSI-(Ag-FTO) with Ag-FTO.

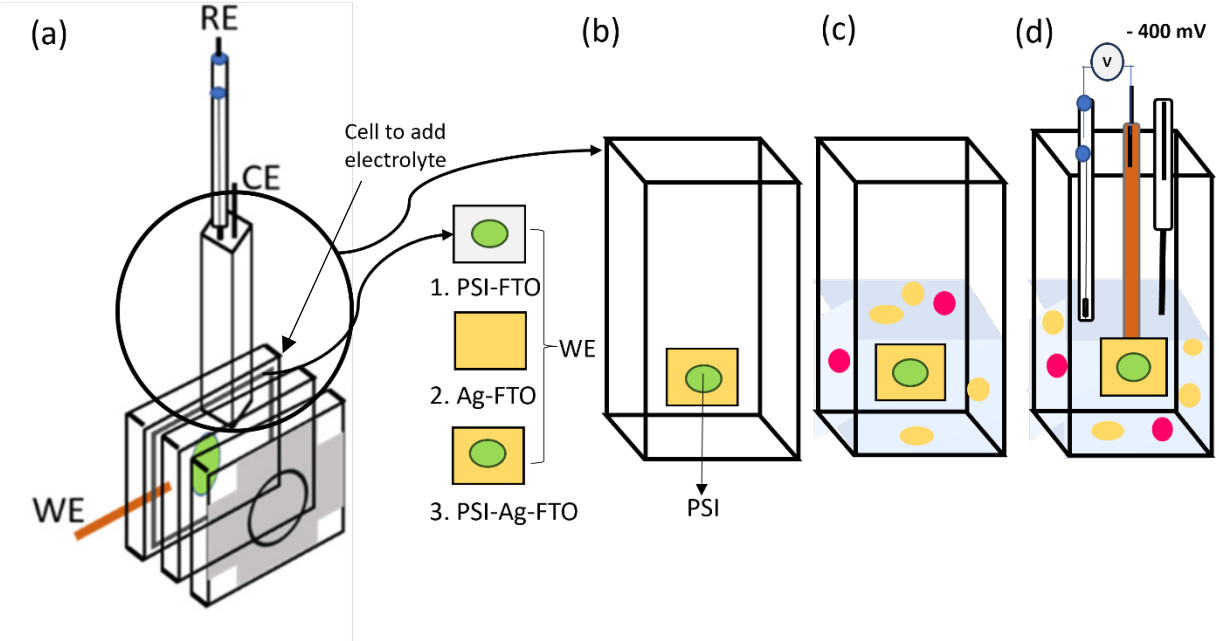

Figure 3.12 Schematic of the **(a)** photoelectrochemical cell used for transient absorption measurements of WE: 1. PSI-FTO, 2. Ag-FTO, and 3. PSI-(Ag-FTO) under different experimental conditions: **(b)** "dry" – without electrolyte, **(c)** with electrolyte containing mediators (ascorbate - yellow dots; DCPIP/PMS – pink dots) and **(d)** same as (c) but with potential applied to WE of -400 mV vs. RE. WE – working electrode, RE – reference electrode (Ag/AgCl), CE – counter electrode (platinum wire). In (d) – from left to right one can see RE, WE, and CE.

3.7 Microscopies

3.7.1. Transmission electron microscopy

Transmission electron microscopy (TEM) measurements were performed by M. Sci. Marcin Kujawa and were conducted in the Laboratory of the Faculty of Biology, Adam Mickiewicz University. TEM micrographs were recorded using a JEM microscope - 1200 EX II (JEOL, Japan) operated at an accelerating voltage of 80 kV. The samples studied were AgNPs suspended in n-hexane and an aqueous solution of AgNPs coated with pluronic F127. These samples for TEM were prepared by placing a drop of the colloidal suspension of AgNPs onto an amorphous carbon-coated copper grid and the respective solvent was allowed to evaporate slowly at room temperature. Histograms presenting the particles size distribution were prepared by measuring the diameter of particles from TEM micrograph using a program written in NI LabVIEW using Particle Analysis function of the NI Vision module by Prof. Mikołaj Pochylski. The diameter of AgNPs distribution obtained from TEM was further described by the log-normal distribution function using Origin software.

3.7.2 Atomic force microscopy

Atomic force microscopy (AFM) experiments were performed by Prof. dr. hab Mateusz Kempiński (Department of Condensed Phase Experimental Physics, Adam Mickiewicz University). The AFM images of PSI derived from the species the cyanobacterium *Synechocystis* sp. 6803 and hydrophobic AgNPs films on FTO were obtained separately using a Park Systems XE7. Cantilever probe of type PPP-NCHR was used in non-contact mode with a nominal spring constant of 42 Nm^{-1} and resonance frequency of 330 kHz.

3.7.3 Scanning electron microscopy

Scanning electron microscopy (SEM) experiments were performed by Prof. dr. hab Mateusz Kempiński (Nanobiomedical Center, Adam Mickiewicz University). SEM images of hydrophobic AgNPs films on FTO were provided by a JEOL 7001TTLS field-emission scanning electron microscope operated at an acceleration voltage of 15 kV. Imaging was performed with the use of a secondary electron detector.

3.8 Photoelectrochemical measurements

Photocurrent measurements were conducted using a custom-designed three-electrode photoelectrochemical cell (PEC), following previously established protocols [1] (Figure 3.13 below). In brief, the setup consisted of thin film samples immobilized on FTO glass as mentioned above serving as the working electrode (WE), a platinum wire acting as the counter electrode (CE), and an Ag/AgCl reference electrode (RE) filled with 3 M KCl (with a potential of 220 mV vs SHE). These three electrodes were submerged in the electrolyte of PEC was and were connected to an Autolab PGSTAT204 potentiostat for data acquisition and control. The electrolyte employed was a 30 mM Bis–Tris buffer pH 7.0, supplemented with 10 mM sodium ascorbate and 200 µM DCPIP, serving as the sacrificial electron donor and mediator, respectively. Illumination was provided by a 685-nm LED with a spectral bandwidth (FWHM) of approximately 24 nm and a light power density of 5.8 mW/cm². The open circuit potential (OCP) was initially determined with the potentiostat in darkness, typically measuring around 100 mV vs SHE. This potential was then applied to the WE throughout the photocurrent experiments to maintain a zero value for the dark current between the WE and CE. Beside experiments at OCP, the dependence of photocurrent on applied potential to the WE was also studied. Finally, the values of internal quantum efficiency (IQE) were estimated following established procedures outlined in previous literature [1].

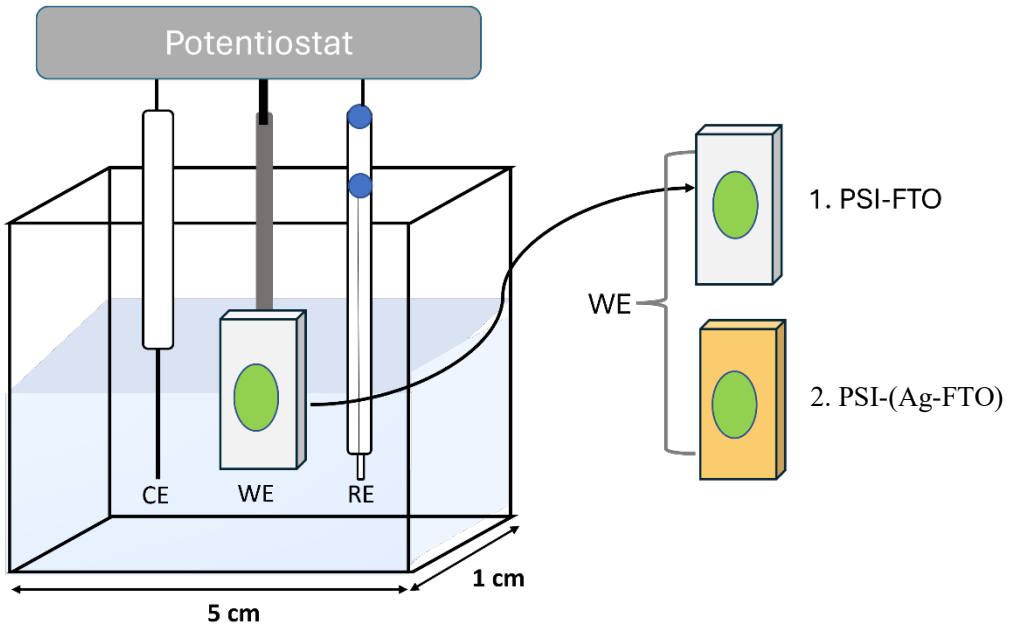

Figure 3.13 Scheme of the three-electrode photoelectrochemical cells used for measurements of photocurrent generated in two types of WE: 1. PSI-FTO and 2. PSI-(Ag-FTO). WE - working electrode, RE - reference electrode, CE – counter electrode.

Chapter 4: Results and Discussions

4.1 Introduction

The first goal of this research was to study and compare the ET inside and outside the PSI particles isolated from the native environment and placed into two artificial systems: an aqueous solution and a film coating FTO conducting glass. Hence, this study was conducted to check if possibly disturbed ET inside PSI complexes placed in the artificial environments or poor coupling between PSI and artificial electron donor and acceptors could be the reasons for the low efficiency of PSI-based biophotovoltaic devices reported in the literature.
The second goal was to improve the low efficiency of biophotovoltaic systems containing PSI by using the surface plasmon resonance of AgNPs to increase light absorption by PSI. To achieve this goal, a detailed methodology was developed to investigate the complexation of PSI particles with AgNPs.
In this chapter (chapter 4), we present the results obtained from the experiments, highlighting the following:

1. Kinetics studies on electron transfer in PSI in solution and immobilized on FTO conducting glass.
2. Fabrication and characterization of colloidal AgNPs.
3. Complexing of PSI with AgNPs in solution and on FTO conduction glass and the characterization of PSI-AgNPs complexes.

Each part contributes to a comprehensive understanding of the interactions and dynamics within the PSI-based photovoltaic systems. The results obtained from kinetic studies on ET in PSI in solution show the factors that limit efficient forward electron transfer, the transfer that is responsible for the photocurrent generated in such devices. Thus, the results obtained for PSI particles in solution shine some light on low efficiency of photocurrent generation in PSI particles deposited on FTO. The fabrication of AgNPs resulted in uniform, spherical shaped AgNPs characterized using optical spectroscopy and microscopy techniques. Furthermore, a systematic comparison of normalized decay associated spectra (DAS) obtained from the fits of the data for the PSI-(Ag-FTO) and Ag-FTO in the blue part of the spectrum (475-630 nm), showed some differences in the spectral characteristics and lifetimes. Ag-FTO showed a shorter-lived signal at 522 nm with a 12 ps lifetime. Whereas, for PSI-(Ag-FTO), a broad band was observed at ~546 nm with a lifetime of ~21 ps. This red-shift of 24 nm and the lifetime extension from 12 to 21 ps may be interpreted as an absorption in the 500-600 nm region caused by the interaction between PSI and AgNPs. Further, the decay kinetics at 546 nm for AgNPs region and at 686 nm for PSI showed the same results. However, the kinetics in the AgNPs region (peak at 546 nm) slows down in the AgNPs region to ~20 ps. It is hypothesized that the interaction between PSI and AgNPs introduces an additional absorption in the 500-600 nm region which decay within the lifetime characteristic for PSI (~20 ps). Therefore, it may be suggested that the energy of light absorbed due to this extra absorption is delivered to the reaction center (RC) and utilized to enhance the charge separation in the RC.

4.2 Electron transfer in and around Photosystem I in solution and immobilized on FTO conducting glass

In this part of our work, we combined the findings from two distinct studies focusing on ET properties in systems containing: 1) PSI complexes isolated from three different species (cyanobacterium *Synechocystis* sp. PCC 6803, red alga *Cyanidioschyzon merolae*, and green alga *Chlamydomonas reinhardtii*) and solubilized in aqueous solutions, and 2) PSI complexes isolated from *Cyanidioschyzon merolae* and immobilized on FTO conducting glass. Respectively, the results from above studies have been published in the following two papers:
1. Goyal, A.; Szewczyk, S.; Burdziński, G.; Abram, M.; Kargul, J.; Gibasiewicz, K. Competition between intra-protein charge recombination and electron transfer outside photosystem I complexes used for photovoltaic applications. Photochem. Photobiol. Sci. **2022**, 21, 319–336. [CrossRef]
2. Szewczyk, S.; Goyal, A.; Abram, M.; Burdzinski, G.; Kargul, J.; Gibasiewicz, K. Electron Transfer in a Bio-Photoelectrode Based on Photosystem I Multilayer Immobilized on the Conducting Glass. Int. J. Mol. Sci. **2022**, 23, 4774. https://doi.org/10.3390/ijms23094774

4.2.1 Electron transfer in and around Photosystem I solubilized in aqueous solutions

This section presents a summary of the key findings and conclusions derived from our initial publication (Goyal et al. 2022). It involves the investigation of five types of PSI particles: two types from cyanobacterium *Synechocystis* sp. PCC 6803 – monomeric PSI (SM) and trimerric PSI (ST), two types from *Cyanidioschyzon merolae* – grown under high light (CmH) and medium light (CmM) conditions, and one type of PSI from *Chlamydomonas reinhardtii* (Cr). These five types of PSI particles were extensively studied by us in the solubilized form (in aqueous solution) using time-resolved absorption spectroscopy. These main studies were complemented with a few control photocurrent measurements of PSI particles immobilized on FTO conducting glass. The studies on solubilized PSI particles yielded crucial insights into: (1) degree of charge separation occurring withing PSI reaction centers (RCs), (2) dynamics of internal charge recombination, and (3) effectiveness/efficiency of electron transfer from PSI to the surrounding electrolyte, which competes with the internal charge recombination within the PSI RC.

4.2.1.1 Control photocurrent measurements

Figure 4.1a displays data from photochronoamperometric measurements recorded for biophotoelectrodes (placed in PEC; see chapter 3, Figure 3.13) composed of FTO plates and PSI complexes sourced from three distinct species investigated in this study. Under OCP, the absence of light resulted in zero dark current, while illumination (685-nm LED with a spectral bandwidth (FWHM) of approximately 24 nm and a light power density of 5.8 mW/cm^2; see chapter 3: Methodology) induced negative photocurrents ranging from 300 to 700 nA/cm^2. These negative photocurrents, similar to previously observed with cyanobacterial PSI-functionalized FTO plates [1], signify electron transfer from the WE (composed of PSI and FTO) through the electrolyte to the CE. All three biophotoelectrodes contained similar chlorophyll quantities, evidenced by similar amplitudes of their steady-state absorption spectra (Figure 4.1b). The absorbance of immobilized PSI complexes at the maximum of Q_y band, corrected for FTO glass absorbance, was measured as $A_{679nm,1\ cm} = 0.030 \pm 0.005$. The absorbance attributed to the photoactive biolayer was estimated to originate from ~5 monolayers (see Eq. 3.1 in chapter 3) of densely packed PSI complexes [1].

The internal quantum efficiency (IQE) of the photovoltaic system is defined by Eq. 4.1

$$IQE = \frac{n_{photoelectrons}}{n_{absorbed\ photons}} \quad (4.1)$$

The number of photoelectrons ($n_{photoelectrons}$) was calculated from the photocurrent measurements, and the number of absorbed photons ($n_{absorbed\ photons}$) from the absorption spectrum of PSI and the spectrum of illuminating light (refer to SI in [1] for detailed information). The calculated IQE values ranged from 0.26% (for CmH) to 0.52% (for ST). These low efficiencies may stem from various factors, including incomplete charge separation within the RCs, charge recombination in the RCs, and poor coupling of PSI with external electron transfer components (mediators and FTO). To ascertain if full charge separation (excitation at 250 nm) was achieved in PSI particles, we compared kinetics of absorption changes originating from the P^+ across all five PSI samples in aqueous solutions. An objective of the following time-resolved absorption studies in solution was to offer a logical explanation for the observed limited IQE and photocurrent density values in the photoelectrodes functionalized with the respective PSI complexes. However, one has to remember that even full charge separation in PSI in solution does not necessarily mean equally effective process in PSI complexes immobilized on FTO due to different conditions of both types of the experiments.

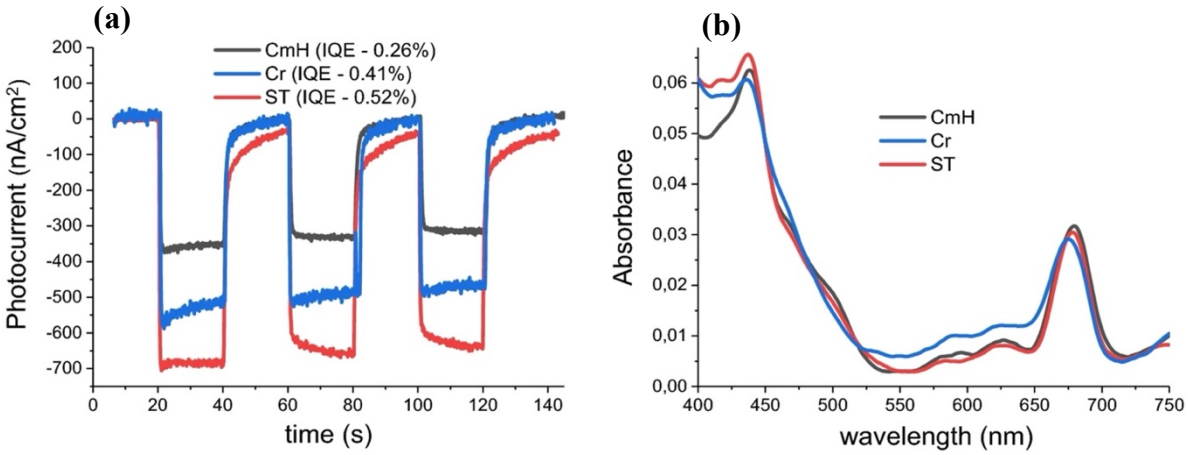

Figure 4.1 (a) Photochronoamperometric and **(b)** steady-state absorption data for PSI complexes isolated from three species and immobilized on FTO glass. IQE – internal quantum efficiency. (Reproduced from [121] under Creative Commons Attribution v4.0 International License[§]).

4.2.1.2 Time-resolved absorption measurements

To find the reasons for the limited efficiency of photocurrent generation in the PSI-FTO-based photoelectrochemical cell (see Figure 4.1a), the ET reactions in and around PSI were studied using time-resolved absorption spectroscopy. Specifically, to assess the efficiency of charge separation in PSI RC and to characterize signal decay dynamics originating from the reduction of the photo-oxidized primary donor P^+, we measured changes in absorption at 700 nm, the wavelength where the neutral primary donor, P, absorbs maximally in its ground state. Upon photo-oxidation of P, we observed an immediate appearance of a photobleaching signal (negative), followed by its decay as P^+ was reduced back to its ground state P. Typically, this reduction of P^+ can occur both through back ET from one of the intrinsic ET acceptors in the RC (charge recombination reactions) and through ET from an external electron donor. However, our experimental conditions, resulted in relatively slow electron donation by external electron donors and the decay of the P^+ signal was attributed exclusively to internal charge recombination within the RC (occurring within a time window of up to 140 ms). ET from external donors to P^+ occurred beyond the experimental time window (between consecutive excitation laser pulses) on a time scale of seconds. Under such conditions it was possible to estimate what percentage of PSI complexes transfer the electrons to the electrolyte (see below).

4.2.1.2.1 Exploring P^+ decay kinetics: dependence on exogenous mediators (sodium ascorbate and DCPIP)

The exemplary photobleaching decay kinetics of P^+ across five distinct PSI aqueous suspensions is shown in Figure 4.2. Each type of PSI complexes was measured first dissolved in a solution without addition of external mediators and then with added mediators: sodium ascorbate and DCPIP. Ascorbate and DCPIP, with standard redox midpoint potentials, E_0 of 60 mV [122] and 217 mV [123, 124], respectively, are suitable for reducing the P^+ primary donor (with an E_0 of P^+/P of 450 mV [5, 125]). Ascorbate, known for its intricate redox chemistry [122], serves as a sacrificial electron donor, while DCPIP functions as an ET mediator [126] that is completely reduced by the surplus of ascorbate (reduction of DCPIP is evidenced by change of the DCPIP solution color from blue without ascorbate to colorless after addition of ascorbate). Studies reported in the literature suggested that the addition of these compounds may reduce P^+ within less than one second [20, 127, 128]. The interaction between ascorbate and DCPIP with PSI is complex, leading to uncertainties about which compound accepts electrons from PSI (F_B^-) as discussed in [1].

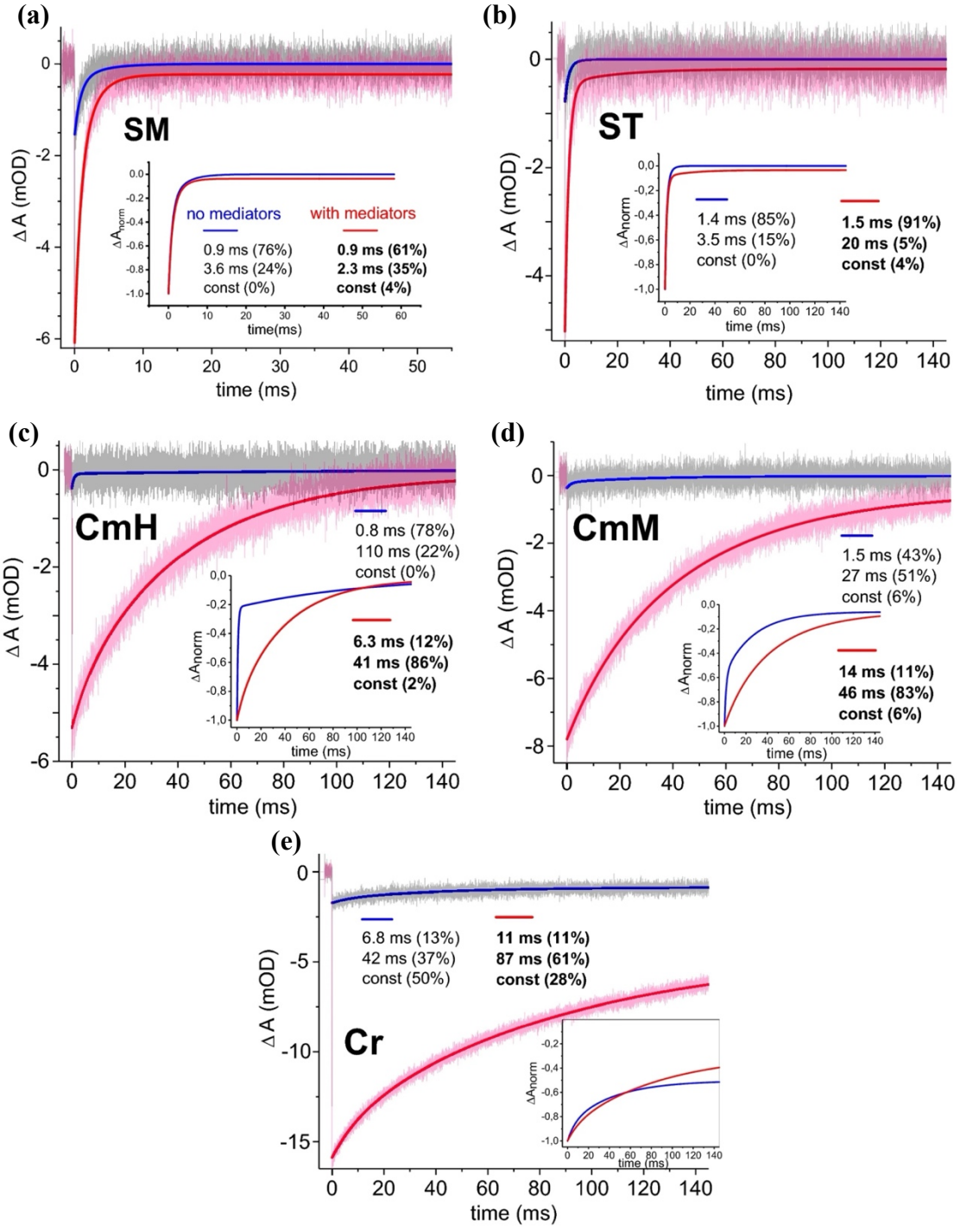

Figure 4.2 Representative time-resolved absorption kinetics of five types of PSI complexes suspended either in buffer only (blue fit curves) or with an addition of saturating amount of mediators (ascorbate: 4–10 mM and DCPIP: 4–40 μM) (red fit curves). Main panels – original kinetics and their two-exponential fits, whose parameters are shown in legends. Insets – respective fits normalized to the same initial amplitudes. See Table 4.1 for further details of experimental conditions and results of data analysis (Reproduced from [121] under Creative Commons Attribution v4.0 International License[§]).

Initial amplitudes

Initial amplitudes under mediators-free conditions

The initial amplitudes of photobleaching signal (ΔA_0) are proportional to the number of PSI complexes containing neutral P before excitation, and thus undergoing charge separation, upon laser flash excitation. One of the general observations was that without the presence of external mediators (this term will be used in the following to both ascorbate and DCPIP), the initial amplitudes of the photobleaching kinetics were notably smaller than in the presence of such mediators in solution, as shown in Figure 4.2a-e (refer to Table 4.1 for exact values). This observation was explained by the quasi-permanent oxidation of P to P^+ in most PSI RCs under mediators-free conditions (RCs with P^+ cannot generate P^+ signal upon excitation flash and thus they cannot give the ΔA signal at 700 nm). Such quasi-permanent oxidation is hypothesized to occur as a result of excitation flashes and, to lesser extent, probe flashes repetitively illuminating the samples (during collection of tens of kinetics to be averaged) and leading to the gradual accumulation of "optically inactive" (*i.e.* with P^+) PSI complexes. The appearance of such inactive fraction can be explained by the electron leakage outside PSI complexes from reduced final PSI electron acceptor (F_X^- or $F_{A/B}^-$), resulting in formation of a long-lived P^+ state (P^+F_X state in Figure 4.4a and $P^+F_{A/B}$ state in Figure 4.4c). It is worthy to note that the terminal electron acceptor in the case of cyanobacterial PSI particles studied in this project was F_X and in the remaining PSI particles – $F_{A/B}$. The hypothetical reason of why the F_X was the terminal acceptor in cyanobacterial PSI particles was that they were stored without glycerol (refer to methodology chapter for details). Such storage is hypothesized to lead to detachment of the peripheral PsaC subunit containing $F_{A/B}$ clusters. Hence, F_X became the final electron acceptor delivering the electron outside the protein. All this reasoning is based on very fast decay of P^+ signal, of the order of 1 ms, characteristic of $P^+F_X^- \rightarrow PF_X$ recombination (see below). The external electron acceptor, to which the electron is transferred, under mediators-free conditions, from F_X^- or $F_{A/B}^-$, is unknown but a possible candidate is oxygen dissolved in the solution or molecules of buffer. The inactive fraction of PSI particles is illustrated in Figure 4.4a, c along with the minor fraction of "optically active" (*i.e.* with P neutral) complexes. In these active complexes, charge recombination efficiently competes with ET escape from PSI, leading to regeneration of neutral P between laser flashes.

Initial amplitudes in the presence of saturating concentrations of mediators

Upon the addition of saturating amounts of ascorbate and DCPIP, the initial amplitudes of the kinetic traces significantly increased up to 4-20 fold, depending on the sample studied (Figure 4.2 and Table 4.1), indicating that the mixture of ascorbate and DCPIP reduces P^+ to P between excitation flashes, restoring the full system's ability to undergo photooxidation of P after each laser flash. Experiments with various concentrations of mediators and two different excitation frequencies (see below) confirmed that the samples with sufficient amount of mediators reached maximal (saturated) initial amplitudes (shown in Figure 4.2), suggesting activity of all PSI complexes under these conditions (Figure 4.3b, d).

Figure 4.2 shows that the saturated initial P^+ signal was 5-6 mOD for cyanobacterial and *C. merolae* CmH samples, ~9 mOD for *C. merolae* CmM sample, and ~16 mOD for Cr PSI sample. These values are roughly proportional to the ratio of the primary donors to the total number of antenna chlorophylls (P/N_{Chls}) in each sample as shown in Figure 4.4 and as expected if all P^+ are effectively rereduced before each excitation laser flash.

Table 4.1 Selected parameters related to the absorbance changes kinetics (at 700 nm) of PSI samples shown in Figure 4.2 (reproduced from [121] under Creative Commons Attribution v4.0 International License[§]).

	$-\Delta A_0$ (mOD)	ΔA_{0rel} (%)	τ_i (ms) A_i (%)				Const (%)	τ_{av} (ms)	τ_{out} (ms)	E_{exc}	f (Hz)	[asc] [DCPIP]
			$P^+F_X^- \rightarrow PF_X$		$P^+F_{A/B}^- \rightarrow PF_{A/B}$							
SM												
Buffer only	1.5	25%	0.9 76%	3.6 24%	_	_	_ 0%	1.5	_	1 mJ	0.5	_
+ mediators	**6.0**	**100%**	**0.9** **61%**	**2.3** **35%**	_	_	_ **4%**	**1.4**	**34**	1 mJ	0.5	10 mM 4 µM
ST												
Buffer only	0.8	16%	1.4 85%	3.5 15%	_	_	_ 0%	1.7	_	1 mJ	0.5	_
+ mediators	**5.0**	**100%**	_	**1.5** **91%**	**20** **5%**	_	_ **4%**	**2.4**	**58**	1 mJ	0.5	10 mM 40 µM
CmH												
Buffer only	0.4	8%	_	0.8 78%	110 22%	_	_ 0%	25	_	1 mJ	0.5	_
+ mediators	**5,3**	**100%**	_		**6.3** **12%**	**41** **86%**	_ **2%**	**37**	**1900**	1 mJ	0.5	10 mM 40 µM
CmM												
Buffer only	0.4	5%	_	1.5 4.3%	27 51%	_	_ 6%	16	_	5 mJ	0.5	_
+ mediators	**7.8**	**100%**	_	_	**14** **11%**	**46** **83%**	_ **6%**	**42**	**660**	1 mJ	0.5	4 mM 40 µM
Cr												
Buffer only	1.7	11%	_		6.8 13%	42 37%	_ 50%	33	_	1 mJ	0.05	_
+ mediators	**16**	**100%**	_	_	**11** **11%**	**87** **61%**	_ **28%**	**75**	**190**	1 mJ	0.05	4 mM 40 µM

ΔA_0 - initial ΔA amplitude just after excitation; $\Delta A_{0rel} = \frac{\Delta A_0}{\Delta A_0(with\ mediators)} 100\% -$ initial ΔA amplitude just after excitation, relative to the initial ΔA amplitude just after excitation in the respective experiment with mediators; τ_i, $A_i, const -$ bi-exponential fit parameters; τ_{av} - an average charge recombination time constant estimated from Eq.3.4 (chapter 3); τ_{out} - time constant of ET outside PSI estimated from Eq. 3.3 (chapter 3); $E_{exc} -$ excitation energy; f - excitation frequency; [asc], [DCPIP] – concentration of ascorbate and DCPIP respectively.

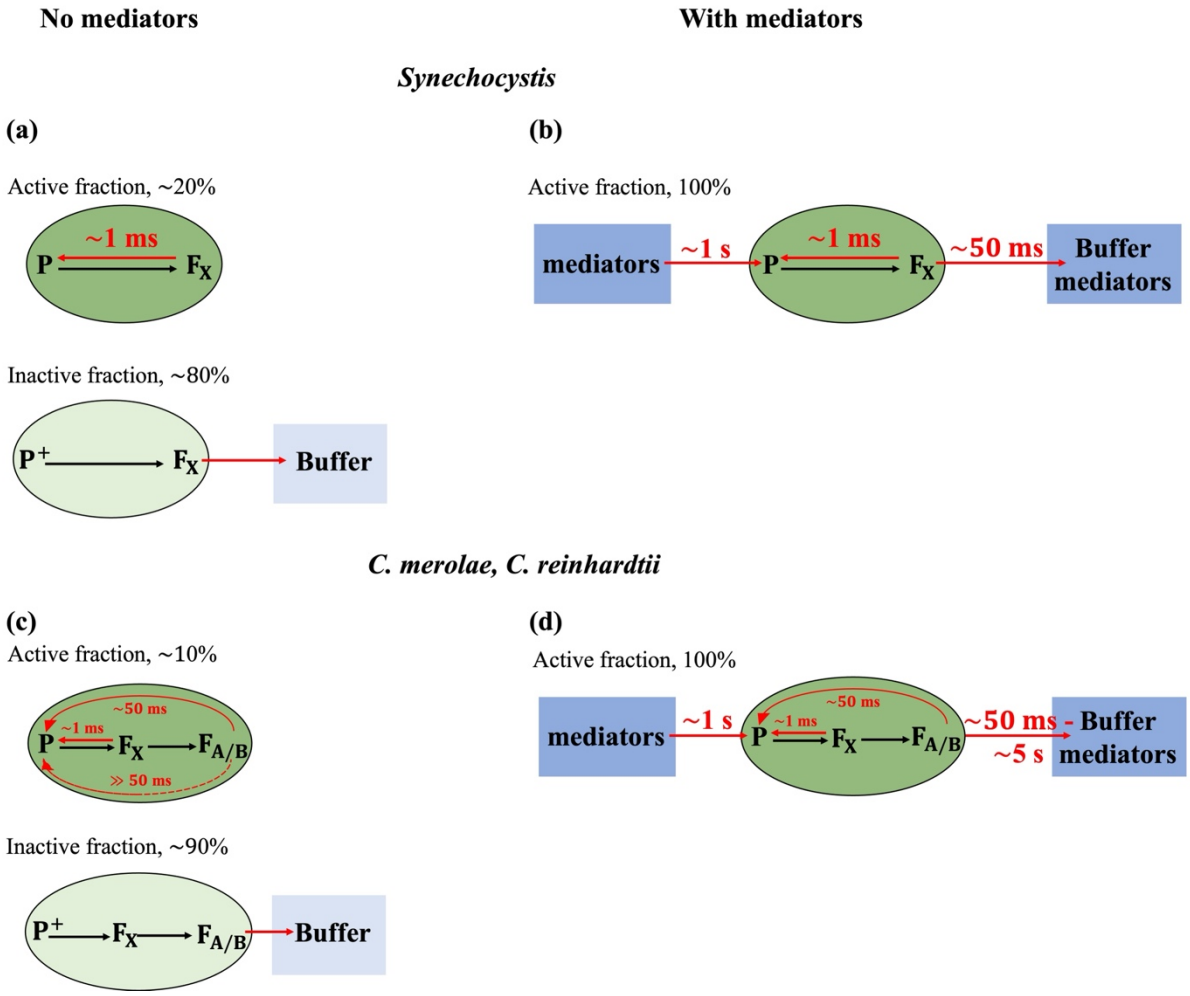

Figure 4.3 Model of ET reactions leading to observed (P^+- P) ΔA signals in PSI complexes from *Synechocystis* (**a**, **b**) and *C. merolae/C. reinhardtii* (**c**, **d**). Panels (**a**) and (**c**)—no ET mediators were present in the buffer solution; panels (**b**) and (**d**)—saturating amount of ET mediators were present in the buffer solution. Black arrows depict fast forward ET steps inside PSI, not resolved in our experiments. Red arrows depict ET steps responsible for the initial amplitudes and decay rates of the P^+ kinetic traces (the ~ 1-ms back ET from F_X^- to P^+ in panel D was not directly observed for Cm and Cr but was taken from the literature [20, 59] and is supposed to affect the 6–14 ms recombination components shown in Table 4.1). Dark green ovals – PSI complexes contributing to the (P^+- P) ΔA signal. Light green ovals – PSI complexes not contributing to the (P^+- P) ΔA signal, due to quasi-permanent oxidation of P. Blue rectangles – solution of buffer with or without ET mediators. Reproduced from [121] under Creative Commons Attribution v4.0 International License[§].

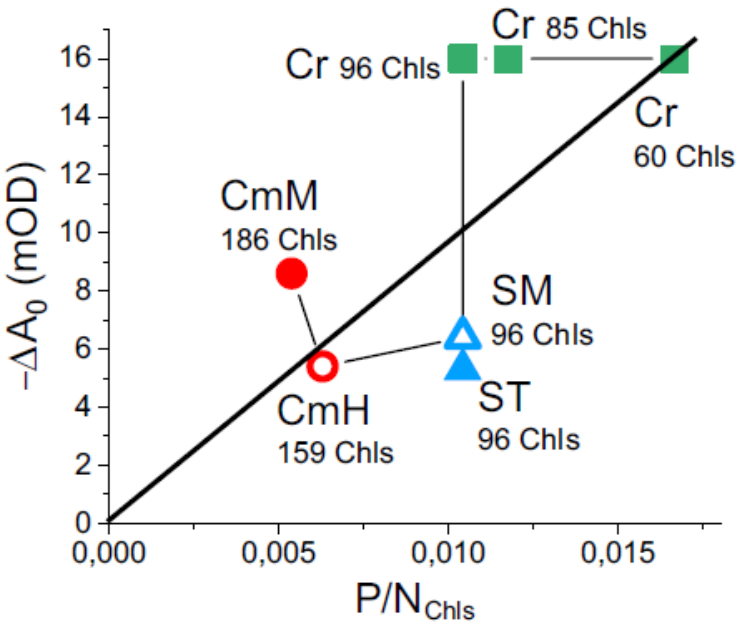

Figure 4.4 Dependence of the maximal initial amplitude ($-\Delta A_0$) for each of the PSI preparation on the P/N_{Chls} ratio in each type of PSI complex (estimated from the kinetics measured in ~ 54–130-ms time windows). N_{Chls} is the number of antenna Chls per one primary donor for the individual type of PSI whereas P/ N_{Chls} is its reciprocal; the N_{Chls} number is shown at each label identifying the individual type of PSI; the three different values of N_{Chls} for the Cr PSI come from three different references (60 Chls – [41], 85 Chls – [42], 96 Chls – [43]). The thick straight line is a theoretical dependence obtained under the assumption that for each sample the $\Delta A_{700nm,1cm}(P^+–P) = \Delta A_{\sim 680nm,1cm}(Chl^*–Chl)$, where the right hand term is absorption change related to photobleaching of one antennas Chl molecule, and that excitation pulse was saturating (oxidizing primary donors in all probed PSI complexes across the cuvette). Reproduced from [121] under Creative Commons Attribution v4.0 International License[§].

P^+ decay kinetics

The decay kinetics of (P^+ - P) ΔA signal (referred in the following as P^+ signal) are different for all five samples studied and also show differences when measured with and without external mediators, as shown in Figure 4.2. The initial amplitudes are significantly larger in the presence of external mediators, hence making the decay kinetics under these conditions more representative of the entire PSI particles populations. Therefore, the analysis is primarily focused on these kinetics for each sample and after that the decay kinetics from the optically active PSI complexes, collected for the solutions without mediators are described.

The P^+ decay kinetics for all samples as shown in Figure 4.2, were analyzed using a bi-exponential decay function and an offset (*const*) (Eq. 3.2, chapter 3). The fit parameters, presented in both Figure 4.2 and Table 4.1, quantify various P^+ decay kinetics among the samples under investigation.

Synechocystis sp. PCC 6803 monomers and trimers

The decay kinetics of P^+ in the *Synechocystis* SM and ST PSI samples mostly occur with approximately 1–2 ms time constant (Figure 4.2a, b), characteristic of $P^+F_X^- \rightarrow PF_X$ charge recombination [20, 59]. The SM sample shows no slower phase, while the ST complexes show an additional 20-ms decay with 5% contribution to the initial signal, attributed to $PF_{A/B}^- \rightarrow PF_{A/B}$ charge recombination [20, 59]. This suggests that in the most of *Synechocystis* PSI particles, the photo-excited electron does not reach the final electron acceptor ($F_{A/B}$), possibly due to structural perturbations in the PSI particles stored at -20°C without glycerol, perhaps involving detachment of the PsaC subunit coordinating F_A and F_B clusters from the PSI complex (see above). In such perturbed PSI particles, the F_X cluster may act as the final intrinsic electron acceptor.

In our model (see Figure 4.3b), the relative value of the non-decaying component, *const* (Eq. 3.2, chapter 3), is roughly proportional to the fraction of RCs in which electron escapes from final intrinsic electron acceptor (F_X^- in cyanobacterial PSI particles under study) to the electrolyte. This electron transfer competes with internal charge recombination reactions. The time constant of electron transfer outside PSI, τ_{out}, can be estimated from Eq. 3.3 and 3.4 in chapter 3 which is based on the model illustrated in Figure 4.3b. For cyanobacterial PSI, $\tau_{out} \approx$ 50 milliseconds for both SM (τ_{out} = 34 ms) and ST (τ_{out} = 58 ms) complexes (Table 4.1). This is significantly faster than the ET from PSI to electrolyte observed in the remaining PSI particles in solution (see below and Table 4.1). On the other hand, due to fast charge recombination, the overall efficiency of electron transfer from PSI to electrolyte is low as reflected by small value of *const* parameter (4% for both SM and ST).

Mediators-free conditions. The *Synechocystis* SM and ST PSI complexes, when suspended in a buffer without external mediators, show P^+ decay kinetics similar to those observed in buffers with mediators, as shown in Figure 4.2a, b and Table 4.1. The key difference was the absence of an offset (*const* = 0) in the PSI complexes in the absence of external mediators. This indicates that in the optically active PSI complexes in solution without mediators, ET from PSI to electrolyte does not occur. Fractions of the active PSI estimated from the initial ΔA signals (without and with mediators) amount to 25% and 16% for the SM and ST samples, respectively.

It is hypothesized that in these fractions, ET from PSI to solution is prevented from occurring likely due to some structural factors. Furthermore, it can be speculated that ET from PSI to electrolyte in the remaining (inactive) fractions (comprising 75% and 84% for SM and ST, respectively) does take place, leading to the formation of a long-lived P^+F_X state undetectable in transient absorption experiments at 700 nm as discussed above. Hence, there is a degree of heterogeneity shown by the *Synechocystis* SM and ST PSI complexes concerning the occurrence of ET from PSI to the solution.

C. merolae

In both the PSI preparations from *C. merolae* (CmM and CmH), the P^+ decay kinetics is mainly characterized by a dominant ~45-ms phase (~85%), attributed to $P^+F_{A/B}^-\rightarrow P\ F_{A/B}$ charge recombination [20, 59], shown in Figure 4.2c, d and Table 4.1. The second P^+ decay kinetic phase characterized by 6-14 ms lifetime (11-12%) is assigned to a mixture of $P^+F_{A/B}^-\rightarrow PF_{A/B}$ charge recombination and $P^+F_X^-\rightarrow PF_X$ charge recombination [59]. The offset in CmH is 2%, and in CmM - 6%. Both these values are comparable to the offset of 4% in cyanobacterial samples. Again, this offset is attributed to a fraction of RCs in which ET from PSI to electrolyte over compete charge recombination inside the RC. However, unlike in cyanobacterial PSI complexes where F_X^- acts as a final acceptor, ET from PSI to electrolyte in *C. merolae* occurs mostly from $F_{A/B}^-$. Similar offset as in cyanobacterial PSI translates into much slower ET from PSI to electrolyte because this ET competes with much slower recombination ($\tau_{avg} \approx 40$ ms) than in cyanobacterial PSI ($\tau_{avg} \approx 2$ ms). The value of τ_{out} in CmM is 660 ms and in CmH - 1900 ms which shows that the time of ET from PSI to electrolyte is three times smaller in case of CmM than CmH and hence ET from CmM PSI to electrolyte is more efficient.

Mediators-free conditions. Small initial amplitude (5-8%; see parameter ΔA_{0rel} in Table 4.1) of P^+ decay kinetics in the absence of external mediators again shows that respectively small fractions of PSI complexes were unable to transfer electron to electrolyte (Table 4.1). The decay kinetics of P^+ in CmH and CmM solutions without mediators occurring within ~1 ms (78% and 43% for CmH and CmM, respectively) reveal large contributions from $P^+F_X^-\rightarrow PF_X$ recombination. This contribution is responsible for an acceleration in the average decay lifetime (τ_{avg}) in comparison to the samples with mediators. The offset of 6% in CmM in the absence of mediators is attributed to unusually slow charge recombination (Figure 4.3c, ">>50 ms") in structurally perturbed proteins that cannot deliver electron to electrolyte. Observation of the signals from small fractions of PSI even without mediators reveals the heterogeneity in the complexes similar to that discussed above for cyanobacterial PSI under mediators-free conditions – active and inactive complexes are, respectively, unable and able to transfer electron to the solution.

C. reinhardtii

The P^+ decay kinetics of *C. reinhardtii* in the presence of mediators are characterized by a dominant ~87 ms (61%) phase and a minor ~11 ms (11%) phase (Table 4.1). The slower phase was attributed to $P^+F_{A/B}^-\rightarrow PF_{A/B}$ charge recombination, and faster one – to the mixture of $P^+F_{A/B}^-\rightarrow PF_{A/B}$ and $P^+F_X^- \rightarrow PF_X$ charge recombinations. There was no ~1-2 ms phase observed in P^+ decay kinetics from *C. reinhardtii*.

It was concluded that the majority of PSI complexes show full charge separation from the primary donor to final acceptor $F_{A/B}$. The offset of 28% observed in presence of mediators is much larger in comparison to other samples (2-6%) studied (see above). This is a net effect of interplay between relatively slow charge recombination (τ_{av} = 75 ms) and fast ET outside PSI (τ_{out} = 190 ms) as shown in Table 4.1.

Mediators-free conditions. In the absence of mediators in PSI solution, the initial amplitude was smaller than for the solution with mediators (ΔA_{0rel} = 11%) and the decay was accelerated (τ_{av} = 33 ms which is twice smaller than 75 ms observed for the solution with mediators). A similar trend was observed in most of the other samples. The 6.8 ms and 42 ms phases observed were attributed to $P^+F_{A/B}^- \rightarrow PF_{A/B}$ charge recombination with contribution from $P^+F_X^- \rightarrow PF_X$ charge recombination to the former (faster) phase. A relatively large value of the offset (50%) in comparison to other samples was attributed to a fraction of PSI RCs (Table 4.1) that are unable to transfer electrons outside PSI but show particularly slow charge recombination (Figure 4.4c, ">>50 ms").

4.2.1.2.2 Exploring P^+ decay kinetics: systematic comparison across multiple experimental conditions

Besides the measurements of P^+ decay kinetics in PSI suspensions with saturating concentrations and without mediators (ascorbate and DCPIP), the samples were also prepared with either ascorbate alone or combined with varying concentrations of DCPIP (4 or 40 μM). The results obtained from such combinations were compared for all the five samples (SM, ST, CmM, CmH, and Cr) at two excitation energies (1 and 5 mJ) and two excitation frequencies (0.5 and 0.05 Hz). Such comparison is illustrated in Figure 4.5. The horizontal axis presents the experimental conditions 1-12 (explained in Table 4.2) arranged in such a way that with an increment in experimental condition number, the reduction of P^+ is more efficient. A general trend is observed for the dependence of initial amplitude ($-\Delta A_0$) and average decay time (τ_{av}) on reduction power, whereas other parameters did not show regular trend probably due to the limited signal-to-noise ratio of the raw kinetics data.

Initial amplitudes of the P^+ decay kinetics ($-\Delta A_0$)

In general, the five samples when compared show that the more reducing conditions (larger experiment number – see Table 4.2) the larger initial amplitudes of the P^+ decay kinetics (Figure 4.5, column I: a,e,i,m,q) (except for experiments 10-12 for SM (Figure 4.5a)). However, this dynamic varies between the samples.

Samples without mediators (experiments 1-3)
For samples without mediators (experiments 1-3), the signal $-\Delta A_0$ is small compared to the samples with mediators. This indicates that, in the absence of mediators, in large majority of PSI complexes, accumulation of the state P^+ occurs which prevents appearance of the signal in response to excitation by laser flashes. As noticed above, such particles may be called inactive or "optically inactive". Observation of small signal under these conditions indicates that a small fraction of PSI particles relaxes between laser flashes (within 2 or 20 s) – P^+ is reduced to P. This fraction may be called "optically active". An increase in the excitation energy from 1 mJ (experiment 1) to 5 mJ (experiment 2) causes only a small increase in the signal. This suggests that 1 mJ is high enough to saturate the signal.

In comparison to the excitation energy (experiment 2), the excitation frequency leaves a stronger impact on the signal when decreased from 0.5 Hz (experiment 1) to 0.05 Hz (experiment 3). This infers that at the lower excitation frequency of 0.05 Hz, accumulation of the state P^+ is lower – *i.e.* larger fraction of PSI (but not all!) relaxes between laser flashes from P^+ to P state. This indicates that in the absence of mediators, reduction of a fraction of P^+ occurs on the time scale of tens of seconds. As discussed above, accumulation of optically inactive PSI particles is probably caused by electron transfer from PSI (specifically from the final electron donor in PSI, F_X or F_A/F_B, to the solution). Such electron transfer leaves PSI particles with long-lived P^+. On the other hand, relaxation of PSI particles may be caused by charge recombination inside the protein (occurring on millisecond or longer time scale and giving rise to the signal under mediators-free conditions) in (active) PSI particles unable to transfer electron to the solution.

Samples with ascorbate (experiments 4-6)

The results of the experiments with the addition of 4-10 mM ascorbate with 1 mJ excitation energy and 0.5 Hz frequency (experiment 4) show an increase in the signal in comparison to experiments without any addition of ascorbate (experiments 1-3). The increase in the signal is larger with addition of 10 mM ascorbate (Figure 4.5a,e,i) than when 4 mM ascorbate is added (Figure 4.5m,q). This is as expected since ascorbate acting as an electron donor reduces P^+ by donating the electron directly to it [52]. Increasing the excitation energy from 1 to 5 mJ (experiment 5) in the presence of ascorbate causes similar slight effect on ΔA_0 signal as in experiments without mediators (compare experiments 1 and 2) confirming that the energy of 1 mJ is saturating. Apparently, 10 mM ascorbate at 0.5 Hz excitation frequency is not enough to fully re-reduce the photo-oxidized primary donor P^+ to its ground state P. Decreasing the excitation frequency to 0.05 Hz (experiment 6) increases the initial signal (compared to experiment 4 at 0.5 Hz) although not to the maximal level characteristic of experiments with the addition of DCPIP (experiments 7-12). These observations indicate that 4-10 mM ascorbate donates the electrons to P^+ on a time scale from single seconds to tens of seconds.

Samples with ascorbate and DCPIP (experiments 7-12)

Addition of 4 μM DCPIP (experiment 7, 0.5 Hz) enhances the signals, particularly in cyanobacterial PSI samples where signals recorded under these conditions showed almost saturating effect (Figure 4.5a and e). For all samples but cyanobacterial PSI, decreasing frequency from 0.5 Hz to 0.05 Hz at 4 uM DCPIP (experiment 9) further increased the signal showing that at 4 μM concentration, 2 seconds is too short time to fully rereduce P^+ by DCPIP, but 20 seconds is time sufficient for that (see the $-\Delta A_0$ signals in experiments 9-12). Comparing experiments 9-12, one concludes that the conditions with concentrations of 4-10 mM ascorbate and 4 μM DCPIP, 0.05 Hz frequency, and 1 mJ excitation energy (or 40 μM DCPIP, 0.5 Hz frequency, and 1 mJ excitation energy) are sufficient for all samples to fully rereduce P^+ to the neutral state P within time interval between consecutive excitation flashes. Interestingly, P^+ in cyanobacterial PSI seems to be more accessible to both ascorbate and DCPIP than P^+ in the remaining PSI complexes – addition ascorbate and 4 μM DCPIP at 0.5-Hz (experiment 7) increases the signal closer to the saturation level in cyanobacterial PSI.

Table 4.2 Experimental conditions of absorbance change measurements in which P^+ decay kinetics were recorded (reproduced from [121] under Creative Commons Attribution v4.0 International License[§]).

Experiment number	[asc]*(mM)	[DCPIP] (μM)	E_{exc} (mJ)	f (Hz)
1	_	_	1	0.5
2	_	_	5	0.5
3	_	_	1	0.05
4	10	_	1	0.5
5	10	_	5	0.5
6	10	_	1	0.05
7	10	4	1	0.5
8	10	4	5	0.5
9	10	4	1	0.05
10	10	40	1	0.5
11	10	40	5	0.5
12	10	40	1	0.05

*In case of CmM and Cr, 4 mM ascorbate was used instead of 10 mM after confirming that the former concentration of ascorbate was sufficient for the reliable analysis using 40 μM DCPIP mediator.

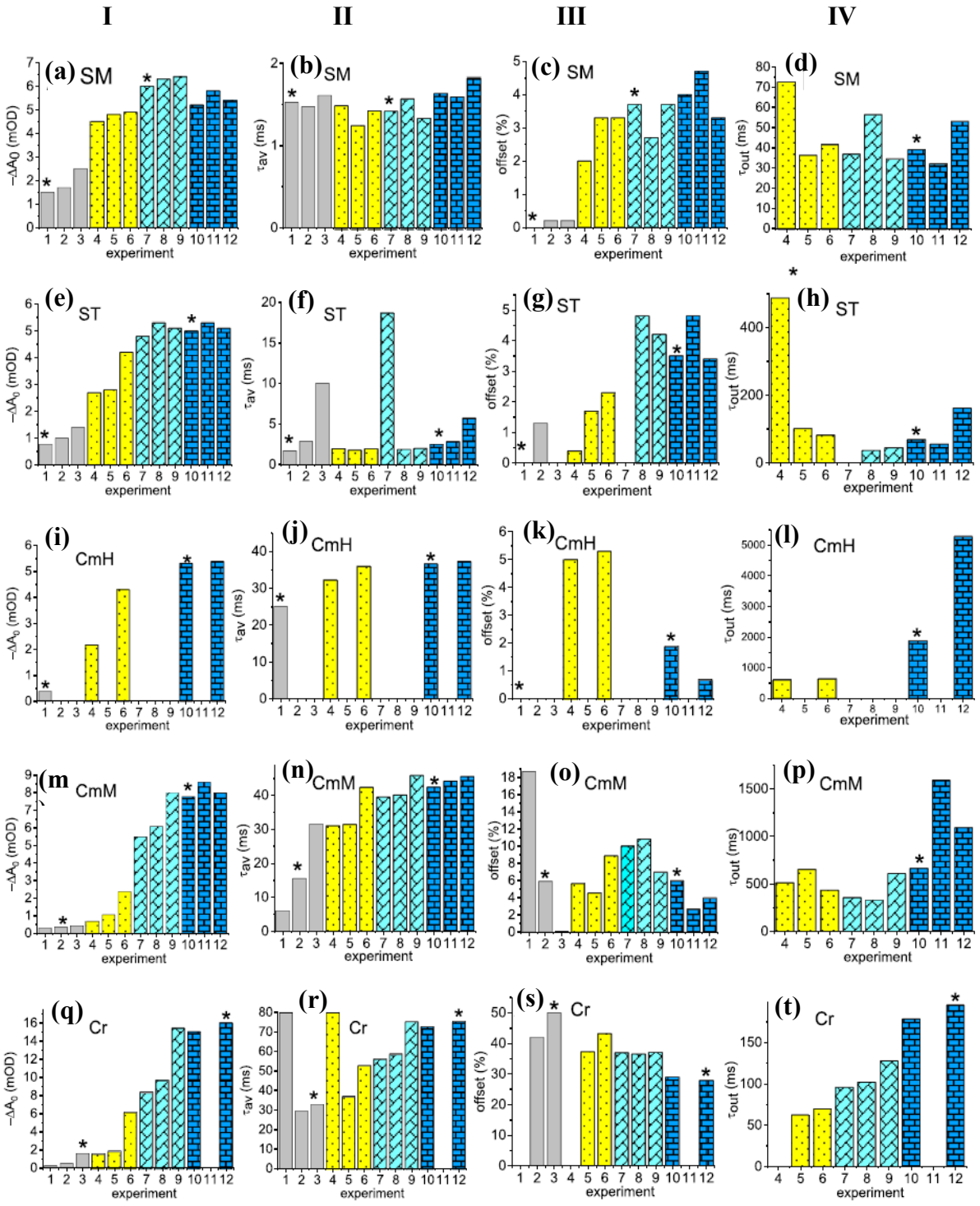

Figure 4.5 Comparison of the results of the P^+ decay measurements performed under a range of experimental conditions (represented by numbers 1–12 shown under the abscissa). The experimental conditions are explained in Table 4.2. The five rows of panels correspond to the five types of PSI complexes. The four parameters correspond to four parameters. The stars indicate the data corresponding to the kinetics presented in Fig. 4.2. $\Delta A_0 = \Delta A(t = 0)$, where $\Delta A(t)$ and offset (*const*) are the quantities shown in Eq. 3.2 (chapter 3). τ_{out} and τ_{av} are the quantities shown in Eqs. 3.3 and 3.4, respectively (refer to chapter 3). Note that for CmH and Cr PSI complexes, some experimental conditions were omitted (Reproduced from [121] under Creative Commons Attribution v4.0 International License[§])

Average time constant of charge recombination (τ_{av})

Figure 4.5 (column II: b, f, j, n, r) compares the average time constants of charge recombination calculated from Eq. 3.4 (refer to chapter 3). Investigating the cyanobacterial samples reveals time constants ranging from ~1.5 ms (SM) to about 2 ms (ST) and shows no noticeable dependence on experimental conditions. These lifetimes correspond to the recombination process of $P^+F_X^-$ to P F_X. Exceptionally large τ_{av} values observed in experiments 3 and 7 (Figure 4.5f) for the ST sample are artifacts stemming from limited signal-to-noise ratio leading to problems with resolving offset component in the respective fits (Figure 4.5g) which in turn increase the average time constant.

Conversely, for the remaining samples (CmH, CmM, and Cr – Figure 4.5j, n, r, respectively), τ_{av} exhibits a gradual increase with the reduction power of the conditions, indicating heterogeneity within PSI complexes: at low reduction power (experiments 1-3) only a small fraction of PSI complexes characterized by fast recombination, contributes to the signal, while at higher reduction power (experiments 4-12) increasing amounts of slowly recombining PSI complexes contribute to the ΔA(t) signal. This observation maybe explained in the following way. Small amount of PSI particles giving the P^+ signal in the absence of redox mediators (experiments 1–3) contain significant fraction of structurally perturbed proteins with charge separation limited to $P^+F_X^-$ state, followed by rapid 1–2 ms $P^+F_X^- \rightarrow PF_X$ recombination (this is particularly well seen in Figure 4.2c,d showing kinetic decay for CmH and CmM). This accelerates average recombination rates. While this effect persists in subsequent experiments (4–12), its relative impact diminishes systematically with increasing reduction power and increasing contribution from undisturbed proteins performing $P^+F_{A/B}^- \rightarrow PF_{A/B}$ recombination [20, 59]. As an effect, τ_{av} reaches values of ~40 ms for CmH and CmM PSI samples and ~80 ms for Cr PSI samples under high reduction power conditions (experiments 10-12). Additionally, the two unusually high τ_{av} values in experiments 1 and 4 for the Cr sample (Figure 4.5r) are artifacts similar to those observed for cyanobacterial PSI (Figure 4.5f) discussed above.

Non-decaying component (offset) and the PSI electron escape time constant (τ_{out})

The origin of the offset is long-lived P^+ state – caused either by electron transfer from PSI to the solution, making charge recombination impossible, or by extremely slow charge recombination in a fraction of disturbed complexes, as discussed above. On the other hand, τ_{out} parameter is calculated from the fit parameters including offset (Eq. 3.3, chapter 3). Since both offset and τ_{out} parameter behave more irregularly with increasing reduction conditions (Figure 4.5 column III and IV respectively) than initial amplitude, ΔA_0, and average decay time, τ_{av}, it is difficult to draw strong conclusions from our data.

However, it is worth to note that for cyanobacterial samples SM and ST, τ_{out} value shows a consistent pattern of oscillation around ~50 ms across most of the experimental conditions. For CmM and CmH, τ_{out} usually exceeds 500 ms, and for Cr, τ_{out} more regularly increases from ~50 ms to ~200 ms with increasing reduction power.

4.2.1.2.3 Conclusions from studies on electron transfer in Photosystem I solubilized in aqueous solutions

Results presented in this chapter show that there exists variety of kinetics of P^+ reduction in five analyzed preparations of PSI. In all PSI samples the kinetics were fitted with two exponential phases which is interpreted in terms of heterogeneity of each of the samples. The faster phase bears the features of $P^+F_X^- \rightarrow PF_X$ charge recombination while the slower one is attributed to $PF_{A/B}^- \rightarrow PF_{A/B}$ charge recombination. Therefore, it can be concluded that the various isolated PSI particles are disturbed to different extent. Differences in accessibility of mediators to the primary donor were detected – with somewhat better accessibility in the case of cyanobacterial PSI than in the remaining complexes. Also, electron transfer from PSI to the electrolyte is the fastest in cyanobacterial PSI, despite it was probably devoid of PsaC subunit containing F_A and F_B acceptors.

The results obtained for PSI particles in solution shine some light on low efficiency of photocurrent generation in photovoltaic cells based on PSI-FTO electrodes (Figure 4.1a). The factors that limit the photocurrent could be the following: 1) disturbance to the natural flow of electrons within the PSI complex, including enhanced charge recombination reactions inside PSI, when it is deposited on the FTO; apparently, in solution, the charge recombination reaction is faster than ET between applied mediators and donor/acceptor sides of PSI, 2) poor electronic coupling between PSI particles and the device's synthetic components (FTO electrodes), and 3) short-circuiting, *i.e.* dissipative ET from acceptor side of one PSI complex to the donor side of another one.

4.2.2 Electron transfer in a bio-photoelectrode based on Photosystem I multilayer immobilized on the conducting glass

This section presents a summary of the key findings and conclusions derived from our second publication (Szewczyk et. al. 2022). Based on the results from the studies of PSI in solution (section 4.2.1), it was concluded that PSI complex from red alga *C. merolae* showed complete charge separation. Hence, in this section, this PSI complex was explored further as a film of ~40 monolayers immobilized on the FTO conducting glass. Time-resolved absorption spectroscopy and chronoamperometry were utilized to study the film under varied electric potentials and electrolyte compositions. The study quantified the efficiency of light-induced charge separation within the PSI film and internal quantum efficiency of photocurrent generation in PSI-based PEC.

4.2.2.1 Photocurrent measurements

Photocurrent measurements were performed using the PEC shown schematically in Figure 3.12. In order to maximize the transient absorption signal, the multilayer of PSI investigated here was thicker (~40 layers, $A_{679nm,1\ cm}$ = 0.27) in comparison to previously studied ~5 monolayers of PSI from *C. merolae* on FTO ($A_{679nm,1\ cm}$ = 0.03; section 4.2.1). Figure 4.6a displays the chronoamperometric data obtained for such a PSI-FTO electrode at OCP = +115 mV. At this potential, the illumination induced negative peak photocurrent of ~200 nA which stabilized after some time reaching a stable value of current ~180 nA. This stable photocurrent corresponds to an IQE of 0.073% which is ~3.5 times smaller than the IQE of 0.26% obtained for PSI-FTO electrode with only 5 layers of PSI proteins (Figure 4.1). These negative photocurrents at OCP signify electron transfer from the FTO to PSI and then through the electrolyte to the CE representing a cathodic photocurrent.

The cathodic photocurrent has been observed also in other biohybrid cells incorporating PSI from *C. merolae* [41, 129, 130].

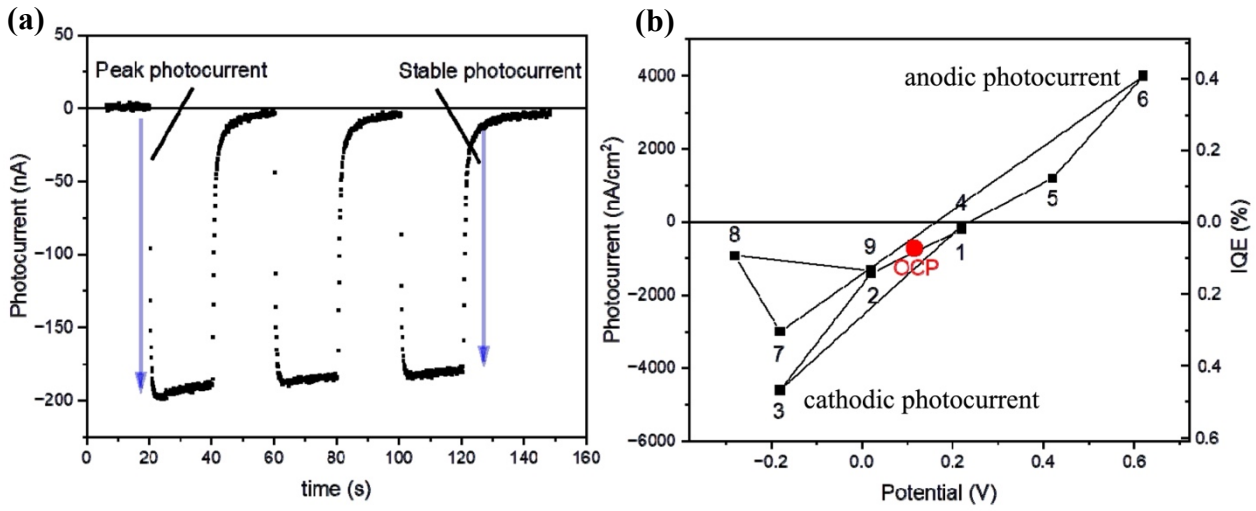

Figure 4.6 Photocurrent generated in the PSI-FTO electrode with ~40 monolayers of PSI complexes. **(a)** Chronoamperometric data recorded for the PSI-FTO electrode of the photoactive surface of ~0.25 cm^2 at OCP (see corresponding red point in panel b); three cycles of light illumination are presented with initial (peak) and stable photocurrents indicated; the electrolyte employed was a 30 mM Bis–Tris buffer pH 7.0, supplemented with 10 mM sodium ascorbate and 200 µM DCPIP and **(b)** stable photocurrent amplitudes (left axis) and corresponding IQE (right axis) vs. potential applied to WE (dark current baseline has been subtracted from the original chronoamperometric data); the numbers at the experimental points show the sequence of the applied potentials; additionally, photocurrent measured at OCP is shown (red point). Note that, in panel b, photocurrent was recalculated per centimeter squared (Reproduced from [113] under Creative Commons Attribution v4.0 International License[§]).

The dependence of photocurrent on the applied potential to the PSI-FTO electrode was studied and is shown in Figure 4.6b. A general observation is that at high positive potentials, anodic photocurrent is observed (points 5 and 6), whereas, at lower potentials, cathodic photocurrent is generated. At moderate potentials (20-220 mV), the current does not depend on the history of previous values of applied potential (points 2 and 9 or 1 and 4). Oppositely, at a relatively low value of potential of –180 mV, the photocurrent is determined by the sequence of preceding potentials (points 3 and 7). A similar behavior has been described in literature for the PSI deposited on FTO from cyanobacterium *Synechocystis* sp. 6803 [1]. An intuitive illustration representing this dependence is shown in Figure 4.7. The photocurrent generated at OCP (red dot in Figure 4.7b) is low due to the competition between the charge recombination and the electron transfer from the PSI to the electrolyte. When the potential is lowered, the efficiency of $P^+(F_{A/B})^- \rightarrow PF_{A/B}$ charge recombination process is decreased because of the delivery of electrons from the FTO to the photooxidized primary donor P^+, re-reducing the P^+ to P (Figure 4.7a). Application of "neutral potential" (+220 mV) almost eliminated the photocurrent (Figure 4.6b: points 1 and 4) due to inefficient transfer of electrons to P^+ by the FTO and charge recombination process increased by electrostatic attraction of electrons to FTO (Figure 4.7c). At a positive potential close to +420 mV or higher (+620 mV) than the redox mid-potential of P^+/P (~+450 mV [5, 125]), the electron transfer from the PSI to electrolyte becomes inefficient

due to the permanent oxidation of primary donor P to P^+, resulting in no generation of photocurrent (Figure 4.7d). According to this, anodic photocurrent observed may have two possible sources. It may originate either from the electrochemical oxidation of photoexcited antenna Chls as also reported in literature for other photosynthetic proteins [1, 131] or due to a small fraction of PSI complexes with acceptor side facing the FTO and still able to effectively sustain forward electron transfer (Figure 4.7d).

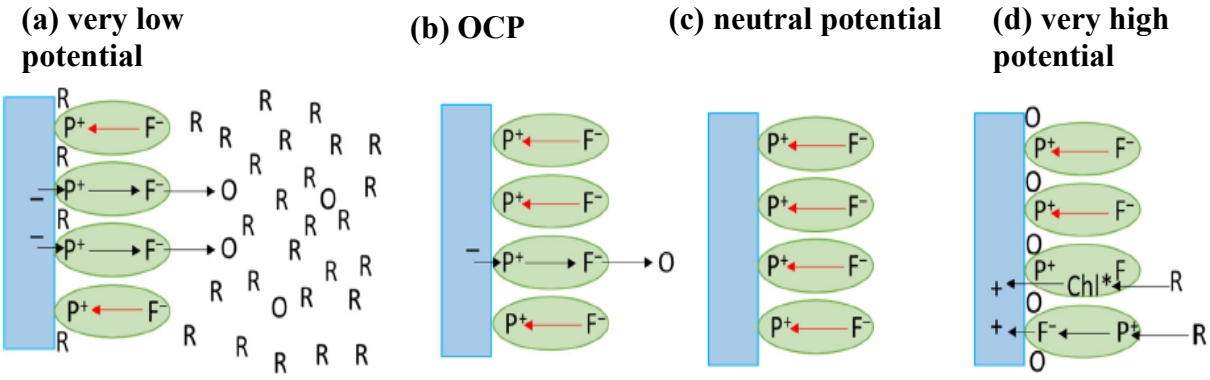

Figure 4.7 Diagrammatic representation of the ET processes in the PSI-based photoelectrode as a function of the external bias. **(a)** Relatively large cathodic photocurrent due to very low potential applied, **(b)** relatively small cathodic photocurrent at OCP, **(c)** no photocurrent at neutral potential and **(d)** relatively large anodic photocurrent due to a very high potential. Blue rectangles—conducting FTO layer. Green ovals—PSI particles. O and R—oxidized and reduced forms of redox compounds in the electrolyte. Excess of R over O forms in panel (a) illustrates the effect of reduced species domination in electrolyte solution close to FTO. Excess of O over R forms in panel (d) illustrates the opposite effect. Black arrows—forward ET, red arrows—back ET. Chl*—photoexcited antenna Chls. F—terminal PSI electron acceptor. (Reproduced from [113] under Creative Commons Attribution v4.0 International License[§]).

Different photocurrents observed at two measurements at low potential of -180 mV (Figure 4.6b, points 3 and 7) can be due to the fact that both the measurements were recorded right after the measurements at very different potentials applied to the PSI-FTO electrode. The measurement 7 was recorded just after a measurement 6 with high positive potential of +620 mV. Therefore, the mediators near the FTO were largely oxidized for some time and their positive potential neutralized partially the negative potential applied to the FTO. Oppositely, the measurement 3 was performed after the measurement 2 with much lower potential of +20 mV. Further, we noticed that decreasing the potential from -180 mV to -280 mV did not result in further expected increase of cathodic photocurrent. This could be due to the low presence of oxidized redox compound, O in the PSI film resulting in slowing down the electron transfer from PSI to the electrolyte and, in consequence, in increased efficiency of charge recombination.

Lastly, it should be noticed that the photocurrent generated at OCP was ~-720 nA/cm² corresponding to IQE = 0.073% and maximum cathodic photocurrent at ~180 mV was ~4600 nA/cm² corresponding to IQE = 0.47%. To dive deeper into the possible reasons of such low efficiencies, we performed time-resolved absorption measurements for PSI deposited on FTO.

4.2.2.2 Time-resolved absorption measurements

Time-resolved absorption measurements were performed using the millisecond setup described in the section 3.6.4.1 and the PEC shown in Figure 3.11.

Maximal values of absorbance change

The absorption spectrum of PSI complexes is dominated by the antenna Chls showing maximum of the Q_y band at ~679 nm (see Figure 4.1b). The contribution from ET cofactors to the absorption spectrum is much lower. This is due to the fact that the investigated PSI complexes from *C. merolae* grown under high-light intensity contained $m \approx 159$ antenna Chls per single PSI particle while each of PSI particles contains only 6 Chl *a* molecules engaged in ET, including 2 Chl *a* molecules forming the primary donor, P, characterized by the Q_y band red-shifted to ~700 nm. Having these numbers and the value of the sample's absorbance at 679 nm (A_{679}) it is possible to estimate the maximal negative value of absorbance change at 700 nm (photobleaching of primary donor, $\Delta A_{0,max}$), caused by saturating excitation, in a sample with all PSI particles active:

$$\Delta A_{0,max} = -\frac{A_{679}}{m}\frac{\Delta\varepsilon_{700}(P^+-P)}{\Delta\varepsilon_{679}(Chl^*-Chl)} \tag{4.2}$$

where the minus sign ensures that $\Delta A_{0,max}$ is negative, and $\frac{\Delta\varepsilon_{700}(P^+-P)}{\Delta\varepsilon_{679}(Chl^*-Chl)}$ is the ratio of differential molar extinction coefficients at 700 nm (related with oxidation of P) and 679 nm (related with excitation of a single Chl *a* antenna molecule), respectively. The value of this ratio is not precisely known but can be estimated as ~1-2 considering that P is a dimer of Chl *a* molecule. Consequently, for A_{679} = 0.27 OD (absorbance of PSI film on FTO plate under investigation), $\Delta A_{0,max}$ is estimated at (1.7-3.4) mOD.

The Eq. 4.2 holds true both for PSI in solution and deposited on FTO. The value of $\Delta A_{0,max}$ for CmH PSI in solution was measured directly ($\Delta A_{0,max} = -5.3$ mOD for the layer of excited solution of the thickness 0.6 cm and absorbance A_{679} = 0.6 OD; see Table 4.3 - part B). Consequently, the value of $\Delta A_{0,max}$ for CmH PSI deposited on FTO may be estimated from simple proportion:

$$\frac{\Delta A_{0,max}(PSI-FTO)}{A_{679}(PSI-FTO)} = \frac{\Delta A_{0,max}(PSI_{aq})}{A_{679}(PSI_{aq})} \tag{4.3}$$

where left side term refers to PSI deposited on FTO and right side – to PSI in solution. Substituting $\Delta A_{0,max}(PSI_{aq}) = -5.3$ mOD, $A_{679}(PSI_{aq}) = 0.6$ OD, and A_{679} (PSI-FTO) = 0.27 OD to Eq. 4.3 one gets $\Delta A_{0,max}$(PSI-FTO) $= -2.4\ mOD$. Next, substituting the latter value to Eq. 4.2, one may estimate the term $\frac{\Delta\varepsilon_{700}(P^+-P)}{\Delta\varepsilon_{679}(Chl^*-Chl)}$ at 1.4 in line with expected range of 1-2.

Initial amplitudes of the P^+ decay kinetics (ΔA_0)

The initial photobleaching amplitude of the P^+ decay kinetic is observed due to oxidation of P to P^+, similarly as in solution. The decay of the signal is, in principle, either due to internal charge recombination or electron transfer to P^+ from an external electron donor or combination of both. However, under our experimental conditions only the former reaction matters (as discussed above for the experiments with PSI particles in solution) and is taken into account. Two exemplary experimental curves ($\Delta A(t)$) are shown in Figure 4.8a, together with fits obtained using Eq. 3.2 and with the resulting parameters noted in Table 4.3. Figure 4.8b-c present all the fitting curves, collected in four groups, with P^+ decay kinetics documented under different experimental conditions such as varying voltages applied to the PSI-FTO electrode, different excitation frequencies (0.5 and 0.05 Hz), and varying concentration of mediators (ascorbate and DCPIP) in the electrolyte. A general observation was that P^+ decay kinetics under different experimental conditions were very different from each other – they were characterized by different sets of amplitudes, lifetimes, and offset (*const*) values.

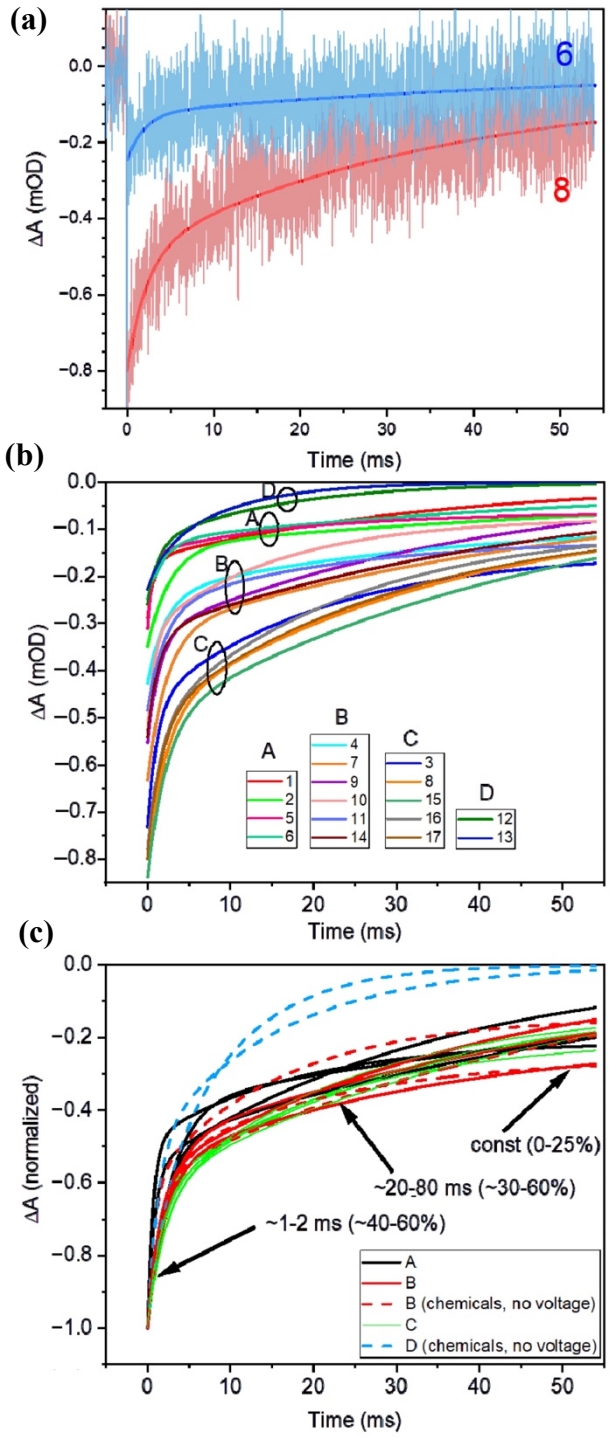

Figure 4.8 The kinetics of the P^+ photobleaching decay at 700 nm in the PSI complexes deposited on FTO glass. **(a)** Examples of experimental kinetics together with fitted bi-exponential curves (fit curves 6 and 8 from Table 4.3), **(b)** the fit curves 1–17 from Table 4.3, lumped into four distinct groups (A–D) and **(c)** normalized fit curves 1–17 (groups A-D from panel b are indicated). Reproduced from [113] under Creative Commons Attribution v4.0 International License[§].

Table 4.3 Experimental conditions and parameters of transient absorption kinetics of CmH PSI complexes recorded at 700 nm. **(A)** PSI complexes deposited on FTO; **(B)** PSI suspended in aqueous solution[(1)] (Reproduced from [113] under Creative Commons Attribution v4.0 International License[§]).

Experiment Number	Experimental Conditions				Parameters of Kinetic Traces					
	Potential (V)	[Asc] (mM)	[DCPIP] (μM)	f (Hz)	$-\Delta A_0$ (mOD)	$\Delta A_{0,rel}$ (%)	τ_1 (ms) A_1	τ_2 (ms) A_2	*const*	τ_{av} (ms)
(A) PSI-FTO, $A_{679} = 0.27$										
(A1) Experiments with variable potential of WE and without redox compounds in electrolyte										
1	0.22 [(2)]	-	-	0.05	0.28	12	0.8 0.44	34 0.56	0.00	19.4
2	0.02	-	-	0.05	0.35	15	2.7 0.61	81 0.39	0.00	33.2
3	-0.18	-	-	0.05	0.73	31	1.1 0.36	21 0.44	0.20	-
4	0.22	-	-	0.05	0.43	18	2.1 0.44	34 0.36	0.20	-
5	0.42	-	-	0.05	0.30	13	0.7 0.53	18 0.29	0.18	-
6	0.62	-	-	0.05	0.25	10	2.0 0.49	59 0.50	0.01	30.5
7	-0.18	-	-	0.05	0.63	26	2.3 0.50	55 0.50	0.00	28.7
8	-0.28	-	-	0.05	0.80	33	2.2 0.39	35 0.56	0.05	-
9	0.02	-	-	0.05	0.55	23	1.5 0.42	40 0.58	0.00	23.8
(A2) Experiments with no potential applied to WE and with redox compounds in electrolyte										
10	-	10	-	0.05	0.52	22	0.8 0.41	16 0.46	0.13	-
11	-	10	4	0.05	0.48	20	2.1 0.44	21 0.31	0.25	-
12	-	10	40	0.5	0.26	11	1.3 0.50	15 0.50	0.00	8.2
13	-	10	200	0.5	0.23	10	2.0 0.29	9.4 0.71	0.00	7.3
14	-	10	200	0.05	0.54	23	1.4 0.41	49 0.59	0.00	29.5
(A3) Experiments with negative potentials applied to WE and with redox compounds in electrolyte										
15	-0.18	10	200	0.05	0.84	35	2.2 0.39	47 0.61	0.00	29.5
16	-0.18	10	200	0.5	0.77	32	1.6 0.34	24 0.55	0.11	-
17	-0.28	10	200	0.5	0.80	33	1.6 0.36	29 0.54	0.10	-
(B) PSI in solution, $A_{679} = 0.6$ [(3)]										
	-	10	40	0.5	5.3	100	6.3 0.12	41 0.86	0.02	37

Amplitudes A_1, A_2 and *const* were normalized: $A_1 + A_2 + const = 1$. $\Delta A_{0,rel}$ is the relative initial transient absorption signal just after the excitation. The average decay time was estimated from the equation $\tau_{av} = \tau_1 A_1 + \tau_2 A_2$, only for kinetics with $const \approx 0$.[(1)] Results taken from [121]. [(2)] No potential was applied, but the measured potential of the solution was 0.22 V. [(3)] $A_{679,0.6cm} = 0.6$ is the absorbance of the PSI solution of 6 mm thickness (defined by the diameter of the excitation beam).

The absolute values of the initial amplitudes, ranging from 0.23 to 0.84 mOD (Table 4.3), were much smaller in comparison to the expected maximal signal of ~2.4 mOD (see above), despite saturating excitation pulses used. It can be concluded that a significant fraction of PSI particles immobilized on FTO remained inactive. To quantify the size of the active fraction, we introduced a new parameter – the relative initial signal, $\Delta A_{0,rel}$:

$$\Delta A_{0,\mathrm{rel}} = \frac{\Delta A_0}{\Delta A_{0,\max}} \times 100\%, \qquad (4.4)$$

where $\Delta A_{0,max}$ was defined above (Eq. 4.2). The Eq. 4.4 may be used both for PSI immobilized on FTO and dissolved in solution.

Dependence of the initial amplitude on the potential applied to the PSI-FTO electrode in the absence of mediators

The dependence of the initial amplitude on the potential applied to PSI-FTO in the absence of mediators is shown in Figure 4.9. A general observation is that the recorded initial P^+ photobleaching signal, presented for convenience as $-\Delta A_0$, is larger at more negative potentials than for more positive potentials, similarly to the observation for the cathodic photocurrent (Figure 4.6b). The values of $-\Delta A_0$ obtained at different applied potentials are listed in sections (A1) and (A3) of Table 4.3. It is to be noted that the sequence of potentials applied to the PSI-FTO WE were kept same as in the photocurrent measurements (Figure 4.6b). It is expected that a high positive potential (higher than mid-point potential of P, +450 mV) should permanently oxidize the primary donor P. However, we observed that still 10% of the PSI complexes were active at +620 mV (point 6) probably due to insufficient electric contact between this fraction of PSI particles and FTO. Further, at a low potential of -280 mV, the initial photobleaching signal increased and ~33% of the PSI complexes were active (point 8). Thus, despite such negative potential, the charge separation was observed only in one third of PSI complexes. Apparently, neither extremely positive nor extremely negative potentials are 100% effective (compare Figure 4.10). Instead, the electric potential may tune the fraction of active PSI particles only between 10 and 33%.

It can be seen from Figure 4.9 that the values of initial amplitude ($-\Delta A_0$) depend not only on the potential applied during the measurement but also on the values of the preceding potentials. The initial signals observed for points 4, 9, and 3 are larger than the signals for points 1, 2, and 7 despite being recorded at the same respective potentials. This effect may be explained by the inertia of the system: photobleaching signals are larger for points 4, 9, and 3 because these measurements were preceded by measurements at lower potentials in comparison to the respective measurements 1, 2, and 7. For instance, point 2 was preceded by point 1 recorded at +220 mV while point 9 is preceded by point 8 recorded at -280 mV. This behavior may be logically explained assuming that prolonged application of the negative potential (-280 mV) during measurement 8, leads to accumulation of electrons/negatively charged species inside the PSI multilayer and the measurement 9 is still affected by this accumulation. Thus, the actual potential near PSI particles during measurement 9 is lower than that during the measurement 2. Comparison of the $\Delta A_0(V)$ data shown in the Figure 4.9 with photocurrent vs. voltage data shown in Figure 4.6b reveals that the values for points 2 and 9 (similarly 1 and 4) are different in the former experiment but identical in the latter one.

This confusing difference maybe related with the fact that in the latter experiment there are mediators in the solution and in the former one – not.

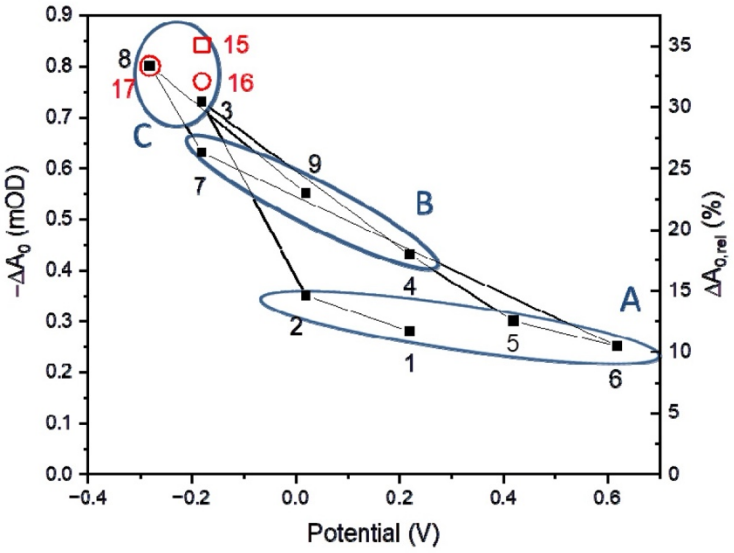

Figure 4.9 Initial photobleaching amplitudes as a function of voltage applied to PSI-FTO electrode. Data points obtained in the absence of redox compounds in the electrolyte are represented by filled squares (first nine numbered data points from Table 4.3). Data collected in the presence of 10 mM ascorbate and 200 μM DCPIP are represented by red symbols (data points 15–17 from Table 4.3). Squares refer to excitation frequency 0.05 Hz, and circles—0.5 Hz. Labels A, B, and C refer to the three distinct groups of kinetics shown in Figure 4.8b. Left axis—absolute amplitudes, right axis—relative amplitudes (Reproduced from [113] under Creative Commons Attribution v4.0 International License[§]).

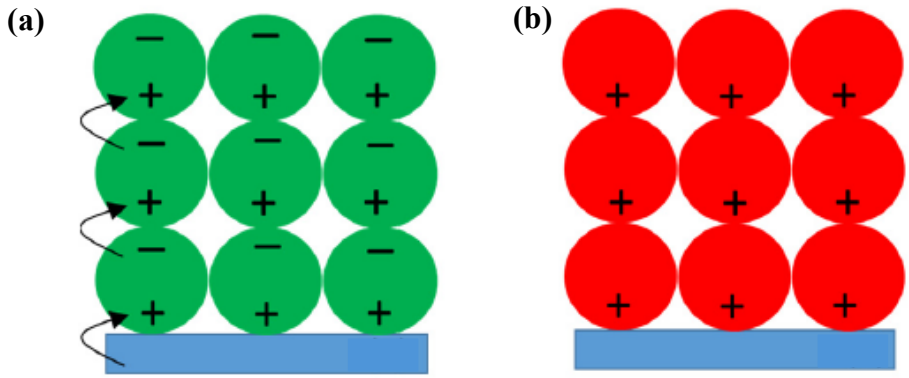

Figure 4.10 Extreme theoretical electric potential effects on the photoactivity of PSI particles in the absence of the mediators in solution. **(a)** Low potential; all PSI complexes are active – charge separation occurs in all PSI particles after saturating excitation, followed by charge recombination and/or ET between proteins (black arrows) and **(b)** High potential – all PSI complexes contain oxidized P quasi-permanently and are unable to support laser-induced charge separation. Green circles—active PSI particles, red circles—inactive PSI particles, blue rectangles—FTO glass slide. Note that, for simplicity, only homogeneous orientation of the PSI particles is depicted (Reproduced from [113] under Creative Commons Attribution v4.0 International License[§]).

P^+ decay kinetics at different potentials applied to the PSI-FTO electrode in the absence of mediators

Kinetic curves obtained from measurements 1-9 showed bi-exponential decay pattern with not so different shapes from each other (Figure 4.8). In some traces, non-decaying component (*const*) was resolved and in some cases, not. The parameters resulting from the fitting are collected in Table 4.3 and their graphical representation is shown in Figure 4.11. The lifetime, τ_1 of the faster decay phase ranged from ~0.5 ms to ~ 2.5 ms with mean value of 1.7 ms. Further, it did not show any orderly dependence on the applied potential as shown in Figure 4.11a. The slower decay component, τ_2 ranged from ~20 ms to ~80 ms with a mean value of 54 ms when *const* = 0 and 27 ms with non-zero *const* with overall mean value of 42 ms. Similar to lifetime τ_1, it also did not show any orderly dependence on potential applied (Figure 4.11b). The wide distribution of lifetimes was ascribed to limited signal-to-noise ratio, with mean value 1.7 ms corresponding to $P^+F_X^- \rightarrow PF_X$ charge recombination [20, 59] and 27-54 ms corresponding to $P^+(F_{A/B})^- \rightarrow PF_{A/B}$ charge recombination [20, 59]. The value of *const* of up to 0.25 (Table 4.3) is assigned to a long-lived P^+ state possibly due to either slow $P^+F_{A/B}^- \rightarrow PF_{A/B}$ charge recombination or electron expulsion from $F_{A/B}$ outside the PSI.

The thorough investigation of the amplitudes associated with fast and slow decay phases showed their orderly dependence on the applied potential as well as its relationship with the dependence of the initial amplitude on the applied potential (Figure 4.11c-e). The initial amplitude, $-\Delta A_0$, increases with the decrease in the electric potential (Figure 4.11c). This trend is accompanied by opposite trend of the fast decay phase amplitude – reduction from ~55 to ~35% (Figure 4.11d) and again increasing trend in the amplitude of the slow decay phase combined with *const* parameter – increase from ~45 to ~65% (Figure 4.11e). Qualitatively similar outcomes were observed in the case of PSI dissolved in aqueous solution where the redox mediators were used instead of low electric potential to increase the PSI's reducing strength (refer to section 4.2.1.2.1, particularly to Figure 4.5). Both for PSI in solution and on FTO, at lower reducing strength relatively more $P^+F_X^- \rightarrow PF_X$ charge recombination was observed (on FTO: τ_1=1.7 ms, A_1=55%) than at higher reducing strength (on FTO: A_1=35%); oppositely, at lower reducing strength, relatively less $PF_{A/B} \rightarrow P^+F_{A/B}^-$ charge recombination (on FTO: τ_2=42 ms, A_2+*const*=45%) was observed than at higher reducing strength (on FTO: A_2+*const*=65%). Also, both for PSI in solution and on FTO, the increase in the initial amplitude with increasing reducing strength is caused by reactivation of PSI particles showing $PF_{A/B} \rightarrow P^+F_{A/B}^-$ recombination rather than by reactivation of PSI particles showing $P^+F_X^- \rightarrow PF_X$ recombination. All these observations may be explained by the fact that the former recombination is slower than the latter one and thus less competitive with P^+ reduction by the reducing agent (mediators or low electric potential). Shortly speaking, the increment of reducing strength (1) reactivates more and more PSI particles and (2) reactivates mostly PSI particles showing slower charge recombination.

Figure 4.12 shows results discussed in the preceding paragraph in a quantitative way. It compares results obtained at two extreme potentials: -280 mV and +620 mV. From the values of $\Delta A_{0,rel}$ shown in Table 4.3 (33% and 10%, respectively) and the values of A_1 and A_2+*const* discussed just above and shown Figure 4.11d-e, one may estimate absolute contributions of the quickly and slowly recombining PSI particles which are, respectively, 12% and 22% at low potential and 5.5% and 4.5% at high potential. These numbers show ~2 fold increase of the "quick" PSI population (from ~5.5% to ~12%) and ~5 fold increase of the "slow" PSI population (from ~4.5% to ~22%) when going from high to low potential.

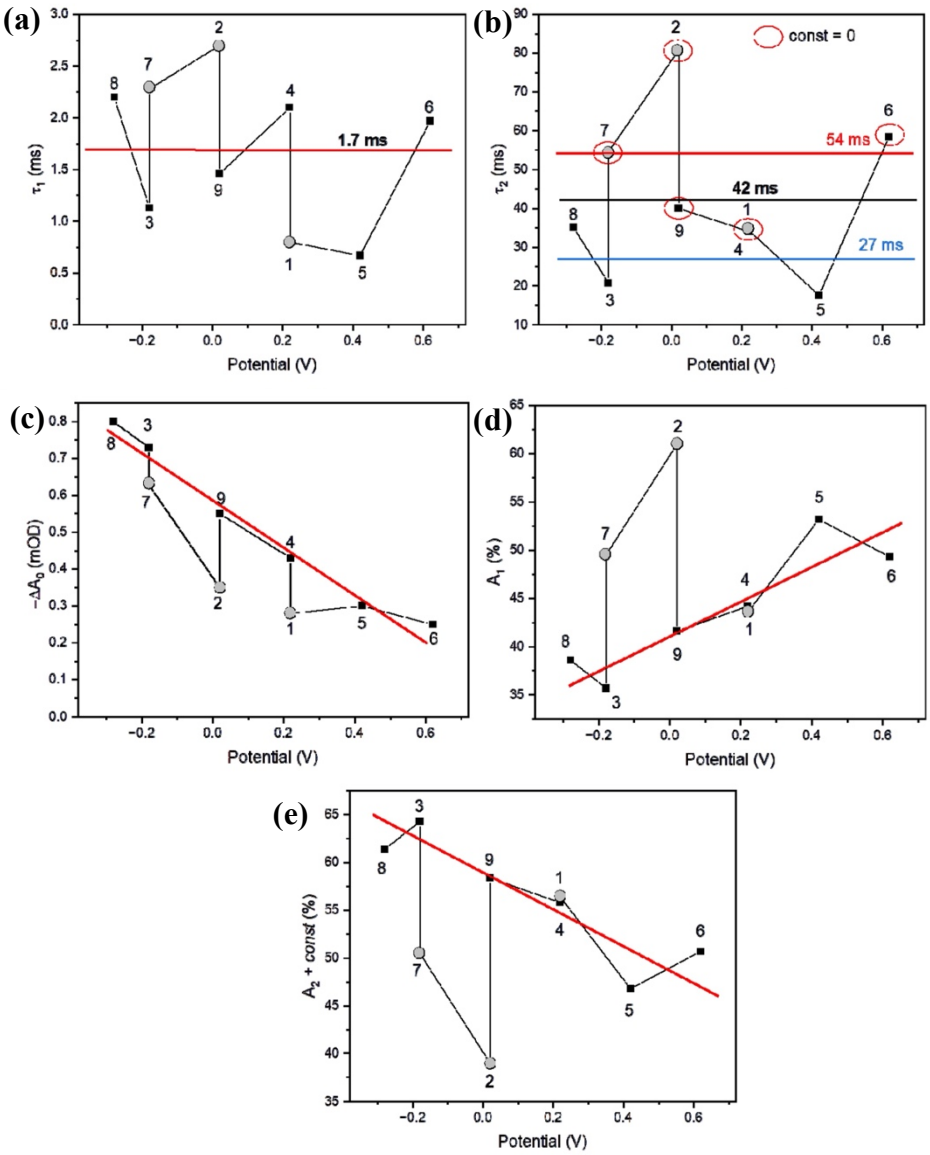

Figure 4.11 Dependence of bi-exponential fit parameters on the potential applied to the PSI-FTO electrode (with no mediators added; experiments no. 1–9 in Table 4.3). **(a)** Lifetime τ_1 with the average value indicated, **(b)** lifetime τ_2 with the average values indicated separately for the kinetics fitted with *const* = 0 (54 ms; points in the red ellipses), *const* ≠ 0 (27 ms; remaining points), and for all kinetics (42 ms), **(c)** initial amplitude, $-\Delta A_0$, **(d)** amplitude A_1 of the fast phase (~1.7 ms) and **(e)** the sum of the amplitude A_2 of the slow phase (~42-ms) and *const* parameter. The points shown as gray circles (1, 2, 7) are those for which the initial amplitude ($-\Delta A_0$; panel **(c)**) deviates from the general trend due to specific sequence of the applied potentials. The red lines in panels c-e indicate trends in the values of the amplitudes with neglected points 1, 2, and 7 (Reproduced from [113] under Creative Commons Attribution v4.0 International License[§]).

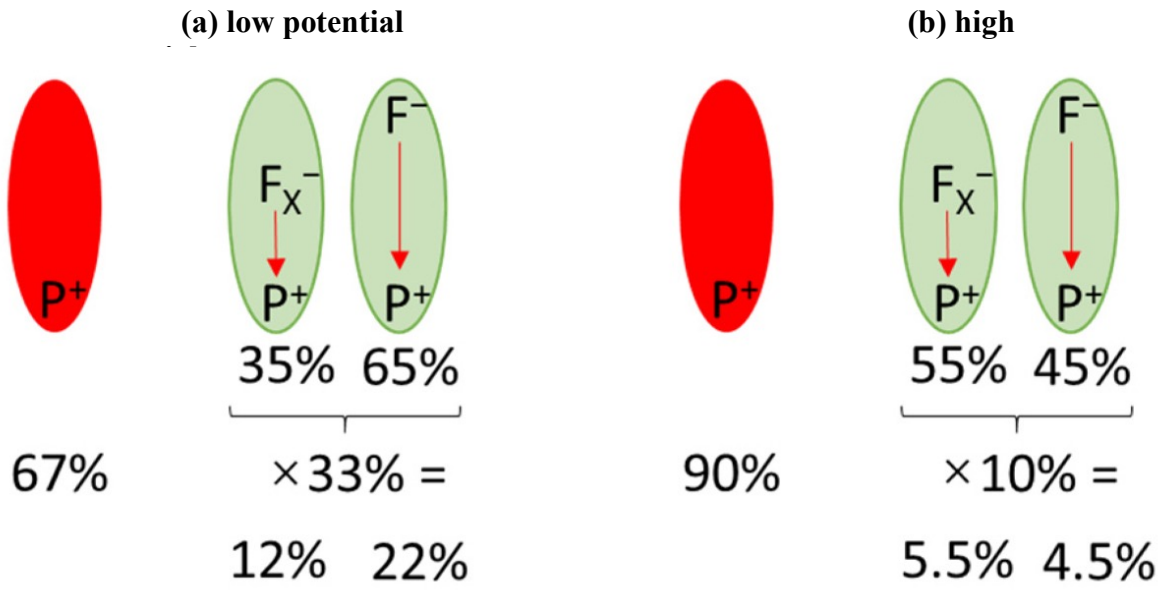

Figure 4.12 Fractions of active (green) and inactive (red) PSI complexes under **(a)** low (-280 mV) and **(b)** high (+620 mV) potential. Within active PSI complexes, fractions recombining from the states $P^+F_X^-$ and $P^+F_{A/B}^-$ are shown. $F_{A/B}$ is abbreviated to F (Reproduced from [113] under Creative Commons Attribution v4.0 International License[§]).

P^+ decay kinetics in the presence of mediators and absence of electric potential

P^+ decay kinetics in the presence of mediators (ascorbate and DCPIP) show that the P^+ gets re-reduced less efficiently in comparison to the low potential applied to the PSI-FTO electrode. This is represented by the initial amplitude of up to ~20-23% in the former case in comparison to ~33% at low potential (compare experiments 10-14 and 8 Table 4.3). Surprisingly, unlike in solution (Figure 4.5), addition of neither 4 µM nor 200 µM DCPIP to the PEC containing 10 mM ascorbate does not increase the initial amplitude $\Delta A_{0,rel}$ (compare experiments 10, 11, 14 in Table 4.3). Expectedly, there is ~2-fold decrease (down to 10-11%) observed in the initial amplitude with decreasing the excitation frequency from 0.5 Hz to 0.05 Hz (dataset 12-13 in Table 4.3; group D in Figure 4.8b). This shows that the time taken by ascorbate molecules to re-reduce P^+ is prominently more than 2 s as also shown in previous studies [121, 128]. With an excitation frequency of 0.05 Hz, the shape of the kinetic curves was similar to curves measured without mediators (see above) with similar fast (~1-2 ms; ~40%) and slow (~20-50 ms; 60% including the offset) decay components attributed to $P^+F_X^- \rightarrow P^+F_X$ and $P^+F_{A/B}^- \rightarrow PF_{A/B}$ recombination, respectively. However, with an excitation frequency of 0.5 Hz, a much faster decay component was observed attributed predominantly (similarly as discussed in the preceding chapter at low reducing strength) to the PSI complexes that were showing $P^+F_X^- \rightarrow PF_X$ charge recombination.

P^+ decay kinetics at negative potentials applied to the PSI-FTO electrode in the presence of mediators

The results from experiments done with application of potential in combination with mediators (10 mM ascorbate and 200 µM DCPIP) are recorded in section (A3) of Table 4.3. It was observed that with the presence of mediators along with negative low potential of -180 mV, the initial amplitude increased by only 4%, from 31% to 35% in comparison to low potential alone (compare datasets 3 and 15 in Table 4.3 and Figure 4.9). It seems like the effects of potential and mediators on re-reduction of P^+ are not additive as could be expected assuming that the electric field can penetrate PSI film only shallowly from one side and mediators can penetrate it shallowly from the other side. This hypothetical situation is illustrated in Figure 4.13a where it is assumed that all PSI complexes in the layer are potentially active. However, the middle region is assumed to be inactive since neither low potential nor mediators cannot access this region and reduce P^+ there. Now, to mimic the experimental values obtained for fractions of PSI that are active in case of low potential of -180 mV alone (~30%), mediators alone (~20%), and combination of both (~35%), another model was built as shown in Figure 4.13b. In this model it was assumed that (1) the penetration depth is much larger (than in the previous model) but still limited, particularly for mediators, and (2) that large fraction of PSI complexes (65%) are permanently inactive and these complexes are homogeneously distributed in the layer; the remaining fraction of the potentially active PSI complexes (35%) may show laser induced charge separation or not depending on the reducing strength of the experimental conditions. The mathematical expressions for this model may be found in the Appendix. Based on this model it was estimated that, that the penetration depth of low potential, was 90% and that of mediators – 65% of the multilayer thickness. In the work by Ciesielski et. al, it was shown that the redox mediators (100 mM ascorbate and 5 mM DCPIP) can fully penetrate the multilayers of PSI although their PSI film was thicker (1-2 µm) than our (0.6 µm) [81]. The possible reason for the difference observed could be different PSI deposition technique and/or higher concentrations of redox mediators in [82].

With an increase in the excitation frequency from 0.05 Hz to 0.5 Hz the initial amplitude decreased only slightly (compare points 15 and 16 in Figure 4.9). Together with the result 13 in Table 4.3 (presence of mediators, no potential, 0.5 Hz frequency) it indicates that the effect of low potential in re-reducing the P^+ is faster than the effect of mediators.

It is worthy to note that for the PSI from C. *merolae* dissolved in solution, we observed 100% of the initial photobleaching signal in the presence of 10 mM ascorbate and 40 µM DCPIP, even for excitation frequency of 0.5 Hz (section B of Table 4.3 and Table 4.1) whereas for PSI immobilized on FTO, only ~20-35% of PSI were in active state in the presence of same mediators. The question that arises is why a major portion of PSI complexes (65%) immobilized on FTO remain permanently inactive, independently of mediators' concentrations and the value of electric potential. One may speculate that (1) either these PSI particles are permanently disturbed by the electrodeposition procedure or (2) the crowded environment blocks electron donation to P^+.

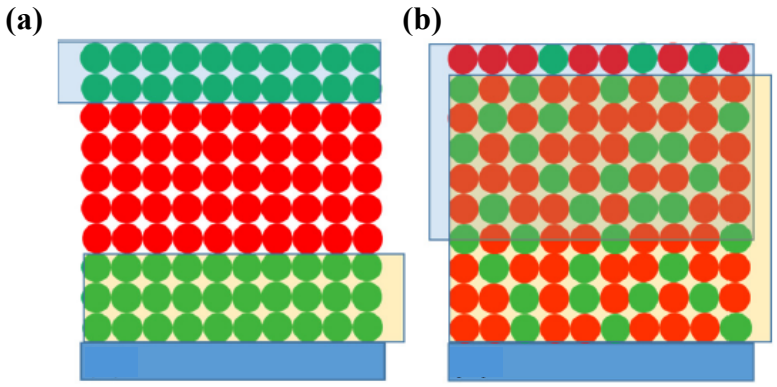

Figure 4.13 (a, b) Two models of the active (green) vs. inactive (red) PSI particles distribution across their multilayer on the FTO substrate. Semi-transparent yellow and blue rectangles are the areas of the effective P^+ re-reduction by the low voltage (-180 mV) and by redox compounds (10 mM ascorbate and 200 µM DCPIP), respectively (Reproduced from [113] under Creative Commons Attribution v4.0 International License[§]).

4.3 Comparison of time-resolved absorption and photocurrent results observed for CmH PSI in solution and immobilized on FTO

Table 4.4 compares the selected results obtained from the studies on the decay kinetics of the oxidized primary donor P^+ using millisecond time-resolved absorption (for CmH PSI both in solution and immobilized on FTO) and the photocurrent measurements described in section 4.2**.**

The first observation from the time-resolved absorption studies was that the fraction of proteins in solution capable of performing charge separation in the presence of mediators was 100% (Table 4.1) and that this fraction decreases to 10–35% when PSI particles were deposited on FTO, the exact value depending on the redox mediator presence/concentrations and electric potential applied to the PSI-FTO electrode (Table 4.3). The second observation was that in the solution, charge recombination was observed in 98% of PSI proteins, while for PSI on FTO it was difficult to determine this quantity precisely. Consequently, only 2% of PSI proteins in solution were able to expel the electron outside PSI due to strong competition from charge recombination. If one assumes the same value of 2% for PSI immobilized on FTO and takes into account that at negative potential of -180 mV only about 20% (≈ 0.64·31% ≈ 0.61·35%; compare values of parameters for experiments 3 and 15 in Tab. 4.3) of immobilized PSI show full charge separation, it is straightforward to get the value of 0.4% for the fraction of PSI particles expelling electrons to the electrolyte (2% out of 20%). At OCP the corresponding value is even lower – 0.14% (calculated as 2% out of 7% (≈ 0.56·12%; compare values of parameters for experiments 1 in Table 4.3). These fractions, 0.14% for OCP and 0.4% for -180 mV estimated from the results of transient absorption experiments for the PSI-FTO electrodes, correspond well with internal quantum efficiencies (IQE, see Eq. 4.1), estimated from the photocurrent measurements for the same electrodes (see section 4.2.2.1) equal to 0.073% and 0.47% at respective potentials. All these numbers are collected in Table 4.4.

From the above results, one may conclude that the charge recombination inside PSI, over competing the ET outside the PSI is the major factor responsible for limited photovoltaic activity of our system. The second important factor is large fraction of inactive PSI complexes in PSI-FTO electrodes (up to 65%).

Table 4.4 Comparison of time-resolved absorption and photocurrent results observed for CmH PSI in solution and immobilized on FTO (Adapted from [113] under Creative Commons Attribution v4.0 International License[§]).

Type of Experiment	Parameter	In Solution[(3)]	Immobilized on FTO			
			No Redox Compound Added		+10 mM Ascorbate +200 μM DCPIP	
			@OCP (+220 mV)	@low Potential (- 180 mV)	@OCP (+115 mV)	@low Potential (- 180 mV)
Time-resolved absorption	Fraction of photoactive PSI[(1)]	100%	12%	31%	-	35%
	Fraction of fully photoactive PSI[(2)]	~90%	~7%	~20%	-	~20%
	Fraction of PSI showing ET outside PSI	2%	(0.14%)[(4)]	(0.4%)[(4)]	-	(0.4%)[(4)]
Photocurrent	IQE	-	-	-	0.073%	0.47%

[(1)] PSI complexes undergoing any of the charge separation steps; [(2)] PSI complexes undergoing full charge separation yielding the final state $P^+F^-_{A/B}$; [(3)] data from [121]; solution contained 10 mM ascorbate and 40 µM DCPIP; [(4)] the values in brackets were estimated assuming 2% efficiency of ET outside immobalized PSI, i.e., the efficiency measured for PSI complexes suspended in solution.

In order to increase the photocurrent generated in PSI-based PEC one could either increase IQE of the system or enhance the absorbance of the PSI itself. In the following, attempts are described realizing the latter strategy. The tested approach was enhancing the absorption of PSI by attaching it to silver nanoparticles which were claimed in the literature to act as plasmonic antenna for PSI complexes. We explored several methods to facilitate attachment between PSI and AgNPs, which will be described and discussed in the following sections.

4.4 Characterization of colloidal silver nanoparticles

The synthesized colloidal hydrophobic AgNPs (AgNPs suspended in n-hexane) and phase transferred hydrophilic AgNPs (suspended in distilled water, see section 3.4) were characterized using optical spectroscopy and microscopy techniques. The results of these studies are described below.

4.4.1 Steady-state absorption spectra and stability of silver nanoparticles

Figure 4.14 (a, b) shows the steady-state absorption spectra of hydrophobic AgNPs (coated with oleylamine) and hydrophilic AgNPs (coated with pluronic F127) dispersed at different concentrations in n-hexane and distilled water, respectively. In literature, it has been shown that the spectral position of SPR peak is sensitive to the size, shape and size distribution of the nanoparticles [132, 133] and ranges from 390 to 470 nm [134, 135]. The bigger the particle size, the more red-shifted the SPR peak [136, 137]. Further, a single SPR peak is representative for spherical morphology of nanoparticles according to Mie theory and in experiments [133 137-139]. The hydrophobic AgNPs showed SPR peak with maximum at ~411 nm (Figure 4.14a) representing uniform, monodispersed and spherical AgNPs [135]. However, a red-shift of this peak was observed for the phase transferred hydrophilic AgNPs. Depending on the detergent utilized, this shift ranged from ~3 nm in case of pluronic F127 to ~23 nm in case of β-DM (Figure 4.14c and Table 4.5). It is to be noted that the different types of detergents were used in this study to optimize the interaction between AgNPs and PSI (refer to section 4.5.1).

Table 4.5 Comparison of SPR peak positions of the AgNPs with different coatings.

AgNPs with different coating	Hydrophobicity/ Hydrophilicity	SPR Peak Position (nm)
AgNPs coated with **oleylamine**	Hydrophobic	411
AgNPs coated with **pluronic F127**	Hydrophilic	414
AgNPs coated with **pluronic P123**	Hydrophilic	423
AgNPs coated with **β-DM**	Hydrophilic	434

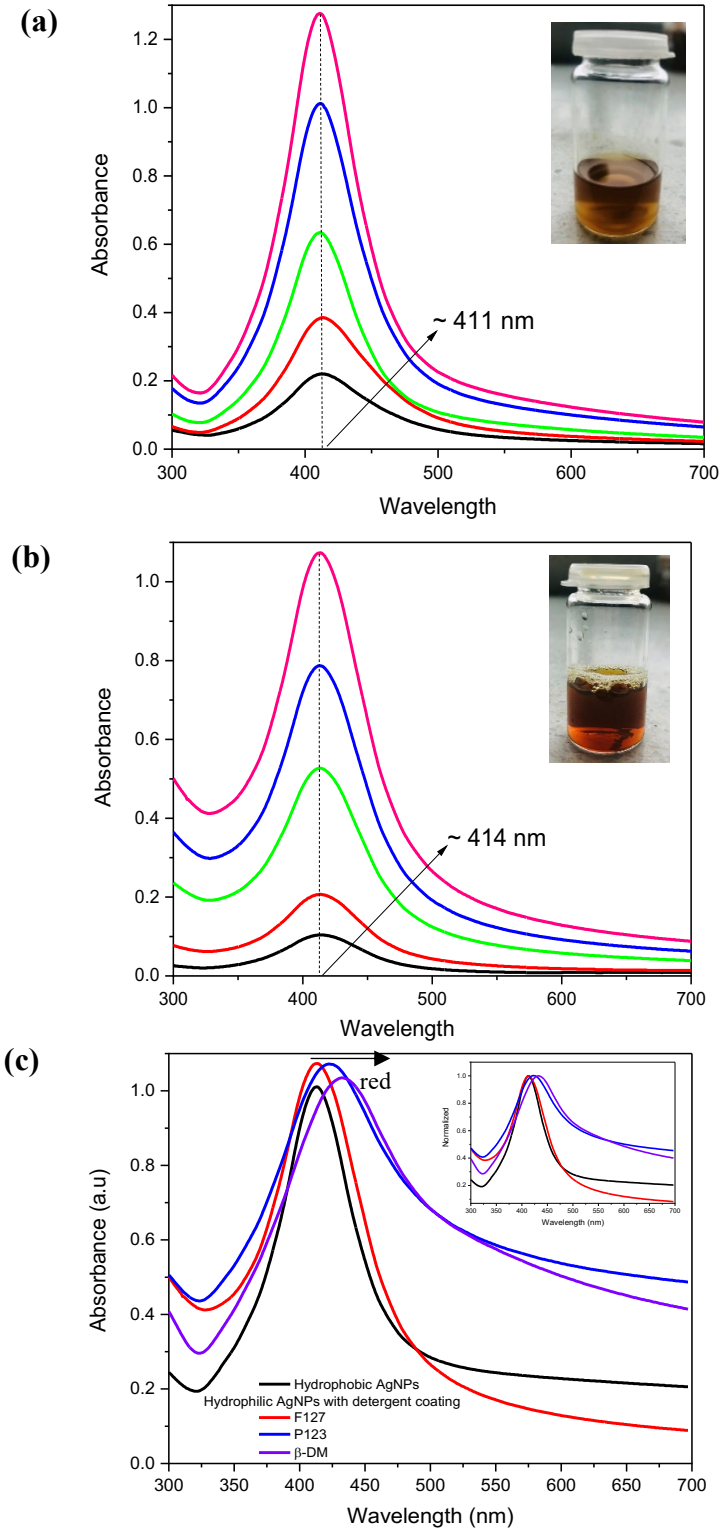

Figure 4.14 Steady-state absorption spectra of **(a)** hydrophobic AgNPs-oleylamine dispersed at different concentrations in n-hexane, **(b)** hydrophilic AgNPs-F127 dispersed at different concentrations in distilled water and **(c)** hydrophilic AgNPs with different detergent coating (F127, P123, and β-DM) compared with hydrophobic AgNPs. Insets in (a) and (b) show the photographic images of diluted AgNPs in n-hexane and distilled water, respectively. Inset in (c) shows the normalized spectra.

The synthesized hydrophobic AgNPs were stable over time. There was negligible change in the SPR peak position or decrease in the absorbance 5 months after their synthesis (Figure 4.15 a). However, the hydrophilic AgNPs, in general, were less stable in comparison to hydrophobic AgNPs. For example, for hydrophilic AgNPs-F127, this was evidenced by a shift in the SPR peak, by about 13 nm from 414 nm to 427 nm within a mere two days after synthesis of these NPs (Figure 4.15b). Further, after 24 hours without disturbing the solution, sedimentation occurred. However, it was easy to resuspend these particles by manual agitation. The AgNPs coated with pluronic P123 and β-DM demonstrated significantly poorer stability compared to AgNPs coated with pluronic F127. There was not only sedimentation when suspension was left undisturbed for 24 hours but resuspension of particles by manual agitating the solution proved more challenging in comparison to hydrophilic AgNPs-F127. The stability of hydrophilic AgNPs for different detergent coating is illustrated in Figure 4.16.

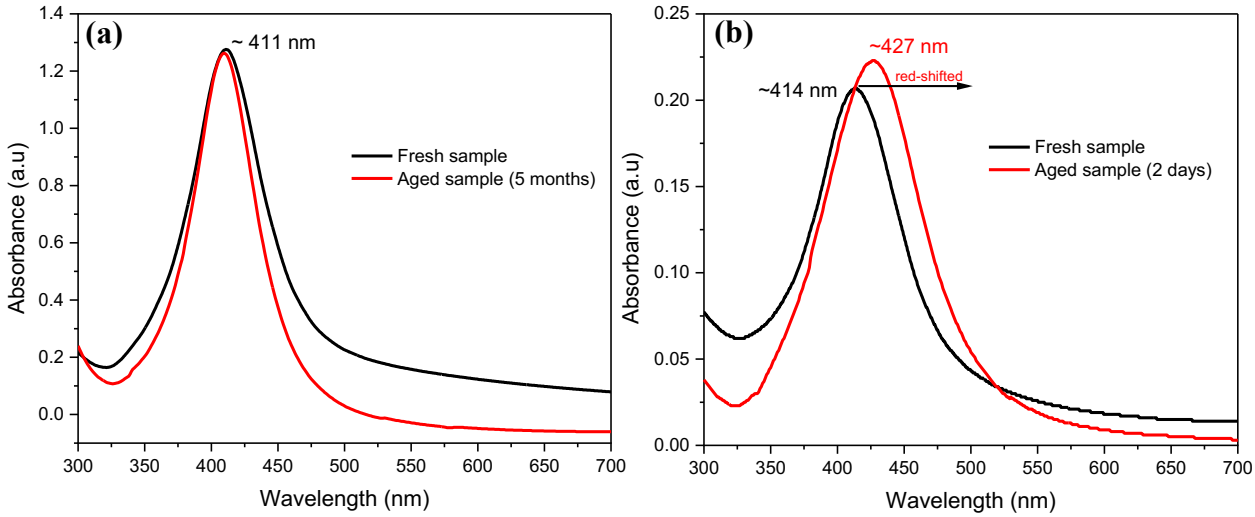

Figure 4.15 Steady-state absorption spectra comparing the stability of **(a)** hydrophobic AgNPs and **(b)** hydrophilic AgNPs-F127 over time labeled as fresh sample (measured right after synthesis) vs. aged sample (measured at different time after fabrication).

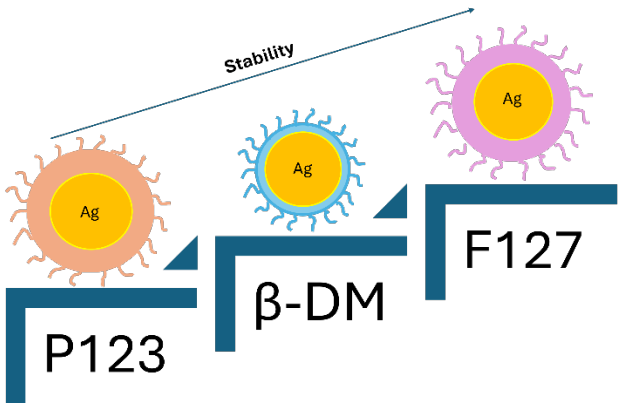

Figure 4.16 Illustration showing **(a)** varying stability of hydrophilic AgNPs coated with different detergents (F127, P123, and β-DM), ranked from least stable to most stable.

4.4.2 Fluorescence spectra

Figure 4.17a,b,c shows fluorescence emission spectra of hydrophobic AgNPs at three excitation wavelengths, λ_{exc} = 250, 325, 415 nm respectively. The bands in Figure 4.17a, 370 nm and 527 nm are assigned to fluorescence [140, 141]. The bands in Figure 4.17(b-c) are assigned to scattered light due to Raman scattering. This identification is supported by calculating the energy shifts between the excitation and Raman peak wavelengths for both the excitation wavelengths using the formula $\Delta\bar{\nu} = (\frac{1}{\lambda_{exc}} - \frac{1}{\lambda_{Raman\ peak}})$, which yields an energetic separation of 3000 cm^{-1} corresponding to CH stretching of hexane (Figure 4.17b,c). Thus, while excitation at 250 nm yields fluorescence bands at around 370 and 530 nm (Figure 4.17a), excitation of the SPR absorption (at 415 nm) band results only in strong scattering band (Figure 4.17c).

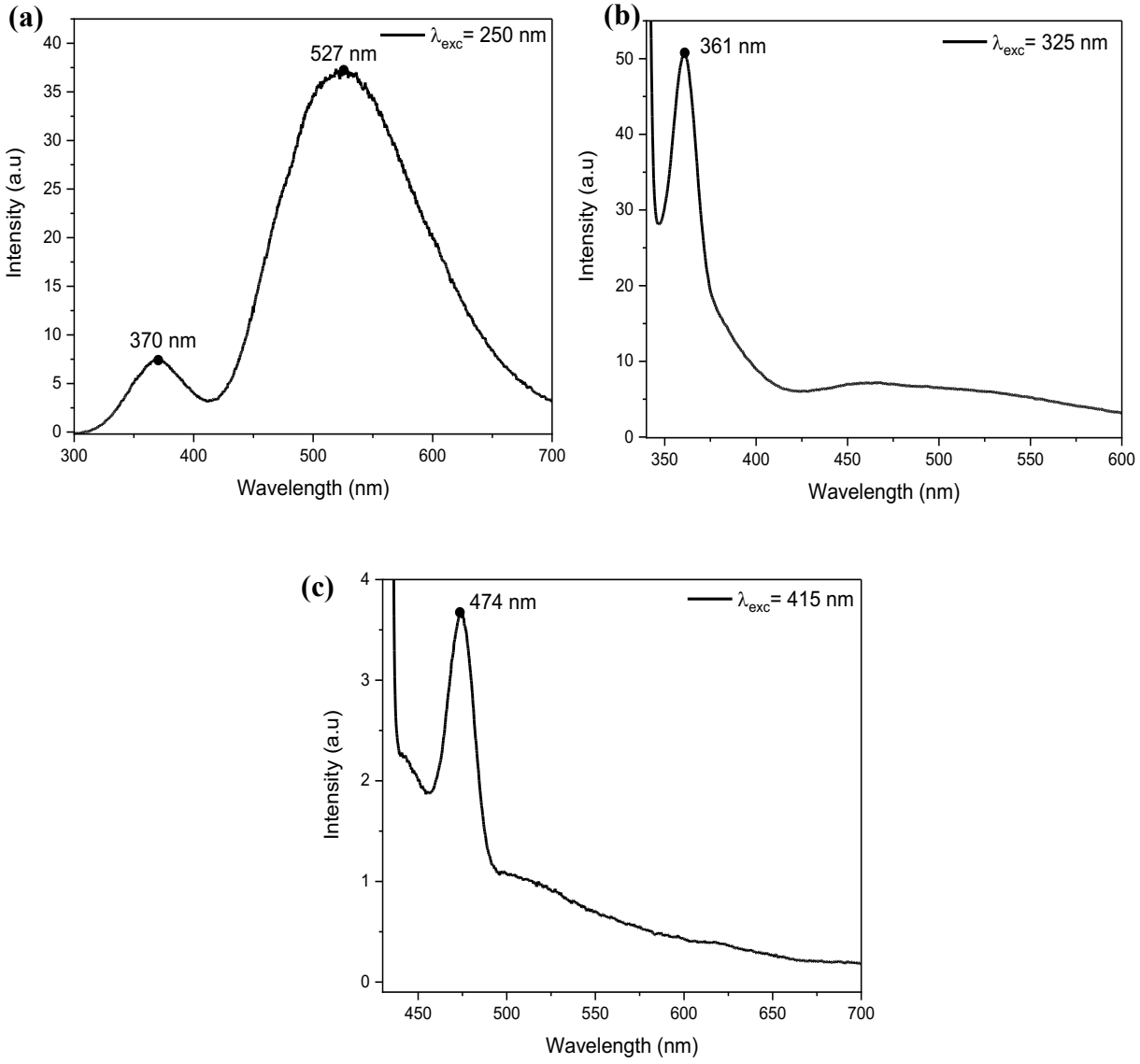

Figure 4.17 Fluorescence emission spectra of hydrophobic AgNPs at excitation wavelengths **(a)** 250 nm, **(b)** 325 nm and **(c)** 415 nm.

Figure 4.18 shows fluorescence emission spectrum of hydrophilic AgNPs-F127 at three excitation wavelengths, λ_{exc} = 250, 325, 415 nm [140, 141]. Fluorescence spectra recorded at 250 nm excitation are similar to those recorded for the hydrophobic AgNPs except for the 3 nm red-shift of the 370 nm band and more pronounced, 27 nm blue-shift of the 527 nm band (compare Figure 4.17a and 4.18a). The 364-nm band observed at 325 nm excitation (Figure 4.18b) can safely be interpreted as a Raman scattering peak due to OH stretching of the water molecules (3300 cm^{-1}). This oscillation is expected to give a Raman peak at 481 nm following excitation at 415 nm (Figure 4.18c). However, such band is very weak. Instead, more pronounced band at 458 nm was observed and its origin is difficult to explain.

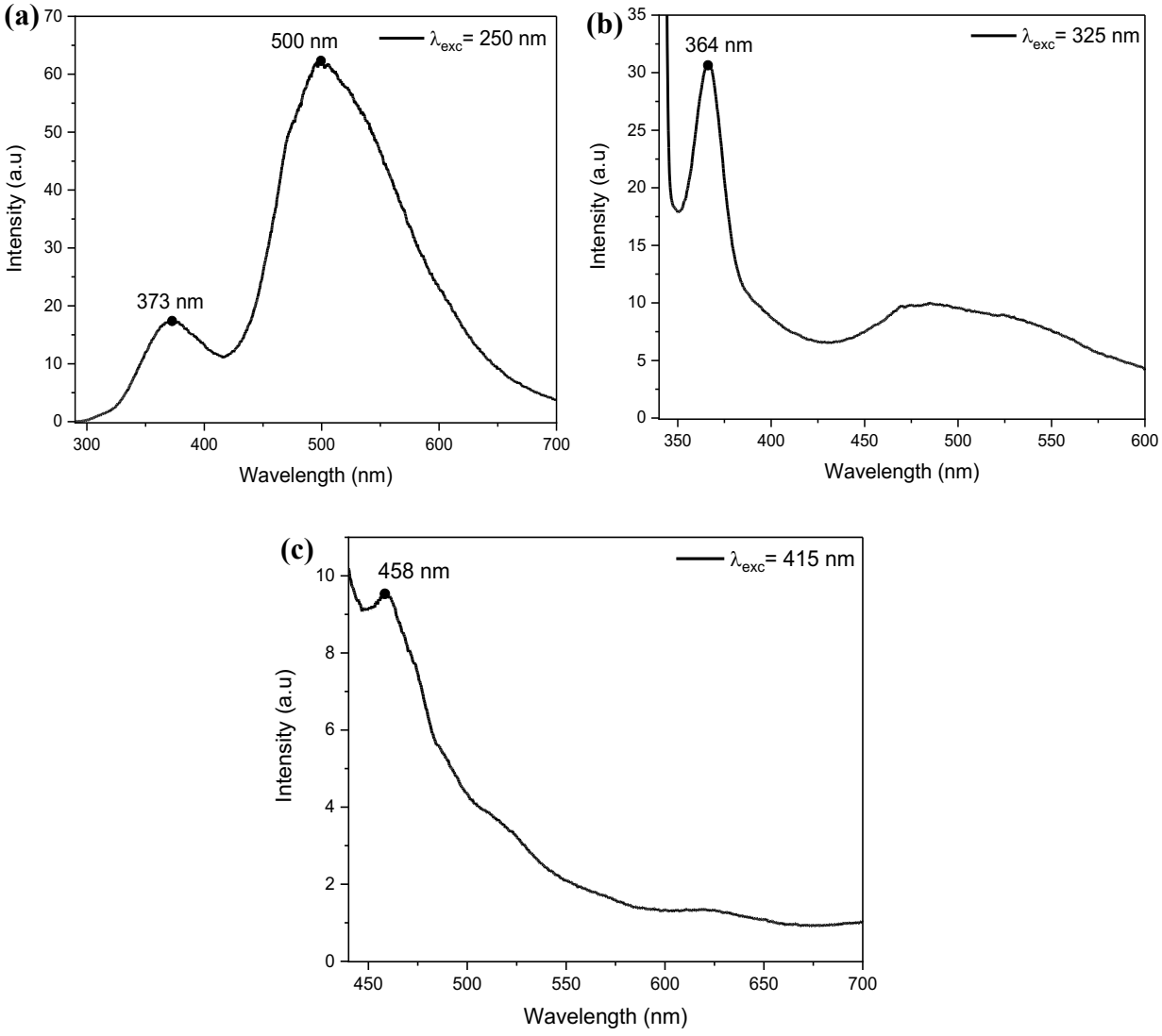

Figure 4.18 Fluorescence emission spectra of hydrophilic AgNPs at excitation wavelengths **(a)** 250 nm, **(b)** 325 nm and **(c)** 415 nm.

4.4.3 Dynamic light scattering - determination of size of silver nanoparticles

Figure 4.19 presents the results of dynamic light scattering (DLS) measurements of the hydrodynamic size distribution of both hydrophobic and hydrophilic AgNPs coated with different types of detergents. The mean hydrodynamic radius of hydrophobic AgNPs is ~6.5 nm. Considering an estimated ~2 nm thickness of oleylamine coating around the core AgNPs [142] the core AgNPs radius is 4.5 nm. This value closely agrees with TEM results showing a radius of 3.75 nm (see below). For the solutions of hydrophilic AgNPs coated with pluronic F127 and P123, DLS measurements revealed two fractions of particles of smaller and bigger size. The solution of AgNPs coated with pluronic F127 contains objects of ~3 nm and ~32 nm mean radii. The solution of AgNPs coated with pluronic P-123 contains objects of 2.7 nm and ~40 nm mean radii. The bigger objects maybe identified as AgNPs coated with very thick layer of pluronics F127 and P123 (see below). The smaller sized objects of about 3 nm radius could be pluronic molecules or their aggregates. The AgNPs coated with β-DM showed a single asymmetric peak with mean hydrodynamic radius of ~9 nm.

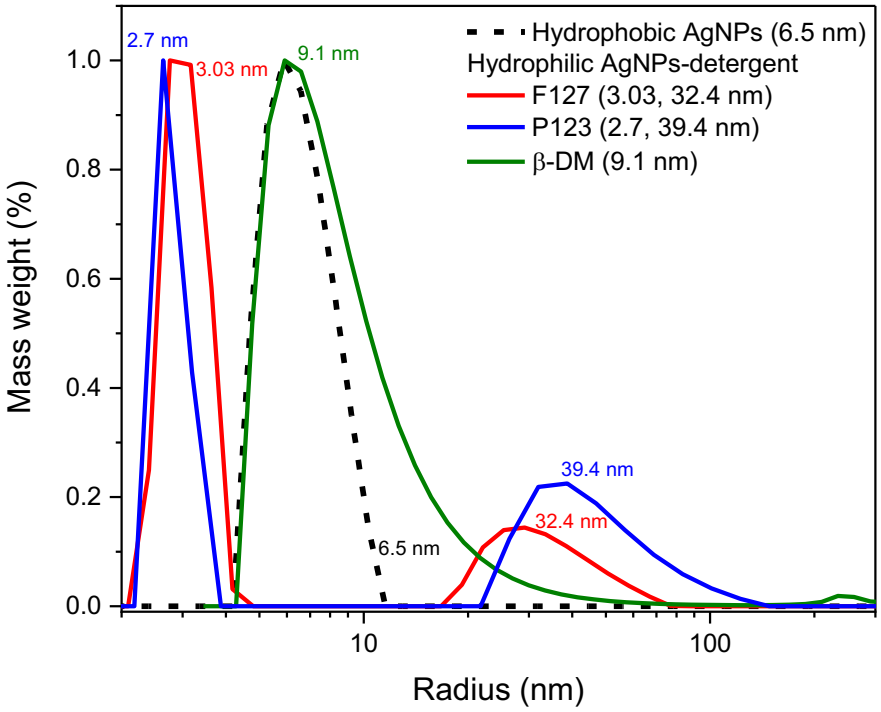

Figure 4.19 Hydrodynamic size distribution of hydrophobic AgNPs coated with oleylamine and hydrophilic AgNPs coated with different detergents (F127, P123, and β-DM) obtained by DLS.

Table 4.6 presents the comparison of the hydrodynamic radii of hydrophilic AgNPs measured by DLS and their theoretical values predicted from the lengths of the hydrophobic parts of the detergents (collected in Table 3.1). The detergents utilized to replace oleylamine in hydrophobic AgNPs, to form hydrophilic ones, contain both hydrophobic units (PPO in pluronics) and hydrophilic (PEO in pluronic) units. To understand the assembling of coatings of detergents (pluronic F127, P123, and β-DM) around the AgNPs, we can consider how these molecules arrange themselves around the AgNPs.

In this setup, the hydrophobic PPO units form the core coating around the nanoparticles while hydrophilic PEO unit assembles to form the outside distended region (Figure 4.20) [116]. By using such structural arrangement of the detergent coating around AgNPs, we can theoretically estimate the hydrodynamic radius of AgNPs with different detergent coatings. For that purpose, starting with the DLS measurement of hydrodynamic radius of 6.5 nm of AgNPs coated with oleylamine, we can subtract the estimated 2 nm oleylamine length [142]. This gives a core radius of 4.5 nm of the bare AgNPs. Now, to estimate the theoretical hydrodynamic radius of AgNPs coated with different detergents, we add the length of the hydrophobic units (see Table 3.1) to the AgNPs core radius (see an example of calculation in the footnote under Table 4.6). The results in Table 4.6 demonstrate that the hydrodynamic radii measured with DLS are consistent with the theoretical ones.

Table 4.6 Comparison between experimental and theoretical hydrodynamic radii of hydrophilic AgNPs coated with different detergents (theoretical calculation were done assuming the core AgNPs radius to be ~4.5 nm).

S.NO	Hydrophilic AgNPs - detergent coating	Hydrodynamic Radius (nm)	
		Experimental	**Theoretical**
1.	F127	32.4	30.5
2.	P123	39.4	32.1
3.	β-DM	9.1	7.3

Theoretical hydrodynamic radii were estimated by adding the hydrodynamic radius of core AgNPs determined from DLS (4.4 nm) and hydrophobic chain length of respective detergent molecule (refer to Table 3.1) Example: Theoretical hydrodynamic radius for AgNPs-F127 = 26 nm (F127 PPO length) + 4.5 nm (core radius of AgNPs) = 30.5 nm.

It is to be noted that the contribution of the PEO chains to the hydrodynamic radius was neglected in our estimations. This could be justified by the fact that the outer (hydrophilic) part of the detergent shell is much less dense than the inner (hydrophobic) shell of the detergent (Figure 4.20) and therefore is largely filled with water. The ranking of the sizes of hydrophilic AgNPs from the smallest to largest is shown in Figure 4.21. This is consistent with the chain lengths or molecular masses of individual detergents shown in Table 3.1 suggesting that the biggest should be hydrophilic AgNPs coated with pluronic P123.

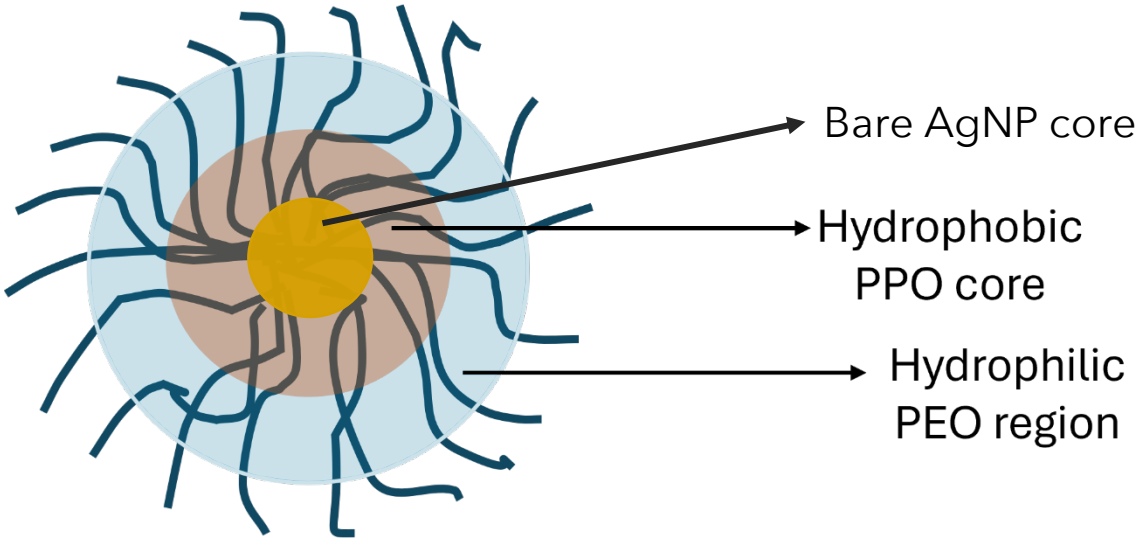

Figure 4.20 Illustration representing the assembling of hydrophobic PPO and hydrophilic PEO pluronic detergent units around AgNP core in aqueous solution (Adapted from [116] under Creative Commons Attribution v4.0 International License§). Note that hydrophilic region is largely composed of water molecules.

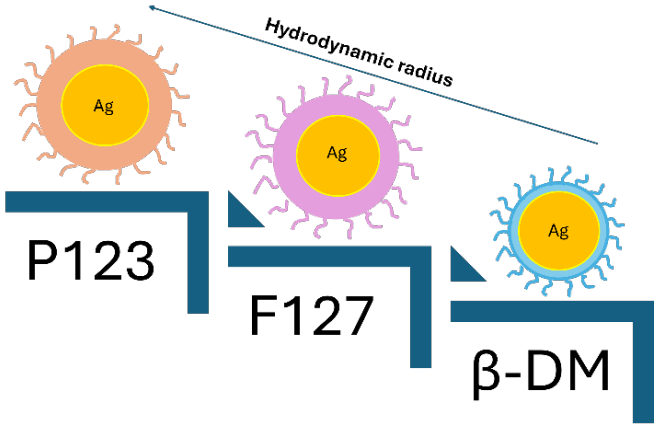

Figure 4.21 Illustration showing hydrophilic AgNPs coated with different detergents (F127, P123, and β-DM), ranked from smallest to largest.

4.4.4 Transmission electron microscopy - determination of size and aggregation of silver nanoparticles

The TEM image presented in Figure 4.22a shows that hydrophobic AgNPs are polydisperse and nearly spherical (see section 3.7.1 for technical details). Similarly, the hydrophilic AgNPs coated with pluronic F127 also display polydispersity and spherical characteristics. The hydrophilic AgNPs form larger spherical entities with presence of individual AgNPs (Figure 4.22b). The formation of these entities maybe an alternative explanation of large objects of about 30 nm radius observed in the DLS experiment (Table 4.6).

The size distribution histograms of AgNPs cores prepared in hydrophobic and hydrophilic forms are shown in Figure 4.22c,d. The histograms were fitted with lognormal size distribution function using ORIGIN software and from the fitting, the mean particles' sizes were determined.

The radius of bare AgNPs core is 3.75 nm and 3.25 nm in hydrophobic and hydrophilic coating respectively. These numbers are roughly similar to the value 4.5 nm estimated from the DLS measurements described above.

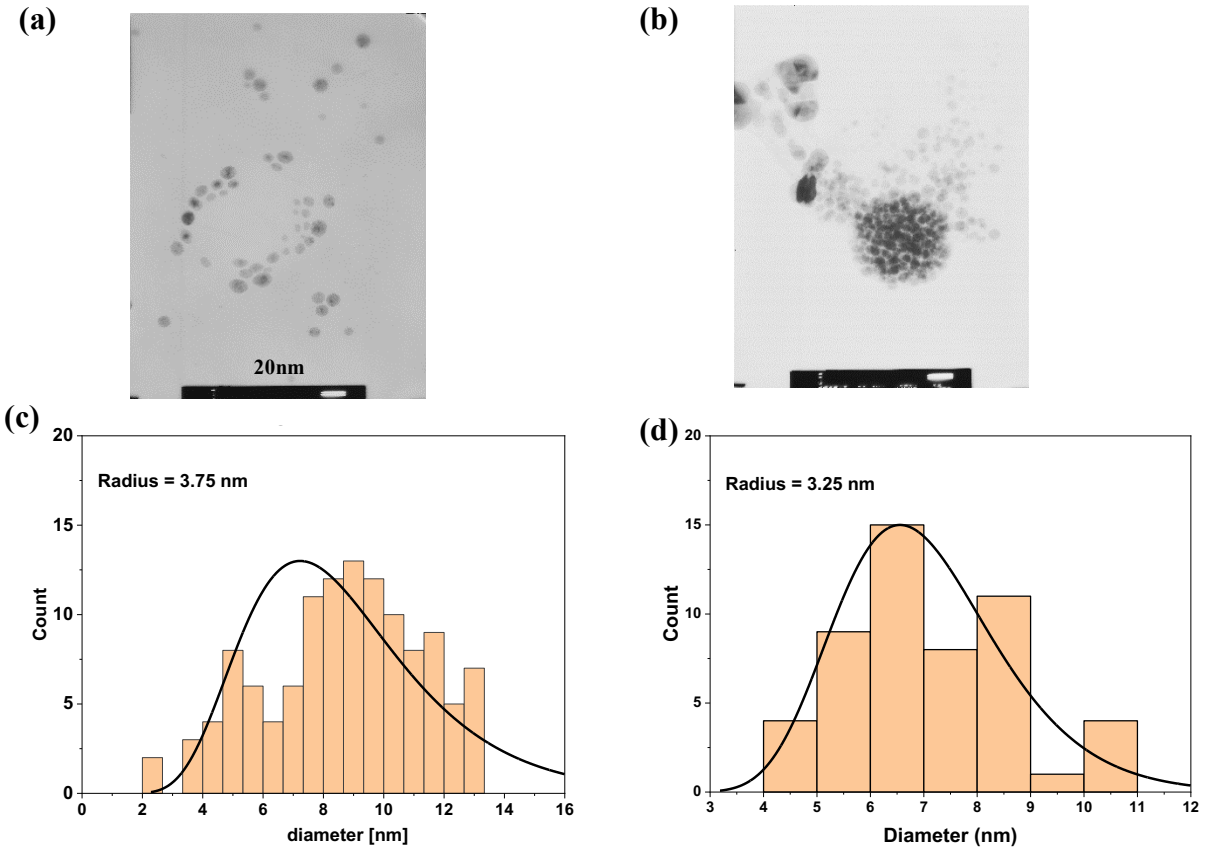

Figure 4.22 TEM micrograph of **(a)** hydrophobic AgNPs in n-hexane and **(b)** hydrophilic AgNPs-F127 in distilled water. Size distribution of AgNPs in **(c)** n-hexane and **(d)** distilled water obtained from analysis of TEM micrographs.

4.5 Outcomes of complexing PSI with both hydrophobic and hydrophilic AgNPs

Different approaches were developed towards fabrication of stable PSI-AgNPs complexes. Results from each approach used are as detailed below. Both hydrophilic and hydrophobic AgNPs were utilized, and the attachment of AgNPs to PSI was tested in solution as well as in thin films. Monomeric PSI particles derived from the cyanobacterium *Synechocystis* sp. 6803 were utilized in these approaches predominantly. However, for PSI complexation in solution, PSI derived from *C. merolae* was employed.

4.5.1 Complexation of PSI particles and hydrophilic AgNPs-F127 in solution

The hydrophilic AgNPs-F127 colloidal solution was the most stable among the other aqueous solutions of AgNPs coated with different detergents (Figure 4.16). Hence, to induce formation of PSI-AgNPs complexes, increasing volume of the AgNPs-F127 solution was mixed with the solution of PSI from C. *merolae* (CmM) and the effect of mixing was tested using the steady-state absorption spectrometer. One may note that the spectra of mixtures look like simple sums of PSI spectra and AgNPs spectra.

To facilitate sufficient interaction between the components, the mixture was incubated for 10 mins at room temperature before the first measurement as well as after addition of every additional volume of AgNPs-F127 solution (see section 3.5.1 for details). Figure 4.23a shows the comparison of the absorption spectra of the solution of CmM PSI with the mixtures of PSI and AgNPs-F127 solutions. It was observed that the absorbance of the mixture of PSI and AgNPs-F127 solutions was increasing in the Soret/AgNPs SPR region (black arrow) with increasing volume of the AgNPs-F127 solution (compare Figure 4.14b).

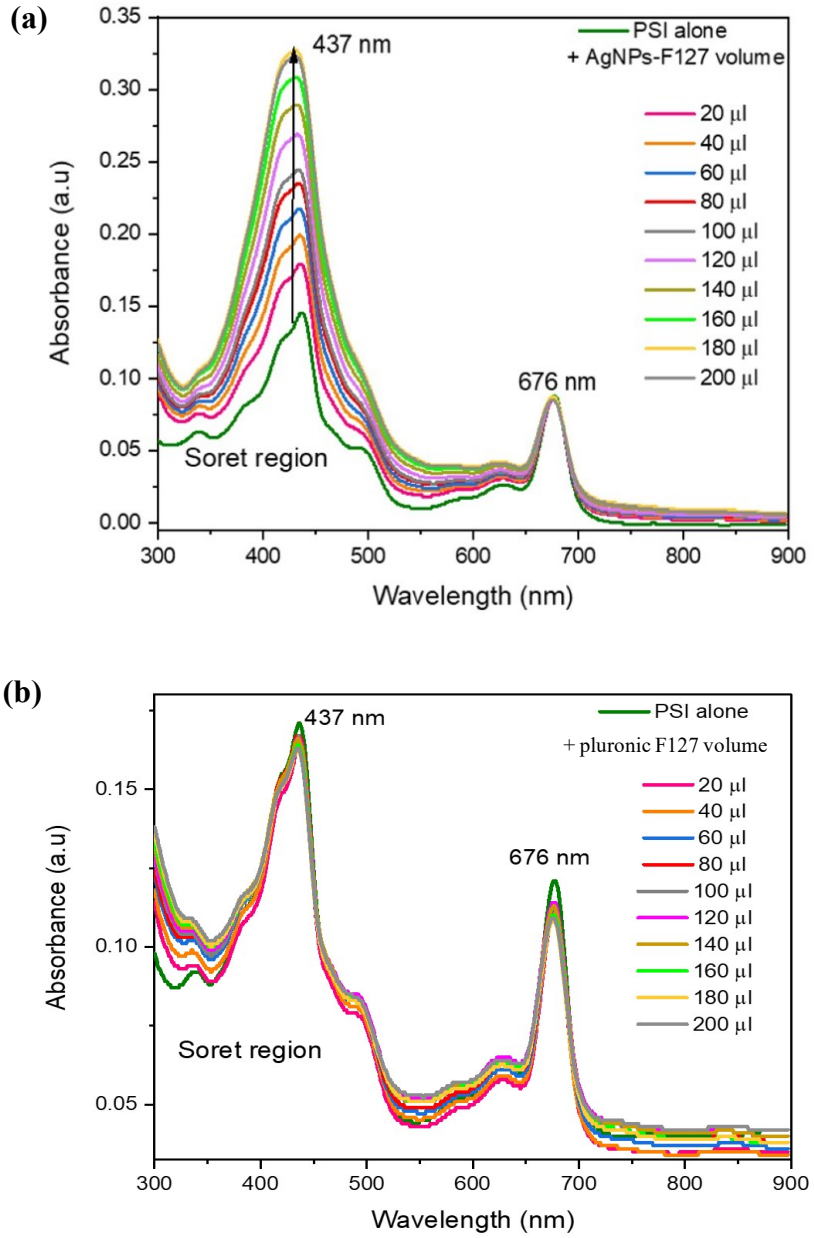

Figure 4.23 Comparison of the absorption spectra of **(a)** 2 ml of *C. merolae* (CmM) PSI complex solution (green dotted) with the mixture of PSI solution and varying volume of hydrophilic AgNPs-F127 solution and **(b)** 2 ml of same PSI complex solution (green dotted) with the mixture of PSI solution and varying volume of pluronic F127 solution. Spectra were measured at room temperature.

Next, a similar control experiment was performed in which solution of AgNPs-F127 was replaced with the solution of F127 alone. Figure 4.23b shows that the pluronic F127 itself did not have a considerable effect on the absorption bands of the PSI. However, it systematically affected the spectra in the low absorption regions (300-350 nm, 500-600 nm, >700 nm).

To further evaluate the interaction between PSI complexes and hydrophilic AgNPs-F127 particles, fluorescence emission spectra measurements were performed at three excitation wavelengths, λ_{exc} = 400 nm, 431 nm, and 437 nm. The spectra with 680 nm emission band of PSI complexes and of the mixtures of PSI and AgNPs-F127, excited at 400 nm, are displayed in Figure 4.24a. It is observed that there is a substantial quenching of the emission after addition of 20 µl of AgNPs-F127 solution by almost twice in comparison to the emission from pure PSI (arrow 1). This observation could suggest binding of the PSI to AgNPs as well as an energy transfer from PSI to the AgNPs. However, with the increasing amount of AgNPs, a continuous increase in the emission is observed (arrow 2) with a blue shift of up to ~6 nm.

Figure 4.24b shows the control experiment of solution containing PSI and pluronic F127. It shows that pluronic F127 has a considerable effect on the emission bands of the PSI similar to that seen in the mixture of PSI and AgNPs-F127. This indicates that characteristic changes in the fluorescence spectra (shown in Figure 4.24a) are rather due to interaction between PSI and detergent and not due to the interaction between PSI and AgNPs.

It may be concluded that neither steady-state absorption nor fluorescence emission studies did not indicate any interaction between hydrophilic AgNPs-F127 and PSI complexes from *C. merole* CmM PSI in solution.

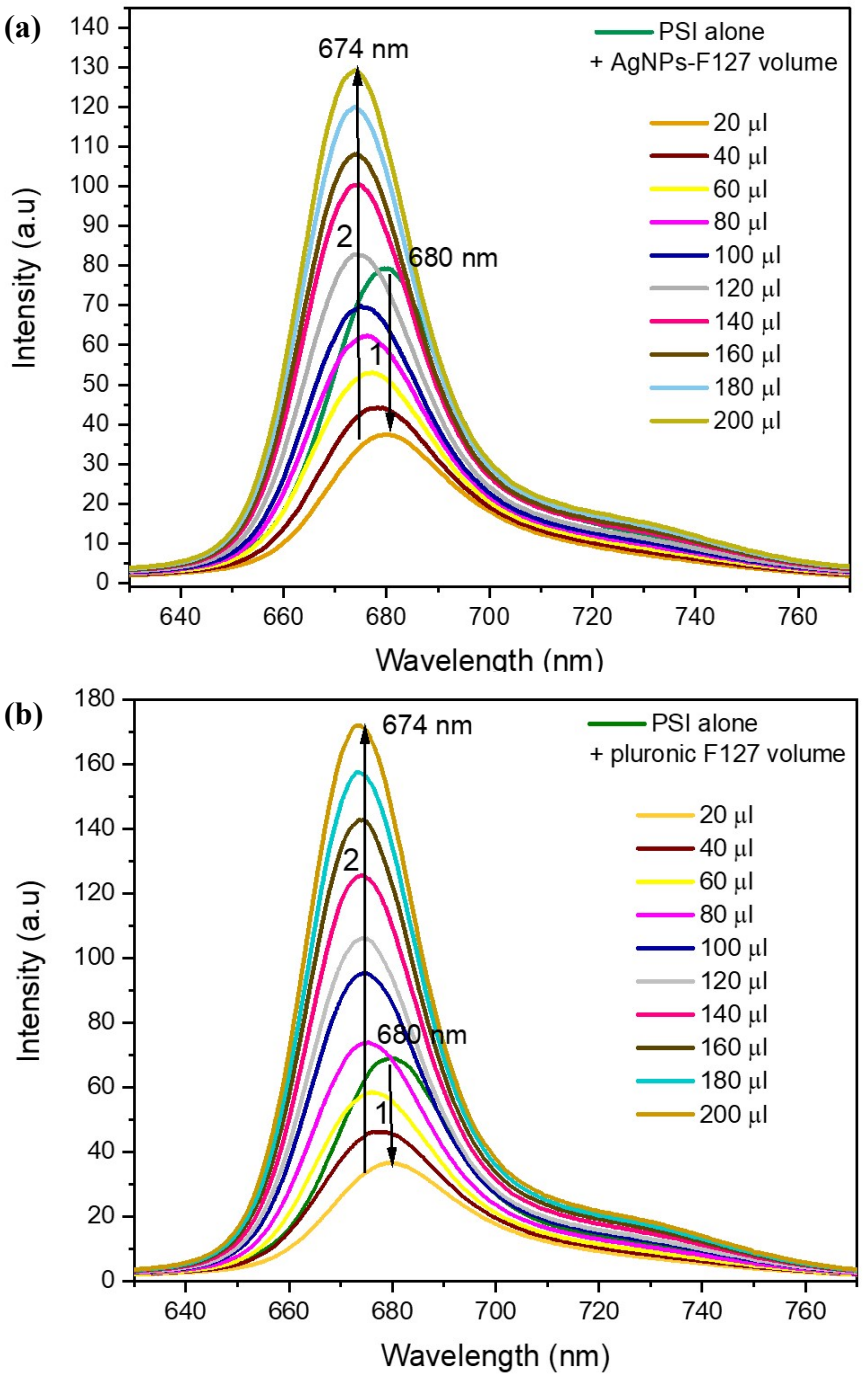

Figure 4.24 Comparison of fluorescence emission spectra of **(a)** *C. merolae* PSI complex alone (green dotted spectra) with the mixture of PSI and varying volume of hydrophilic AgNPs with pluronic F127 coating and **(b)** PSI complex alone with the mixture of PSI and varying volume of pluronic F127. Spectra were measured at room temperature. Excitation wavelength was 400 nm.

4.5.2 Characterization of PSI-AgNPs films on FTO substrates

A few different approaches towards fabrication of PSI-AgNPs films on FTO substrates have been tested and are described below. This section reports on the investigation of PSI monomeric particles from cyanobacterium *Synechocystis* sp. PCC 6803.

4.5.2.1 PSI electrodeposited on FTO coated with hydrophobic AgNPs (PSI-(Ag-FTO))

Figure 4.25a shows typical steady-state absorption spectra of the samples studied subsequently by the time-resolved absorption: PSI-(Ag-FTO) and a few control samples – PSI-FTO, Ag-FTO, Buffer-Ag-FTO, and AgNPs dispersed in n-hexane. Description of preparation of all these samples can be found in the Methodology chapter. The features of these spectra are described in the following paragraphs.

PSI-FTO. The steady state absorption spectrum of PSI-FTO (blue coloured) shown in Figure 4.25a (see also Figures 4.1b and 4.26a) is dominated by Soret band (at ~437 nm) and Qy band (at 678 nm) of chlorophyll *a* from PSI. This spectrum is similar to the spectrum of PSI in solution (Figure 4.23).

Ag-FTO. The steady state absorption spectrum of the AgNPs film on FTO (Ag-FTO) (sintered at 80 °C, orange coloured spectrum), is shown in Figure 4.25a. For comparison, the AgNPs dispersion in n-hexane is shown in the inset. The SPR band for colloidal AgNPs in n-hexane was observed at 411 nm. Interestingly, deposition of AgNPs on FTO significantly modifies the spectrum of AgNPs. The spectrum of Ag-FTO shows two bands – the smaller one is slightly blue-shifted relative to AgNPs dispersed in n-hexane, to ~400 nm, and the bigger one is red-shifted to 485 nm. There may be a few reasons for this redshift. Firstly, it can be attributed to a higher mutual proximity of silver nanoparticles in the films [143]. The closeness of metal nanoparticles can result in a decrease in the plasmon resonance energy, producing shifts towards longer wavelengths in the spectrum. Secondly, when depositing AgNPs on a substrate, it is important to consider effects that can be related with the substrate's density and refractive index [143]. Thirdly, the redshift may be caused by the sintering of the AgNPs at 80 °C. This effect can be assigned to the increasing size of the metal nanoparticles with the thermal treatment, due to the coalescence mechanism [143]. On the other hand, the blue-shifted peak with maximum at ~ 400 nm could result from a fraction of the smallest NPs that did not join together to form bigger structures. As a result, the size and spectral position of these nanoparticles are similar to AgNPs in n-hexane dispersion. Thus, the presence of the two bands, at ~400 and 485 nm, may reflect heterogeneity of sizes of the AgNPs in Ag-FTO samples. The AgNPs films present brownish color and transparency similar to the AgNPs n-hexane dispersion as can be seen in Figure 4.25b and Figure 4.14a, which is typical of spherical and well-dispersed AgNPs [144, 145].

PSI-(Ag-FTO). We studied the steady-state spectra of the PSI-(Ag-FTO) shown in Figure 4.25a (purple coloured) to find any manifestation of the interaction between the PSI and AgNPs. The absorption spectrum of this sample has a broad band at 485 nm attributed to the surface plasmon of AgNPs. Peaks at 416 nm and 437 nm are attributed to Soret band of chlorophyll *a* from PSI while the absorption band at 678 nm is due to the Qy band of these chlorophylls.

The 416 nm and 437 nm peaks are contributed also by AgNPs as judged from comparison of PSI-(Ag-FTO) spectrum with that of Ag-FTO.

As described in the chapter 1, some studies suggested that AgNPs can increase the absorbance of the PSI by acting as antenna effectively storing the incident energy in the localized surface plasmon mode [8, 9, 51, 53, 146]. Therefore, the absorption spectrum of PSI-(Ag-FTO) could be not a simple sum of the absorbances of PSI and AgNPs but it may additionally possess some features revealing interaction between these two components. However, due to significant variety of PSI-FTO, Ag-FTO, and PSI-(Ag-FTO) spectra (Figure 4.26) we are not able to conclude on the manifestation of possible PSI-AgNPs interaction based on the steady-state absorption spectra.

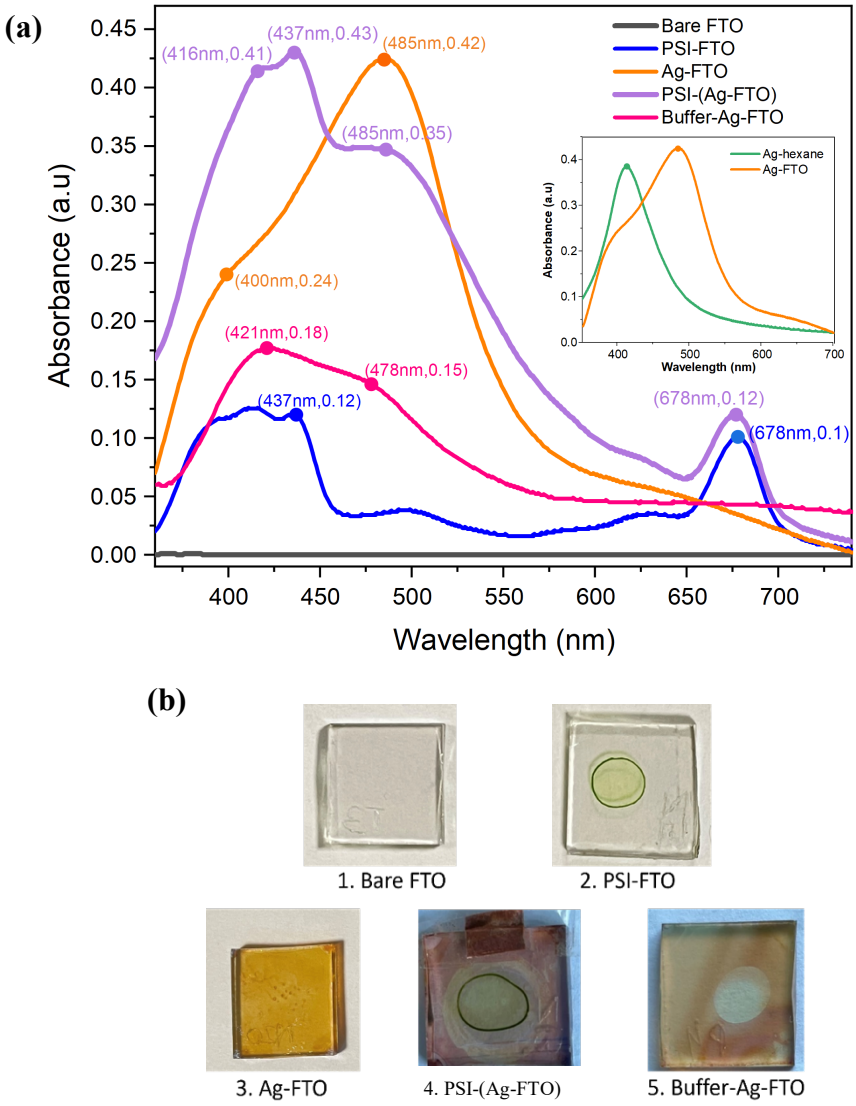

Figure 4.25 (a) Comparison of steady-state absorption spectra of PSI-FTO (blue colored), Ag-FTO (orange colored), PSI-(Ag-FTO) (purple colored), and Buffer-Ag-FTO (magenta colored). Inset shows steady-state spectra of hydrophobic AgNPs in n-hexane dispersion and deposited on FTO films (Ag-FTO) and **(b)** Photographic images of the studied samples: PSI-FTO, Ag-FTO, PSI-(Ag-FTO), and Buffer-Ag-FTO. The absorption spectra shown in (a) were measured only from the central areas where PSI or buffer were deposited in samples PSI-FTO, PSI-(Ag-FTO), and Buffer-Ag-FTO.

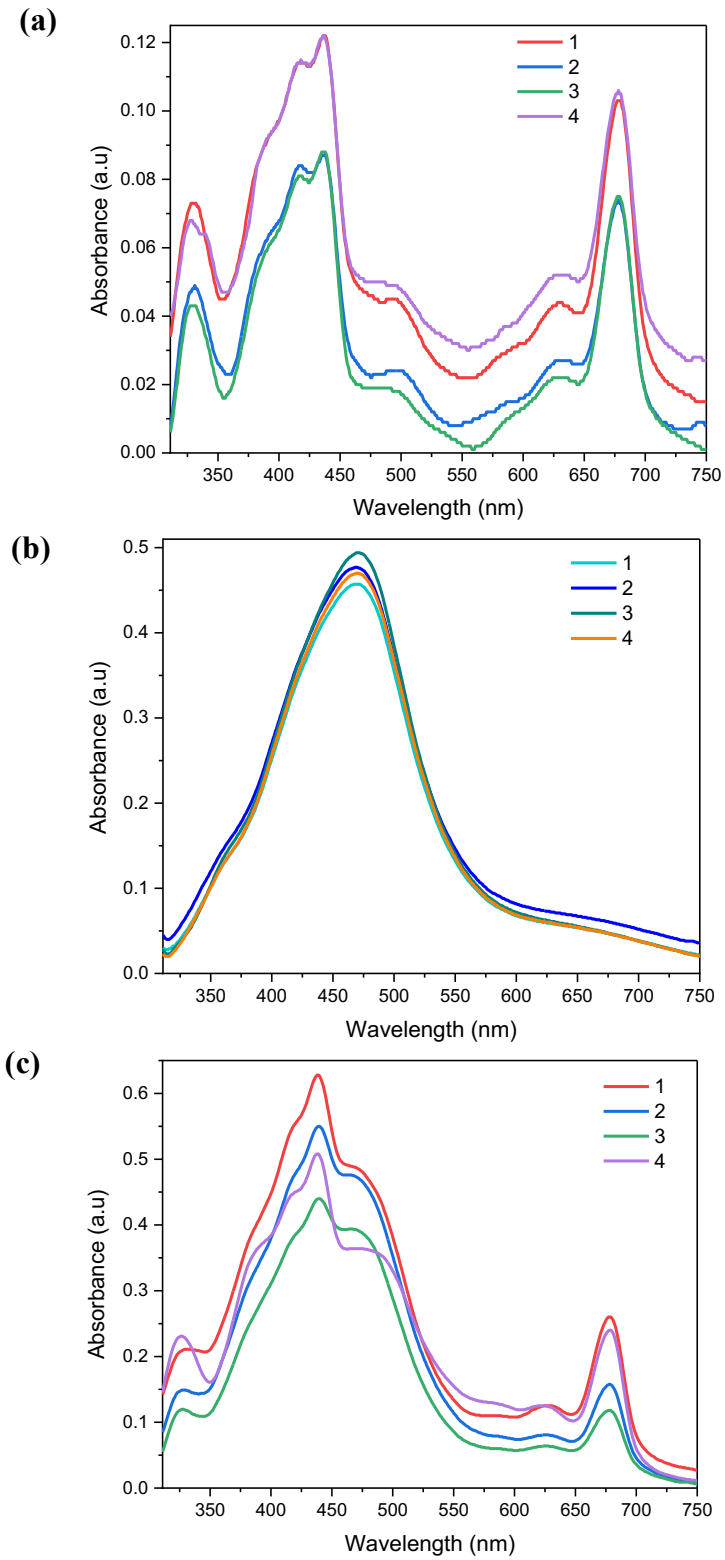

Figure 4.26 Spectral variety among various samples: **(a)** PSI-FTO absorption spectra, **(b)** Ag-FTO absorption spectra and **(c)** PSI-(Ag-FTO) absorption spectra. The term variety refers to variations in both relative amplitudes and peak positions within each type of samples.

Buffer-Ag-FTO. As a control experiment, we deposited a droplet of buffer used to suspend PSI complexes (see section 3.3 for composition) on Ag-FTO under exactly the same conditions that were used to electrodeposit PSI on Ag-FTO (refer to the section 3.5.2.1). This buffer-treated Ag-FTO is labeled "Buffer-Ag-FTO" (Figure 4.25a, magenta colored). This spectrum exhibits a prominent and well-defined peak at 421 nm, accompanied by a discernible shoulder at 478 nm. The peaks at 421 nm and at 478 nm are reminiscent of the peaks at 400 and 485 nm of Ag-FTO (orange colored). Clearly, buffer deposited on Ag-FTO makes the brownish color of Ag-FTO much less intensive (compare red and orange spectra in Figure 4.25a with pictures of the respective samples, Buffer-Ag-FTO and Ag-FTO, in Figure 4.25b). Overall, it looks like buffer washes out part of the AgNPs layer from FTO. Before the buffer treatment, the 485-nm band was much more intensive than that at ~400 nm. After the treatment, the relative amplitudes of the 400/421 nm and 485/478 nm bands invert: the 421-nm band is more intensive than that at 478 nm. We speculate that the there are two layers of AgNPs on the surface of FTO: bottom layer composed of smaller NPs (peaking at 400/421 nm) and top layer composed of larger NPs (peaking at 478/485 nm) and during the buffer treatment mostly the top layer is washed out. This explanation seems reasonable since the surface of FTO is uneven (Figure 4.27a,c) and smaller NPs may be located deeper, in small "valleys" of the FTO surface, while the bigger ones (unable to penetrate deeper and possibly further enlarged as the result of elevated temperature treatment, as described above) may be better exposed to the buffer and easier to remove. The heterogeneity of the sizes of AgNPs on FTO may be noticed in AFM and even better in SEM pictures (Figure 4.27b,d). Interestingly, the treatment of Ag-FTO with PSI dispersed in the same buffer leads to a much lower decrease in the optical density of the Ag-FTO at ~485 nm (compare orange and purple spectra in Figure 4.25a or pictures of Ag-FTO and PSI-(Ag-FTO) in Figure 4.25b). It seems that the presence of PSI complexes in buffer protects to some degree the AgNPs from being washed out by the buffer.

AFM and SEM images

AFM and SEM images show that the surface of FTO layer is pretty rough (Figure 4.27a,c). Respective images of FTO plates coated with a layer of AgNPs show that some of the AgNPs are trapped deeper between the FTO protrusions and some are closer to the upper parts of these protrusions. An expected effect of the presence of AgNPs filling the "valleys" between the protrusions is a decrease of the roughness. In order to quantify this effect, the root mean square (RMS) roughness of the FTO surface was measured using AFM. It turned out that the RMS value was 11.24 for bare FTO and only 9.33 for Ag-FTO, as expected.

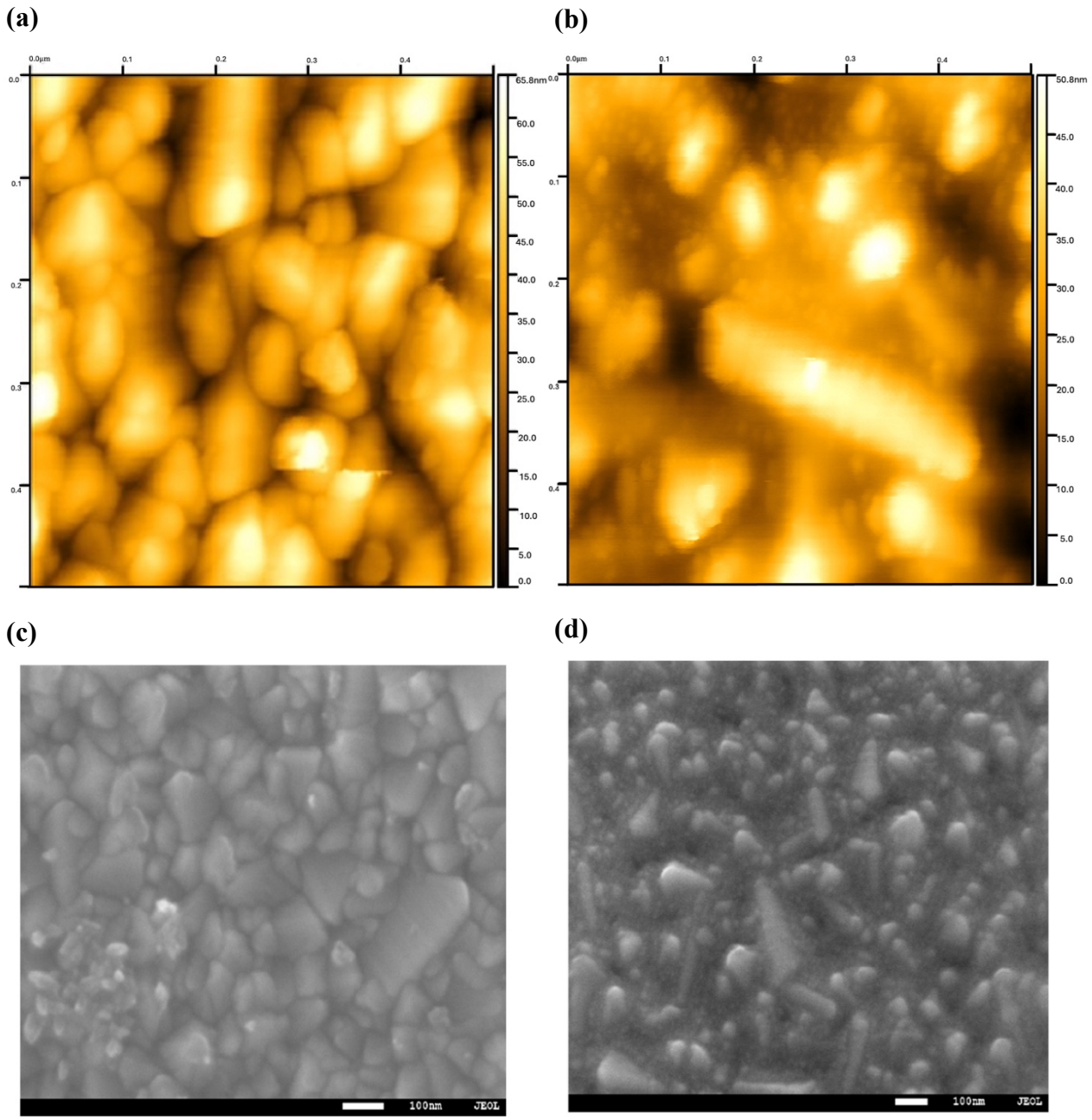

Figure 4.27 AFM images of **(a)** bare FTO and **(b)** Ag-FTO, and SEM images of **(c)** bare FTO and **(d)** Ag-FTO. The Ag-FTO samples were sintered at 80 before the AFM and SEM measurements.

Ultrafast transient absorption spectroscopy

All the samples characterized above – Ag-FTO, PSI-FTO, PSI-(Ag-FTO), Buffer-Ag-FTO, and AgNPs dispersed in n-hexane – were studied using femtosecond transient absorption spectroscopy to detect possible interaction between PSI and AgNPs. The temporal evolution of absorbance changes following laser excitation at 425 nm, the wavelength of the overlap of strong absorption both by PSI and AgNPs, was analyzed globally. The results of this analysis and their discussion is presented below. The technical details on how the experiments were conducted including a scheme of PEC (Figure 3.12) in which the samples were kept during measurements and how the global analysis were performed maybe found in section 3.6.4.2.

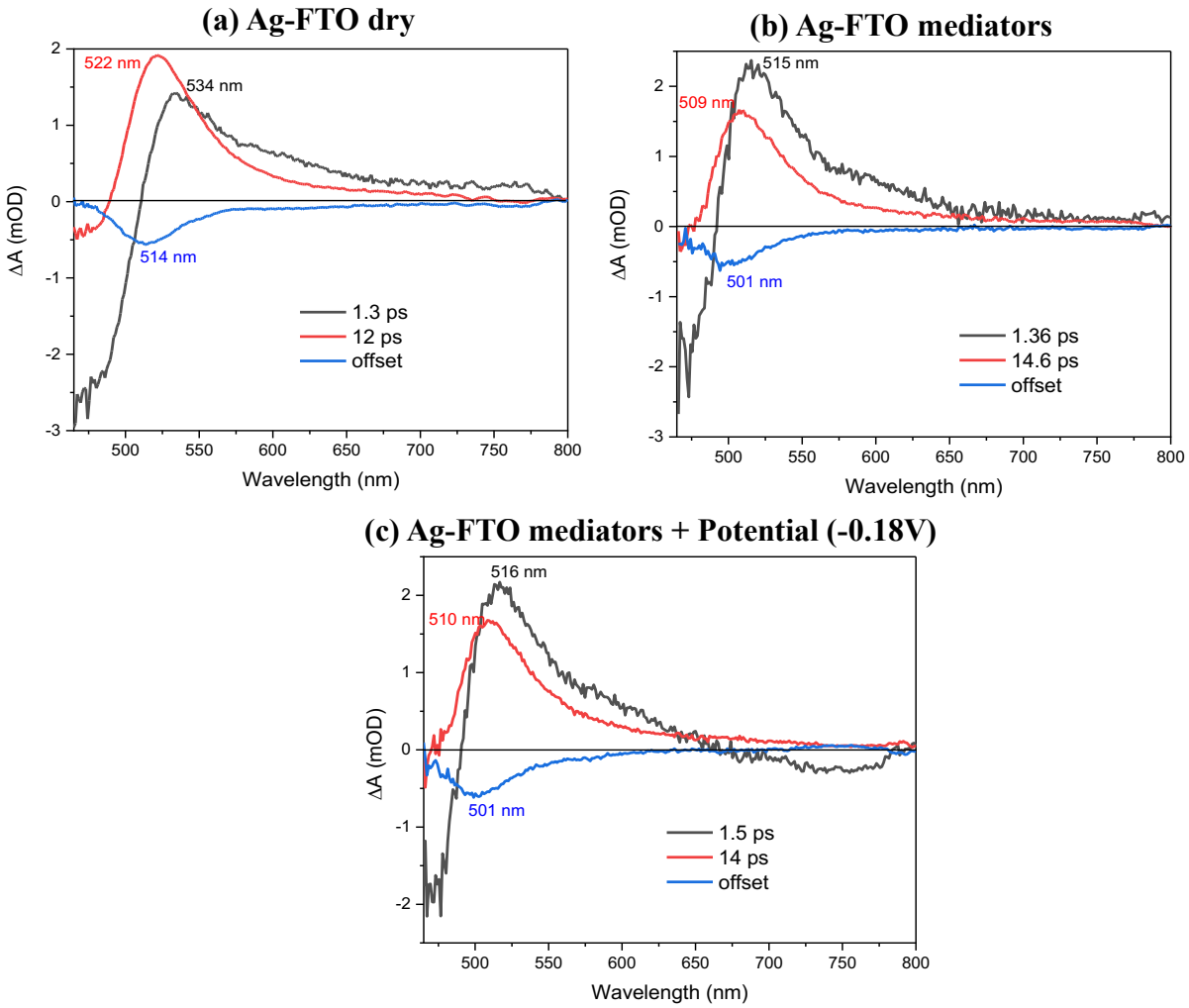

Figure 4.28 Comparison of the results of time-resolved absorbance measurements of the Ag-FTO plate placed in PEC at different experimental conditions: **(a)** dry Ag-FTO plate (without electrolyte in contact with the Ag-FTO plate), **(b)** Ag-FTO plate in PEC filled with electrolyte containing mediators (20 mM ascorbate and 10 μM PMS), and **(c)** same as (b) but with potential of -180 mV applied to the Ag-FTO plate. Excitation wavelength was 425 nm.

Ag-FTO. Figure 4.28 compares the results of global analysis (Decay Associated Spectra, DAS) of the absorbance changes over time, collected for Ag-FTO sample in the range 460-800 nm at three different experimental conditions (refer to section 3.6.4.2). These conditions were the following: (1) dry Ag-FTO electrode, (2) Ag-FTO electrode in contact with electrolyte containing ET mediators and (3) as (2) but with electric potential applied to Ag-FTO electrode. Following the excitation of Ag-FTO at 425 nm, we observed absorbance changes mostly within the 460–620 nm range and occurring on the picosecond time scale (except for the component non-decaying in the 3 ns time window). The extracted lifetimes and spectral features at all experimental conditions exhibited consistent similarities (Figure 4.28): presence of 1.3-1.5-ps DAS, 12-15-ps DAS, and a non-decaying component (offset) of similar respective spectral shapes. The only significant difference is that DASes obtained for dry sample, are characterized by bands which are red-shifted by 13-19 nm with respect to the spectra obtained under two other experimental conditions.

Drawing insights from the research conducted by Bigot and colleagues on AgNPs embedded in a glass matrix under dry condition, who investigated energy relaxation following nanoparticle excitation with femtosecond pulses at various time scales, we can infer potential explanations for components observed in our experiments [54]. Specifically, we assign the ~1.3 -1.5 ps component to the electron-electron scattering, the ~12-15 ps component – to the electron-phonon scattering, and the slowest non-decaying component (offset) – to heat transfer to the surrounding medium.

PSI-FTO. Experiments with PSI-FTO plate were performed under the same conditions as for Ag-FTO plates. Figure 4.29 illustrates that the lifetimes and spectral characteristics under these conditions are largely similar to each other, but specific differences may also be noticed. Under the dry conditions (Figure 4.29a), the fastest dynamics is characterized by a 4.5 ps component with a characteristic minimum at 680 nm. This phase arises from both rapid excitation decay (due to quenching by the reaction center and possibly singlet-singlet annihilation related to relatively strong excitation energy) and the transfer of excitation energy from the bulk to red Chls (revealed by a small positive amplitude at about 710 nm) [1]. A slower component of 26 ps is observed, attributed to the decay of the excited state equilibrated over the bulk and red-shifted Chls. The long-lived component (offset) is of a very small amplitude. This component showing a minimum at ~675 nm reveals a very minor amount of long-lived ("uncoupled") chlorophylls. These chlorophylls are unable to deliver their excitation to the reaction center and decay on a time scale of a few nanoseconds. Lack of any signal at 700 nm in this DAS indicates that the primary donor P is quasi-permanently oxidized to P^+ under the "dry" conditions [1].

After addition of buffer solution with mediators to the cell containing PSI-FTO plate, the fastest component of 4.3 ps is quite similar to the respective component measured under "dry" conditions (compare Figure 4.29a and Figure 4.29b). However, its interpretation is somewhat different. Now it describes not only excitation decay and energy transfer to red-shifted Chls (as under dry conditions), but additionally it depicts formation of charge separated states in the reaction center. This difference is manifested as disappearance of the small positive band at about 710 nm (seen in Figure 4.29a but not in Figure 4.29b). This disappearance is caused by appearance of photobleaching of reaction center molecules taking part in the charge separation. Observation of charge separation is possible due to the presence of mediators which rereduce P^+ to P between consecutive laser flashes exciting PSI.

The intermediate component is characterized by a longer lifetime (39 ps vs. 26 ps). The larger lifetime of this component is compensated by its smaller amplitude (compared to dry conditions) which together are well known computational effects related with limited signal to noise ratio of the experimental data. However, extended lifetime of the second component is also related with evolution of charge separated states in the reaction center, which occur on somewhat longer time scale than slow phase (26 ps) of excitation decay recorded under dry conditions. Small differences in the respective shapes of the ~4 ps and 26/39 ps DASes at wavelengths longer than ~700 nm is assigned to laser light-induced formation of the state P^+ under conditions with mediators (Figure 4.29b) and absence of such formation under the "dry" conditions (Figure 4.29a) (see below).

An important effect of the presence of mediators in solution is the appearance of the negative band at ~700 nm in the offset component (Figure 4.29b). This band is a well-known in the literature effect of oxidation of P due to electron transfer from P to nearby electron acceptor (A_0) occurring within a few picoseconds after arrival of an excitation from the excited antenna

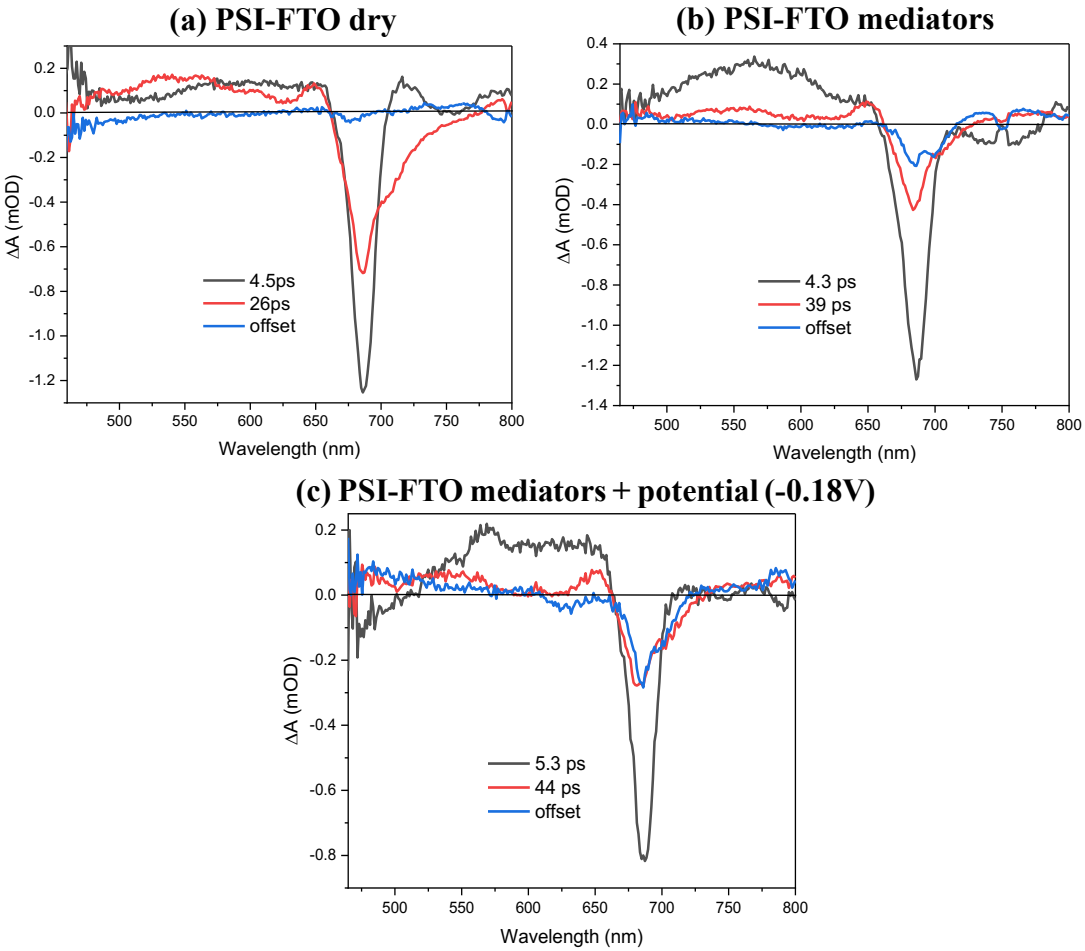

Figure 4.29 Comparison of the results of time-resolved absorbance measurements of the PSI-FTO plate placed in PEC at different experimental conditions: **(a)** without electrolyte in PEC (dry conditions), **(b)** with electrolyte containing mediators (20 mM ascorbate and 10 µM PMS), and **(c)** same as (b) but with potential of -180 mV applied to the PSI-FTO plate. Excitation wavelength was 425 nm.

to the reaction center [147]. The offset contains also another band at ~685 nm caused probably both by uncoupled Chls seen also under "dry" conditions and discussed above (see Figure 4.29a) and by P^+ [111]. The difference in the shape of offset in Figure 4.29a and b is clear evidence that mediators efficiently re-reduce P^+ to P (between the laser flashes exciting the sample) and that lack of mediators ("dry" conditions) leads to quasi-permanent accumulation of P^+ (PSI complexes are inactive in terms of normal charge separation). The photobleaching signal from P^+ at 700 nm observed in the femtosecond experiments is the same signal whose decay on millisecond time scale was characterized in the preceding section (Figure 4.2 and Figure 4.8).

Applying a negative potential of -180 mV to the PSI-FTO plate (Figure 4.29c), further increases the signal at 700 nm in the offset indicating more efficient re-reduction of P^+ by combination of mediators and low potential. Similar effect was observed for millisecond studies described in section 4.2.2.2 (Table 4.3 and Figure 4.9). Unexpectedly, the negative potential increased also the shorter-wavelength band of the offset spectrum peaking at 686 nm. At the moment there is no good explanation for this effect. The two remaining components are rather similar to those observed in the experiments without potential (Figure 4.29b).

PSI-(Ag-FTO). Transient absorption data collected for PSI-(Ag-FTO) sample were satisfactorily fitted, similarly as for Ag-FTO and PSI-FTO, with three components (Figure 4.30). A higher number of components resulted in physically non-interpretable DAS due to limited signal to noise ratio of the experimental data. Since the lifetime components obtained for Ag-FTO were ~1.4 ps, ~14 ps and offset, while for PSI-FTO – we obtained ~5 ps, ~ (30-40) ps and offset, one could expect – in the simplest case – that the fit with the same number of parameters for the PSI-(Ag-FTO) sample will give intermediate values of the respective lifetimes. Indeed, as data in Figure 4.30 show, the lifetime of the fastest component ranges from 1 to 5 ps and the intermediate component ranges from 18 to 25 ps. Moreover, at a first glance, the shape of the DAS spectra in Figure 4.30 looks like a sum of respective spectra shown in Figure 4.28 and Figure 4.29. To obtain more conclusive results from the measurements on PSI-(Ag-FTO), and in particular to detect any possible interactions between PSI and AgNPs in the PSI-(Ag-FTO) film, we decided to perform independent kinetic analysis in the blue and red spectral regions separately. Let us notice that absorption changes in Ag-FTO occur mostly in the blue part of the spectrum (below 630 nm, Figure 4.28) while those in PSI-FTO – mostly in the red part of the spectrum (above 630 nm, Figure 4.29). Therefore, separate global analysis in the blue part should minimize the effect of artificial influence of longer lifetimes of own PSI dynamics on the faster dynamics of AgNPs but at the same time, it should reveal possible real effects of interactions between PSI and AgNPs on the dynamics of AgNPs. And vice versa, separate global analysis in the red part of the spectrum is expected to reveal possible effects of interactions on the dynamics of PSI.

In Figure 4.31 we present systematic comparison of normalized DASes obtained from the fits of the data for the PSI-(Ag-FTO) and Ag-FTO samples, performed in the blue part of the spectrum (475-630 nm). Under the “dry” conditions (Figure 4.31a) a broad positive band with a lifetime of ~21 ps and maximum at ~546 nm is observed for the PSI-(Ag-FTO) sample (solid red). Corresponding band observed for the Ag-FTO sample is characterized by much shorter lifetime of 12 ps and maximum at 522 nm, blue-shifted by ~24 nm (dashed red) with respect to the 21 ps DAS. Since in this region the transient absorption from PSI is small (compare Figure 4.29a), it is unlikely that the extension of lifetime comes from the contribution of the 26 ps DAS from the PSI-FTO sample (from Figure 4.29a). Therefore, we claim that the unique shape of the 21-DAS may be caused by interaction between PSI and AgNPS in the PSI-(Ag-FTO) samples. The red-shift and the lifetime extension of the 12/21 ps DAS maybe interpreted as an increase of PSI transient absorption in the ~500-600 nm region caused by the interaction between PSI and AgNPs. Similar observations and similar interpretation regarding the red-shift and lifetime extension of the intermediate component apply to the other two experimental conditions (Figure 4.31b,c).The slow down of the kinetic decays at 546 nm is evidently shown in Figure 4.32a-c.

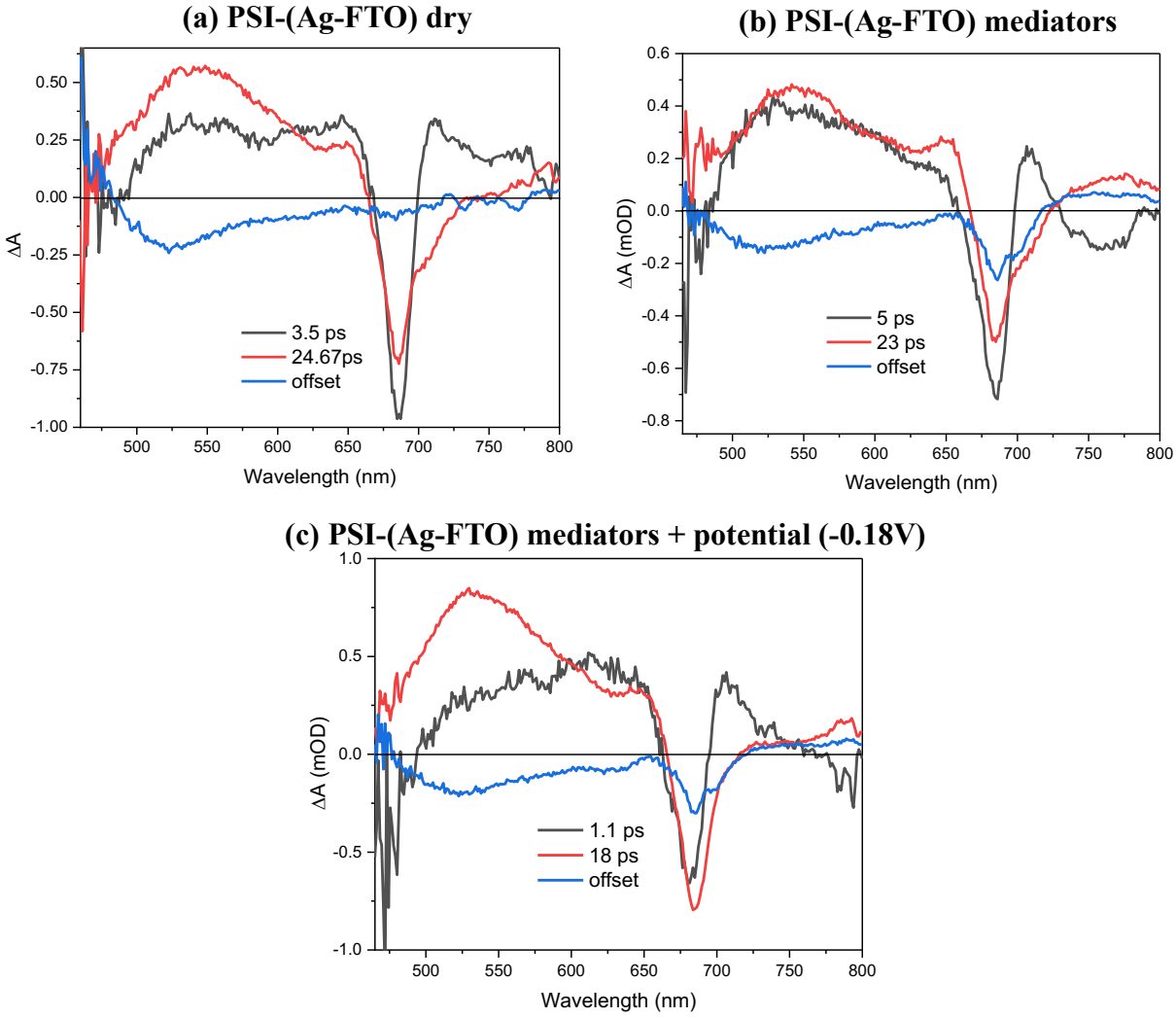

Figure 4.30 Comparison of the results of time-resolved absorbance measurements of the PSI-(Ag-FTO) plate in PEC at different experimental conditions: **(a)** without electrolyte in PEC (dry conditions), **(b)** with electrolyte containing mediators (20 mM ascorbate and 10 μM PMS), and **(c)** same as (b) but with potential of -180 mV applied to the PSI-(Ag-FTO) plate. Excitation wavelength was 425 nm.

A separate global analysis in the red part of the spectrum did not reveal significant effect of the interaction between PSI and AgNPs on the dynamic of PSI. The kinetics at Qy band maximum at 686 nm (Figure 4.32d-f) are rather similar for Ag-FTO and PSI-(Ag-FTO) samples. This observation suggests that the rate of decay of the excited state in PSI is not affected by the proximity of AgNPs.

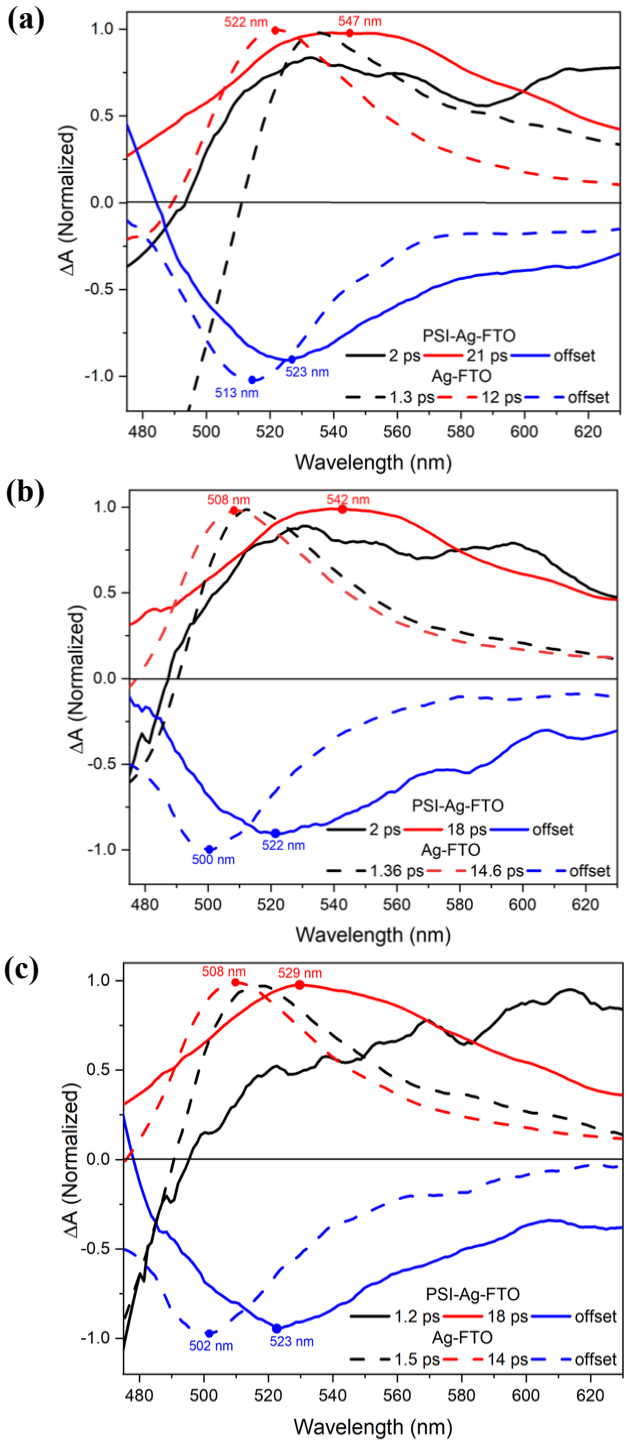

Figure 4.31 Comparison of normalized DASes obtained from the fits of the data for the PSI-(Ag-FTO) and Ag-FTO samples at different experimental conditions: **(a)** without electrolyte (dry conditions), **(b)** with electrolyte containing mediators (20 mM ascorbate and 10 μM PMS), and **(c)** – same as (b) but with potential of -180 mV applied to the PSI-(Ag-FTO) plate. Excitation wavelength was 425 nm. Unlike in Figures 4.28-4.30, where fits were performed for the data from ~460 nm to 800 nm, here the fitted range was narrower: from 475 nm to 630 nm.

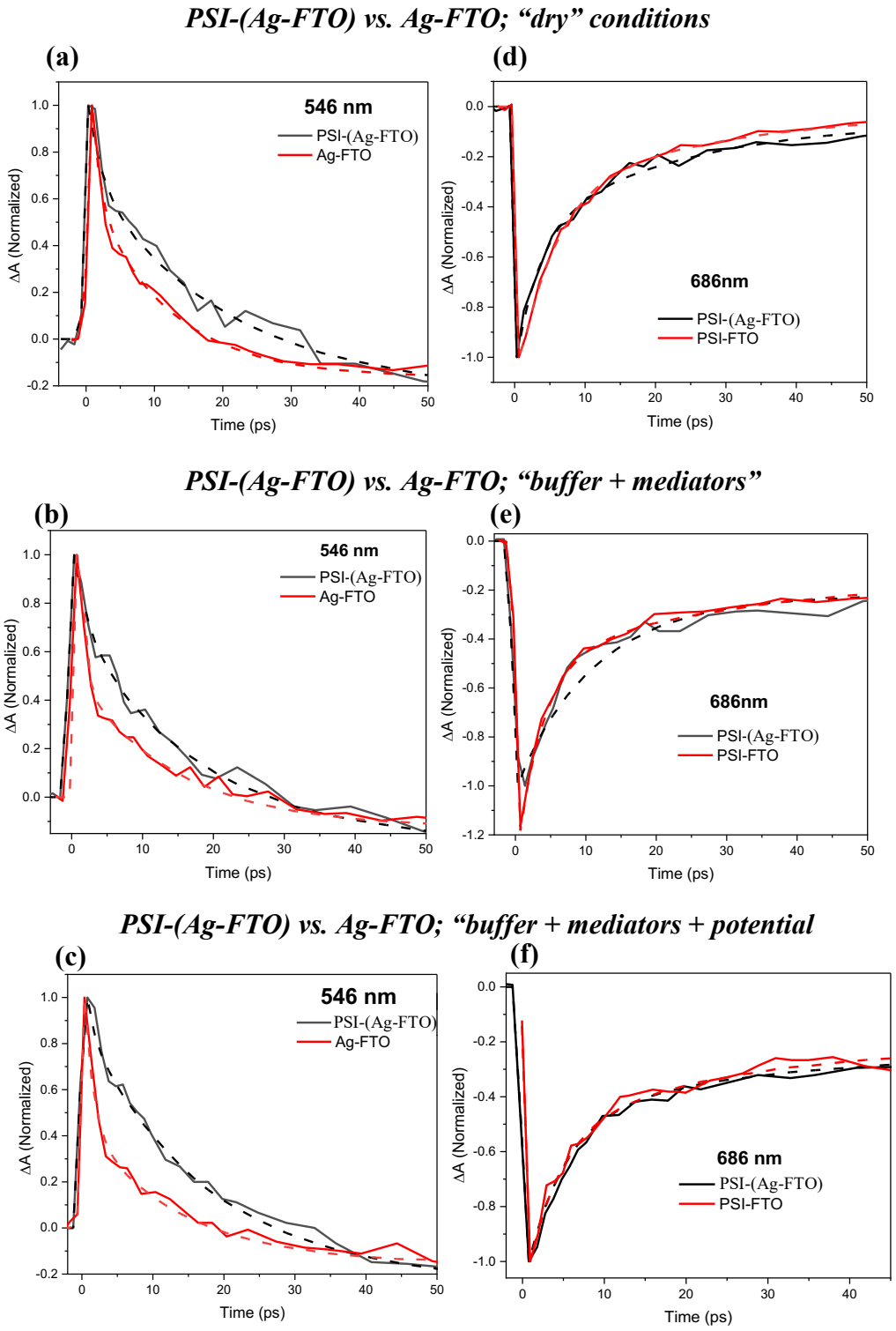

Figure 4.32 Comparison of decay kinetics at 546 nm and 686 nm obtained from the fits of the data for the PSI-(Ag-FTO) and Ag-FTO samples at different experimental conditions: **(a)** without electrolyte (dry conditions), **(b)** with electrolyte containing mediators (20 mM ascorbate and 10 μM PMS), and **(c)** – same as (b) but with potential of -180 mV applied to the PSI-(Ag-FTO) plate.

Photocurrent from PSI-FTO and PSI-(Ag-FTO)

The monomeric PSI of $A_{679nm,1\ cm}$ = 1 from cyanobacterium *Synechocystis* sp. 6803 was electrodeposited on bare FTO and Ag-FTO for photocurrent measurements. Figure 4.33 displays the chronoamperometric curves obtained for PSI-FTO and PSI-(Ag-FTO) electrodes prepared in a similar way as used in the time-resolved absorption studies described above.

At OCP, the illumination induced a negative photocurrent of ~90 nA for PSI-FTO (Figure 4.33a) and only ~25 nA for the PSI-(Ag-FTO) electrode (Figure 4.33b). We conclude that the layer of AgNPs does not improve photovoltaic output under the applied conditions.

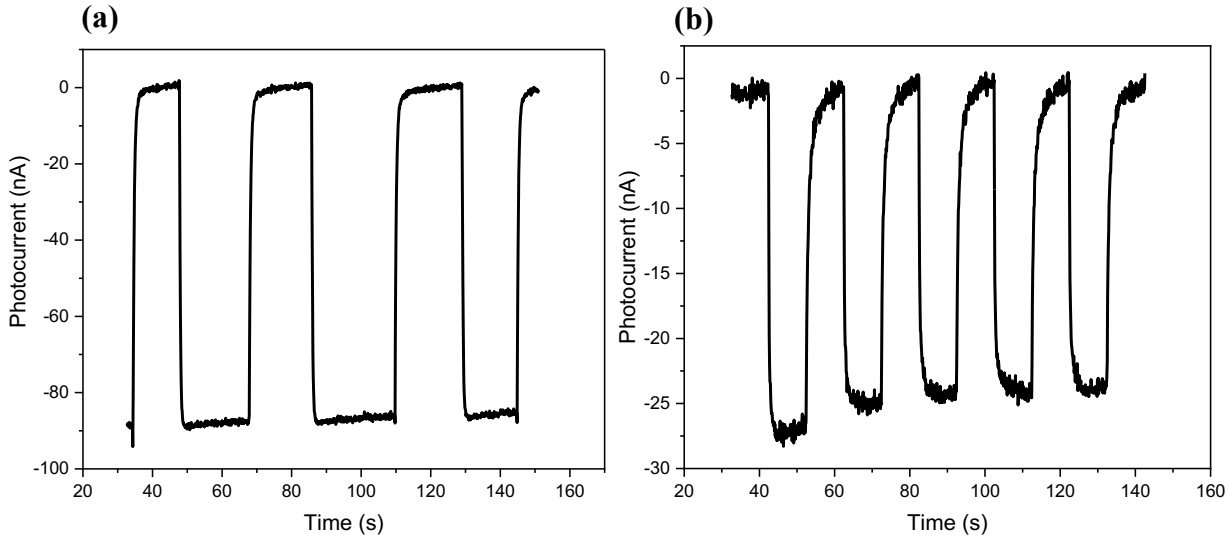

Figure 4.33 Chronoamperometric data recorded at OCP obtained in three-electrode system showing net cathodic photocurrent for **(a)** PSI-FTO and **(b)** PSI-(Ag-FTO) WE. The electrolyte employed was a 30 mM Bis–Tris buffer pH 7.0, supplemented with 10 mM sodium ascorbate and 200 µM DCPIP, serving as the sacrificial electron donor and mediator, respectively. Illumination was provided by a 685-nm LED with a spectral bandwidth (FWHM) of approximately 24 nm and a light power density of 5.8 mW/cm².

4.5.2.2 PSI electrodeposition on FTO coated with hydrophilic/hydrophobic AgNPs with 3-MPA as a linker

This section shows various procedures that were implemented to form an attachment between PSI and AgNPs using 3-MPA as a linker. The aim was to functionalize the FTO or AgNPs by utilizing the thiol and carboxylic group of 3-MPA to be attached to AgNPs and PSI, respectively, thereby facilitating a linkage between PSI and AgNPs with adherence to FTO as well.

The structure of 3-MPA is represented in Figure 4.34a. It has been presented in literature that the thiol group (-SH) forms a stable bond with the metal nanoparticles such as gold, silver, and copper. The carboxylic group (-COOH) influences the surface properties of monolayer film formed by 3-MPA [148-150]. The 3-MPA can be adsorbed on AgNPs in either trans or gauche conformations as shown in Figure 4.34b [148]. Further, the alkyl chain in chemisorbed 3-MPA resembles the environment of a biological membrane (i.e., the lipid bilayers consisting of hydrocarbon chains) which is expected to help in the interaction with PSI protein without causing its denaturation.

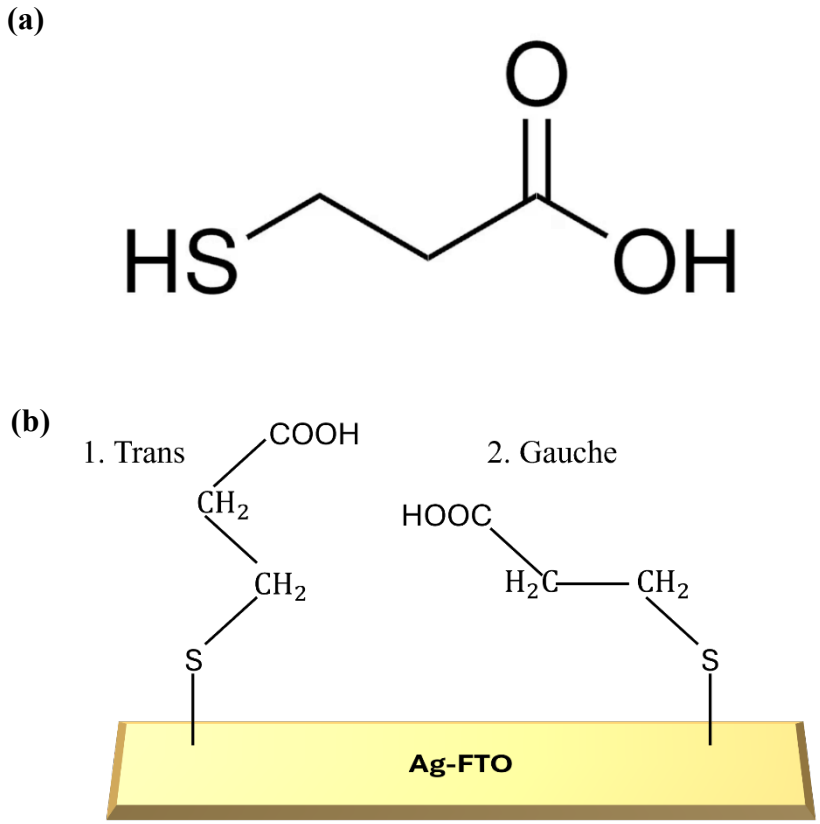

Figure 4.34 (a) Structure of 3-MPA and **(b)** 3-MPA molecule adsorbed on Ag-FTO in: 1. Trans, and 2. gauche conformations (Reproduced with changes from [148] under Creative Commons Attribution v4.0 International License[§]).

4.5.2.2.1 PSI electrodeposition on (Ag-MPA)-FTO – (PSI-(Ag-MPA)-FTO)

Figure 4.35(a,b) shows the samples right after hydrophilic AgNPs coated with 3-MPA (Ag-MPA) were drop casted on FTO and after sintering (Ag-MPA)-FTO, respectively. Here, instead of spin-coating, drop-casting technique was used for the deposition of AgNPs-MPA due to observed challenges in retaining the hydrophilic AgNPs-MPA on the FTO substrate (Figure 4.35a) - it should be noted that the entire volume of the solution dispersed away from the FTO surface during spin-coating. As a next step, PSI was electrodeposited on (Ag-MPA)-FTO (Figure 4.35c).

To observe the effect of 3-MPA on the attachment of PSI and AgNPs, the steady-state absorption spectra of the (Ag-MPA)-FTO and PSI-(Ag-MPA)-FTO plates (Figure 4.35c) were measured as shown in Figure 4.36. The spectrum for PSI-(Ag-MPA)-FTO (blue curve) shows a shoulder peak at ~500 nm attributed to SPR of AgNPs, Soret band at 439 nm (due to chlorophyll *a*), and an absorption band at 675 nm (Q_y band of chlorophyll *a*). The red curve of (Ag-MPA)-FTO shows a broad peak at 482 nm due to the SPR of AgNPs. Compared to the Ag-FTO spectrum with a peak at 485 nm (orange curve in Figure 4.25), the (Ag-MPA)-FTO spectrum in Figure 4.36 is much broader, and the peak is slightly blue-shifted to 482 nm. Additionally, the peak at 400 nm seen in the Ag-FTO spectrum (Figure 4.25) is absent in the (Ag-MPA)-FTO spectrum. These differences could be due to (1) the use of a different deposition technique, drop-casting, in this case, compared to the spin-coating method used for Ag-FTO in Figure 4.25, and (2) the impact of 3-MPA, possibly due to its refractive index effect [143]. Further, the washing effect of buffer used as a solvent of PSI on Ag-MPA should also be considered, similar to what was described in section 4.5.2. Clearly, PSI solution deposited on on (Ag-MPA)-FTO makes the brownish color of (Ag-MPA)-FTO much less intensive which is reflected by lower absorption after deposition of PSI on (Ag-MPA)-FTO seen in Figure 4.36. Further, an additive effect in the absorbance is seen as a presence of both PSI and AgNPs features in the blue curve (Figure 4.36). This shows that there is an attachment between PSI and AgNPs. However, there is no clear change in the absorption spectrum indicating any strong interaction between PSI and AgNPs.

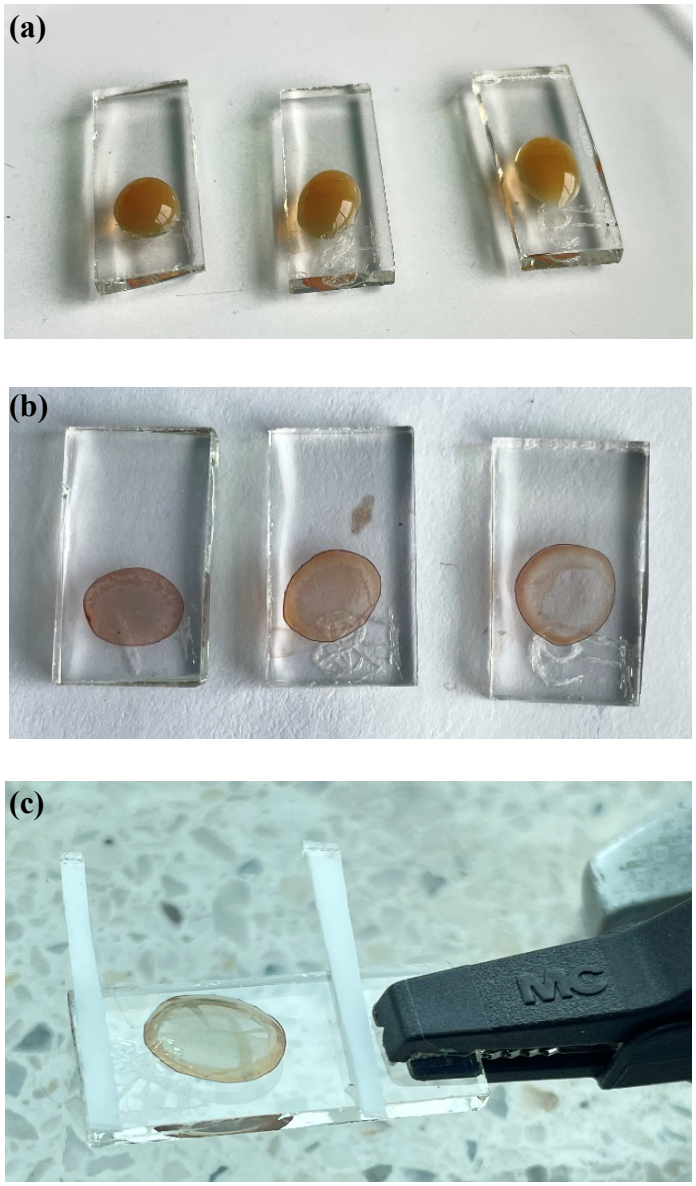

Figure 4.35 Photographic images of (Ag-MPA)-FTO sample **(a)** before sintering, **(b)** after sintering (refer to section 3.5.2.1) and **(c)** a droplet of PSI solution on the (Ag-MPA)-FTO plate before electrodeposition.

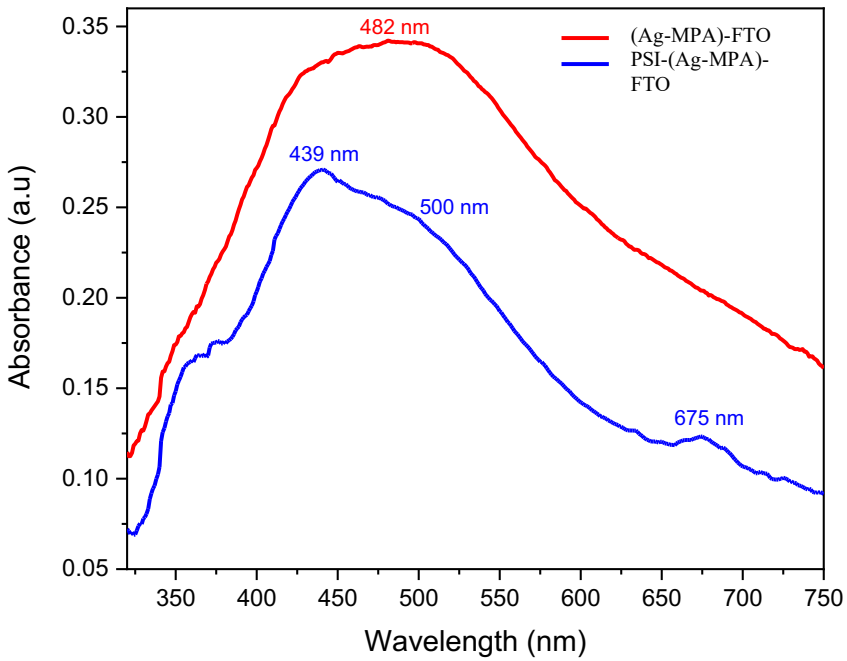

Figure 4.36 Comparison of steady-state absorption spectra of the (Ag-MPA)-FTO (red colored) and PSI-(Ag-MPA)-FTO plates (blue colored). The absorption spectra were measured only from the central area of the sample where PSI was deposited onto the (Ag-MPA)-FTO plate.

4.5.2.2.2 PSI electrodeposition on 3-MPA treated FTO coated with hydrophobic AgNPs – (PSI-Ag-(MPA-FTO))

In the second approach for an attempt to form an attachment between PSI and AgNPs using 3-MPA as a linker, the bare FTO was functionalized with 3-MPA (MPA-FTO) before spin coating with hydrophobic AgNPs followed by electrodeposition of PSI. The resulting plate is labeled PSI-Ag-(MPA-FTO). Figure 4.37 presents the comparison between the spectrum obtained for the samples: MPA-FTO, Ag-(MPA-FTO), and PSI-Ag-(MPA-FTO). It is to be noted that the same piece of FTO was used following the exact sequence of sample preparation described above to obtain the final sample, PSI-Ag-(MPA-FTO).

The spectra of FTO immersed in a 3-MPA solution (MPA-FTO) were measured every hour for 5 hours and then after a 24-hour period. Each spectrum of MPA-FTO maintained a similar shape, with absorbance peaks at 390 nm and 498 nm.

In the spectrum of Ag-(MPA-FTO) (red curve), a surface plasmon resonance (SPR) peak appeared at 421 nm with a broad shoulder at 512 nm. Compared to the Ag-FTO spectrum with a peak at 400 nm and 485 nm (orange curve in Figure 4.25), both the peaks in Ag-(MPA-FTO) spectrum in Figure 4.37 has red-shifted to 421nm and 512 nm, respectively. Interestingly, the spectrum of Ag-(MPA-FTO) is significantly different from that of (Ag-MPA)-FTO shown in Figure 4.36 (red curve).

The spectrum for PSI-Ag-(MPA-FTO) (black curve) exhibited more than three-fold increase in absorbance compared to Ag-(MPA-FTO). It displayed the characteristic SPR peak at 440 nm, attributed to AgNPs, and an absorption band at 676 nm, corresponding to the Qy band of

chlorophyll a. However, the peak at 512 nm observed in the Ag-MPA-FTO spectrum (red curve) almost disappeared in the PSI-Ag-(MPA-FTO) spectrum.

Notably, negative absorbance was observed in each curve. We do not have a good explanation for this observation. However, the resulting negative absorbance has been reproducible in the case of (MPA-FTO) used as a substrate.

The strong increase of absorbance in the blue region after deposition of PSI was very promising (Figure 4.37). However, the experiment repeated under same conditions did not reproduce similar results. Hence, we did not proceed further with it.

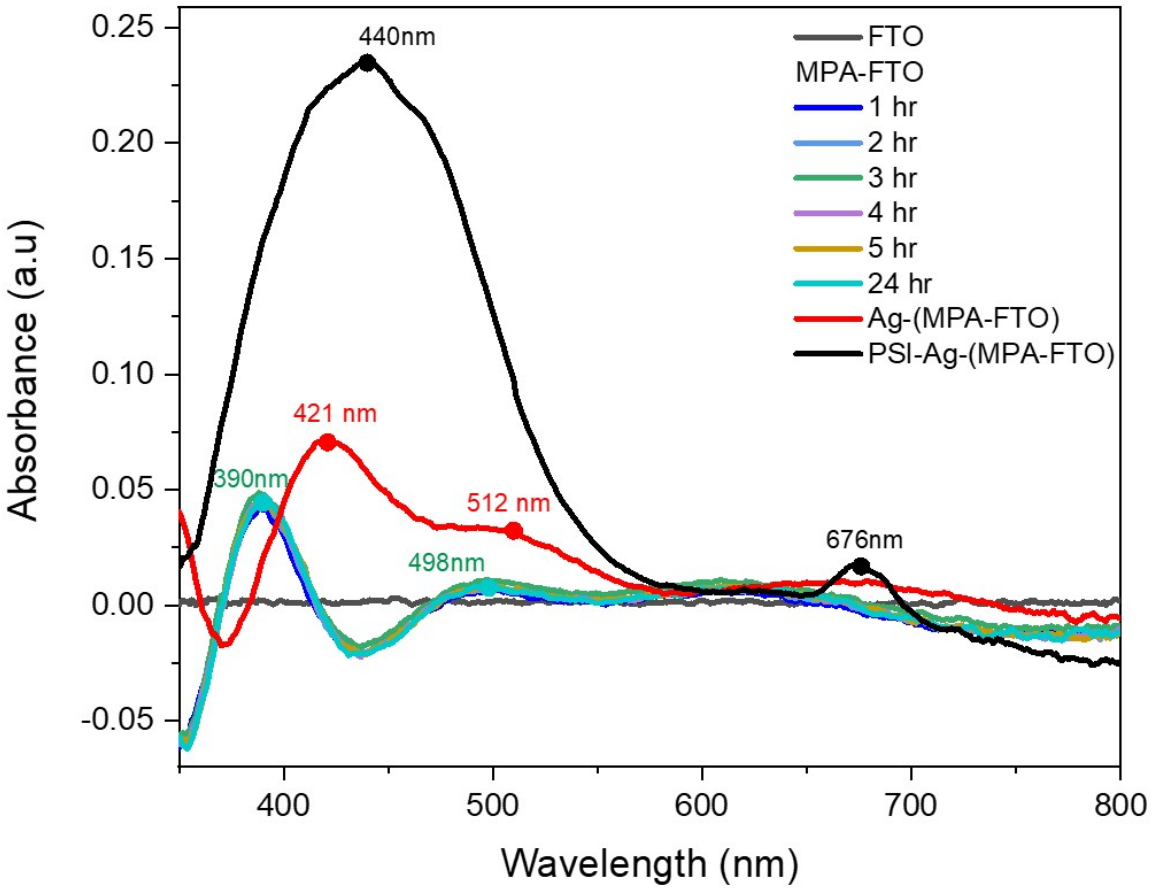

Figure 4.37 Absorption spectra of MPA-FTO (light blue "24 hr"), AgNPs spin-coated on MPA-FTO (red), PSI electrodeposited on Ag-(MPA-FTO) (black).

4.5.2.2.3 PSI electrodeposition on 3-MPA treated Ag-FTO substrates – (PSI-MPA-(Ag-FTO))

In the third approach for an attempt to form an attachment between PSI and AgNPs using 3-MPA as a linker, the Ag-FTO was functionalized with 3-MPA labelled as MPA-(Ag-FTO) followed by electrodeposition of PSI labelled as PSI-MPA-(Ag-FTO). Figure 4.38 presents the comparison of the spectra obtained for the samples: 1) Ag-FTO, 2) MPA-(Ag-FTO), and 3) PSI-MPA-(Ag-FTO). It is to be noted that the same piece of FTO was used following the exact sequence of sample preparation described above to obtain the final sample, PSI-MPA-(Ag-FTO).

The spectra of Ag-FTO (red curve) shows a broad peak at 454 nm attributed to SPR of AgNPs. Compared to the Ag-FTO spectrum (with Ag-FTO prepared in the same way) with a peak at 485 nm (orange curve) in Figure 4.25, the Ag-FTO spectrum in Figure 4.38 is broader, and the peak shows a blue-shift of about 30 nm. Additionally, the peak at 400 nm seen in the Ag-FTO spectrum shown in Figure 4.25 is absent in the Ag-FTO spectrum shown in Figure 4.38. The spectra of Ag-FTO immersed in a 3-MPA solution MPA-(Ag-FTO) were measured every hour for 5 hours and then after a 24-hour period maintained a characteristic shape with two distinct peaks at 416 nm and 490 nm reminiscent to those shown in Figure 4.25a. There was a small decrease in absorbance of MPA-(Ag-FTO) when measured right after immersion in 3-MPA solution. With time, more decrease was observed for the peak at 490 nm (arrow 2) than for the peak 416 nm (arrow 1). Further, after a total of 24 hours of being immersed in 3-MPA solution, there was a noticeable decrease observed in the absorbance of MPA-(Ag-FTO) (thick blue curve). There was also a blue-shift of ~14 nm from 416 nm to 402 nm and a small red-shifting of peak 490 nm to 498 nm. The negative absorbance was observed in each curve similarly as discussed above in section 4.5.2.2.2.

The spectrum for PSI-MPA-(Ag-FTO) (black colored) exhibited a similar shape as MPA-(Ag-FTO) curve (blue colored) with an overall decrease in the absorbance. It displayed the characteristic SPR peaks at 508 nm and 394 nm, attributed to AgNPs, and to the soret band of chlorophylls in PSI – 394 nm band, and an absorption band at 676 nm, attributed to the Qy band of chlorophyll a. All the results obtained did not show any significant features of interaction between PSI and AgNPs. Instead, prolong incubation of (Ag-FTO) plates (with hydrophobic AgNPs) in aqueous solution of 3-MPA and then deposition of a droplet of aqueous solution of PSI caused systematic washing of AgNPs out from the surface of FTO, as evidenced by the decreasing absorption.

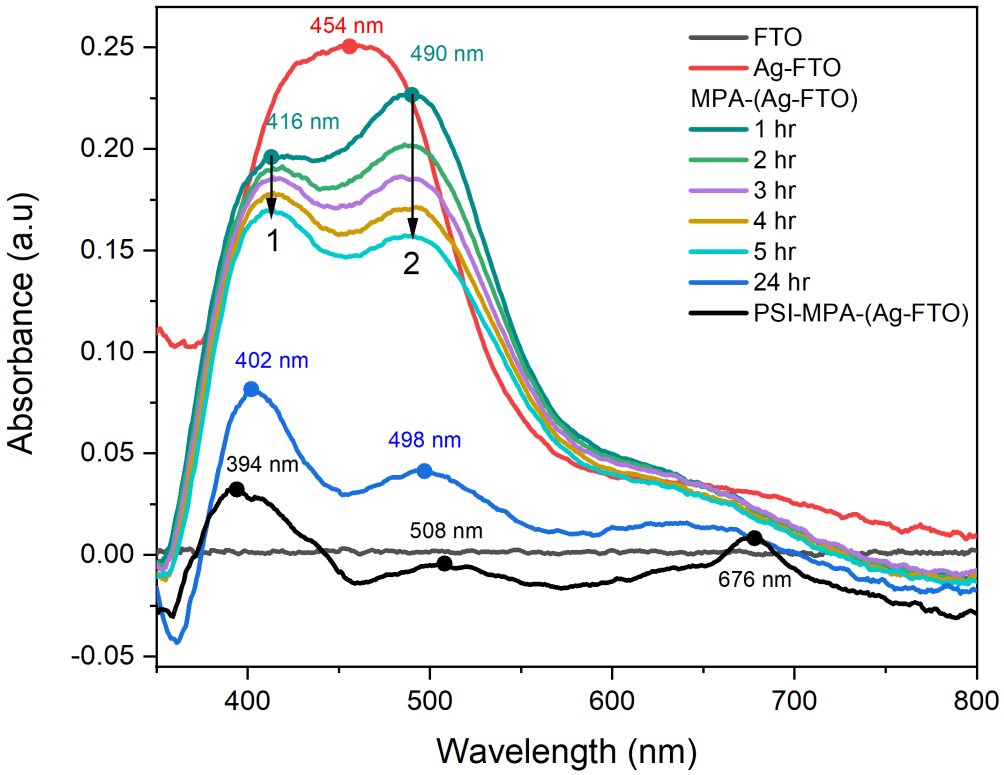

Figure 4.38 Absorption spectra of Ag-FTO (red), Ag-FTO immersed in 3-MPA solution: MPA-(Ag-FTO) (blue), PSI electrodeposited on MPA-(Ag-FTO) (black).

All the procedures performed using 3-MPA as a linker to facilitate the attachment between PSI and AgNPs did not give steady-state absorption spectra clearly showing interaction between PSI and AgNPs.

Chapter 5: Conclusion

5.1 Conclusions

This dissertation studied 1) the electron transfer dynamics to find the reasons for the low efficiency of photovoltaic systems containing Photosystem I and 2) various methods to improve the low efficiency of biophotovoltaic systems containing PSI by using the surface plasmon resonance of AgNPs.

PSI complexes isolated from different species were placed into two artificial systems: an aqueous solution and thin layers electrodeposited on fluorine-doped tin oxide (FTO) glass. When incorporating the isolated PSI into an artificial system, two issues are of particular importance in order to utilize their full functionality.

(a) To which extent the natural ET properties are preserved inside the PSI complex and
(b) What is the efficiency of coupling the donor and acceptor sides of the PSI with artificial electron mediators.

In order to assess these two issues, we studied and compared the results of the decay kinetics of the oxidized primary donor P^+ using transient absorption measurements (in both artificial systems) and the photocurrent for the electrochemical system containing PSI-based electrode at a range of electric potentials applied to the working electrode and at different compositions of artificial mediators. Time-resolved absorption spectroscopy results demonstrated the following observations:

1. The fraction of proteins able to perform charge separation was 100% in solution and it decreased to 10–35% after their deposition on FTO, depending on the potential applied and the concentration of the mediators
2. The efficiency of internal charge recombination in PSI proteins which showed charge separation was about 98%
3. Consequently, an ability to expel the electron outside PSI was observed only in a fraction of 2% of PSI proteins showing full charge separation.
4. Internal quantum efficiency (IQE) of photocurrent generation in PSI-FTO electrodes did not exceed ~0.5%.

Apparently, the limitation in IQE could be due to due to: (1) enhanced charge recombination reactions inside PSI when deposited on FTO, (2) poor electronic coupling between PSI particles and both FTO and electrolyte, and (3) short-circuiting *i.e.* dissipative ET from acceptor side of one PSI complex to the donor side of another one.

In order to increase the photovoltaic activity of the PSI-based electrodes, we utilized the surface plasmon resonance (SPR) of silver nanoparticles (AgNPs). The idea was to use the strong local field enhancement around the AgNPs that can increase the absorbance of PSI by acting as an antenna effectively storing the incident energy in the localized surface plasmon mode. For this purpose, uniform hydrophobic AgNPs were fabricated and characterized using various spectroscopy and microscopy techniques. To study the interaction between the PSI and AgNPs, in some experiments, the AgNPs were dispersed in water. Hence, the hydrophobic AgNPs were transformed into hydrophilic ones coated with different detergents (pluronic F127 and P123, and β-DM).

Among these, AgNPs-F127 exhibited the highest stability and were used for PSI-AgNPs complex formation in solution as well as in thin films. However, steady-state absorption and fluorescence measurements did not indicate any interaction between PSI derived from *C. merolae* and AgNPs-F127 in solution.

Next, the PSI particles from *Synechocystis* sp. PCC 6803 immobilized on hydrophobic Ag-FTO substrates (PSI-(Ag-FTO)) were fabricated and analyzed using ultrafast transient absorption spectroscopy. A systematic comparison of normalized decay associated spectra (DAS) obtained from the fits of the data for the PSI-(Ag-FTO) and Ag-FTO in the blue part of the spectrum (475-630 nm), showed some differences in the spectral characteristics and lifetimes. Ag-FTO showed a shorter-lived signal at 522 nm with a 12 ps lifetime. Whereas, for PSI-(Ag-FTO), a broad band was observed with flat maximum at ~546 nm with a lifetime of ~21 ps. This broadening and red-shift of 24 nm as well as lifetime extension may be interpreted as an increased absorption in the 500-600 nm region caused by the interaction between PSI and AgNPs. Further, the decay kinetics at 546 nm at the AgNPs region and at 686 nm for PSI were similar to each other. This observation further supports the view that the enhanced absorption in the AgNPs region supports the antenna function of AgNPs for PSI. A separate global analysis in the red part of the spectrum did not reveal significant effect of the interaction between PSI and AgNPs on the excitation dynamics of PSI. The kinetics at Qy band maximum at 686 nm were rather similar for PSI-FTO and PSI-(Ag-FTO) samples. This observation suggests that the rate of decay of the excited state in PSI is not affected by the proximity of AgNPs. Comparing the results of photocurrent measurements for PSI-FTO and PSI immobilized on Ag-FTO showed that the layer of silver nanoparticles did not improve the photovoltaic output probably due to some additional effects.

After exploring various methods to facilitate interaction between PSI and AgNPs, we also tested 3-mercaptopropionic acid (3-MPA) as a linker. It has been suggested in literature that the alkyl chain in 3-MPA resembles the environment of a biological membrane i.e., the lipid bilayers containing hydrocarbon chains) which is expected to help in the interaction with PSI protein without causing its denaturation. However, all the procedures performed using 3-MPA as a linker to facilitate the attachment between PSI and AgNPs did not give steady-state absorption spectra clearly showing interaction between PSI and AgNPs.

5.2 Limitations of the study and future recommendations

Despite the valuable insights gained from this study, there are limitations that must be acknowledged. One of the challenges encountered during the study was the difficulty in successfully implementing the same phase transfer protocol for detergents (pluronic P123 and β-DM) other than pluronic F127. It still remains an open question as why this approach failed for other detergents and could influence the reproducibility of the method. While hydrophobic AgNPs were stable in solution as well as on FTO substrate, it should be noted that hydrophilic AgNPs were less stable producing stable hydrophilic AgNP layers on FTO remains a significant challenge, as these nanoparticles tend to wash away when exposed to electrolyte solutions during photocurrent measurements. Future work should explore improved strategies for stabilizing hydrophilic AgNP layers to ensure their long-term adhesion and functionality within photoelectrochemical cells. Further, phase transfer protocols need optimization for detergents other than pluronic F127. Other alternatives to 3-mercaptopropionic acid (3-MPA) should be tested for attachment between PSI and AgNPs. Furthermore, integrating PSI with nanomaterials or other metal nanoparticles may enhance charge transport efficiency.

Appendix

Models for penetration effects of electrode potential and redox mediators

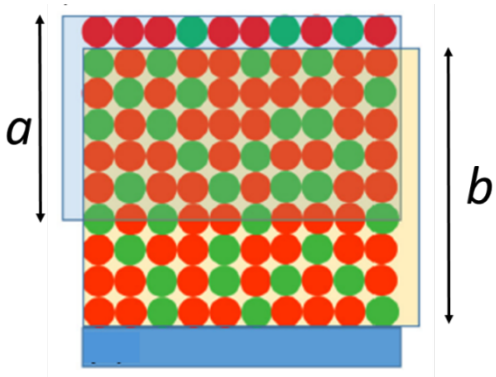

Figure A1. Model 2 for penetration effects of electrode potential and redox mediators.

Figure 4.13 presents two models of penetration effects of electrode potential and redox mediators. Model 1 (Figure 4.13a) assumes additivity of these effects and contradicts experimental observations. Model 2 (Figure 13b) assumes that the regions of penetrations of electric potential and mediators largely overlaps. It also assumes that: (1) the distribution of permanently inactive PSI particles is homogenous across the thickness of PSI layer and that 65% of PSI particles are permanently inactive; (2) low potential alone is able to reactivate those PSI particles which are not permanently inactive (this fraction amounts to 35%) and the potential may penetrate only to the limited thickness of PSI layer – denoted with letter *b* in Figure A1; (3) similarly, redox mediators alone are able to reactivate those PSI particles which are not permanently inactive and the mediators may also penetrate only to the limited thickness of PSI layer – denoted with letter *a* in Figure A1. Consequently, thicknesses *a* and *b* may be estimated from the following formulas:

$$a = \frac{\Delta A_{0,\mathrm{rel}}(\mathrm{med})}{\Delta A_{0,\mathrm{rel}}(\mathrm{tot})}, \qquad \text{(Eq. A1)}$$

$$b = \frac{\Delta A_{0,\mathrm{rel}}(\mathrm{pot})}{\Delta A_{0,\mathrm{rel}}(\mathrm{tot})}, \qquad \text{(Eq. A2)}$$

where $\Delta A_{0,\mathrm{rel}}(\mathrm{med})$ is the initial relative photobleaching signal in the presence of mediators only, $\Delta A_{0,\mathrm{rel}}(\mathrm{pot})$ is the initial relative photobleaching signal in the presence of low potential (-0.18 V) only, and $\Delta A_{0,\mathrm{rel}}(\mathrm{tot})$ is the initial relative photobleaching signal in the presence of both mediators and low potential. As can be seen in Table 4.3, these values amount to 23%, 31% and 35%, respectively.

References

1. Szewczyk, S., Białek, R., Burdziński, G., & Gibasiewicz, K. (2020). Photovoltaic activity of electrodes based on intact photosystem I electrodeposited on bare conducting glass. Photosynthesis Research, 144, 1–12.

2. Ciesielski, P. N., Faulkner, C. J., Irwin, M. T., Gregory, J. M., Tolk, N. H., Cliffel, D. E., & Jennings, G. K. (2010). Enhanced photocurrent production by Photosystem I multilayer assemblies. Advanced Functional Materials, 20, 4048–4054.

3. Fromme, P. & Grotjohann, I. (2008). Photosynthetic Protein Complexes: A Structural Approach. Wiley-Blackwell.

4. Jordan, P., Fromme, P., Witt, H. T., Klukas, O., Saenger, W., & Krauss, N. (2001). Three-dimensional structure of cyanobacterial Photosystem I at 2.5A resolution. Nature, 411, 909–917.

5. Brettel, K., & Leibl, W. (2001). Electron transfer in Photosystem I. Biochimica et Biophysica Acta (BBA) - Bioenergetics, 1507, 100–114.

6. Dulkeith, E., Morteani, A., Niedereichholz, T., Klar, T., Feldmann, J., Levi, S., Van Veggel, F., Reinhoudt, D., Möller, M., & Gittins, D. (2002). Fluorescence Quenching of Dye Molecules Near Gold Nanoparticles: Radiative and Nonradiative Effects. Physical Reviews Letters, 203002, 89.

7. Mackowski, S., Wormke, S., Maier, A. J., Brotosudarmo, T. H. P., Harutyunyan, H., Hartschuh, A., Govorov, A. O., Scheer, H., & Brauchle, C. (2008). Metal-Enhanced Fluorescence of Chlorophylls in Single Light-Harvesting Complexes. Nano letters, 8(2), 558–564.

8. Czechowski, N., Lokstein, H., Kowalska, D., Ashraf, K., Cogdell, R. J., & Mackowski, S. (2014). Large plasmonic fluorescence enhancement of cyanobacterial photosystem I coupled to silver island films. Applied Physics Letters, 105(4).

9. Teodor, A. H., & Bruce, B. D. (2020). Putting Photosystem I to work: Truly green energy. Trends in Biotechnology, 38(12), 1329–1342.

10. Ng, F. L., Phang, S. M., Periasamy, V., Yunus, K., & Fisher, A. C. (2014). Evaluation of algal biofilms on indium tin oxide (ITO) for use in biophotovoltaic platforms based on the photosynthetic performance, PLOS ONE, 9 (5).

11. Blankenship R.E. (2002). Molecular Mechanisms of Photosynthesis. Oxford, UK: Blackwell Science Ltd.

12. Szewczyk, S., Giera, W., D'Haene, S., van Grondelle, R., & Gibasiewicz, K. (2017). Comparison of excitation energy transfer in cyanobacterial Photosystem I in solution and immobilized on conducting glass. Photosynthesis Research, 132(2), 111–126.

13. Tan, S., Cunningham, F. X. Jr., & Gantt E. (1997). LhcaR1 of the red alga Porphyridium cruentum encodes a polypeptide of the LHCI complex with seven potential chlorophyll a-binding residues that are conserved in most LHCs. Plant Molecular Biology, 33, 157-167.

14. Antoshvili, A., Caspy, I., Hippler, M., Nelson, N. (2018). Structure and function of photosystem I in *Cyanidioschyzon melorae.* Photosynthesis Research, 139, 499-508.

15. Merchant, S.S., Prochnik, S. E., Vallon, O., Harris, E. H., Karpowicz, S. J., Witman, G. B., Terry, A., Salamov, A., Fritz-Laylin, L. K., Maréchal-Drouard, L., Marshall, W. F., Qu, L. H., Nelson, D. R., Sanderfoot, A. A., Spalding, M. H., Kapitonov, V. V., Ren, Q., Ferris, P., Lindquist, P., Shapiro, H., Lucas, S. M., Grimwood, J., Schmutz, J., Grigoriev, I. V., Rokhsar, D. S., Grossman, A. R. (2007). The Chlamydomonas Genome Reveals the Evolution of Key Animal and Plant Functions. Science, 318, 245.

16. Elrad, D. & Grossman, A. R. (2004). A genome's-eye view of the light-harvesting polypeptides of *Chlamydomonas reinhardtii*. Current Genetics, 45, 61-75.

17. Busch, A. & Hippler, M. (2011). The structure and function of eukaryotic photosystem I. Biochemica et Biophysica Acta (BBA) - Bioenergetics, 1807, 864-877.

18. Saenger, W., Jordan, P., & Krauß, N. (2002). The assembly of protein subunits and cofactors in photosystem I. Current Opinion in Structural Biology, 12(2), 244-254.

19. https://en.wikipedia.org/wiki/Photosystem_I (2024, April 4).

20. Kurashov, V., Gorka, M., Milanovsky, G. E., Johnson, T. W., Cherepanov, D. A., Semenov, A. Y., & Golbeck, J. H. (2018). Critical evaluation of electron transfer kinetics in P700–FA/FB, P700–FX, and P700–A1 Photosystem I core complexes in liquid and in trehalose glass. Biochimica et Biophysica Acta (BBA) - Bioenergetics, 1859, 1288–1301.

21. Shukla, A. K., Sudhakar, K., & Baredar, P. (2014). A comprehensive review on design of building integrated photovoltaic system. Energy and Buildings (ENB), 128, 99-110.

22. Kim, J., Hong, Z., Li, G., Song, T. B., Chey, J., Lee, Y. S., You, J., Chen, C. C., Sadana, D. K., & Yang, Y. (2015). 10.5% efficient polymer and amorphous silicon hybrid tandem photovoltaic cell. Nature Communications, 6, 6391.

23. Essig, S., Allebé, C., Remo, T., Geisz, J. F., Steiner, M. A., Horowitz, K., Barraud, L., Ward, J. S., Schnabel, M., Descoeudres, A., Young, D. L., Woodhouse, M., Despeisse, M., Ballif, C., & Tamboli, A. (2017). Raising the one-sun conversion efficiency of III–V/Si solar cells to 32.8% for two junctions and 35.9% for three junctions. Nature Energy, 2, 17144.

24. Qiu, L., He, S., Liu, Z., Ono, L. K., Son, D. Y., Liu, Y., Tong, G., & Qi, Y. (2020). Rapid Hybrid Chemical Vapor Deposition for Efficient and Hysteresis-Free Perovskite Solar Modules with Operation Lifetime Exceeding 800 Hours. Journal of Materials Chemistry A, 8, 23404-23412.

25. Chen, P., Wang, Z., Wang, S., Lyu, M., Hao, M., Ghasemi, M., Xiao, M., Yun, J. H., Bai, Y., & Wang, L. (2020). Luminescent europium-doped titania for efficiency and UV-stability enhancement of planar perovskite solar cells. Nano Energy, 69, 104392.

26. Białek, K. P., Drushliak, V., Coy, E., Załeski, K., Flach, J., Idígoras, J., Bernal, L. C., Hagfeldt, A., Anta, J. A., & Ziołek, M. (2020). Understanding the Interfaces between Triple-Cation Perovskite and Electron or Hole Transporting Material. Applied Materials and Interfaces, 12, 30399-30410.

27. Hagfeldt, A., Boschloo, G., Sun, L., Kloo, L., & Pettersson, H. (2010). Dye-Sensitized Solar Cells. Chemical Reviews, 110, 6595-6663.

28. Feldt, S. M., Gibson, E. A., Gabrielsson, E., Sun, L., Boschloo, G., & Hagfeldt, A. (2010). Design of Organic Dyes and Cobalt Polypyridine Redox Mediators for High-Efficiency Dye-Sensitized Solar Cells. Journal of American Chemical Society, 132, 16714-16724.

29. Cavinato, L. M., Fresta, E., Ferrara, S., & Costa, R. D. (2021). Merging Biology and Photovoltaics: How Nature Helps Sun-Catching. Advanced Energy Materials, 11(43), 2100520.

30. Yum, J. H., Baranoff, E., Wenger, S., Nazeeruddin, Md. K., & Gratzel, M. (2011). Panchromatic engineering for dye-sensitized solar cells. Energy and Environmental Science, 4, 842.

31. Bella, F., Gerbaldi, C., Barolob, C., & Gratzel, M. (2015). Aqueous dye-sensitized solar cells. Chemical Society Reviews, 44, 3431-3473.

32. McConnell, I., Li, G., & Brudvig, G. W. (2010). Energy Conversion in Natural and Artificial Photosynthesis. Chemistry and Biology Review, 17(5), 434-447.

33. National Renewable Energy Laboratory. Best Research-Cell Efficiency Chart. 2020. URL: https://www.nrel.gov/pv/cell-efficiency.html (Accessed 21 May 2024).

34. Haehnel, W., Heupel, A., & Hengstermann, D. (1978). Investigations on a Galvanic Cell Driven by Photosynthetic Electron Transport. Z. Naturforsch. 33c, 392-401.

35. Janzen, A. F. (1980). Photoelectrochemical conversion using reaction-centre electrodes. Nature, 286, 584-585.

36. LeBlanc, G., Chen, G., Gizzie, E. A., Jennings, G. K., & Cliffel, D. E. (2012). Enhanced Photocurrents of Photosystem I Films on p-Doped Silicon. Advanced Materials, 24(44), 5959-5962.

37. Kondo, M., Amano, M., Joke, T., Ishigure, S., Noji, T., Dewa, T., Amao, Y., Nango, M. (2014). Immobilization of photosystem I or II complexes on electrodes for preparation of photoenergy -conversion devices. Research on Chemical Intermediates, 40, 3287-3293.

38. Ravi, S. K. & Tan, S. C. (2015). Progress and Perspectives in Exploiting Photosynthetic Biomolecules for Solar Energy Harnessing. Energy and Environmental Science, 8, 2551-2573.

39. Shah, V. B., Henson, W. R., Chadha, T. S., Lakin, G., Liu, H., Blankenship, R. E., & Biswas, P. (2015). Linker-Free Deposition and Adhesion of Photosystem I onto Nanostructured TiO_2 for Biohybrid Photo-electrochemical Cells. Langmuir, 31, 1675-1682.

40. Plumeré, N., Nowaczyk, M.M. (2016). Biophotoelectrochemistry of Photosynthetic Proteins. Advances in Biochemical Engineering/Biotechnology, 158, 111-136.

41. Kiliszek, M., Harputlu, E., Szalkowski, M., Kowalska, D., Unlu, C. G., Haniewicz, P., Abram, M., Wiwatowski, K., Jönsson, J. N., Maćkowski, S., Ocakoglu, K., & Kargul, J. (2018). Orientation of photosystem I on graphene through cytochrome c_{553} leads to improvement in photocurrent generation. Journal of Materials Chemistry A, 6, 18615-18626.

42. Wey, L. T., Bombelli, P., Chen, X., Lawrence, J. M., Rabideau, C. M., Rowden, S. J. L., Zhang, J. Z., & Howe, C. J. (2019). The Development of Biophotovoltaic Systems for Power Generation and Biological Analysis. Chemistry Europe, 6, 5375-5386.

43. Than, L., Wolfe, K. D., Cliffel, D. E., & Jennings, G. K. (2023). Drop-casted Photosystem I/cytochrome c multilayer films for biohybrid solar energy conversion. Photosynthesis Research, 155, 299-308.

44. Iwuchukwu, I. J., Vaughn, M., Myers, N., O'Neill, H., Frymier, P., & Bruce, B. D. (2009). Self-organized photosynthetic nanoparticle for cell-free hydrogen production. Nature Nanotechnology, 5, 73-79.

45. You, J., Arakawa, T., Munaoka, T., Akiyama, T., Takahashi, Y., & Yamada, S. (2011). Silver-Nanoparticle-Assisted Photocurrent Generation in Polythiophene–Fullerene Thin Films. Japanese Journal of Applied Physics, 50.

46. Niroomand, H., Pamu, R., Mukherjee, D., Khomami, B. (2018). Tuning the photocurrent generations from photosystem I assembled in tailored biotic-abiotic interfaces. MRS Communications 8, 823–829.

47. Torres, R., Diz, V. E., & Lagorio, M. G. (2018). Effects of gold nanoparticles on the photophysical and photosynthetic parameters of leaves and chloroplasts. Photochemical and Photobiological Sciences, 17, 505-516.

48. Antonacci, A., & Scognamiglio, V. (2019). Photosynthesis-based hybrid nanostructures: Electrochemical sensors and photovoltaic cells as case studies. Trends in Analytical Chemistry, 115, 100-109.

49. Kelly, K. L., Coronado, E., Zhao, L. L. & Schatz, G. C. (2002). The Optical Properties of Metal Nanoparticles: The Influence of Size, Shape, and Dielectric Environment. Journal of Physical Chemistry B, 107, 668-677.

50. Govorov, A. O., & Carmeli, I. (2007). Hybrid Structures Composed of Photosynthetic System and Metal Nanoparticles: Plasmon Enhancement Effect. Nano Letters, 7, 620-625.

51. Carmeli, I., Lieberman, I., Kraversky, L., Fan, Z., Govorov, A. O., Markovich, G., & Richter, S. (2010). Broad band enhancement of light absorption in Photosystem I by metal nanoparticle antennas. Nano letters, 10, 2069-2074.

52. Hussels, M., Nieder, J. B., Elsässer, C., & Brecht, M. (2012). Interactions of Photosystem I with Plasmonic nanostructures. Acta Physica Polonica A, 122, 269-274.

53. Kim, I., Bender, S. L., Hranisavljevic, J., Utschig, L. M., Huang, L., Wiederrecht, G. P., & Tiede, D. M. (2011). Metal Nanoparticle Plasmon-Enhanced Light-Harvesting in a Photosystem I Thin Film. Nano Letters, 11, 3091-3098.

54. Bigot, J. Y., Halte, V., Merle, J. C., & Daunois, A. (2000). Electron dynamics in metallic nanoparticles. Chemical Physics, 251, 181-203.

55. Gaál, A., Bugár, I., Capek, I., Fialová, L., Pálszegi, T., Szöcs, V., Satka, A., & Uherek, F. (2009). Femtosecond Multicolor Transient Absorption Spectroscopy of Colloidal Silver Nanoparticles. Laser Spectroscopy, 19, 961-968.

56. Warth, A., Lange, J., Graener, H., & Seifert, G. (2011). Ultrafast Dynamics of Femtosecond Laser-Induced Shape Transformation of Silver Nanoparticles Embedded in Glass. The Journal of Physical Chemistry, 115, 23329-23337.

57. Kreibig, U., & Vollmer, M. (1995). Optical Properties of Metal Clusters. Springer Series in Materials Science.

58. Voloshin, R.A., Kreslavski, V.D., Zharmukhamedov, S.K., Bedbenov, V.S., Ramakrishna, S., Allakhverdiev, S.I. (2015). Photoelectrochemical cells based on photosynthetic systems: a review. Biofuel Research Journal, 6, 227-235.

59. Vassiliev, I. R., Jung, Y. S., Mamedov, M. D., Semenov, A. Y., & Golbeck, J. H. (1997). Near-IR Absorbance Changes and Electrogenic Reactions in the Microsecond-to-Second Time Domain in Photosystem I. Biophysical Journal, 72, 301-315.

60. Mershin, A., Matsumoto, K., Kaiser, L., Yu, D., Vaughn, M., Nazeeruddin, Md. K., Bruce, B. D., Graetzel, M., & Zhang, S. (2012). Self-assembled photosystem-I biophotovoltaics on nanostructured TiO_2 and ZnO. Scientific Reports, 2, 234.

61. Lau, N. S., Matsui, M., & and Abdullah, A. Al-A. (2015). Cyanobacteria: Photoautotrophic Microbial Factories for the Sustainable Synthesis of Industrial Products. BioMed Research International, 2015, 1-9.

62. Gibasiewicz, K., Ramesh, V. M., Lin, S., Woodbury, N. W., & Webber, A. N. (2002). Excitation Dynamics in Eukaryotic PS I from Chlamydomonas reinhardtii CC 2696 at 10 K. Direct Detection of the Reaction Center Exciton States. Journal of Physical Chemistry B, 106, 6322-6330.

63. Muller, M. G., Niklas, J., Lubitz, W., & Holzwarth, A. R. (2003). Ultrafast Transient Absorption Studies on Photosystem I Reaction Centers from Chlamydomonas reinhardtii. 1. A New Interpretation of the Energy Trapping and Early Electron Transfer Steps in Photosystem I. Biophysical Journal, 85, 3899-3922.

64. Ramesh, V. M., Gibasiewicz, K., Lin, S., Bingham, S. E., & Webber, A. N. (2004). Bidirectional electron transfer in Photo-system I: Accumulation of A_0- in A-side or B-side mutants of the axial ligand to chlorophyll A_0. Biochemistry, 43(5), 1369–1375

65. Haniewicz, P., Abram, M., Nosek, L., Kirkpatrick, J., El-Mohsnawy, E., Olmos, J. D. J., Kouril, R., & Kargul, J. M. (2018). Molecular Mechanisms of Photoadaptation of Photosystem I Supercomplex from an Evolutionary Cyanobacterial/Algal Intermediate. Plant Physiology, 176, 1433-1451.

66. Longatte, G., Rappaport, F., Wollman, F.-A. A., Guille-Collignon, M., & Lemaître, F. (2017). Electrochemical Harvesting of Photosynthetic Electrons from Unicellular Algae Population at the Preparative Scale by Using 2,6-Dichlorobenzoquinone. Electrochimica Acta, 236, 337–342.

67. Hasan, K., Bekir Yildiz, H., Sperling, E., Conghaile, P. Ó., Packer, M. A., Leech, D., Hägerhäll, C. & Gorton, L. (2014). Photo-electrochemical communication between cyanobacteria (Leptolyngbia sp.) and osmium redox polymer modified electrodes. Physical Chemistry Chemical Physics, 16, 24676–24680.

68. McCormick, A. J., Bombelli, P., Bradley, R. W., Thorne, R., Wenzel, T., & Howe, C. J. (2015) Biophotovoltaics: oxygenic photosynthetic organisms in the world of bioelectrochemical systems. Energy & Environmental Science, 8, 1092–1109.

69. Kothe, T., Poller, S., Zhao, F., Fortgang, P., Rogner, M., Schuhmann, W., Plumere, N. (2014). Engineered electron-transfer chain in photosystem 1 based photocathodes outperforms electron-transfer rates in natural photosynthesis. Chemistry, 20, 11029–11034.

70. Stieger, K.R., Feifel, S.C., Lokstein, H., Hejazi, M., Zouni, A., Lisdat, F. (2016). Biohybrid architectures for efficient light-to-current conversion based on photosystem I within scalable 3D mesoporous electrodes. Journal of Materials Chemistry A, 4, 17009–17017.

71. Csiki, R., Drieschner, S., Lyuleeva, A., Cattani-Scholz, A., Stutzmann, M., Garrido, J.A. (2018). Photocurrent generation of biohybrid systems based on bacterial reaction centers and graphene electrodes. Diamond and Related Materials, 89, 286–292.

72. Das, R., Kiley, P. J., Segal, M., Norville, J., Amy Yu, A., Wang, L., Trammell, S. A., Reddick, L. E., Kumar, R., Stellacci, F., Lebedev, N., Schnur, J., Bruce, B. D., Zhang, S., & Baldo, M. (2004). Integration of Photosynthetic Protein Molecular Complexes in Solid-State Electronic Devices. Nano Letters, 4, 1079-1083.

73. Gunther, D., LeBlanc, G., Prasai, D., Zhang, J. R., Cliffel, D. E., Bolotin, K. I., & Jennings, G. K. (2013). Photosystem I on Graphene as a Highly Transparent, Photoactive Electrode. Langmuir, 29, 4177-4180.

74. Dervishogullari, D., Gizzie, E.A., Jennings, G.K., & Cliffel, D.E. (2018). Polyviologen as electron transport material in photosystem I-based biophotovoltaic cells. Langmuir, 34, 15658–15664.

75. Darby, E., LeBlanc, G., Gizzie, E.A., Winter, K.M., Jennings, G.K., & Cliffel, D.E. (2014). Photoactive films of photosystem I on transparent reduced graphene oxide electrodes. Langmuir, 30, 8990–8994.

76. Gizzie, E.A., Niezgoda, J.S., Robinson, M.T., Harris, A.G., Jennings, G.K., Rosenthal, S.J., Cliffel, D.E. (2015). Photosystem I-polyaniline/TiO2 solid-state solar cells: Simple devices for biohybrid solar energy conversion. Energy & Environmental Science, 8, 3572–3576.

77. Beam, J.C., LeBlanc, G., Gizzie, E.A., Ivanov, B.L., Needell, D.R., Shearer, M.J., Jennings, G.K., Lukehart, C.M., & Cliffel, D.E. (2015). Construction of a semiconductor-biological interface for solar energy conversion: P-doped silicon/photosystem I/Zinc oxide. Langmuir, 31, 10002–10007.

78. Kazemzadeh, S., Riazi, G., & Ajeian, R. (2017). Novel approach of biophotovoltaic solid state solar cells based on a multilayer of PS1 complexes as an active layer. ACS Sustainable Chemical Engineering, 5, 9836–9840.

79. Feifel, S.C., Stieger, K.R., Lokstein, H., Lux, H., & Lisdat, F. (2015). High photocurrent generation by photosystem I on artificial interfaces composed of pi-system-modified graphene. Journal of Material Chemistry A, 3, 12188–12196.

80. Cadirci, B.H. (2018). An electricity production study by Rhodobacter sphaeroides. International Journal of Hydrogen Energy, 43, 18001–18006.

81. Ciesielski, P.N., Hijazi, F.M., Scott, A.M., Faulkner, C.J., Beard, L., Emmett, K., Rosenthal, S.J., Cliffel, D., & Jennings, G.K. (2010). Photosystem I—Based biohybrid photoelectrochemical cells. Bioresource Technology, 101, 3047–3053.

82. Sekar, N., & Ramasamy, R. P. (2015). Recent advances in photosynthetic energy conversion. Journal of Photochemistry and Photobiology C: Photochemistry Reviews, 22, 19–33.

83. Yang, S., Robinson, M. T., Mwambutsa, F., Cliffel, D. E., & Jennings, G. K. (2016). Effect of Cross-linking on the Performance and Stability of Photocatalytic Photosystem I Films. Electrochimica Acta, 222, 926-932.

84. Robinson, M.T., Cliffel, D.E., & Jennings, G.K. (2018). An electrochemical reaction-diffusion model of the photocatalytic effect of photosystem I multilayer films. Journal of Physical Chemistry B, 122, 117–125.

85. Stieger, K.R., Feifel, S.C., Lokstein, H., & Lisdat, F. (2014). Advanced unidirectional photocurrent generation via cytochrome c as reaction partner for directed assembly of photosystem I. Physical Chemistry Chemical Physics, 16, 15667–15674.

86. Ocakoglu, K., Krupnik, T., van den Bosch, B., Harputlu, E., Gullo, M.P., Olmos, J.D.J., Yildirimcan, S., Gupta, R.K., Yakuphanoglu, F., Barbieri, A., Reek, J. N. H., & Kargul, J. (2014). Photosystem I-based biophotovoltaics on nanostructured hematite. Advanced Functional Materials, 24, 7467–7477.

87. Ciesielski, P.N., Scott, A.M., Faulkner, C.J., Berron, B.J., Cliffel, D.E., & Jennings, G.K. (2008). Functionalized nanoporous gold leaf electrode films for the immobilization of photosystem I. ACS Nano, 2, 2465–2472.

88. LeBlanc, G., Gizzie, E., Yang, S., Cliffel, D.E., & Jennings, G.K. (2014). Photosystem I protein films at electrode surfaces for solar energy conversion. Langmuir, 30, 10990–11001.

89. Yamanoi, Y., Terasaki, N., Miyachi, M., Inoue, Y., & Nishihara, H. (2012). Enhanced photocurrent production by photosystem I with modified viologen derivatives. Thin Solid Films, 520, 5123–5127.

90. Bennett, T., Niroomand, H., Pamu, R., Ivanov, I., Mukherjee, D., & Khomami, B. (2016). Elucidating the role of methyl viologen as a scavenger of photoactivated electrons from photosystem I under aerobic and anaerobic conditions. Physical Chemistry Chemical Physics, 18, 8512–8521.

91. Baker, D.R., Simmerman, R.F., Sumner, J.J., Bruce, B.D., & Lundgren, C.A. (2014). Photoelectrochemistry of photosystem I bound in nafion. Langmuir, 30, 13650–13655.

92. Ciornii, D., Feifel, S.C., Hejazi, M., Kolsch, A., Lokstein, H., Zouni, A., & Lisdat, F. (2017). Construction of photobiocathodes using multi-walled carbon nanotubes and photosystem I. Physica Status Solidi A, 214, 1700017.

93. Ashraf, I., Konrad, A., Lokstein, H., Skandary, S., Metzger, M., Djouda, J. M., Maurer, T., Adam, P. M., Meixner, A. J. & Brecht, M. (2017). Temperature dependence of metal enhanced fluorescence of photosystem I from Thermosynechococcus elongatus. Royal Society of Chemistry, 9, 4196.

94. Jung, H., Gulis, G., Gupta, S., Redding, K., Gosztola, D.J., Wiederrecht, G.P., Stroscio, M.A., & Dutta, M. (2010). Optical and electrical measurement of energy transfer between nanocrystalline quantum dots and photosystem I. Journal of Physical Chemistry B, 114, 14544–14549.

95. Nieder, J. B., Bittl, R., & Brecht, M. (2010). Fluorescence Studies into the Effect of Plasmonic Interactions on Protein Function. Angewandte Chemie International Edition, 49, 10217-10220.

96. Olejnik, M., Krajnik, B., Kowalska, D., Lin, G., & Mackowski, S. (2013). Spectroscopic studies of plasmon coupling between photosynthetic complexes and metallic quantum dots. Journal of Physics.: Condened. Matter, 25**,** 19.

97. Czechowski, N., Lokstein, H., Kowalska, D., Ashraf, K., Cogdell, R. J., & Mackowski, S. (2014). Large plasmonic fluorescence enhancement of cyanobacterial photosystem I coupled to silver island films. Applied Physics Letters, 105(4).

98. Kaminska, I., Bohlen, J., Mackowski, S., Tinnefeld, P., & Acuna, G. P. (2018). Strong Plasmonic Enhancement of a Single Peridinin–Chlorophyll *a*–Protein Complex on DNA Origami-Based Optical Antennas. ACS Nano, 12(2), 1650–1655.

99. Kowalska, D., Szalkowski, M., Sulowska, K., Buczynska, D., Niedziolka-Jonsson, J., Jonsson-Niedziolka, M., Kargul, J., Lokstein, H., & Mackowski, S. (2020). Silver Island Film for Enhancing Light Harvesting in Natural Photosynthetic Proteins. International. Journal of Molecular Sciences**,** 21(7), 2451.

100. Szalkowski, M., Harputlu, E., Kiliszek, M., Unlu, C. G., Maćkowski, S., Ocakoglu, K., Kargul, J., & Kowalska, D. (2020). Plasmonic enhancement of photocurrent generation in a photosystem I-based hybrid electrode. Journal of Materials Chemistry C, 8, 5807-5814.

101. Szalkowski, M., Kowalska, D., Olmos, J. D. J., Kargul, J., & Maćkowski, S. (2022). Improving Photostability of Photosystem I-Based Nanodevice by Plasmonic Interactions with Planar Silver Nanostructures. International Journal of Molecular Sciences, 23(6), 2976.

102. Szalkowski, M., Kiliszek, M., Harputlu, E., Izzo, M., Unlu, C. G., Mackowski, S., Ocakoglu, K., Kargul, J., & Kowalska, D. (2025). Bimodal functionality of highly conductive nanostructured silver film towards improved performance of photosystem I-based graphene photocathode, Bioelectrochemistry, 161, 108825.

103. Averitt, R. D., Westcott, S. L., & Halas, N. J. (1998). Ultrafast electron dynamics in gold nanoshells. Physical Review B, 58, 16.

104. Lehmann, J., Merschdorf, M., Pfeiffer, W., Thon, A., Voll, S., & Gerber, G. (2000). Surface Plasmon Dynamics in Silver Nanoparticles Studied by Femtosecond Time-Resolved Photoemission. Physical Review Letters, 85, 2921-2924.

105. Hodak, J. H., Henglein, A., & Hartland, G. V. (2000). Electron-phonon coupling dynamics in very small (between 2 and 8 nm diameter) Au nanoparticles. Journal of Chemical Physics, 112, 5942-5947.

106. Lysenko, S., Jimenez, J., Zhang, G., & Liu, H. (2006). Nonlinear Optical Dynamics of Glass-Embedded Silver Nanoparticles. Journal of Electronic Materials, 35, 1716-1721.

107. Gaál, A., Bugár, I., Capek, I., Polovková, J., Szőcs, V., Pálszegi, T., Šatka, A., Michalka, M. & Uherek, F. (2009). Picosecond Characteristics on Transient Absorption Spectra of Silver Nanoparticles. International Conference on Transparent Optical Networks, Ponta Delgada, Portugal, 1-4.

108. Abram, M., Białek, R., Szewczyk, S., Karolczak, J., Gibasiewicz, K., & Kargul, J. (2020). Remodeling of excitation energy transfer in extremophilic red algal PSI-LHCI complex during light adaptation. Biochimica et Biophysica Acta (BBA) - Bioenergetics, 1(1861), 148093.

109. Giera, W., Szewczyk, S., McConnell, M. D., Snellenburg, J., Redding, K. E., van Grondelle, R., & Gibasiewicz, K. (2014). Excitation dynamics in Photosystem I from Chlamydomonas reinhardtii. Comparative studies of isolated complexes and whole cells. Biochimica et Biophysica Acta (BBA) - Bioenergetics, 1837, 1756–1768.

110. Owens, T. G., Webb, S. P., Mets, L., Alberte, R. S., & Fleming, G. R. (1989). Antenna structure and excitation dynamics in photosystem I. Studies with mutants of *Chlamydomonas reinhardtii* lacking photosystem II. Biophysical Journal, 56, 95–106.

111. Gibasiewicz, K., Ramesh, V. M., Melkozernov, A. N., Lin, S., Woodbury, N. W., Blankenship, R. E., & Webber, A. N. (2001). Excitation dynamics in the core antenna of PS I from *Chlamydomonas reinhardtii* CC 2696 at room temperature. Journal of Physical Chemistry B, 105, 11498–11506.

112. Su, X., Ma, J., Pan, X., Zhao, X., Chang, W., Liu, Z., Zhang, X., & Li, M. (2019). Antenna arrangement and energy transfer pathways of a green algal photosystem-I–LHCI supercomplex. Nature Plants, 5, 273–281.

113. Szewczyk, S., Goyal, A., Abram, M., Burdziński, G., Kargul, J., & Gibasiewicz, K. (2022). Electron Transfer in a Bio-Photoelectrode Based on Photosystem I Multilayer Immobilized on the Conducting Glass. International journal of molecular sciences. 23, 4774.

114. Chandni, Andhariya, N., Pandey, OP., & Chudasama, B. (2013). A growth kinetic study of ultrafine monodispersed silver nanoparticles. The Royal Society of Chemistry, 3, 1127-1136.

115. Soto-Quintero, A., Guarrotxena, N., García, O. *et al.* Curcumin to Promote the Synthesis of Silver NPs and their Self-Assembly with a Thermoresponsive Polymer in Core-Shell Nanohybrids. *Sci Rep* **9**, 18187 (2019).

116. Behera, S.K., Mohanty, M.E. & Mohapatra, M. (2021). A Fluorescence Study of the Interaction of Anticancer Drug Molecule Doxorubicin Hydrochloride in Pluronic P123 and F127 Micelles. Journal of Fluorescence, 31, 17–27.

117. https://www.sigmaaldrich.com/PL/pl/product/sigma/d4641

118. Alexandridis, P., & Hatton, T. A. (1995). Poly(ethylene oxide) poly(propylene oxide) poly(ethylene oxide) block copolymer surfactants in aqueous solutions and at interfaces: thermodynamics, structure, dynamics, and modelling. Colloids and Surfaces A: Physicochemical and Engineering Aspects, 96, 1-46.

119. Dupuy, C., Auvray, X., & Petipas, C. (1997). Anomeric Effects on the Structure of Micelles of Alkyl Maltosides in Water. Langmuir, 13, 3965-3967.

120. Burdzinski, G., Bayda, M., Hug, G., Majchrak, M., Marciniec, B., Marciniak, B. (2011). Time-resolved studies on the photoisomerization of a phenylene-silylene-vinylene type compound in its first singlet excited state. Journal of Luminescence, 131, 577–580.

121. Goyal, A., Szewczyk, S., Burdziński, G., Abram, M., Kargul, J., Gibasiewicz, K. (2022). Competition between intra-protein charge recombination and electron transfer outside photosystem I complexes used for photovoltaic applications. Photochemical Photobiological Science, 21, 319–336.

122. Sapper, H., Kang, S. O., Paul, H. H., & Lohmann, W. (1982). The reversibility of the vitamin C redox system: Electrochemical rea-sons and biological aspects. Z. Naturforsch C Bioscience, 37(10), 942–946.

123. Kennet, E. C., & Kuchel, P. W. (2003). Redox reactions and elec-tron transfer across the red cell membrane. International Union of Biochemistry and Molecular Biology, 55(7), 375–385.

124. Efimov, I., Parkin, G., Millett, E. S., Glenday, J., Chan, C. K., Weedon, H., Randhawa, H., Basran, J., & Raven, E. L. (2014). A simple method for the determination of reduction potentials in heme proteins. FEBS Letters, 588(5), 701–704.

125. Nakamura, A., Suzawa, T., & Watanabe, T. (2004). Spectroelec-trochemical determination of the redox potential of P700 in spin-ach with an optically transparent thin-layer electrode. Chemistry Letters, 33(6), 688–689.

126. Izawa, S. (1980). Acceptors and donors and chloroplast electron transport. Methods in Enzymology, 69, 413–434.

127. Nguyen, K., & Bruce, B. D. (2014). Growing green electricity: Progress and strategies for use of Photosystem I for sustainable photovoltaic energy conversion. Biochimica et Biophysica Acta (BBA) - Bioenergetics, 9(1837), 1553–1566.

128. Trubitsin, B. V., Mamedov, M. D., Semenov, Y. A., & Tik-honov, A. N. (2014). Interaction of ascorbate with Photosystem I. Photochemical & Photobiological Sciences. Photosynthesis Research, 122(2), 215–231.

129. Izzo, M., Jacquet, M., Fujiwara, T., Harputlu, E., Mazur, R., Wróbel, P., Góral, T., Unlu, C.G., Ocakoglu, K., Miyagishima, S., Kargul, J. (2021). Development of a novel nanoarchitecture of the robust photosystem I from a volcanic microalga *Cyanidioschyzon merolae* on single layer graphene for improved photocurrent generation. International Journal of Molecular Sciences, 22, 8369.

130. Szalkowski, M., Harputlu, E., Kiliszek, M., Unlu, C.G., Mackowski, S., Ocakoglu, K., Kargul, J., Kowalska, D. (2020). Plasmonic enhancement of photocurrent generation in a photosystem I-based hybrid electrode. Journal of Material Chemistry C, 8, 5807–5814.

131. Zhang, J.Z., Sokol, K.P., Paul, N., Romero, E., van Grondelle, R., Reisner, E. (2016). Competing charge transfer pathways at the photosystem II-electrode interface. Nature Chemical Biology, 12, 1046–1052.

132. Kerker, M., Wang, D. S., & Chew, H. (1980). Surface enhanced Raman scattering (SERS) by molecules adsorbed at spherical particles: errata. Applied Optics, 19, 4128-4129.

133. Huang, H. H., Ni, X. P., Loy, G. L., Chew, C. H., Tan, K. L., & Loh, F. C., Deng, J. F., & Xu, G. Q. (1996). Photochemical Formation of Silver Nanoparticles in Poly(N-vinylpyrrolidone). Langmuir, 12, 909-912.

134. Chen, M., Feng, Y. G., Wang, X., Li, T. C., Zhang, J. Y., & Qian, D-Jin. (2007). Silver Nanoparticles Capped by Oleylamine: Formation, Growth, and Self-Organization. Langmuir, 23, 5296-5304.

135. Chudasama, B., Vala, A. K., Andhariya, N., Mehta, R. V., & Upadhyay, R. V. (2010). Highly bacterial resistant silver nanoparticles: synthesis and antibacterial activities. Journal of Nanoparticle Research, 12, 1677-1685.

136. Amirjani, A., Firouzi, F., & Haghshenas, D. F. (2020). Predicting the Size of Silver Nanoparticles from Their Optical Properties. Plasmonics, 15, 1077-1082.

137. Heard, S. M., Grieser, F., & Barraclough, C. J. (1983). The Characterization of Ag Sols by Electron Microscopy, Optical Absorption, and Electrophoresis. Journal of Colloid and Interface Science, 93, 545-555.

138. Kreibig, U. & Zacharias, P. (1970). Surface Plasma Resonances in Small Spherical Silver and Gold Particles. Zeitschrift für Physik A Hadrons and nuclei, 231, 128-143.

139. Quinten, M., & Kreibig, U. (1986). Optical Properties of Aggregates of Small Metal Particles. Surface Science, 172, 557-577.

140. Jiang, Z., Yuan, W., & Pan, H. (2005). Luminescence effect of silver nanoparticle in water phase. Spectrochimica Acta part A, 61, 2488-2494.

141. Alqudami, A., & Annapoorni, S. (2007). Fluorescence From Metallic Silver and Iron Nanoparticles Prepared by Exploding Wire Technique. Plasmonics, 2, 5-13.

142. Wang, Z., Wen, X. D., Hoffmann, R., Son, J. S., Li, R., Fang, C. C., Smilgies, Detlef-M. & Hyeon, T. (2010). Reconstructing a solid-solid phase transformation pathway in CdSe nanosheets with associated soft ligands. The Proceedings of the National Academy of Sciences, 107, 17119-17124.

143. Schneid, A. C., Pereira, M. B., Horowitz, F., Mauler, R. S., Matte, C. R., Klein, M. P., Hertz, P. F., Costa, T. M. H., de Menezes, E. W., & Benvenutti, E. V. (2015). Silver Nanoparticle Thin Films Deposited on Glass Surface Using an Ionic Silsesquioxane as Stabilizer and as Crosslinking Agent. Journal of the Brazilian Chemical Society, 26, 1004-1012.

144. Schneid, A. C., Roesch, E. W., Sperb, F., Matte, U., da Silveira, N. P., Costa, T. M. H., Benvenutti, E. V., & de Menezes, E. W. (2014). Silver nanoparticle–ionic silsesquioxane: a new system proposed as an antibacterial agent. Journal of Material Chemistry B, 2, 1079-1086.

145. Wei, D., Sun, W., Qian, W., Ye, Y., & Ma, X. (2009). The synthesis of chitosan-based silver nanoparticles and their antibacterial activity. Carbohydrate Research, 344, 2375-2382.

146. Brecht, M., Hussels, M., Nieder, J. B., Fang, H., & Elsässer, C. (2012). Plasmonic interactions of photosystem I with Fischer patterns made of Gold and Silver. Chemical Physics, 406, 15-20.

147. Savikhin, S., Peter, Xu, W., Martinsson, P., Chitnis, P. R., & Struve, W. S. (2001). Kinetics of Charge Separation and $A_0^- \rightarrow A_1$ Electron Transfer in Photosystem I Reaction Centers**,** Biochemistry, 40 (31), 9282–9290.

148. Kudelski, A. (2002). Raman study on the structure of 3-mercaptopropionic acid monolayers on silver. Surface Science, 502-503, 219-223.

149. Marques, F. C., Oliveira, G. P., Teixeira, R. A. R., Justo, R. M. S., Neves, T. B. V., & Andrade, G. F. S. (2018). Characterization of 11-mercaptoundecanoic and 3-mercaptopropionic acids adsorbed on silver by surface-enhanced Raman scattering, Vibrational Spectroscopy. Vibrational Spectroscopy, 98, 139-144.

150. Nuzzo, R. G., Dubois, L. H., & Allara, D. L. (1990). Fundamental Studies of Microscopic Wetting on Organic Surfaces. 1. Formation and Structural Characterization of a Self-Consistent Series of Polyfunctional Organic Monolayers. American Chemical Society, 112, 558-569.

Journal Contribution

Statements of the Co-authors

mgr Alice Goyal
Faculty of Physics and Astronomy
Adam Mickiewicz University, Poznań
Ul. Uniwersytetu Poznańskiego 2
61-614 Poznań, Poland
Email: aligoy@amu.edu.pl

Contribution statement

Hereby, I declare my contribution to the following publications:

1. Goyal, A., Szewczyk, S., Burdziński, G., Abram, M., Kargul, J., Gibasiewicz, K. (2022). Competition between intra-protein charge recombination and electron transfer outside photosystem I complexes used for photovoltaic applications. Photochemical Photobiological Science, 21, 319–336.
https://doi.org/10.1007/s43630-022-00170-x

   I declare the following contribution to this publication:
   - Preparation of samples for steady state absorption, transient absorption spectroscopy and photocurrent measurements
   - Participation in time-resolved absorption and photocurrent measurements
   - Data analysis and calculations
   - Participation in discussion of results
   - Participation in preparation of the drafts of this manuscript

2. Szewczyk, S., Goyal, A., Abram, M., Burdziński, G., Kargul, J., & Gibasiewicz, K. (2022). Electron Transfer in a Bio-Photoelectrode Based on Photosystem I Multilayer Immobilized on the Conducting Glass. International Journal of Molecular Sciences, 23, 4774.
https://doi.org/10.3390/ijms23094774

   I declare the following contribution to this publication:
   - Preparation of samples for steady state absorption, transient absorption spectroscopy and photocurrent measurements
   - Participation in time-resolved absorption and photocurrent measurements
   - Data analysis and calculations
   - Participation in discussion of results
   - Participation in preparation of the drafts of this manuscript

3. Koralewski, M., Paprzycka, M., Goyal, A., & Gibasiewicz, K. (2023). Faraday rotation enhancement for colloidal spherical Au and Ag nanoparticles and their mixtures. Journal of magnetism and Magnetic Materials, 588, 171461. https://doi.org/10.1016/j.jmmm.2023.171461

I declare the following contribution to this publication:

- Preparation of colloidal spherical Ag nanoparticles
- Participation in characterization of Ag nanoparticles

Signature

Statements of the Co-authors

dr hab. Krzysztof Gibasiewicz, prof. UAM
Faculty of Physics and Astronomy
Adam Mickiewicz University, Poznań
Ul. Uniwersytetu Poznańskiego 2
61-614 Poznań, Poland
Email: krzyszgi@amu.edu.pl

Contribution statement

Hereby, I declare my contribution to the following publications:

1. Goyal, A., Szewczyk, S., Burdziński, G., Abram, M., Kargul, J., Gibasiewicz, K. (2022). Competition between intra-protein charge recombination and electron transfer outside photosystem I complexes used for photovoltaic applications. Photochemical Photobiological Science, 21, 319–336.
https://doi.org/10.1007/s43630-022-00170-x

   I declare the following contribution to this publication:

   - Conceptualization of studies
   - Planning and supervising time-resolved absorption measurements
   - Supervising data analysis
   - Writing the first draft and editing the final version of manuscript

2. Szewczyk, S., Goyal, A., Abram, M., Burdziński, G., Kargul, J., & Gibasiewicz, K. (2022). Electron Transfer in a Bio-Photoelectrode Based on Photosystem I Multilayer Immobilized on the Conducting Glass. International journal of molecular sciences, 23, 4774.
https://doi.org/10.3390/ijms23094774

   I declare the following contribution to this publication:

   - Conceptualization of studies
   - Planning and supervising time-resolved absorption measurements
   - Supervising data analysis
   - Creating model of multilayer film
   - Writing the first draft and editing the final version of manuscript

3. Koralewski, M., Paprzycka, M., Goyal, A., & Gibasiewicz, K. (2023). Faraday rotation enhancement for colloidal spherical Au and Ag nanoparticles and their mixtures. Journal of magnetism and Magnetic Materials, 588, 171461. https://doi.org/10.1016/j.jmmm.2023.171461

I declare the following contribution to this publication:

- Consulting the project of studies
- Participation in editing the final version of manuscript

K. Gibasiewicz

Signature

dr Sebastian Szewczyk
Faculty of Physics and Astronomy
Adam Mickiewicz University, Poznań
Ul. Uniwersytetu Poznańskiego 2
61-614 Poznań, Poland
Email: sszew@amu.edu.pl

Contribution statement

Hereby, I declare my contribution to the following publications:

1. Goyal, A., Szewczyk, S., Burdziński, G., Abram, M., Kargul, J., Gibasiewicz, K. (2022). Competition between intra-protein charge recombination and electron transfer outside photosystem I complexes used for photovoltaic applications. Photochemical Photobiological Science, 21, 319–336.
https://doi.org/10.1007/s43630-022-00170-x

   I declare the following contribution to this publication:

   - Isolation of the PSI particles (cyanobacterial, green algae)
   - Preparation of samples for steady state absorption, transient absorption spectroscopy in solution as well as on the surface
   - Performing photocurrent measurements
   - Participation in time-resolved absorption measurements
   - Participation in editing the draft and final version of manuscript

2. Szewczyk, S., Goyal, A., Abram, M., Burdziński, G., Kargul, J., Gibasiewicz, K. (2022). Electron Transfer in a Bio-Photoelectrode Based on Photosystem I Multilayer Immobilized on the Conducting Glass. International journal of molecular sciences, 23, 4774.
https://doi.org/10.3390/ijms23094774

   I declare the following contribution to this publication:

   - Preparation of the PSI multilayer on the surface
   - Preparation of samples for steady state absorption and transient absorption spectroscopy
   - Performing photocurrent measurements

- Performing time-resolved absorption measurements – spectroelectrochemical cell assembly and controlling the applied potential during experiments.
- Data analysis of the electrochemical measurements
- Participation in editing the draft and final version of manuscript

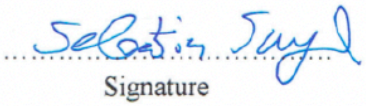

Signature

Statements of the Co-authors

dr hab. Joanna Kargul, prof. UW
Solar Fuels Laboratory, Centre of New Technologies,
University of Warsaw, Warsaw
ul. Banacha 2C, 02-097 Warszawa, Poland
Email: j.kargul@cent.uw.edu.pl

Contribution statement

Hereby, I declare my contribution to the following publications:

1. Goyal, A., Szewczyk, S., Burdziński, G., Abram, M., Kargul, J., Gibasiewicz, K. (2022). Competition between intra-protein charge recombination and electron transfer outside photosystem I complexes used for photovoltaic applications. Photochemical Photobiological Science, 21, 319–336.
https://doi.org/10.1007/s43630-022-00170-x

   I declare the following contribution to this publication:

   - Conceptualization of studies
   - Supervising data analysis
   - Writing the first draft and editing the final version of manuscript

2. Szewczyk, S., Goyal, A., Abram, M., Burdziński, G., Kargul, J., & Gibasiewicz, K. (2022). Electron Transfer in a Bio-Photoelectrode Based on Photosystem I Multilayer Immobilized on the Conducting Glass. International journal of molecular sciences, 23, 4774.
https://doi.org/10.3390/ijms23094774

   I declare the following contribution to this publication:

   - Conceptualization of studies
   - Supervising data analysis
   - Writing the first draft and editing the final version of manuscript

Joanna Kargul; Uniwersytet Warszawski
Digitally signed by Joanna Kargul; Uniwersytet Warszawski
Date: 2025.05.27 21:56:16 +02'00'

Signature

Statements of the Co-authors

dr Mateusz Abram
Centre of the New Technologies
University of Warsaw, Warsaw
ul. Stefana Banacha 2c
02-097 Warszawa, Poland
email: m.abram@cent.uw.edu.pl

Contribution statement

Hereby, I declare my contribution to the following publications:

1. Goyal, A., Szewczyk, S., Burdziński, G., Abram, M., Kargul, J., Gibasiewicz, K. (2022). Competition between intra-protein charge recombination and electron transfer outside photosystem I complexes used for photovoltaic applications. Photochemical Photobiological Science, 21, 319–336.
https://doi.org/10.1007/s43630-022-00170-x

   I declare the following contribution to this publication:

   - Red algal controlled culture preparation and the isolation of the thylakoid membranes
   - Isolation and characterisation of the active photosynthetic complexes
   - Cooperation in designing the treatment of the active PSI supercomplexes

2. Szewczyk, S., Goyal, A., Abram, M., Burdziński, G., Kargul, J., & Gibasiewicz, K. (2022). Electron Transfer in a Bio-Photoelectrode Based on Photosystem I Multilayer Immobilized on the Conducting Glass. International journal of molecular sciences, 23, 4774.
https://doi.org/10.3390/ijms23094774

   I declare the following contribution to this publication:

   - Red algal controlled culture preparation and the isolation of the thylakoid membranes
   - Isolation and characterisation of the active photosynthetic complexes
   - Cooperation in designing the treatment of the active PSI supercomplexes

Mateusz Abram
.....
Signature

Statements of the Co-authors

Prof. hab. Gotard Burdziński
Faculty of Physics and Astronomy
Adam Mickiewicz University, Poznań
Ul. Uniwersytetu Poznańskiego 2
61-614 Poznań, Poland
Email: gotardb@amu.edu.pl

Contribution statement

Hereby, I declare my contribution to the following publications:

1. Goyal, A., Szewczyk, S., Burdziński, G., Abram, M., Kargul, J., Gibasiewicz, K. (2022). Competition between intra-protein charge recombination and electron transfer outside photosystem I complexes used for photovoltaic applications. Photochemical Photobiological Science, 21, 319–336. https://doi.org/10.1007/s43630-022-00170-x

   I declare the following contribution to this publication:

   - Set up the laser flash photolysis apparatus and assisted with transient absorption measurements
   - Reviewed and made minor corrections to the final version of the manuscript

2. Szewczyk, S., Goyal, A., Abram, M., Burdziński, G., Kargul, J., & Gibasiewicz, K. (2022). Electron Transfer in a Bio-Photoelectrode Based on Photosystem I Multilayer Immobilized on the Conducting Glass. International journal of molecular sciences, 23, 4774. https://doi.org/10.3390/ijms23094774

   I declare the following contribution to this publication:

   - Set up the laser flash photolysis apparatus and assisted with transient absorption measurements
   - Reviewed and made minor corrections to the final version of the manuscript

Gotard Burdziński
.....
Signature

Statements of the Co-authors

Prof. dr hab. Marceli Koralewski
Faculty of Physics and Astronomy
Adam Mickiewicz University, Poznań
Ul. Uniwersytetu Poznańskiego 2
61-614 Poznań, Poland
Email: koral@amu.edu.pl

Contribution statement

Hereby, I declare my contribution to the following publications:

1. Koralewski, M., Paprzycka, M., Goyal, A., & Gibasiewicz, K. (2023). Faraday rotation enhancement for colloidal spherical Au and Ag nanoparticles and their mixtures. Journal of Magnetism and Magnetic Materials, 588, 171461. https://doi.org/10.1016/j.jmmm.2023.171461

I declare the following contribution to this publication:

- Conceptualization of studies
- Participation and supervising measurements
- Participation and supervising data analysis
- Writing the first draft and editing the final version of manuscript

Koralewski

Signature

Declaration

I hereby declare that except where specific reference is made to the work of others, the contents of this dissertation are original and have not been submitted in whole or in part for consideration for any other degree or qualification in this, or any other university. This dissertation is my own work and all the contents of the dissertation have been obtained by legal means.

.....

mgr Alice Goyal Wypychowska